N°d'ordre NNT : 2022ISAL0129

# THESE de DOCTORAT DE L'UNIVERSITE DE LYON
opérée au sein de
**L'Institut National des Sciences Appliquées de Lyon**

**Ecole Doctorale** N° ED 34
**Matériaux de Lyon**

**Spécialité/discipline de doctorat** : Science des Matériaux

Soutenue publiquement le 12/12/2022, par:
**Javier Antonio Gonzalez Joa**

---

# Mesoscale dislocation simulation accounting for surfaces using the superposition method: application to nanomechanics

---

Devant le jury composé de :

| | | | |
|---|---|---|---|
| Dan Mordehai | Associate Professor | Technion | Rapporteur |
| Fabien Onimus | Chercheur CEA | CEA Saclay | Rapporteur |
| Celine Gerard | Chargé de Recherche CNRS | ENSMA | Examinatrice |
| Karine Masenelli-Varlot | Professeur des Universités | INSA-LYON | Examinatrice |
| David Rodney | Professeur des Universités | Univ. LYON | Examinateur |
| Laurent Pizzagalli | Directeur de Recherche CNRS | Univ. Poitiers | Examinateur |
| Marc Fivel | Directeur de Recherche CNRS | INP Grenoble | Invité |
| Laurent Dupuy | Chercheur CEA | CEA Saclay | Invité |
| Peter Råback | Docteur | CSC-IT | Invité |
| Michel Perez | Professeur des Universités | INSA-LYON | Directeur de thèse |
| Jonathan Amodeo | Chargé de Recherche CNRS | AMU | Directeur de thèse |

# Département FEDORA – INSA Lyon - Ecoles Doctorales

| SIGLE | ECOLE DOCTORALE | NOM ET COORDONNEES DU RESPONSABLE |
|---|---|---|
| **CHIMIE** | **CHIMIE DE LYON**<br>**https://www.edchimie-lyon.fr**<br>Sec. : Renée EL MELHEM<br>Bât. Blaise PASCAL, 3e étage<br>secretariat@edchimie-lyon.fr | **M. Stéphane DANIELE**<br>C2P2-CPE LYON-UMR 5265<br>Bâtiment F308, BP 2077<br>43 Boulevard du 11 novembre 1918<br>69616 Villeurbanne<br>**directeur@edchimie-lyon.fr** |
| **E.E.A.** | **ÉLECTRONIQUE, ÉLECTROTECHNIQUE, AUTOMATIQUE**<br>**https://edeea.universite-lyon.fr**<br>Sec. : Stéphanie CAUVIN<br>Bâtiment Direction INSA Lyon<br>Tél : 04.72.43.71.70<br>secretariat.edeea@insa-lyon.fr | **M. Philippe DELACHARTRE**<br>INSA LYON<br>Laboratoire CREATIS<br>Bâtiment Blaise Pascal, 7 avenue Jean Capelle<br>69621 Villeurbanne CEDEX<br>Tél : 04.72.43.88.63<br>**philippe.delachartre@insa-lyon.fr** |
| **E2M2** | **ÉVOLUTION, ÉCOSYSTÈME, MICROBIOLOGIE, MODÉLISATION**<br>**http://e2m2.universite-lyon.fr**<br>Sec. : Bénédicte LANZA<br>Bât. Atrium, UCB Lyon 1<br>Tél : 04.72.44.83.62<br>secretariat.e2m2@univ-lyon1.fr | **Mme Sandrine CHARLES**<br>Université Claude Bernard Lyon 1<br>UFR Biosciences<br>Bâtiment Mendel<br>43, boulevard du 11 Novembre 1918<br>69622 Villeurbanne CEDEX<br>**sandrine.charles@univ-lyon1.fr** |
| **EDISS** | **INTERDISCIPLINAIRE SCIENCES-SANTÉ**<br>**http://ediss.universite-lyon.fr**<br>Sec. : Bénédicte LANZA<br>Bât. Atrium, UCB Lyon 1<br>Tél : 04.72.44.83.62<br>secretariat.ediss@univ-lyon1.fr | **Mme Sylvie RICARD-BLUM**<br>Institut de Chimie et Biochimie Moléculaires et Supramoléculaires (ICBMS) - UMR 5246 CNRS - Université Lyon 1<br>Bâtiment Raulin - 2ème étage Nord<br>43 Boulevard du 11 novembre 1918<br>69622 Villeurbanne Cedex<br>Tél : +33(0)4 72 44 82 32<br>**sylvie.ricard-blum@univ-lyon1.fr** |
| **INFOMATHS** | **INFORMATIQUE ET MATHÉMATIQUES**<br>**http://edinfomaths.universite-lyon.fr**<br>Sec. : Renée EL MELHEM<br>Bât. Blaise PASCAL, 3e étage<br>Tél : 04.72.43.80.46<br>infomaths@univ-lyon1.fr | **M. Hamamache KHEDDOUCI**<br>Université Claude Bernard Lyon 1<br>Bât. Nautibus<br>43, Boulevard du 11 novembre 1918<br>69 622 Villeurbanne Cedex France<br>Tél : 04.72.44.83.69<br>**hamamache.kheddouci@univ-lyon1.fr** |
| **Matériaux** | **MATÉRIAUX DE LYON**<br>**http://ed34.universite-lyon.fr**<br>Sec. : Yann DE ORDENANA<br>Tél : 04.72.18.62.44<br>yann.de-ordenana@ec-lyon.fr | **M. Stéphane BENAYOUN**<br>Ecole Centrale de Lyon<br>Laboratoire LTDS<br>36 avenue Guy de Collongue<br>69134 Ecully CEDEX<br>Tél : 04.72.18.64.37<br>**stephane.benayoun@ec-lyon.fr** |
| **MEGA** | **MÉCANIQUE, ÉNERGÉTIQUE, GÉNIE CIVIL, ACOUSTIQUE**<br>**http://edmega.universite-lyon.fr**<br>Sec. : Stéphanie CAUVIN<br>Tél : 04.72.43.71.70<br>Bâtiment Direction INSA Lyon<br>mega@insa-lyon.fr | **M. Jocelyn BONJOUR**<br>INSA Lyon<br>Laboratoire CETHIL<br>Bâtiment Sadi-Carnot<br>9, rue de la Physique<br>69621 Villeurbanne CEDEX<br>**jocelyn.bonjour@insa-lyon.fr** |
| **ScSo** | **ScSo***<br>**https://edsciencessociales.universite-lyon.fr**<br>Sec. : Mélina FAVETON<br>INSA : J.Y. TOUSSAINT<br>Tél : 04.78.69.77.79<br>melina.faveton@univ-lyon2.fr | **M. Bruno MILLY**<br>Université Lumière Lyon 2<br>86 Rue Pasteur<br>69365 Lyon CEDEX 07<br>**bruno.milly@univ-lyon2.fr** |

*ScSo : Histoire, Géographie, Aménagement, Urbanisme, Archéologie, Science politique, Sociologie, Anthropologie

# Acknowledgements

First of all, I would like to thank Pr. Dan Mordehai and Dr. Fabien Onimus, reviewers of my thesis manuscript as well as acknowledge all the members of my PhD jury for their helpful advices.
I would like to express my deepest gratitude to my supervisors: Dr. Jonathan Amodeo and Pr. Michel Perez; for their support, constant encouragement and guidance. Indeed, it was a huge learning step to produce a research work under your supervision. Furthermore, thank you very much for your courage and patience.
To Pr. Laurent Dupuy; for all his support and knowledge that have made this work possible. Thank you very much for sharing Numodis with me, your home, and for all the time dedicated to produce El-Numodis.
To Dr. Peter Råback (principal developer of the FEM software Elmer) for the time shared with us, and the first scripts that latter on becomes El-Numodis. It was a pleasure to make science with you.
Also I would like to thanks Pr. Marc Fivel for his reviews and help regarding El-Numodis and some of the benchmarks presented in this work.
I would like to mention my gratitude to Dr. Christophe Le-Bourlot, Dr. Sylvain Dancette and Dr. Joel Lachambre for all our technical discussions that helped to improve El-Numodis.
In the same way I would like to thanks Dr. Pierre Antoine Geslin and Dr. Ali Rida for all our discussion that helped me to interpret some of the simulations performed with El-Numodis.
I general, I am happy to express my gratitude to all members of the MATEIS laboratory, for all the time shared during this four years; and for allowing me to be part of such a healthy group.
Last but not least, to my family. To my mother and father, for their understanding and encouraging even being far. To Rachel and Inti for all their support of each day.

To all of you; thanks a lot.

# Abstract

Nano-objects (wires, particles, thin films) are known for their outstanding mechanical properties when compared to their bulk counterparts. Various experimental techniques (transmission and scanning electron microscopy, X-ray diffraction) are used to investigate nano-objects, all complemented by computational approaches such as molecular dynamics. While modelling atomic-scale processes in the details, molecular dynamics is limited in terms of sample size and strain rates opening doors to other methods such as the discrete dislocation dynamics. Discrete dislocation dynamics is able to describe the evolution of a dislocation population at the mesoscale but is mostly used to describe quasi-infinite ensembles using either particularly large simulation cells or relying on periodic boundary conditions. Consequently, standalone discrete dislocation dynamics cannot provide a complete description of sample surfaces that are known to be at the roots of several nanoscale processes.

This study aims at better and faithfully model the mechanics of nano-objects accounting for the complex interactions between dislocations and surfaces. For this purpose, a new tool called El-Numodis was developed. El-Numodis relies on the coupling of the discrete dislocation dynamics code Numodis with the finite elements code Elmer using the superposition method in which the stress field generated by a dislocation population is corrected at the virtual surfaces of a finite-size sample using a finite-element elastic solver. In this work, we present the main development stages of El-Numodis (coupling drivers, dislocation image forces, nucleation algorithm, etc.) as well as several applications including analytically soluble elasticity problems in which surfaces are involved. As an example, the modelling of face-centered cubic metal thin films practically demonstrates the influence of surfaces on nano-objects mechanics. Finally, El-Numodis is used to model the mechanics of ceramics nanoparticles for which atomistically-informed dislocation nucleation as combined to the transition state theory allow to investigate the role of size, temperature and strain rate on the mechanical properties of MgO nanoparticles.

# Résumé en français

Les nano-objets (fils, particules, films minces) sont connus pour leurs propriétés mécaniques exceptionnelles au regard de leurs homologues massifs. Diverses techniques expérimentales (microscopie électronique à transmission ou à balayage, diffraction des rayons X) sont utilisées pour étudier les nano-objets, complétées par des approches numériques telle que la dynamique moléculaire. Bien que fournissant des détails à l'échelle atomique, la dynamique moléculaire reste limitée en termes de taille et de vitesse de déformation, ouvrant la porte à d'autres méthodes comme la dynamique des dislocations discrète. La dynamique des dislocations discrète permet de décrire l'évolution d'une population de dislocations à l'échelle du grain mais est généralement utilisée dans des ensembles quasi-infinis en utilisant des cellules de simulation particulièrement grandes ou des conditions limites périodiques. Par conséquent, la dynamique des dislocations discrète seule ne peut fournir une description physique des surfaces d'un échantillon, surfaces à l'origine de nombreux processus à l'échelle nanométrique.

Cette étude vise à modéliser mieux et plus fidèlement la mécanique des nano-objets en tenant compte des interactions complexes entre les dislocations et les surfaces. Pour ce faire, un nouvel outil appelé El-Numodis a été développé. El-Numodis repose sur le couplage du code de dynamique des dislocations discrète Numodis avec le code d'éléments finis Elmer en utilisant la méthode de superposition. Nous présentons ici les étapes de développement d'El-Numodis (pilotes de couplage, forces d'image des dislocations, algorithme de nucléation, etc.) ainsi que plusieurs applications incluant des problèmes d'élasticité classiques dans lesquels des surfaces sont impliquées. A titre d'exemple, la modélisation de films minces métalliques fcc montre l'influence majeure des surfaces sur la mécanique des nano-objets. Enfin, El-Numodis est utilisé pour modéliser la mécanique de nanoparticules céramiques où la nucléation de dislocation informée de manière atomistique, combinée à la théorie de l'état de transition, permet d'étudier le rôle de la taille, température et de la vitesse de déformation sur la déformation de nanocubes de MgO.

# List of acronyms and abbreviations

| | |
|---|---|
| **BC** | Boundary Condition |
| **BCC** | Body Centered Cubic |
| **BEM** | Boundary Elements Method |
| **BVP** | Boundary Value Problem |
| **CPU** | Central Processing Unit |
| **DCM** | Discrete Continuous Method |
| **DD** | Dislocation Dynamics |
| **DDD** | Discrete Dislocation Dynamics |
| **DOF** | Degree Of Freedom |
| **FCC** | Face Centered Cubic |
| **FEM** | Finite Element Method |
| **FFT** | Fast Fourier Transform |
| **FIB** | Focused Ion Beam |
| **FR** | Frank-Read |
| **GB** | Grain Boundary |
| **GW** | Gosling and Willis |
| **HCP** | Hexagonal Close Packed |
| **HL** | Hirth and Lothe |
| **ID** | Identity |
| **KMC** | Kinetic Monte-Carlo |
| **MD** | Molecular Dynamics |
| **MS** | Molecular Statics |
| **NC** | Nanocubes |
| **NEB** | Nudged Elastic Band |
| **NP** | Nanoparticle |
| **NW** | Nanowires |
| **PBC** | Periodic Boundary Condition |
| **SDN** | Surface Dislocation Nucleation |
| **SEM** | Scanning Electron Microscopy |
| **SPM** | Superposition Method |
| **TEM** | Transmission Electron Microscopy |
| **TST** | Transition State Theory |
| **URN** | Uniform Random Numbers |

# Contents

**Liste des écoles doctorales** **i**

**Acknowledgements** **iii**

**Abstract** **v**

**Résumé en français** **vii**

**List of acronyms and abbreviations** **ix**

**Contents** **xi**

**General introduction** **1**

**1 Literature review** **5**

- 1.1 Mechanics at small-scales . . . . . 6
  - 1.1.1 Decreasing the grain size of bulk materials . . . . . 6
  - 1.1.2 Deformation of micro- and nano-objects . . . . . 11
- 1.2 Surfaces and dislocations at the nanoscale . . . . . 22
  - 1.2.1 Surfaces and nano-objects . . . . . 22
  - 1.2.2 Modeling surface and dislocation interactions . . . . . 24
    - 1.2.2.1 The superposition method . . . . . 24
    - 1.2.2.2 The discrete-continuous method . . . . . 25
    - 1.2.2.3 Fast Fourier transform based method . . . . . 27
- 1.3 Conclusion . . . . . 30

**2 Numerical methods and parent tools** **33**

- 2.1 Generalities about discrete dislocation dynamics . . . . . 34
  - 2.1.1 Nodal and lattice-based approaches . . . . . 35
  - 2.1.2 Stress and dislocation velocity . . . . . 36
  - 2.1.3 Boundary conditions . . . . . 37
  - 2.1.4 Initial configuration and loading modes . . . . . 38
  - 2.1.5 Dislocation short-range interactions . . . . . 39

2.2 Introduction to Numodis . . . . . . . . . . . . . . . . . . . . . . . . . . 41
  2.2.1 Nodal forces and energy . . . . . . . . . . . . . . . . . . . . . . . 41
  2.2.2 Equation of motion and time integration . . . . . . . . . . . . . . . . 42
  2.2.3 Dislocation stress field calculation . . . . . . . . . . . . . . . . . . 43
  2.2.4 Dislocation displacement field calculation . . . . . . . . . . . . . . . 44
  2.2.5 Dislocation meshing . . . . . . . . . . . . . . . . . . . . . . . . . 46
2.3 Introduction to Elmer and the finite-element method . . . . . . . . . . . . . 47
  2.3.1 Elmer software . . . . . . . . . . . . . . . . . . . . . . . . . . . 47
  2.3.2 Linear static elastic solver . . . . . . . . . . . . . . . . . . . . . 50
2.4 Conclusion . . . . . . . . . . . . . . . . . . . . . . . . . . . . . . . 52

**3 El-Numodis 55**

3.1 The superposition method . . . . . . . . . . . . . . . . . . . . . . . . 56
3.2 El-Numodis . . . . . . . . . . . . . . . . . . . . . . . . . . . . . . . 58
  3.2.1 Introduction to El-Numodis framework . . . . . . . . . . . . . . . . . 58
  3.2.2 External drivers and main functions . . . . . . . . . . . . . . . . . . 60
  3.2.3 Stress-to-force conversion . . . . . . . . . . . . . . . . . . . . . . 62
  3.2.4 Stress interpolation . . . . . . . . . . . . . . . . . . . . . . . . . 64
  3.2.5 Loading . . . . . . . . . . . . . . . . . . . . . . . . . . . . . . . 65
  3.2.6 Mirror dislocation . . . . . . . . . . . . . . . . . . . . . . . . . . 67
3.3 Conclusion . . . . . . . . . . . . . . . . . . . . . . . . . . . . . . . 68

**4 Solving boundary problems 71**

4.1 Self-stress of an infinite dislocation . . . . . . . . . . . . . . . . . . . 72
4.2 Infinite edge dislocation near a free-surface . . . . . . . . . . . . . . . . 74
  4.2.1 The image method . . . . . . . . . . . . . . . . . . . . . . . . . . 74
  4.2.2 The Airy functions . . . . . . . . . . . . . . . . . . . . . . . . . . 77
  4.2.3 Influence of the pseudo-mirror dislocation construction . . . . . . . . 82
4.3 Square-loop dislocation near a free-surface . . . . . . . . . . . . . . . . 85
  4.3.1 The Gosling and Willis method . . . . . . . . . . . . . . . . . . . . 86
4.4 Test case: thin films tensile test . . . . . . . . . . . . . . . . . . . . . 89
  4.4.1 Numodis *vs.* El-Numodis: surface effects comparison . . . . . . . . . 95
4.5 Conclusion . . . . . . . . . . . . . . . . . . . . . . . . . . . . . . . 100

**5 Compression of MgO nanoparticles 103**

5.1 Introduction to dislocation nucleation and harmonic transition state theory 104
5.2 Dislocation nucleation in El-Numodis . . . . . . . . . . . . . . . . . . . 106
  5.2.1 Simplified approach (constant stress) . . . . . . . . . . . . . . . . . 106
    5.2.1.1 Post-nucleation site shutdown . . . . . . . . . . . . . . . . 107
    5.2.1.2 Algorithm and implementation . . . . . . . . . . . . . . . . 107
    5.2.1.3 Applications . . . . . . . . . . . . . . . . . . . . . . . . 111

5.2.2 Extended approach: application to MgO nanoparticles . . . . . . . . 114
5.2.2.1 Introduction to atomic-scale dislocation nucleation in MgO nanoparticles . . . . . . . . . . . . . . . . . . . . . . . . . . 114
5.2.2.2 Extension of the dislocation nucleation algorithm . . . . . 116
5.3 Mesoscale modeling of dislocation nucleation in MgO nanoparticles under compression . . . . . . . . . . . . . . . . . . . . . . . . . . . . . . . . 122
5.3.1 Deformation at extreme strain rate . . . . . . . . . . . . . . . . . . . . 122
5.3.1.1 Mechanical response . . . . . . . . . . . . . . . . . . . . . . . 123
5.3.1.2 Corner dislocation nucleation . . . . . . . . . . . . . . . . . 123
5.3.2 Towards experimental conditions of deformation . . . . . . . . . . . 127
5.3.2.1 Influence of strain rate . . . . . . . . . . . . . . . . . . . . . 127
5.3.2.2 Influence of temperature . . . . . . . . . . . . . . . . . . . . 129
5.3.2.3 Size-effects and limitations . . . . . . . . . . . . . . . . . . . 132
5.4 Conclusion . . . . . . . . . . . . . . . . . . . . . . . . . . . . . . . . . . 137

**Conclusion and perspectives** **139**

**References** **143**

# General introduction

The recent progresses observed in various fields of technological applications (like medicine, electronics and mechanics) are often implicitly related to the study of nano-objects *i.e.,* sample with dimensions of few tens nm. Their broad field of applications is related to the radical changes in their physical properties. For instance in medicine, encapsulated nanoparticles with high chemical absorption are used as drugs delivers [MOH 07] or for imagery and pathology treatments [PAR 14]. In information storage technology, nanowires are used for their superparamagnetic capabilities including very fast response to external fields with almost zero remanence [LU 07, ZHA 10]. In the fields of tribology and mechanics, nanoparticles are used to improve the performance of lubricants [AKB 12, CUI 20] or to make implants [LI 13] due to their high resistance.

On the other hand, nanocrystals and their improved mechanical properties are used to enhance materials with larger dimensions. At higher scales, nanoparticles are used as building blocks of nanocrystalline materials to be sintered and compacted to improve the properties of compounds later used in devices requiring high mechanical resistance. Nanowires can also be used as strengthening constituents [ELS 07, SHE 19]. When built from smaller grains, the mechanical performances of nanocrystalline materials are impacted by the fabrication method, the size, shape and distribution of nanograins as well as by the presence of pores and other defects [ALA 15]. In most of the cases, the strength variations observed in nanocrystalline materials are related to the grain size following the Hall-Petch, or at even smaller size, the inverse Hall-Petch model [HAN 04, PAD 01]. In the inverse Hall-Petch regime, elementary processes implying shear processes within the grain boundaries are also involved. Understanding the mechanics of nanocrystalline materials requires the investigation of both; the isolated nanograin and the nanopowders used for their fabrication in a bottom-up approach.

Besides classical bulk characterization, nanomaterials can be investigated running mechanical tests on individual building grains that generally follow the "smaller is stronger" paradigm [UCH 09, GRE 11]. The strength increase of nanocrystals is also concomitant to an increase of their ductility. However, the reasons for such mechanical improvements are many and can vary depending on sample shape or aspect ratio. Several numerical and experimental methods exist to investigate the mechanical properties of nano-objects. For example, nanocompression in the scanning or transmission electron microscope are the most used techniques for nanoparticles experimental characterization. Experiments are reported for size ranging from few 100 nm down to few tens nm and for low deformation rate (from $10^{-4}$ to $\sim 1$ $s^{-1}$). While the use of the transmission electron microscope allows for microstructure, defect and surface characterizations, it is still a complex and tedious method and several intrinsic or extrinsic problems including sample misalignment, contamination and oxidation are commonly reported [WIL 96, ZAE 11].

On the other hand, computational methods provide a support often used to help to interpret experimental outcomes. Molecular dynamics is the most-employed numerical technique used to simulate the mechanical properties of nano-objects [KOM 01, AMO 21b]. It is based on interatomic potentials that allow to compute atomic forces and integrate the dynamics of all the atoms present in a sample under load. However, due to computational costs, sample size is limited to few tens of nm in molecular dynamics and simulations are performed at super high strain rate ($\sim 10^8$ $s^{-1}$). Moreover, the discrete dislocation dynamics (also called dislocation dynamics) simulation technique allows to increase sample dimensions (up to a few hundred microns) and reduce the strain rate, both getting closer to experimental conditions. Discrete dislocation dynamics allows to model dislocation lines based on constitutive equations rather than atomic interactions, therefore, discrete dislocation dynamics simulations computationally overcomes the size and time limits of molecular dynamics. However, discrete dislocation dynamics codes are generally developed for bulk applications and often lack of nanoscale specifications. For examples, former discrete dislocation dynamics codes missed a criterion for dislocation nucleation that we will see is a crucial process in nanomechanics. They also generally do not account for the interaction between dislocations and surfaces as well as images forces generated by free surfaces.

Based on these considerations, one can rise the question on the necessity of a numerical tool to investigate the mechanical properties of nano- and micro-objects including the effect of sample size and strain rate as well as the ability to account for most of nanoscale elementary deformation processes. In other words; is it possible to break the spacial and temporal limits of the current simulations tools considering the effects of surfaces when modeling small-scale mechanics?

Here we will see that the answer might rely on the development of a multi-scale modeling approach (Figure 1) that partly consist in using the discrete dislocation dynamics method combined with a numerical solver in charge of the boundary value problems. Previous cases exists. In 1995, Van der Giessen and Needleman proposed a coupling strategy using the superposition method applicable to two dimensional problems [Van 95]. Latter on, the superposition method was extended to tree dimensional prob-

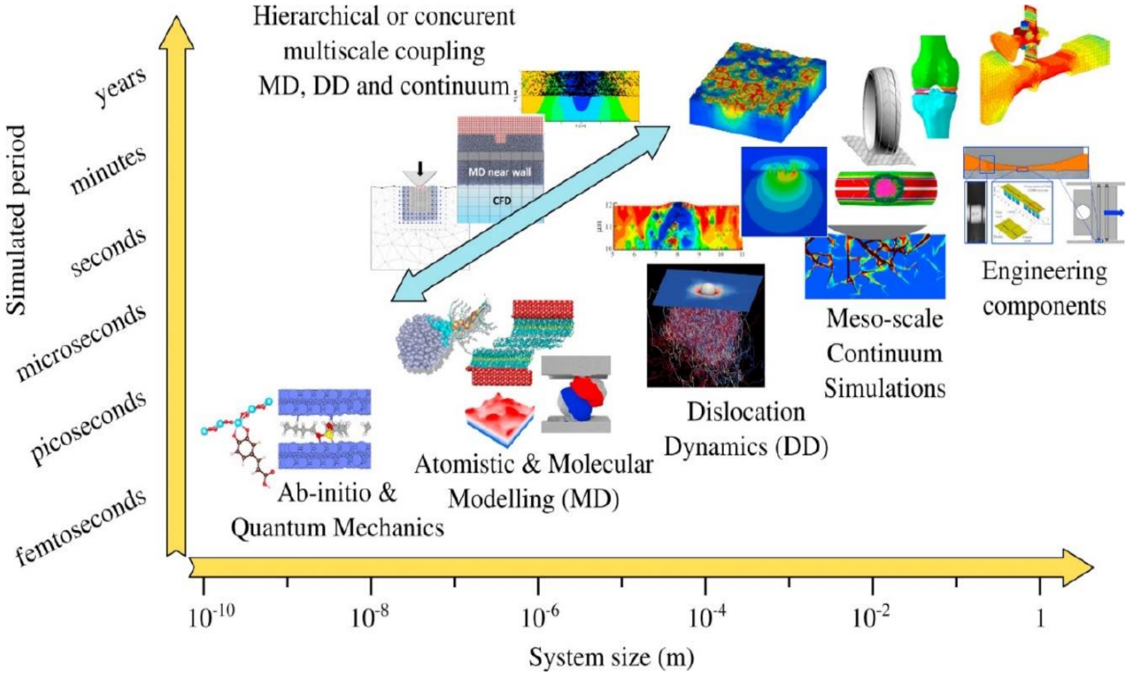
Hierarchical or concurent multiscale coupling MD, DD and continuum
MD near wall
CFD
Simulated period
years
minutes
seconds
microseconds
picoseconds
femtoseconds
Ab-initio & Quantum Mechanics
Atomistic & Molecular Modelling (MD)
Dislocation Dynamics (DD)
Meso-scale Continuum Simulations
Engineering components
$10^{-10}$
$10^{-8}$
$10^{-6}$
$10^{-4}$
$10^{-2}$
1
System size (m)

Figure 1: Characteristic lengths and time scales of simulation techniques [GOE 20].

lems by Fivel and collaborators [FIV 97, FIV 98, CHA 10]. In 1999, Lemarchand and coworkers proposed an alternative formulation known as the discrete continuous method [LEM 99a, LEM 99b, LEM 01] based on the eigenstrain formalism of Mura [MUR 87]. Overall, the discrete continuous method consists on a more elaborated approach than the superposition method, however the superposition method is easier to implement [CUI 15]. Here we will go further developing this type of approach for nanomechanics applications.

In this thesis, we review the superposition method to investigate the mechanics of nano-objects using the discrete dislocation dynamics nodal code Numodis [DRO 14, SHI 15] and the finite element software Elmer [MAL 13] to build a unique coupling tool: El-Numodis. The aim of this study is to provide a multi-scale simulation tool accounting for surface effects with the capability of both dislocation nucleation and initial dislocation microstruture evaluation.
The thesis manuscript is organized as follows. In the first chapter, we review the mechanical properties of small-scale objects starting from noncrystalline materials down to the individual crystal. Also, a literature review on dislocation dynamics/finite element coupling methods currently used in multi-scale simulations is provided. Examples on the effect of surfaces on the mechanical properties at the nano- and micro-scales are presented. In chapter two, we introduce discrete dislocation dynamics theoretical basics and the Numodis code including the treatment of boundary conditions and short-range dislocation *vs.* dislocation interactions for linear isotropic media. The linear elastic boundary value prob-

lem; the finite element method and Elmer are presented at the end of this chapter. In the third chapter, we describe the implementation of El-Numodis. Details about the boundary conditions, data array interchanges and other features implemented are provided. First results and benchmarks (dislocation stress fields, dislocation *vs.* surfaces simple cases, etc.) obtained using El-Numodis are presented in chapter four. This chapter ends with an application of El-Numodis to thin-film mechanics. In chapter five, we present the methodology to integrate the dislocation nucleation processes into El-Numodis. It starts with few theoretical aspects about the harmonic transition state theory and kinetic Monte-Carlo statistics. Then, toy simulations and more quantitative one are presented using creep and constant strain rate simulations on face-centered cubic materials. A case-study on the role of temperature on the dislocation nucleation process is presented as well as a direct comparison to molecular dynamics nanocompression simulation [ISS 15] using an atomistically-informed database computed for the surface dislocation nucleation process in MgO nanocubes [AMO 21a]. Finally, deeper details about the role of temperature on the yield stress stress of MgO nanocubes as well as the influence of the sample size and strain rate on mechanical properties are developed. A general conclusion about the main results obtained during this PhD work as well as some perspectives and recommendations to improve El-Numodis are provided at the end of the manuscript.

# Chapter 1

# Literature review

This chapter provides a literature review of the mechanics of micro- and nano-objects. It starts with a description of how mechanical properties vary with size *i.e.,* the "smaller is stronger" trend, from nanocrystalline materials to small individual objects. Indeed, wires, pillars and particles are commonly investigated using *in situ* transmission electron microscopy and molecular dynamics, both techniques being presented with their own pros and cons. Then, the effect of surfaces on the mechanical properties of small-scale objects is presented and discussed. Finally, a formal introduction to hybrid mechanical simulation methods coupling discrete dislocation dynamics and finite-element methods is provided.

## Contents

**1.1 Mechanics at small-scales . . . . . . . . . . . . . . . . . . . . . . . . 6**
1.1.1 Decreasing the grain size of bulk materials . . . . . . . . . . . . . . . . 6
1.1.2 Deformation of micro- and nano-objects . . . . . . . . . . . . . . . . . . 11
**1.2 Surfaces and dislocations at the nanoscale . . . . . . . . . . . . . . 22**
1.2.1 Surfaces and nano-objects . . . . . . . . . . . . . . . . . . . . . . . . . 22
1.2.2 Modeling surface and dislocation interactions . . . . . . . . . . . . . . 24
**1.3 Conclusion . . . . . . . . . . . . . . . . . . . . . . . . . . . . . . . . 30**

## 1.1 Mechanics at small-scales

In the recent years, the study of micro- and nanomaterials has shown a renewed interest due to the radical changes in their physical properties with respect to their bulk counterparts [ODE 01, SON 08, FIN 20]. In fact, this size dependence mostly arises from the increasing surface over volume ratio when scaling down. In the following, we introduce some of the main aspects associated with the improvements of the mechanical properties when decreasing the characteristic sizes of materials.

### 1.1.1 Decreasing the grain size of bulk materials

Before detailing mechanical specific aspects of individual micro- and nanocrystals lets first focus on what happens when decreasing the grain-size of bulk materials at such small-scales. Most of the answer relies on the Hall-Petch behavior (Figure 1.1) that consists in the strengthening of the material inversely with the overall grain size [HAL 51, PET 53, SUR 04]. The Hall-Petch model links the yield stress $\sigma_y$ of the sample to the grain size $d$ through equation 1.1, were $\sigma_0$ is a friction stress and $A$ is a constant. The parameter $x$ varies as a function of the material and grain size.

$$\sigma_y = \sigma_0 + Ad^{-x} \tag{1.1}$$

For materials with millimeter grain size down to several tens of nm the material strengthening with sample-size reduction is due to the reduction of the mean free path of dislocations [BEN 07, BOU 10]. Indeed, the plastic deformation is associated in this case with the multiplication of dislocations and each mechanism impinging the glide of dislocations tends to increase the strength of the material. With decreasing the grain size the dislocation-dislocation and dislocation-defect interactions are promoted but a massive effect is attributed to grain boundaries (GBs). Indeed, reducing the grain-size increases the GB over perfect crystal volume ratio what reduces the defect-free perfect crystal volume allowed for the dislocations to glide enhancing the dislocation pile-up process [PAN 93, Wan 95, FED 03, MEY 06]. However, below a critical size, the material strength decreases again with reducing the grain size. Explanations for such inverse Hall-Petch effect includes grain rotation, GB sliding and shearing as well as emission and absorption of dislocations at the GBs [FAN 05, KOL 07, GUO 18, YU 18].

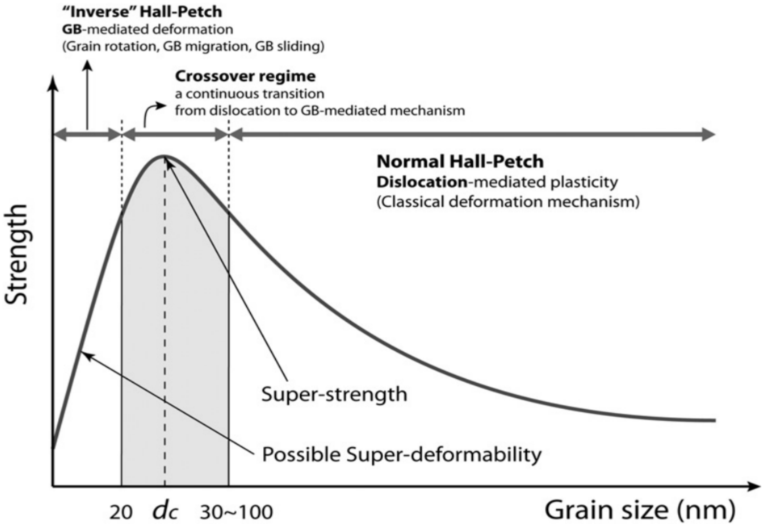

Figure 1.1: Stress dependence with grain size for nanocrystalline materials: Hall-Petch and inverse Hall-Petch regimes. Image from [GRE 11].

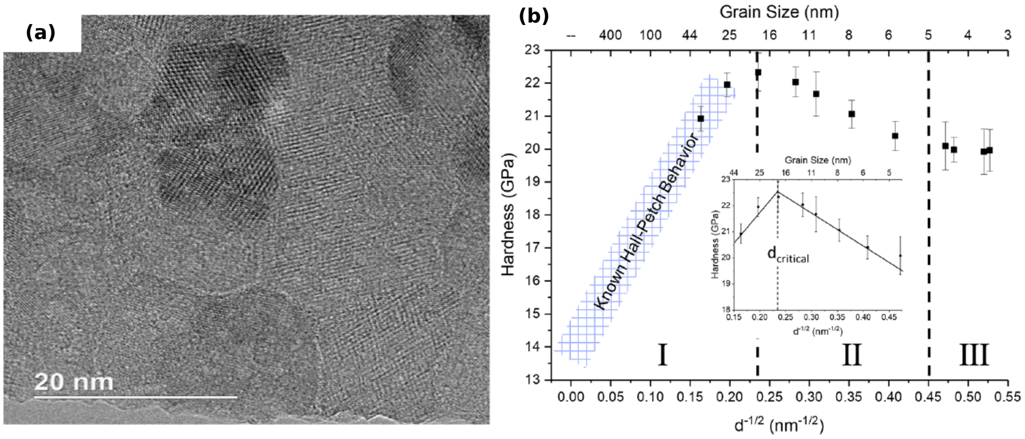

Figure 1.2: Hall-Petch behavior in a nanocrystalline ceramic. (a) High magnification TEM image of $MgAl_2O_4$ thin GBs region. The image emphasize the GBs without porosity. (b) three regions identified related to Hall-Petch (I), inverse Hall-Petch (II) and a plateau without size effect (III). Image adapted from [RYO 18].

Several studies focus on characterizing the yield-strength dependence on grain size as well as the transition region from the Hall-Petch to the inverse Hall-Petch regime using

both experiments and simulations.
As an example, Ryou *et al.* [RYO 18] studied the Hall-Petch breakdown in ceramic nanocrystalline materials. $MgAl_2O_4$ ceramics can be synthesized via environmentally controlled pressure-assisted sintering techniques ending up in material with grain size from 37.5 down to 3.6 nm without porosity (Figure 1.2 (a)). Indentation was performed at 35, 1, 0.1 and 0.05 $s^{-1}$ strain rates and the samples were characterized using transmission electron microscopy (TEM). The authors observed the conventional Hall-Petch effect compressing particles with grain size down to 18.0 nm (Figure 1.2 (b)). The inverse Hall-Petch regime was observed for grain size ranging from 10.8 to 4.6 nm. The final stage identified as plateau was found under 4.6 nm where neither conventional or inverse Hall-Petch holds.

Another example is the work of Jang *et al.* [JAN 11] in which Ni-W (4.4 %) polycrystalline nanopillars with grain size of 60 nm were studied by uniaxial compression (Figure 1.3 (a,b,c)) and tension (Figure 1.3 (d,e,f)). Figures 1.3 (a,d) show scanning electron microscopy (SEM) images of the pillar before deformation. Figures 1.3 (b,c and e,f) show the pillar pushed and pulled respectively. The behavior showed in the Figures 1.3 (g) for compression and (h) for tension is completely different from what is expected from both; the bulk sized nanocrystalline and nanometer sized single-crystalline metals. For both experiments there is a remarked weakening with the decrease of the size. The authors reported a deformation mechanisms transition from dislocation-driven deformation to GB-mediated deformation in pillars of 100 nm and below. They concluded that the presence of free surfaces activates these grain-boundary-mediated deformation processes at much larger grain sizes than observed in the case of the bulk material.

A theoretical model describing the grain size dependence of the flow strength suggesting a competition between dislocation slip (over a critical grain size $d_c$) and the GBs activity (below $d_c$) was reported by Fan *et al.* [FAN 05]. The authors assumed elastic grains free of dislocation, surrounded by an amorphous structure, and the model was used to correctly fit experimental results on copper and nickel.
Using molecular dynamics (MD), Schiotz *et al.* [SCH 98] investigate the inverse Hall-Petch regime in noncrystalline copper with grain size from 3.3 to 6.6 nm. They reported that both the yield and flow stresses decrease with the grain size.

In another study, Chen *et al.* used MD to investigate $CoNiFeAl_xCu_x$ nanocrystalline alloys with face-centered cubic (FCC) or body-centered cubic (BCC) structures [CHE 20a]. $CoNiFeAl_xCu_x$ is knows to change from FCC to BCC when the local lattice strain exceed the stress required for BCC nucleation or by tuning the Al concentration. The authors deformed $30 \times 30 \times 30$ $nm^3$ samples with grain sizes from 7.2 to 18.8 nm in case of FCC phases and 7.2 to 23.4 in case of BCC. The simulations were carried at room temperature with an strain rate of $2 \times 10^8$ $s^{-1}$. They found the transition from Hall-Petch to inverse Hall-Petch for grain size of 12.1 nm in the case of FCC structured alloys (Figure 1.4) and 18.9 nm for the BCC alloy. The main factors associated to the strength of the FCC

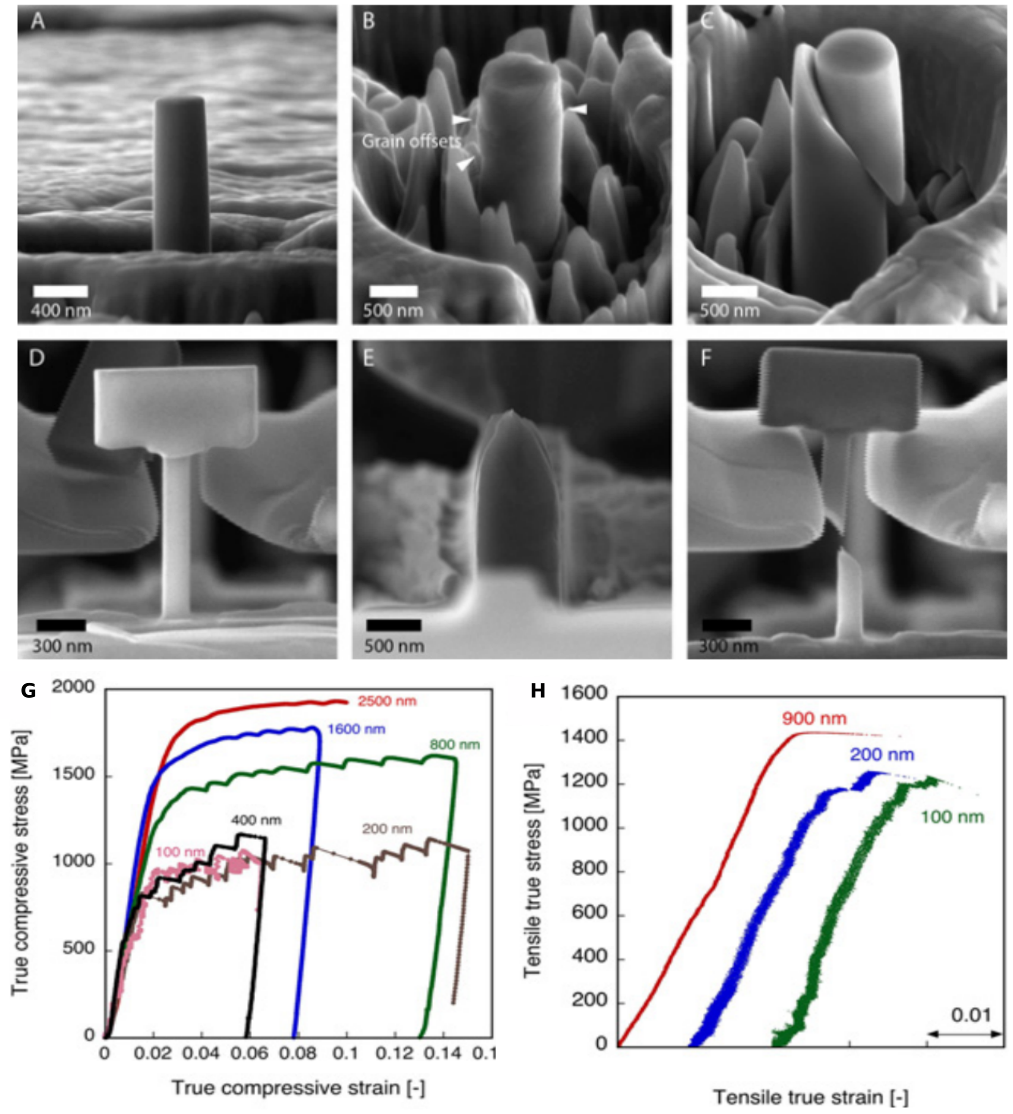

Figure 1.3: Experimental study of Ni-W nanopillars. SEM images of (a) as fabricated pillars and (b,c) deformed by compression. SEM images of square pillars deformed under tension: (d) as fabricated and deformed (e,f). Stress-stain curves are showed in (g) for compression test and (h) for tension. Images from [JAN 11].

alloy are the continuous emission and propagation of partial dislocations that cross the grains before being stopped or absorbed at the other side of the sample (depending on the coherence and orientation of the grains and GBs) or adjacent partial dislocations leading to deformation twining mechanism.

In general, experimental studies reveal that most of nanocrystalline metals or ceramics exhibit a limited ductility [MEY 06] what constrains the field of applications of such materials. However, some investigations show that rooms exist to improve it. Koch [KOC 03]

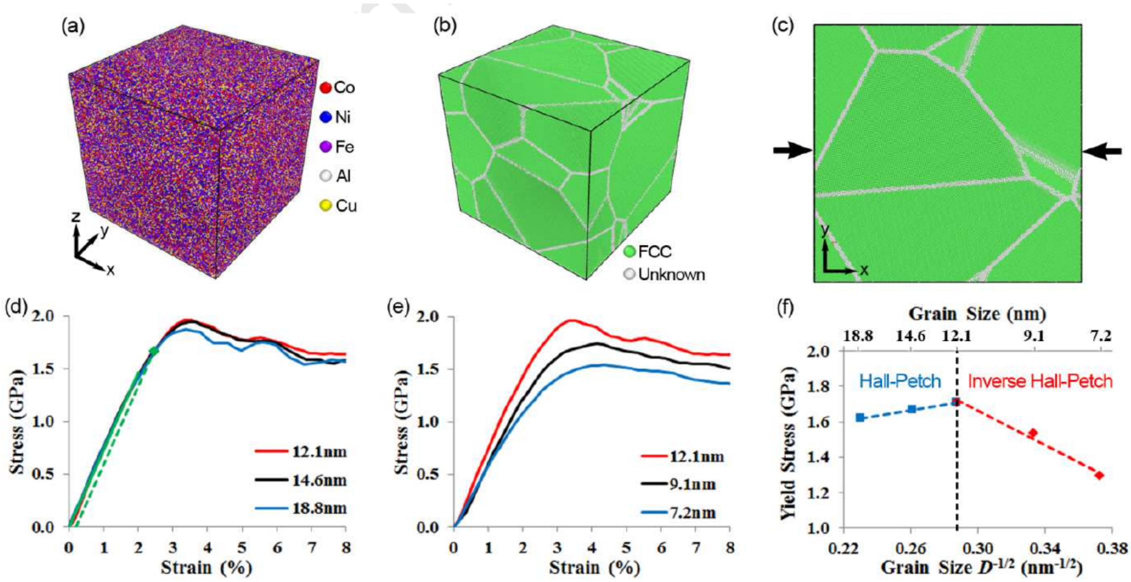

Figure 1.4: MD simulation of CoNiFeAl$_x$Cu$_x$ alloys with FCC phases. Images indicates the atom type (a), and phase (b) and compression direction (c). Stress-strain curves for sample sizing from 12.1 to 18.8 nm (d) and from 7.2 to 12.1 nm (e) are shown. (f) Relation between the yield strength and grain size. Image from [CHE 20a].

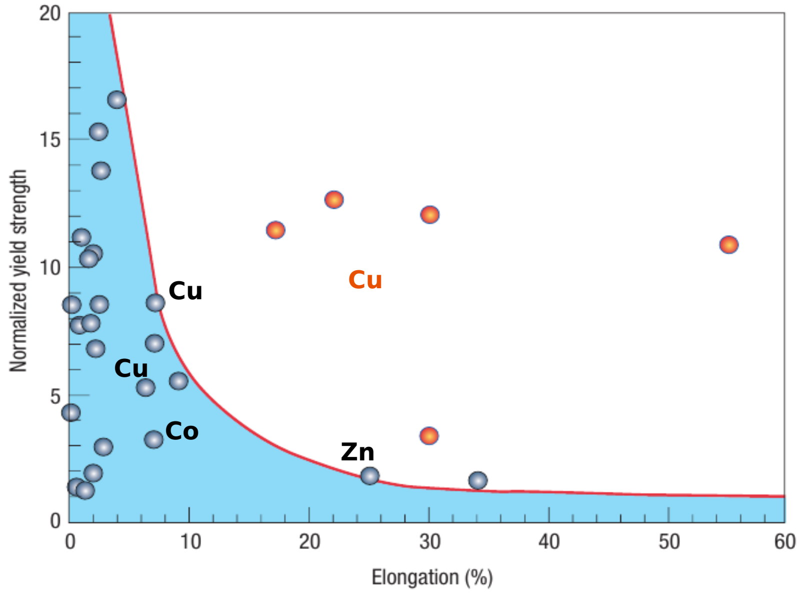

Figure 1.5: Normalized yield strength and ductility for Cu, Co and Zn nanostructured materials (grey symbols). The blue area under the red line represent the trade-off zone (high strength and low ductility). The orange symbols represent Cu nanostrucutured samples with improved ductility and high strength. Figure adapted from [KOC 03] and [ZHU 04].

discussed the possibility to optimize strength but also ductility of ultra-fine nanocrystalline materials building an appropriate grain size distribution and introducing secondary phases

(Figure 1.5). Zhu and Liao [ZHU 04] suggested that ductility can be increased by prestraining the samples at high strain rate using a long fabrication process that produces sharp and narrow grains. Also Farkas and Hyde [FAR 05], showed using using Molecular Statics (MS) and MD that the fracture resistance of BCC nanocrystalline materials increases below a critical size. They also reported that adding impurities can enhance GB cohesion and avoid the inter-granular failure mechanism.

To improve and better understand the mechanical behavior of small-grain materials, several research groups (including MATEIS) investigate oligocrystals made of only few grains or even isolated single crystals and develop bottom-up approaches [LAI 13, ISS 15, ISS 21]. These last decades, several micro- and nano-mechanical tests were developed on pillars, particles, wires or thin films to better understand dislocation processes at small-scale. In the next section, we will introduce several elements related to this subject with a specific emphasize on the roles of size and shape on the strength and elementary deformations processes of surface-dominating samples.

### 1.1.2 Deformation of micro- and nano-objects

In the early 00', Uchic *et al.* performed compression tests on metal micropillars with the aim to propose a quick-and-cheap method for testing miniaturized materials that could be transferred up to the industry [UCH 04]. However, the authors have observed a significant size-effect on the yield stress of Ni an NiAl micropillars similar to the aforementioned Hall-Petch effect but here in single-crystals *i.e.*, without GBs (Figure 1.6). This work opened a highway to a huge amount of studies focusing on the mechanics of micro- and nano-objects, not only related to their possible applications but also to understand the underneath size-effect and, more broadly, improve our general understanding of small-scale mechanics.

Among the many studies devoted to metal micro- and (then) nano-pillars, one can notice the intensive work performed by the Greer's group at Caltech including among others FCC (Cu, Al, Ni) and BCC (Mo) metals. In Jennings *et al.* [JEN 10], compression experiments were performed on single crystalline $\langle 111 \rangle$-oriented Cu nanopillars with diameters between 100 and 500 nm made by lithography with nonzero initial dislocation densities. Such method produces smaller concentration of dislocations per m$^2$ as compared with the traditional focused ion beam (FIB). The deformation was performed at a constant displacement rate of 2 nm/s using a flat punch. Figure 1.7 (a) shows the stress-strain curves of four samples with different diameters. A strength increase is observed with the diameter reduction. Several models are suggested to justify this strengthening in single-crystals including dislocation source controlled plasticity, dislocation source truncation or exhaus-

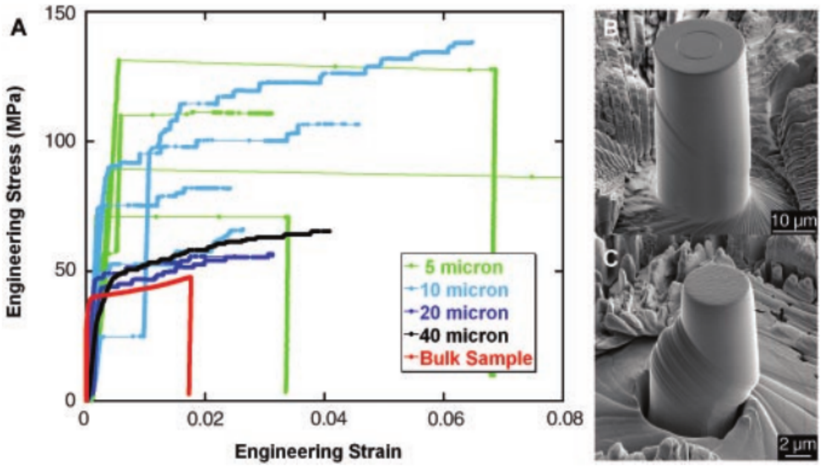

Figure 1.6: Experimental deformation at room temperature of pure Ni micropillars with $\langle 134 \rangle$ orientation. (a) Stress-strain curves of pillars with diameter sizes ranging from 5-40 μm. The curves are compared to the mechanical response of a bulk single crystal. (b) SEM image of a 20 μm diameter pillar at 4 % strain. (c) SEM image of a 5 μm diameter pillar after reaching 19 % strain. Image from [UCH 04].

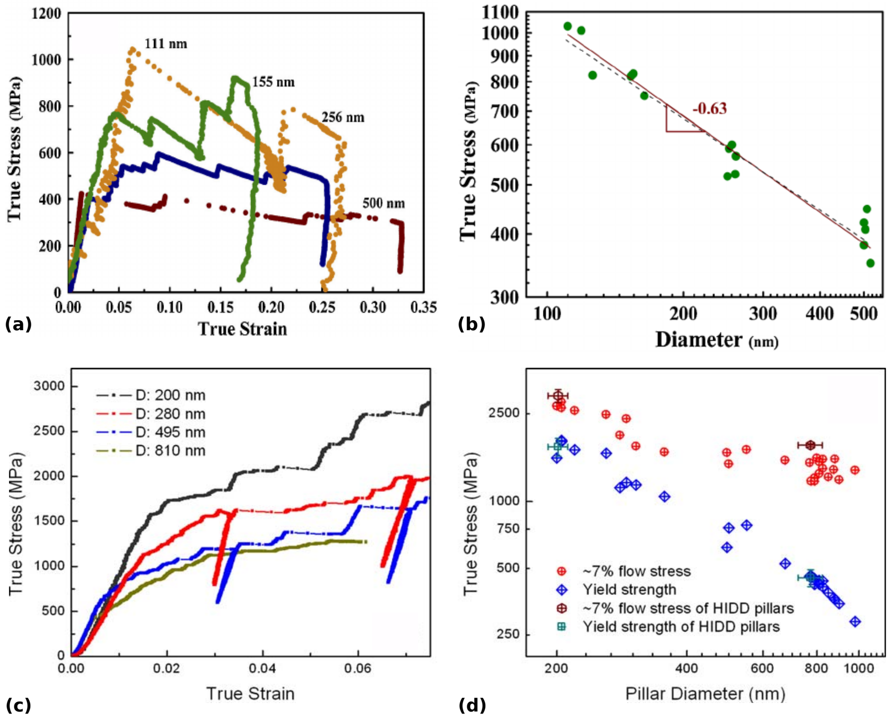

Figure 1.7: Submicronic pillars compression of FCC and BCC metals. Stress-Strain curve for Cu (a) and Mo (c) nanopillars of different diameters showing the "smaller is stronger" trend. Yield stress *vs.* pillar diameter for Cu (b) and Mo (d) with slopes -0.63 and -0.44 respectively. Images from [JEN 10] and [KIM 08].

tion, starvation or nucleation-controlled plasticity [KRA 10, GRE 11]. Also, Figure 1.7 (a) shows strain bursts that are classically observed in all nano- and micro-pillar compression tests when performed under load-control (in contrast with displacement-controlled tests). A log-log plot of the flow stress at 10 % strain against the pillar diameter is showed in Figure 1.7 (b). The strength follows a power law dependence wit the slope around $-0.63 \pm 0.04$ in consistency with values reported for other metallic pillars. The author concluded that the plasticity at the sub-micron scale is strongly dependent of the dislocation microstructure.

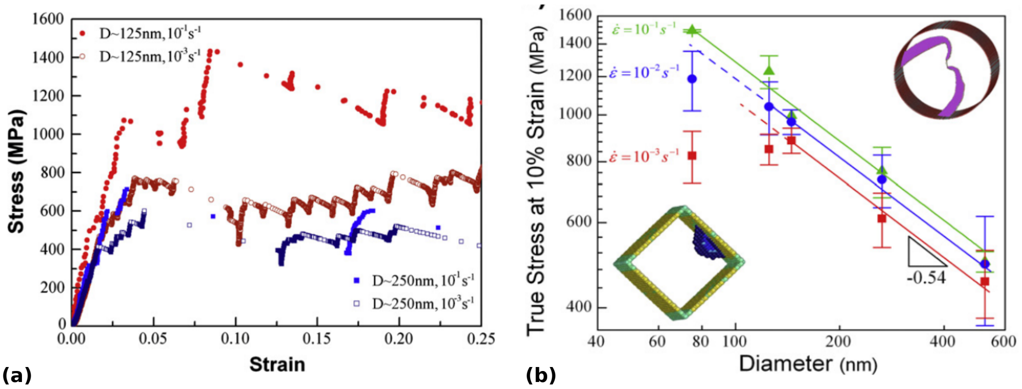

Figure 1.8: Size effect observed in Cu nanopillars. (a) Four characteristic stress-strain curves plotted for pillars of two different diameters, 125 and 250 nm, each deformed at two different strain rates, $10^{-3}$ and $10^{-1}$ $s^{-1}$. At a constant strain rate, smaller pillars have higher strengths, whereas at constant diameter, faster strain rates result in higher strengths. (b) Strength as a function of diameter for three different strain rates (log–log scale). Trend lines denote power-law strengthening where plasticity is governed by collective dislocation dynamics. Images from [JEN 11b].

In another study focusing on BCC Mo [KIM 08], the same group reported a size-effect observed in nanopillars with diameter between 200 to 900 nm compressed at the same constant displacement rate of 2 nm/s. Figures 1.7 (c) shows stress-strain curves and Figures 1.7 (d) illustrates flow stress and yield strength *vs.* pillar diameter, respectively with slopes of -0.44 and -1.07 indicating that the size-effect is more pronounced in the yield strength rather than in the flow stress. Finally, the authors justify the size-effect as a pure consequence of the sample size without considering the influence of the initial dislocation density or surface defects hardening. The effect of the strain rate was investigated during compression of different nanopillars diameters in [JEN 11a, JEN 11b]. The compression tests were performed for five different sample diameters (500, 250, 150, 125 and 75 nm) under nominal constant strain rates of $10^{-1}, 10^{-2}$ and $10^{-3}$ $s^{-1}$. Figure 1.8 (a) shows the stress-strain curves for samples with size 125 and 250 nm deformed at at high $10^{-1}$ and slow $10^{-3}$ $s^{-1}$ strain rates. At constant strain rate, the smaller samples are stronger while at constant diameter the stronger samples are those deformed at high strain rate. Increasing the strain rate by two orders of magnitude results only in a 15 % strength increase in the 250 nm pillars, while the strength in 125 nm pillars increases by almost 100 %.

In Figure 1.8 (b), a log–log plot of flow stress at 10 % strain as a function of the pillar diameter for different strain rates is presented. For the three different strain rates, the power-law exponent remains nearly constant. Transition from dislocation multiplication to dislocation nucleation is reported.

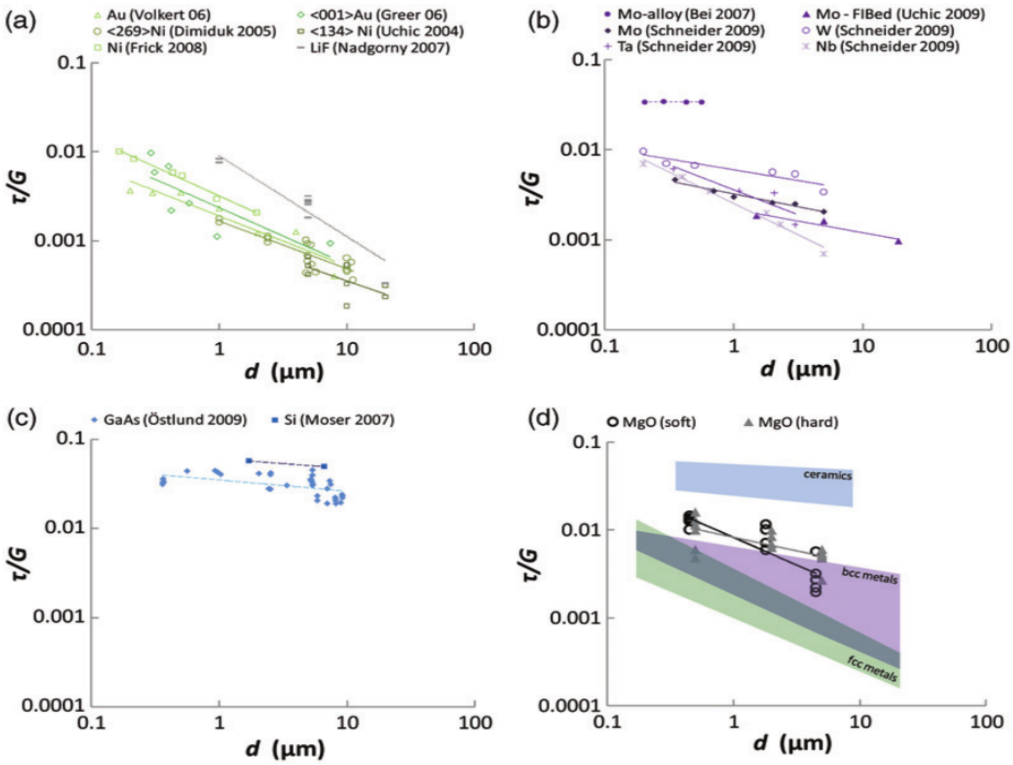

Figure 1.9: Dependence of the normalized yield stress (shear yield stress over the shear modulus) in function of the pillar diameter and its respective power-law fit for different materials. The figures are ordered in function of the lattice resistance to dislocation motion: (a) FCC metals carrying low lattice resistance. (b) BCC metals with intermediate lattice resistance. (c) Ceramics. (d) MgO together with all the data shown in (a-d) represented by colored areas. Images from [KOR 11].

Ceramics micro- and nano-objects are also concerned by size-effect. As an example, Korte *et al.* [KOR 11] investigated MgO micropillars under compression and compared them to metals and ceramic semi-conductors (Figure 1.9). The samples were prepared using FIB milling and were deformed under load control using a flat punch in the SEM. The authors have investigated the two slip modes of MgO changing the compression direction. The soft slip system $\frac{1}{2}\langle 110\rangle\{110\}$ is activated while compressing along the [100] direction and slip on the hard slip system $\frac{1}{2}\langle 110\rangle\{100\}$ is observed when compressing along [111] (Figure 1.9 (d)). The authors observed higher yield stresses in the smaller pillars with the larger values obtained for samples compressed along [111]. The results show that the MgO soft slip system have a size effect similar to BCC metals.

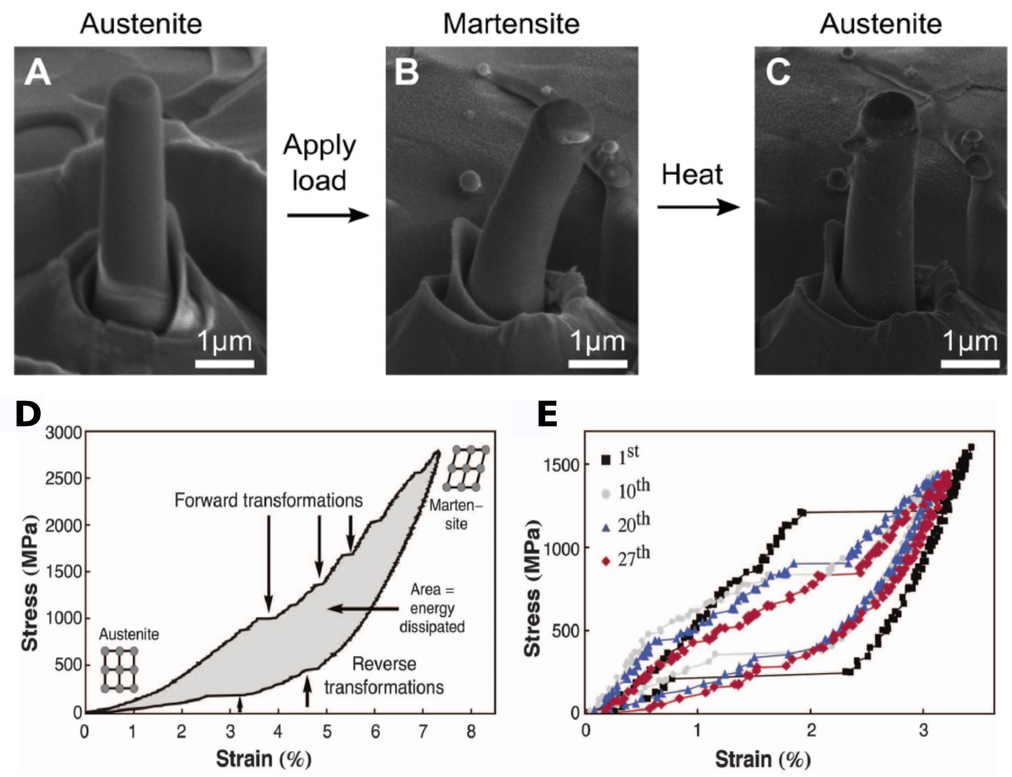

Figure 1.10: Shape memory and superplasticity in zirconia pillars. Example of shape recovery after loading deformation by using thermal treatment (a-c). Stress-strain curve characteristic of a superplastic deformation and shape recovery obtained by load-unload experiment (d). Evolution of the hysteresis loop with respect to the number of cyclic load-unload deformations (e). Images from [LAI 13].

In addition, shape-memory ceramics were investigated by Schuh and collaborators [LAI 13, DU 15, ZEN 17]. Indeed, the failure associated to the brittle zirconia-based ceramics can be delayed due to a transformation-induced plasticity effect tuned by the alloying composition. In particular, the authors investigate these outstanding mechanical properties in olygocrystals. Under those conditions, the internal stress mismatch is corrected allowing the ceramic to withstand several elasto-plastic cycles reaching very large strains. Using zirconia pillars primarily in the austenite phase (tetragonal structure), the authors have shown that a conversion to martensite (monoclinic) was promoted by loading at room temperature (Figure 1.10 (a-b)). A backward transformation to austenite with the initial shape recovered is found when thermal treatment is applied (Figure 1.10 (c)). The same phase transformation and shape recovering is obtained by loading-unloading processes (Figure 1.10 (d)). Cyclic deformations lead to a gradual evolution of the hysteresis loop suggesting that the material becomes “trained” to a transformation pathway (Figure 1.10 (e)).

These studies show that even originally brittle materials such as ceramics can withstand significant amount of stress and strain when decreasing size.

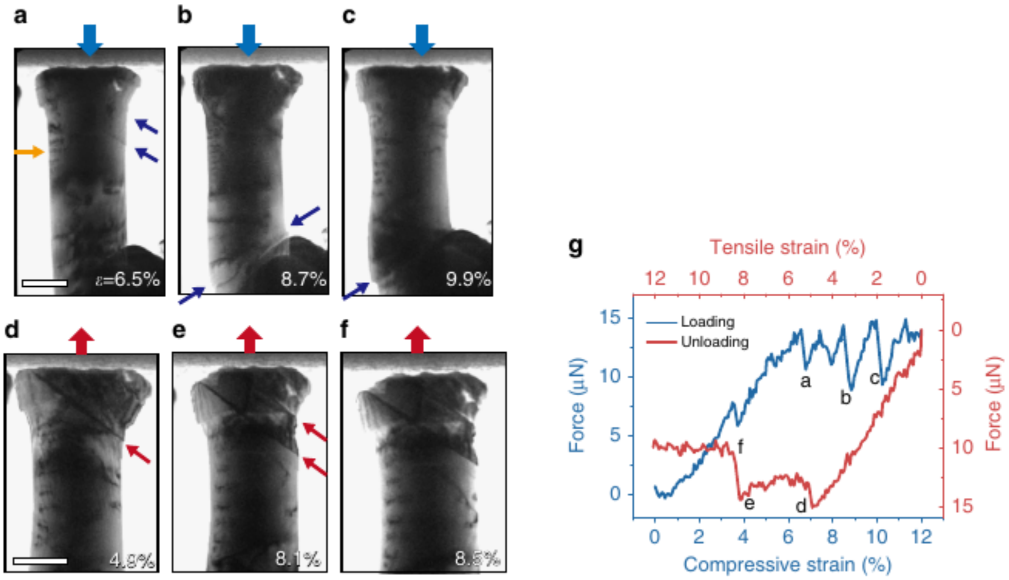

Figure 1.11: Mechanical test of gold NWs using *in situ* TEM (scale bar of 100 nm). (a-c) Images taken after the load drops in the compressive loading; the traces in the lateral surfaces of a dislocation slip mechanism are showed with blue arrows. (d-f) Unloading the sample sowing the nucleation and extension of nanotwin. (g) Recorded force versus strain during the compressive (blue) and subsequent tensile (red) loading. Images from [LEE 14].

To study mechanics at even lower scale *i.e.*, at the nanoscale, nanowires (NWs) can also be deformed under tension, bending or (scarcely) under compression. For example, the transition from dislocation slip to deformation twining as function of loading conditions (Figure 1.11) as well as detwinning and memory shape is reported by Lee *et al.* using both *in situ* TEM and MD [LEE 14]. During the first stages of compression, the authors observed the nucleation of perfect dislocations in the region near the sample top and the flat punch. Such dislocations immediately glide and escape near the contact region leaving the NW top with a mushroom shape. Further half loops were reported in regions far from the NW's top. The adhesive contact formed between the NW and the flat punch during the compressive deformation allows to perform tensile test by simply reversing the loading direction. At the initial stages of the tensile test the pre-existing dislocations that formed during compression slip back. Then, the mechanism predominantly observed is deformation twinning. The force *vs.* strain curve is represented in Figure 1.11 (g) for both compression and tension experiments. Once a twining region is formed, the compressive deformations allows for detwinning rather than forming partial dislocations. Figure 1.12 (a) shows TEM images of a twinning region formed during tension that completely disappear once compression is initiated. The subsequent compressive deformation acts in favor of detwinning. The trailing partial dislocation formed near the twining boundaries eliminated its stacking fault removing the twin region. The MD sim-

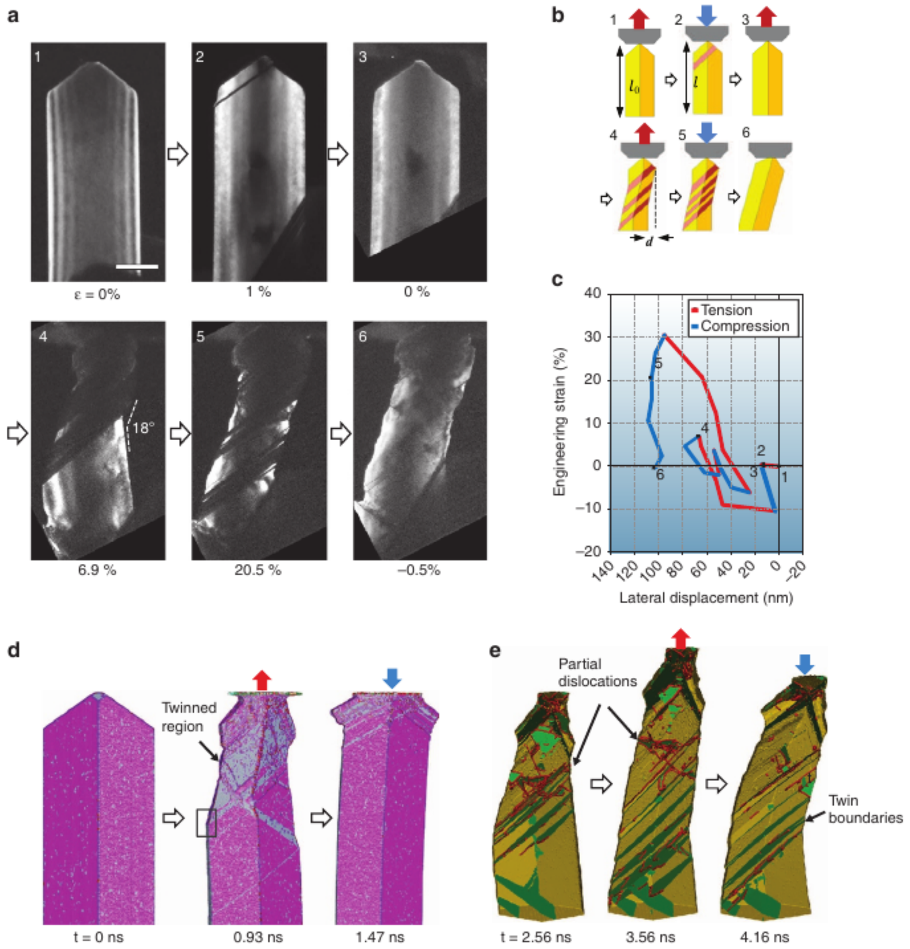
a
1
2
3
ε = 0%
1 %
0 %
4
5
6
18°
6.9 %
20.5 %
−0.5%
b
1
2
3
$l_0$
$l$
4
5
6
$d$
c
Tension
Compression
Engineering strain (%)
40
30
20
10
0
−10
−20
140
120
100
80
60
40
20
0
−20
Lateral displacement (nm)
d
Twinned region
t = 0 ns
0.93 ns
1.47 ns
e
Partial dislocations
Twin boundaries
t = 2.56 ns
3.56 ns
4.16 ns

Figure 1.12: Reversible transitions by twinning and detwinning on gold NWs trough a cyclic tension and compression deformation observed on experiments (scale bar 100 nm) and simulations. (a) *in situ* TEM images captured during cyclic tension–compression. A single nanotwin was formed near the tensile grip (image 1 to 2) at the first tensile load and then eliminated by detwinning during compression (image 2 to 3). Nucleation and propagation of twins along the same slip system (image 4 to 5) was observed when subsequent tensile deformation was applied. (b) Representation of the experimental loading. (c) Axial strain and lateral displacement obtained during the tension-compression experiments. (d) Twinning and detwinning process using MD simulations. (e) MD simulation images showing the glide of partial dislocations (red) and the respective twinned and detwinned regions (green). Images from [LEE 14].

ulations support the preferential activation of the twinning and detwinning processes and the reversible transition between the two mechanisms during cyclic tension–compression loading. One can also mention the huge experimental work of Richter and colleagues [QIN 15, CHE 17, CHE 20b, LAM 20] and the one of Cai from a modeling point of view [MAR 04, KAN 07, PAR 09, WEI 12]

Nanoparticles (NPs) are another kind of nano-objects that can be used to investigate nanoscale plasticity under compression. In contrary to pillars, they usually benefit of soft

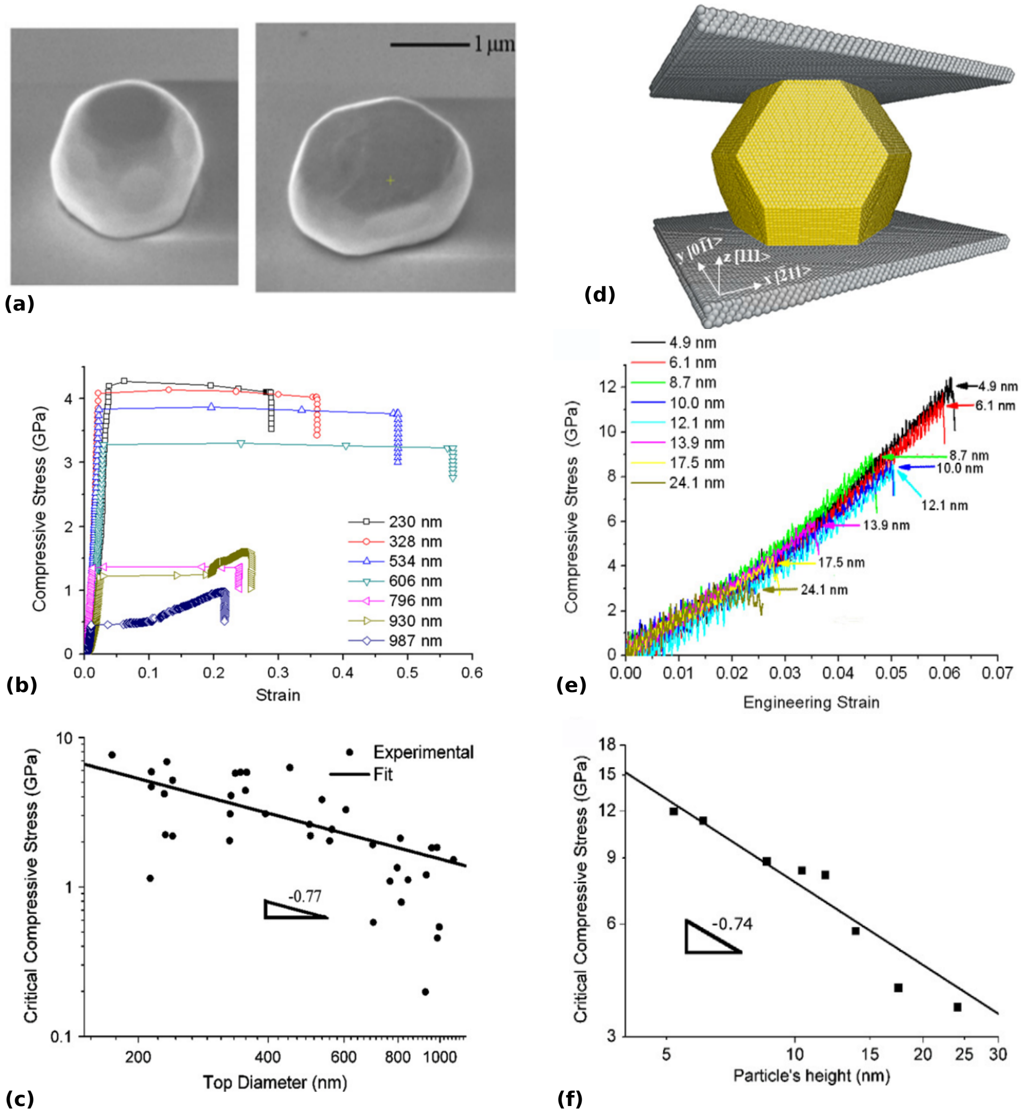

Figure 1.13: Study of the size effect on Au samples. (a) SEM image of a faceted Au microparticle with top face diameter in the range of 800 nm before and after compression. (b) Experimental stress-strain curves of Au nano- and microparticles with different sizes. (c) Dependence of compressive stress on the top face regarding its diameter. (d) Atomic configuration of one of the samples (4.9 nm height) used in the MD study. (e) Strain-stress curves of the MD simulation for particles with height from 4.9 to 24.1 nm. (f) Linear dependence of the yield stress with the particle height. Images from [MOR 11].

fabrication routes without FIB and are usually interdependent of a substrate. Mordehai *et al.* have reported a size-effect in gold faceted micro- and NPs [MOR 11]. In this study, experimental compression of Winterbottom shaped particles are performed in the SEM at a constant nominal displacement rate of 2 nm/s. Figure 1.13 (a) shows the microparticles before and after deformation. The upper facet diameter of the particle varies form approximately 200 nm to 1 µm. The size-effect on sample strength is illustrated in Figure 1.13 (b) showing the increase of the yield stress with the reduction of the size. The dependence of the compressive stress in function of the top face diameter is reported to scale with the particle radius $R$ as $R^{-n}$ with $n$ = -0.77 ± 0.16 as shown in Figure 1.13 (c). MD was used with the aim to explain elementary deformation processes and justify stress tendencies. Several atomic Winterbottom shape NPs (Figure 1.13 (d)) with height range from 4.9 to 24.1 nm are deformed at constant displacement rate of 1 m/s. Figure 1.13 (e) shows the stress-strain curve for the different samples. An abrupt stress drop marks the nucleation of dislocations from the surface. The simulation also shows a non brittle behavior as observed in the experiment. Figure 1.13 (f) shows the linear dependence of the nucleation stress with the particle height.

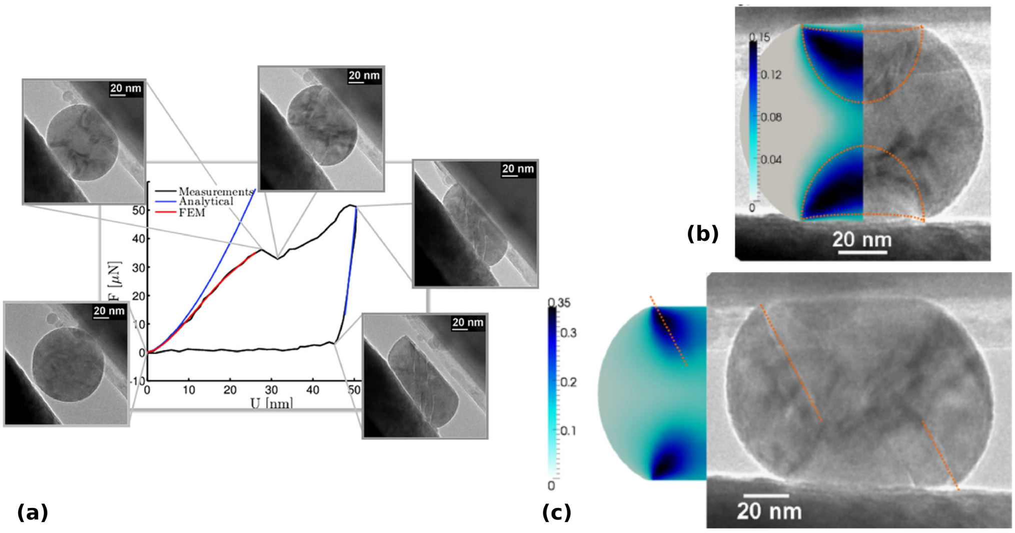

Figure 1.14: Analytical and experimental study of spherical $Al_2O_3$ NPs deformation. (a) Different stages during an *in situ* TEM compression of a 96 nm diameter nano-sphere. Simulation using digital image correlation with FEM (red line) and analytical using a Hertzian model for loading and Oliver and Pharr model during unloading. (b) Map of the total equivalent plastic strain superposed to the contrast observed during experiment. (c) Tresca stress comparison to the experimental observation of the first cracks direction (dotted line). Images from [CAL 14].

Also, Calvie *et al.* have investigated at MATEIS the mechanical response of alumina ($Al_2O_3$) ceramics nanospheres using *in situ* nanocompression inside the TEM [CAL 12]. Specimen with diameter size ranging from 40 and 120 nm were compressed at a controlled displacement rate of 2.5 nm/s with and without thermal pre-treatment. The authors report that the smaller nanospheres can withstand several plastic deformation without failure. However a brittle behavior is reported for the particles with larger size. As a result, a critical size of about 40 nm is found to delimit the brittle-to-ductile transition. The same group also proposed a methodology to determine constitutive laws suitable for the mechanics of alumina NPs [CAL 14]. In this study, they compressed alumina nanospheres with diameter of 96 nm at a displacement controlled rate of 0.5 nm/s using *in situ* TEM (Figure 1.14 (a)). Experiments were compared with finite-element method

(FEM) simulations by using digital image correlation and reporting estimated values of Young's modulus and yield stress. This work also discussed the link between observed Bragg fringes and possible plastic deformation events (Figure 1.14 (b)); The simulated Tresca shear stress was shown to match the direction of the crack propagation observed during the experiments (Figure 1.14 (c)).
Still at MATEIS, Issa *et al.* used *in situ* TEM and MD to compress MgO nanocubes (NCs) [ISS 15, ISS 21]. The experiments are performed at controlled displacement rate of 2 nm/s along the [001] direction. Three sizes are investigated 90, 120 (Figure 5.25 (a)) and 140 nm observing the well known increase of the strength with the reduction of the size. Nucleation of dislocation were reported to occur at surfaces and edges of the cubes. In parallel MD simulations were preformed at room temperature for dislocation free NCs at smaller sizes (Figure 5.25 (b)) ranging from 4.2 to 12.7 nm. Compression test were performed in the [001] direction with a displacement rate equivalent to $10^8$ $s^{-1}$ strain rate. Both the experiments and simulations show that MgO NPs can deform up to extreme strain without cracking. MD simulations helped to interpret the surface dislocation nucleation (SDN) deformation. The same group recently discussed the size-dependent transition from SDN and starvation (samples lower than 200 nm) to bulk-like dislocation multiplication (larger samples) in MgO NCs *in situ* experiments [ISS 21].

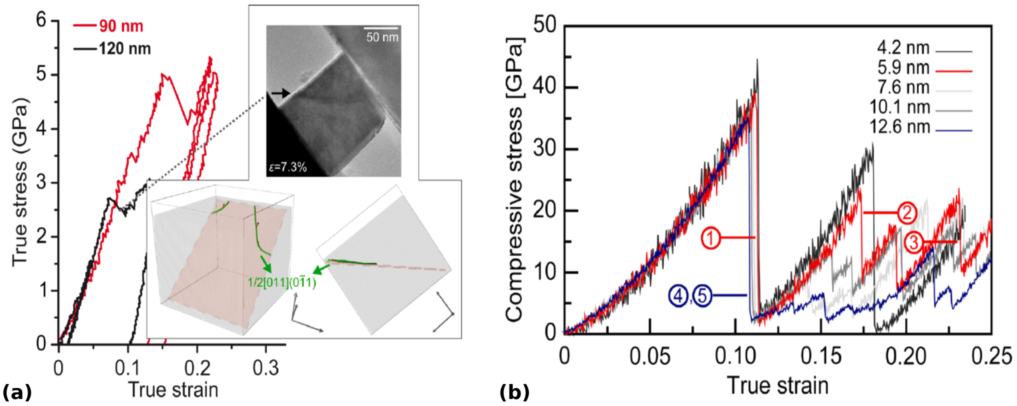

Figure 1.15: MgO NPs deformation using *in situ* TEM and MD. (a) Stress-strain curve for two MgO NPs of 90 and 120 nm size deformed inside the TEM. Inset: TEM image of an SDN event corroborated by MD simulation. (b) MD stress-strain curves of MgO NCs under compression. Images from [ISS 15].

Recently, Amodeo *et al.* used the nudged-elastic band (NEB) method to compute the site-dependence of energy barrier for SDN in MgO NCs under compression (Figure 1.16) [AMO 21a]. The authors computed maps of dislocation nucleation activation energy (and nucleation radii) for the surface nucleation sites in MgO NCs deformed at 11 % strain. They reported that the most favorable sites were at edges and corners of the specimen as observed in [ISS 15]. Also, they have shown using the transition state theory (TST) that dislocations were able to nucleate from regions located at the center of the lateral surfaces when heating the sample up to intermediate temperatures. The nucleation energy database developed by Amodeo *et al.* will be used later in this study. About modeling NPs mechanics, one can also mention the work of Wang [BIA 13, YAN 17, BIA 18] or the one of Pizzagalli's group [Bel 17, KIL 18, KIL 19]. Moreover, Amodeo and Pizzagalli recently published a review article on the topic in which all details on the multi-scale modeling of NPs mechanical properties can be found [AMO 21b].

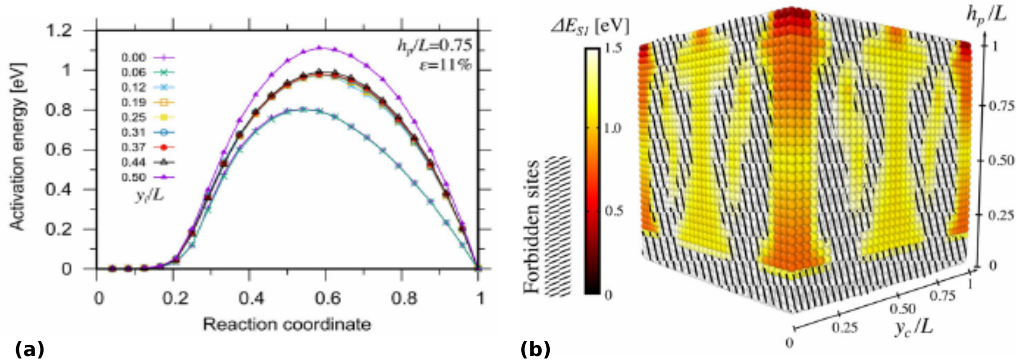

Figure 1.16: Dislocation nucleation in MgO NCs using NEB and TST, (a) Example of SDN energy barrier as function of site localization at 11 % strain. (b) Energy map for SDN in MgO NCs projected on the more probable nucleation centers. The gray colors shows the forbidden cites. Images from [AMO 21a].

The first part of this literature chapter evidences the "smaller is stronger" trend and the super-plastic behavior currently reported in small-scale objects. Also, it is commonly observed that surface nucleation is the mechanism ruling plasticity in the smallest defect-free nano-objects due to a more intense effect of free surfaces when scaling down. In this context, nanomechanical experiments can suffer of several drawbacks that impede trustworthy mechanical characterization as *e.g.,* surface roughness, misalignment or irradiation effects [YU 15, HIN 09, ISH 97, MIA 17, NAG 15, MIC 08, DON 06]. Thus, they often require simulations to be fully interpreted. Simulations allows for a precise control of defects and avoid contamination during sample preparation (as reported in some experiments). In this context, MD seems to be the best candidate to model nanomechanical tests as it allows to model SDN processes as well as other deformation processes at the atomic-scale. However, MD also carries limitations. The computational costs involved by MD simulations keep the sample size limited to few ten nm while the strain rate is found to be particularly high ($>10^6$ s$^{-1}$). In the next section, we will focus on the other methodologies available in the literature that allow for the modeling of mechanical properties accounting for surfaces as required by the physics of small-scale experiments.

## 1.2 Surfaces and dislocations at the nanoscale

As previously discussed, the mechanical properties of materials radically change when decreasing size at the micro- and, then, at the nanoscale, due to the increase of the surface over volume ratio. For instance, the surface atoms of a 25 nm edge size NC represents 8.5 % of the total number of atoms (simple cubic crystallography, lattice parameter 3 Å) while it increases up to 42 % for a 4.2 nm sample suggesting that at small scales, the effect of surfaces can not be negligible. In particular, surfaces are the source of image forces that can strongly influence dislocation processes. Thus, any simulation method used to model nano-objects should include a rigorous treatment of the surface effects. In this section, we present some aspects on the effect of surfaces at the nanoscale as well as a review of the simulation methods currently used to manage dislocation *vs.* surface interactions.

### 1.2.1 Surfaces and nano-objects

The surfaces of nano-objects can be the source of various physical properties different from bulk. For example, the chemical reactivity or the atomic diffusion can be strongly enhanced in nano-objects leading to specific applications *e.g.,* in catalysis or lubrication [ROY 09, CHE 19, DAI 16, RUB 17]. In the field of nanomechanics, surfaces influence both the elastic and plastic properties. Liang and Upmanyu [LIA 05] used MS simulations to study the elasticity of copper NWs oriented along [001], [110] and [111] crystallographic directions (Figure 1.17). The authors attribute the changes (with respect to bulk) to the nonlinear response of the NW core and the action of surface stress. In addition, they show that the surface elasticity effects are moderated for NWs oriented along [001] and [110], and negligible for those oriented along [111]. McDowell *et al.* performed MD simulations on Ag NWs and have shown that factors as geometry and surface structure are responsible for the changes in elastic modulus observed with size reduction and may explain the differences between experiments and computational trends [MCD 08]. On the other hand, we have emphasized in the previous section how the surfaces play a role at the onset of plasticity as being the source of the heterogeneous dislocation nucleation process. Still in this context, image forces that apply to a dislocation close to an interface (surface, GBs, etc.) is a long-time known aspect of the dislocation theory that takes all its sense in nano-objects. As an example, Gryaznov *et al.* evaluate the critical size below which a dislocation is dragged out from a small particle due to image forces [GRY 89]. As shown in Gerberich *et al.*, a rough calculation including a friction stress of 50 MPa for iron at room temperature leads to a critical size of 400 nm below which a dislocation escapes due to image forces [GER 17]. This simple calculation shows the key contribution of image forces to NPs mechanics.

Also at small-scales, the sample preparation influences the dislocation microstructure

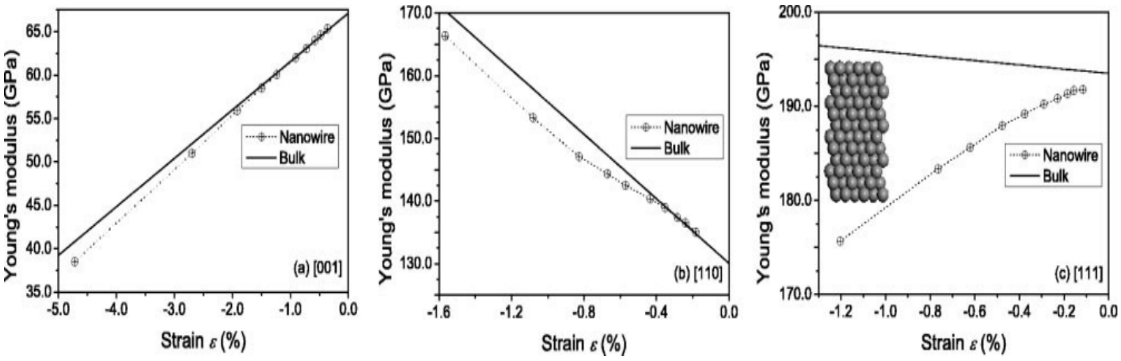

Figure 1.17: Dependence of the Young's modulus with strain for copper NW and bulk material using MD simulations for samples oriented along [001] (a), [110] (b) and [111] (c). A longitudinal view of the [111] oriented NW showing surfaces irregularities is at the inset of (c). Figure from [LIA 05].

and, with it, the mechanical properties of the material. Example of the effect of surface passivation and its influence on thin-films strength is reported by Keller using *in situ* TEM [KEL 98]. The authors discuss how the effect of surface may change the way a dislocation glide and bend along a passivated surface. In [OH 09], the authors discussed the effect of surface oxidation during the elongation of sub-micron aluminum single crystal using TEM. They reported that during the escape, the first dislocations were stopped at the surface due to the action of the oxide layer. Also, they explain that the dislocation density remains constant at strain rate of $10^{-4}$ s$^{-1}$ in the contrary to the case of $10^{-3}$ s$^{-1}$ what indicates the strain rate sensitivity of submicron crystals. The effect of the initial dislocation microstructure on the strength of bulk materials was also discussed in Mg crystals [LAV 75]. Jennings *et al.* also discussed the effect of FIB on sample preparation and strength [JEN 10]. Both studies conclude that the mechanical response of nanoscale crystals depends rather on the initial dislocation microstructure than on size, regardless the fabrication method.

The TEM lamella case is maybe one of the best case-study were surface and sample preparation face together at the nanoscale. Indeed, TEM observations require particularly thin regions (few tens nm thin) to enable the matter penetration by the electrons. Thus, one can expect the surfaces to play a key role influencing measurements for example when measuring dislocation densities using TEM [LAV 75, KIE 11, OH 09].
Several models and approaches were developed to handle dislocation and surface interactions: the classical image dislocation in semi-infinite space [HEA 53], the half-space Peierls–Nabarro model [LEE 07, LEE 08], the Gosling and Willis Green's function method [GRO 70, FIV 96], the Lothe's energy theorem [LOT 82], the superposition method based on the Boussinesq problem [HAR 99, FIV 96], the infinite image dislocation series in thin films [HAR 99] or the average image stresses method of Mori *et al.* [MOR 73]. All of them applicable to linear isotropic media. More recently, Wu proposed a method to consider

arbitrary defects in thin films using anisotropic elasticity [WU 12]. The classical image stress method consist on replicating a dislocation beyond a free surface including a secondary stress function to cancel the remaining shear and normal stress, satisfying the free surface conditions [HIR 82]. For complex dislocation configurations and boundary value problems (BVPs), the image stress can be computed using FEM [Van 95] leading to "hybrid methods" coupling *e.g.,* discrete dislocation dynamics (DDD) and FEM simulations. Few of these methods are described in the following.

### 1.2.2 Modeling surface and dislocation interactions

As emphasized in previous sections, MD is naturally able to tackle surface of nano-objects. However, it is restricted to relatively small samples and extremely elevated strain-rates. In this thesis, we will focus on a mesoscale approach with the aim of opening new routes to model nano-objects accounting for their surfaces on larger sizes and timescales.

The DDD method (that will be described in the Chapter 2) allows to compute dislocation dynamics using the elastic theory as defined in a infinite continuum [VAS 06, HUL 11, KUB 13]. It can therefore not solve boundary surface problems by itself. However, stress-free boundary conditions (BCs) can be addressed using DDD coupled with an external elastic solvers as FEM or boundary elements methods (BEM). Two approaches are mainly known. The first one is the superposition method (SPM) proposed by Van der Giessen and Needleman [Van 95] that will be discussed in details in the next chapters. The second refers to the discrete continuous method (DCM) proposed by Lemarchand and co-workers [LEM 99a, LEM 99b, LEM 01] that is based on the eigenstrain formalism of Mura [MUR 87] and formally developed and used by Devincre and collaborators [GRO 04, GRO 03, VAT 10, VAT 14] and Liu [LIU 09]. In addition, fast Fourier transform (FFT) based methods are also more and more used in the community [BER 15, BER 19, KOH 20].

#### 1.2.2.1 The superposition method

Lubarda *et al.* [LUB 93] proposed to use numerical methods to solve BVPs of a dislocation microstructure in equilibrium using the image stress correction concept of Volterra [VOL 07]. The variational formulation of the SPM was later developed by Van der Giessen and Needleman [Van 95] applicable to interface and voids and with the introduction of displacement BCs corrections. Those two pioneer papers provide the basis of SPM as the original coupling method between FEM (or BEM) and DDD simulations. The early implementation of the image stress concept was limited to two dimensions. It was extended to three dimensions by Fivel *et al.* [FIV 97, FIV 98] to model dislocation evolution in nanoidentation. SPM has been widely applied later on and examples of application can be found in [ZBI 02a, ZBI 02b, ELA 08, LIU 09, ZHO 10, GAO 10, CUI 15]. Briefly, SPM consists in using the stress and displacement field generated by dislocations from a DDD simulation (*i.e.* computed using an infinite continuum) extracted at virtual boundaries to correct BVPs using a FEM solver [Van 95]. Then, the elastic stress solved by FEM is superimposed to the internal stress over the dislocations lines and used to change the current microstructure along time. A detailed analysis about this method will be presented in Chapter 3. Yasin [YAS 01] performs simulations on cubic aluminum sample with random distribution of Frank-Read (FR) sources loaded at a strain rate of 10 $s^{-1}$ in the [001] direction and found that for this case the effect of the surface softens the sample. The same result was obtained by Yan [YAN 04] as shown in Figure 1.18. SPM was successfully used for several case studies. Nanoidentation simulations studies are reported by Fivel and co-workers [CHA 10, FIV 98]), Mordehai and co-workers [ROY 19]. Studies in pillars where thin persistent slip bands are observed in the work of Po *et al.* [PO 14].

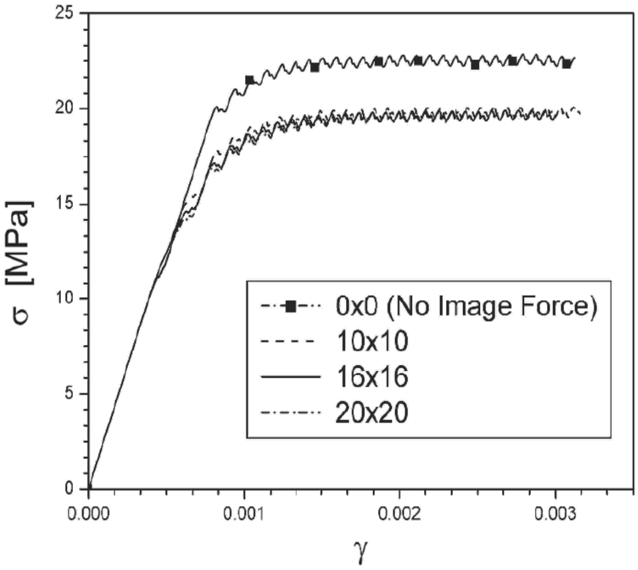

Figure 1.18: Effect of surfaces on the stress-strain curve computed by DDD simulations for a cube (few micron edge length) deformed with fix tensile strain rate of 10 $s^{-1}$. The traction free conditions are achieved by the introduction of a continuous array of prismatic loops covering the area of the surface. The simulation is performed using one FR source located in the middle of the cube. 10×10, 16×16 and 20×20 refers to the amount of loops used along the free surfaces. The curve with square symbols represent the case where no traction-free BC was considered. Figure from [YAN 04].

#### 1.2.2.2 The discrete-continuous method

In brief, the DCM is based on the work of Mura [MUR 87] which describes dislocations as inclusions that generate homogeneous plastic strain fields called eigenstrains. DCM also requires DDD that is used to compute dislocation glide from which the DCM computes corresponding eigenstresses that directly deal with the boundaries. In contrary to SPM, no corrections of the BCs are thus required when relying on the DCM. In the DCM method, the displacement field is obtained from the plastic strain field yielded by the dislocations. It is computed using interpolation and homogenization (or regularization). Stress interpolation is done in two steps. First, the stress at the Gauss points of the mesh is transformed to a nodal stress using the pseudo inverse of the shape function. Then, the nodal stresses are interpolated to the dislocations segment middle points. The stress everywhere ($\sigma$) is related to the total deformation calculate at the mesh Gauss points ($\epsilon_n^t$) and the plastic strain solution of the last DDD step ($\epsilon_{n-1}^p$) by the elastic modulus $C$ through equation 1.2.

$$\sigma = C(\epsilon_n^t - \epsilon_{n-1}^p) \tag{1.2}$$

Regularization is also performed in two steps. The slip produces by the dislocation is extended over a slab of finite thickness to replace the real dislocation by a continuous distribution of parallel infinitesimal dislocations. Theoretically, this is equivalent to substitute the dislocation line by a disinclination dipole of height equal to the slab thickness [Esh 66]. The second step is to redistribute these homogenized amount of slip (tensorial plastic shear) at Gauss points of the FEM mesh. This is done using the Orowan's law (equation 1.3 ) where $\mathit{\Delta}\gamma$ is the total shear increment, $b$ the Burgers vector, $V$ is the representative volume and $\mathit{\Delta}S$ the area swept by the dislocation. It follows that the precision of such method relies on the type of mesh, on the integration timestep of the numerical solver and on the amplitude of the deformation increment.

$$\mathit{\Delta}\gamma = \frac{b\mathit{\Delta}S}{V} \tag{1.3}$$

Critical aspects of the DCM rely on the way the regularization method is applied and its direct implication on the calculation of the image forces. Different regularization methods were proposed for the DCM. Lemarchand *et al.* proposed a slight modification of equation 1.3 where the interception area of the previously mentioned slab with thickness $h$ and the elementary volume is calculated [LEM 01]. If each integration point is denoted by $i$ then $\mathit{\Delta}\gamma$ is localized at each integration point by:

$$\mathit{\Delta}\gamma^{(i)} = \frac{\mathit{\Delta}V_s^i/h}{S} \cdot \mathit{\Delta}\gamma \tag{1.4}$$

With the term in the numerator being the effective area corresponding to the "ith" integration point. Another modification was proposed by Vattre *et al.* using intercepting spheres [VAT 14]. The difficulty of this approach arises from the fact that some swept area may be included in two or more elementary spheres.

$$\mathit{\Delta}\gamma^{(i)} = \frac{S_{sphere}^{(i)}}{S} \cdot \mathit{\Delta}\gamma^{sphere} \tag{1.5}$$

Liu *et al.* proposed a different approach from the previous version using a weight function $w^{(i)}$ at each integration point normalized by the contribution of the total number of integration points $n$ [LIU 09]. The weight function is expressed as a function of isotropic Burgers vector density function, based on the non-singular continuum theory of dislocations developed by Cai *et al.* [CAI 06].

$$\varDelta\gamma^{(i)} = \frac{w^{(i)}}{\sum_{i=1}^{n} w^{(i)}} \cdot \varDelta\gamma \tag{1.6}$$

Finally Cui proposed a new method based on a modification to the Liu solution where the weight function of each integration point is also normalized by the swept areas of each elementary volume [CUI 15, CUI 16].

The comparison of these regularization methods is benchmarked in Refs [CUI 15, CUI 16] considering a 40 µm length cubic crystal and an edge dislocation placed in the middle of the crystal in the (010) slip plane with Burgers vector in the [001] direction at a distance $Z$ from the top surface (Fig 1.19 (a)). Isotropic elastic constants were considered with shear modulus $\mu = 51$ GPa and Poisson's ratio $\nu = 0.37$. Quadratic hexahedron elements with 20 nodes and 8 Gauss points are used with size $L = 0.85$ µm. The image force induced by the top surface is calculated for different values of $Z$. Using DCM with all the previous regularization methods a comparison is made regarding the SPM and an analytical solution (Fig 1.19 (b)). The results shows that the DCM method does not reproduce correctly the image forces at region near the free surface while, for the same conditions, the SPM offers a better result. Correct reproduction of the image forces using DCM can be obtained refining the mesh at the outermost domains. This of course increasing the computational time, mostly for a 3D problem. Cui used the hybrid method proposed by Tang [TAN 06] where the singular part of the image stress is obtained by an analytical solution and the non-singular part is calculated by the SPM. Tang's method was used in the DCM method to evaluate the image forces exerted by the left-free lateral surface when the dislocation intercepts it. Comparison of the image force of the lateral free surface is reported in Figure 1.20 (a) where the DCM is used with the regularization method proposed by Cui and it is compared to the SPM and the analytical solution. A comparison of the DCM using Tang hybrid proposition for image force calculation as compared to the normal DCM is shown Figure 1.20 (b). The use of Tang formulation allow for the better calculation of the image forces whiting the DCM approach.

#### 1.2.2.3 Fast Fourier transform based method

FFT based method for mechanics of materials was originally developed by Moulinec and Suquet to allow for fast computation of the local response in composite materials [MOU 94, MOU 98]. Lebenson and coworkers latter extended the method to viscoplas-

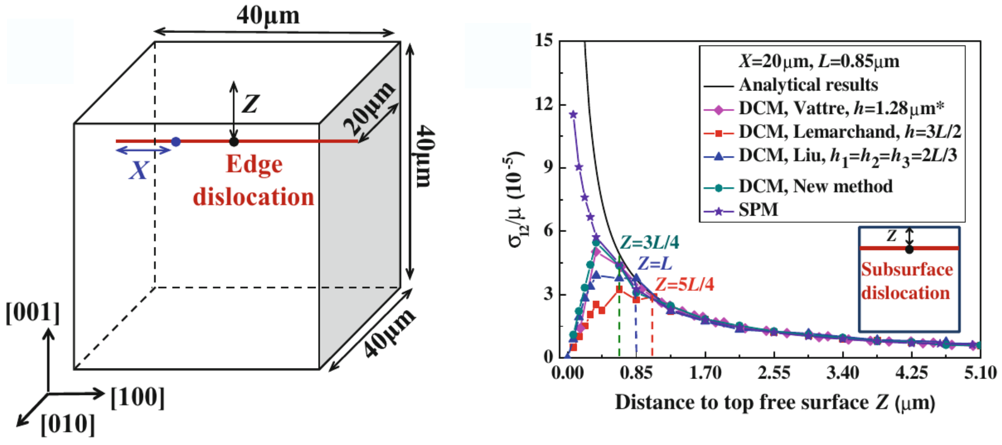

**(a)** **(b)**

Figure 1.19: Benchmark of the different regularization methods proposed for the DCM. (a) Simulation setup made of a square box with an edge dislocation along the [100] direction. (b) Image forces computed by DCM, SPM and analytical methods for different dislocation *vs.* free surface distance $Z$. The SPM reproduces better the analytical solution. Figure from [CUI 16].

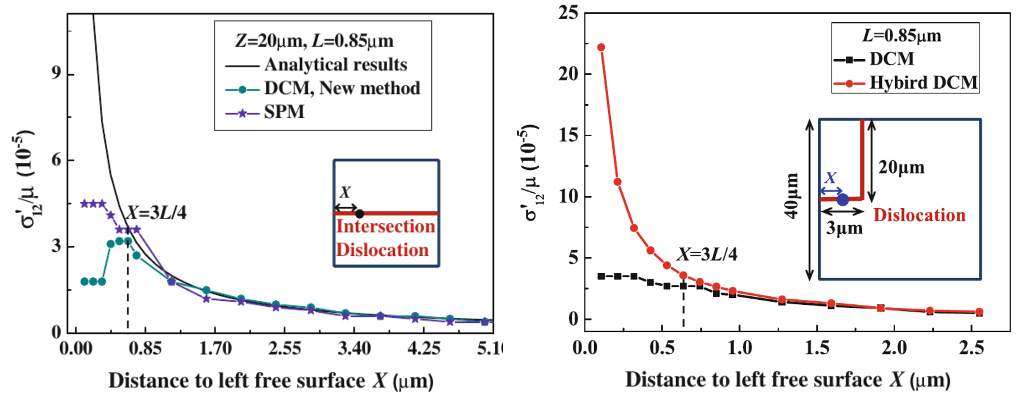

**(a)** **(b)**

Figure 1.20: Image stress calculated form the left free surface (Figure 1.19 (a)). (a) image stress comparison of the DCM method using Cui regularization regarding the SPM and the analytical solution. (b) comparison of the DCM using Cui and Tang hybrid proposition. Figure from [CUI 16].

tic [LEB 01] and elasto-viscoplastic [LEB 12] polycrystal simulations. The FFT method solves the mechanical equilibrium equations in the Fourier space assuming that the mechanical fields are periodic in the three directions. The strain field calculated in the Fourier space is traduced into the real space using the inverse discrete Fourier transform. Applications of FFT include approaches where dislocation lines are not tracked individually such as the level-set method [XIA 03] and phase-field approaches [WAN 01, HUN 11]. The two previous method account for dislocation elastic interactions but intrinsically fail at describing dislocation contact reactions such as the junction formation. Using FFT, Capolungo and collaborators improved the efficiency of the DCM [BER 15]. In this case

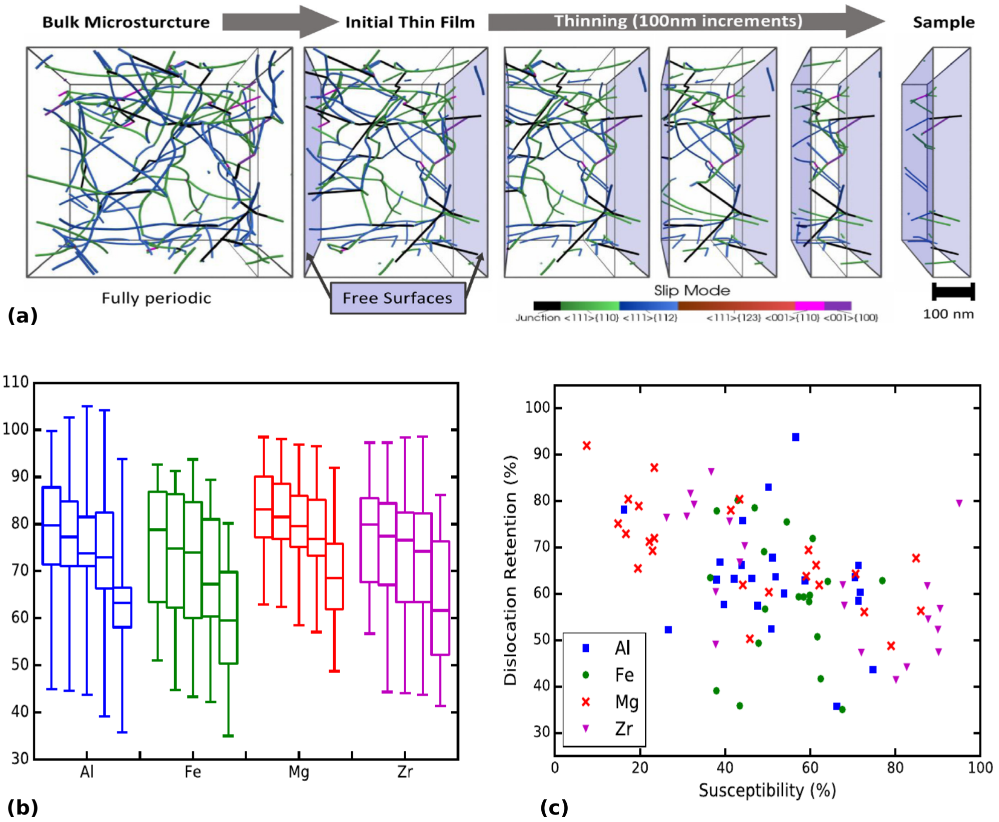

Figure 1.21: DCM-FFT study on modeling TEM lamella and surface-effects on dislocation microstructure in metals. (a) Sample preparation starting from the periodic cell (left) and further thin film size reduction and relaxation up to 100 nm thickness (right). (b) Dislocation retention fraction for each material after consecutive slicing. (c) Dislocation retention as a function of the orientation susceptibility. Figure from [KOH 20].

the stress obtained in the Fourier space contains long-range elastic interactions. It is also demonstrated that the approach allows for the treatment of anisotropic elasticity with similar computational costs than that of isotropic elasticity. In general, the introduction of the FFT-based method into the DDD framework improves the computational cost of the simulations.

The DCM-FFT approach was used to study the effect of the image stress in TEM experimental conditions [KOH 20]. Indeed, TEM lamella preparation can change the stress state associated with the traction-free conditions at the free-surfaces and change the dislocation microstructure. To investigate this problematic, the authors considered several samples with different crystallographic structures: FCC (Al), BCC (Fe), hexagonal closed-packed (HCP) (Zr, Mg). The virtual sample preparation relies on forming a cubic box of lateral size from 620 to 720 nm with an initial dislocation microstructure distributed on the various slip systems. Few hundred MPa were applied in order to activate the slips systems and promote dislocation multiplication before the load was removed to allow sample relaxation down to zero stress. This latter step is presumed to generate a simulation configuration comparable to the bulk-relaxed conditions in the experiment. At this stage, the computed dislocation density varies from $3 \times 10^{13}$ to $3 \times 10^{14}$ $\mathrm{m}^{-2}$. Virtual material slices were generated leading to thin films of 500 nm periodic along $x$ and $y$ with two free-surfaces perpendicular to $z$. Under these conditions, the sample was also relaxed *in silico* and the dislocation density was measured again. This three steps (slice, relaxation and dislocation density measuring) were repeated systematically thickening the virtual lamella down to a thickness of 100 nm. Each time, an amount 100 nm was removed as shown in Figure 1.21 (a). The dislocation retention fraction is computed as the ratio of the dislocation density in the lamella after each reduction step and the initial dislocation density (Figure 1.21 (b)). For each material, the dislocation reduction represent a 30 to 40 % regarding the bulk microstructure. Also the dislocation retention regarding the crystal orientation seems to be slightly larger for HCP systems as shown in Figure 1.21 (c).

## 1.3 Conclusion

In this chapter, we have seen that the mechanical properties of materials were strongly influenced by size leading to the well-known paradigm “smaller is stronger”. The different phenomena related to small-scale plasticity are generally, at first, studied using experimental techniques such as *in situ* TEM or SEM. However, computational methods represent a fast and cheaper way to characterize material properties and elementary-deformation processes at small-scale. While MD is commonly used in parallel to experiments as a complement to help to interpret the different processes of deformation, it shows significant limitations regarding the sample size an strain rate. DDD simulations allow to model larger sample sizes and strain rates more comparable to those obtained in the experiments. However, several limitations including BC (often limited to periodic) and the non-ability to correctly account for free-surface effects are prohibitive for small-scale mechanics simulation purposes. Some improvements can be noticed including the hybrid method proposed by Tang *et al.* based on the use of the Yoffe analytical solution for straight dislocation intercepting a free surface [YOF 61, TAN 06]. Weygand *et al.* also proposed a pseudo-mirror method to account for the image stress that will be detailed in the next chapters [WEY 02]. In our nanomechanics context, another limitation of DDD codes is that they usually do not allow for a proper dislocation nucleation process. A nucleation algorithm can be integrated to account for the statistical nature of dislocation nucleation but still with some limitations when compared to MD. We will also come back on this aspect later in the manuscript. Finally, DDD generally assumes homogeneous applied stress what definitely restricts sample shapes to be modelled and is not in accordance with classical nanomechanics experiments. One solution is to develop a modeling framework including simulation conditions comparable to those of experiments (sample size and strain rate) and accounting for surfaces effects using *e.g.,* a DDD-FEM method such as the SPM or the DCM. It has been shown that SPM is particularly suited to solve the influence of free surface on the dislocation miscrostructure at costs of a relative easy coupling implementation. As we will show latter, the SPM only consists in interchanging data arrays at each simulation timesteps without changing drastically neither the FEM or the DDD workflow. The use of a DDD-FEM coupled method allows not only to simulate samples with complex shapes but also to perform various kinds of experiments where the sample need to be tilted or rotated as *e.g.,* in the case of nanoindentation studies within the small perturbation approach [CHA 10]. Using a FEM elastic solver, one can compute stress concentrations and possibly predict dislocation nucleation events as *e.g.,* in Ref. [ROY 19].

During the PhD, we have developed a tool called El-Numodis that relies on the coupling between the DDD nodal code Numodis [DRO 14, SHI 15] with the Elmer FEM solver [MAL 13] using the SPM as proposed by Needleman. In the next chapter, we will introduce the main aspects of both DDD and FEM elastic solver simulations as well as El-Numodis parent codes: Elmer and Numodis.

**Chapter 1: to remember**

- Mechanical properties of materials at the micro- and nanoscale differ from those of their bulk counterpart.
- A general “smaller stronger” trend is observed when size scales down.
- At the nanoscale, the dislocation multiplication process is progressively replaced by a dislocation nucleation/starvation process.
- Currently, the main method used to characterize small-scale mechanics of materials are *in situ* transmission electron microscopy and molecular dynamics but both of them rely on different spatial and temporal scales.
- The influence of surfaces on the mechanical and dislocation properties can not be neglected at the nanoscale.
- Coupling methods (*e.g.,* between discrete dislocation dynamics and finite elements) can provide a multi-scale framework to investigate nanomechanics issues taking into account surfaces.

# Chapter 2

# Numerical methods and parent tools

In this thesis, we develop a multi-scale modeling tool called El-Numodis that relies on the superposition method to solve a combination of dislocation dynamics and boundary value problems. The development of such tool requires basics about the physical problems involved as well as some hints about computational implementations and methodologies. Numodis [DRO 14, SHI 15], a nodal based discrete dislocation dynamics software, and Elmer [MAL 13], a multi-physics open source finite-element software, are used at the roots of El-Numodis. This second chapter starts by a selective introduction to dislocation dynamics focusing on the various kinds of implementations, details about boundary conditions and a description of short-range dislocation-dislocation interactions. Then, Numodis specific features are presented.

**Contents**

**2.1 Generalities about discrete dislocation dynamics . . . . . . . . . . 34**
2.1.1 Nodal and lattice-based approaches . . . . . . . . . . . . . . . . . . . . . 35
2.1.2 Stress and dislocation velocity . . . . . . . . . . . . . . . . . . . . . . . . 36
2.1.3 Boundary conditions . . . . . . . . . . . . . . . . . . . . . . . . . . . . . 37
2.1.4 Initial configuration and loading modes . . . . . . . . . . . . . . . . . . 38
2.1.5 Dislocation short-range interactions . . . . . . . . . . . . . . . . . . . . 39
**2.2 Introduction to Numodis . . . . . . . . . . . . . . . . . . . . . . . . . . 41**
2.2.1 Nodal forces and energy . . . . . . . . . . . . . . . . . . . . . . . . . . . 41
2.2.2 Equation of motion and time integration . . . . . . . . . . . . . . . . . . 42
2.2.3 Dislocation stress field calculation . . . . . . . . . . . . . . . . . . . . . 43
2.2.4 Dislocation displacement field calculation . . . . . . . . . . . . . . . . . 44
2.2.5 Dislocation meshing . . . . . . . . . . . . . . . . . . . . . . . . . . . . . 46
**2.3 Introduction to Elmer and the finite-element method . . . . . . . 47**
2.3.1 Elmer software . . . . . . . . . . . . . . . . . . . . . . . . . . . . . . . . 47
2.3.2 Linear static elastic solver . . . . . . . . . . . . . . . . . . . . . . . . . . 50
**2.4 Conclusion . . . . . . . . . . . . . . . . . . . . . . . . . . . . . . . . . 52**

## 2.1 Generalities about discrete dislocation dynamics

The DDD simulation is used to investigate plasticity at sizes between the atomic and the macroscopic scales. Simulation basics rely on integrating dislocation displacements using the elastic theory, *i.e.* dislocations are described as immersed in an infinite elastic medium while the plastic strain is derived from the area swept by the dislocations. The aim of DDD simulations is to investigate plastic deformation problems and provide outcomes such as stress response and dislocation microstructure evolution at the mesoscale using pre-defined conditions like material elastic properties, starting dislocation microstructure, dislocation mobility law, deformation conditions (imposed strain-rate, creep) and temperature. Specific dislocation processes such as cross-slip, junction formation or climb can be taken into account depending on the complexity of the derived model.

For simple cases when only one or few dislocations are studied, it is possible to find a mathematical solution for the forces acting on the dislocation lines and predict their future evolution. When several dislocations are accounted, analytical predictions are more complex to handle. Indeed, each dislocation portion generates a stress field that impacts all the other surrounding dislocations within the simulation domain [HIR 82]. DDD was developed to tackle this kind of issue and describe plastic deformation and dislocation microstructure evolution at the mesoscale.

### 2.1.1 Nodal and lattice-based approaches

DDD codes can be classified in two kinds regarding the dislocation line discretization, *i.e.* the lattice-based (also called segment-based) and nodal-based approaches (Figure 2.1). In lattice-based codes, a grid of points is predefined inside the simulation cell. Based on the grid structure, a curved dislocation line is divided into segments of constant line length and character and restricted orientations (*e.g.* 4 directions for edge/screw models). The motion of the dislocation is made perpendicularly to the segment line *i.e.,* the degree of freedom of the simulation is imposed by a list of segments and vectors.
In a nodal-based code, curved dislocation lines are discretized using nodes and not segments, explicitly. Nodes are interconnected by elements with no limitation regarding their orientation. The nodal connection is performed by shape functions. In the simplest case, a linear shape function connects two nodes using a straight line. This approach allows for a more detailed description of curved dislocations when compared to the segment approach.

Here is a classical DDD workflow:

- Dislocation discretization
- Force/stress calculation
- Dislocation velocity and hypothetical displacement
- Obstacle management
- Dislocation displacement

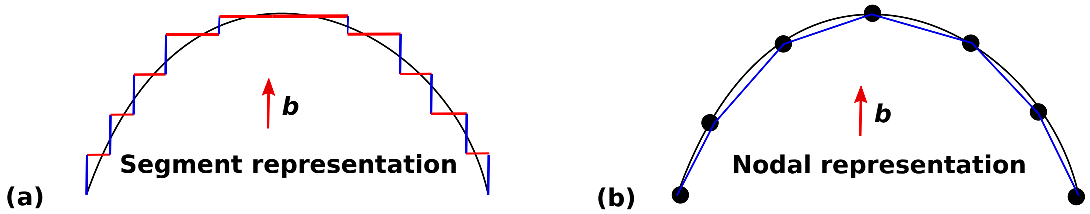

Figure 2.1: DDD Dislocation line discretization, (a) lattice-based approach where the dislocation line is discretized into segments (edge/screw model), (b) nodal-based approach with a discretization of the dislocation into curves of various orientation with respect to the Burgers vector.

Examples of lattice-based codes are microMegas [DEV 11], developed by Devincre and co-workers (LEM, France) and Tridis developed by Fivel (SIMaP, France) and collaborators [FIV 96, FIV 97]. Among their specificities, microMegas uses edge, screw and mixed segments for dislocation discretization while Tridis in the other hand relies on an edge-screw model only. Another lattice-based codes is MobiDic [MAD 13] developed by Madec (DAM, CEA, France). On the other hand, Paradis is maybe the most used nodal code around the world [ARS 07]. It is developed at the Lawrence Livermore National Laboratory and is currently maintained by Arsenlis and collaborators. Details about Paradis can be found in Ref.[VAS 06]. Another example of nodal code is micro3D developed by Yasin and collaborators [YAS 01]. In this thesis, El-Numodis will rely on Numodis that is developed by Dupuy and collaborators at SRMA, CEA (France). Further details about DDD codes and implementations can be found in Ref. [KUB 13].

### 2.1.2 Stress and dislocation velocity

Whatever the discretization model used, the effective shear stress $\tau_{eff}$ is computed at the middle of all dislocation segments, at each DDD time step. Each segment is then translated perpendicular to its line direction by a distance $v \cdot dt$, where $v$ is the dislocation velocity proportional to $\tau_{eff}$. Dislocation velocities in general can be described as a function of several variables (drag forces, applies forces, temperature, enthalpy, *etc.*). In the simple viscous case, the dislocation velocity follows a linear relation:

$$v = \frac{\tau_{eff}.b}{B} \tag{2.1}$$

with $B$ the drag coefficient. $\tau_{eff}$ can be computed as the contribution of various stress components including the projection of the Peach-Koehler force $\tau^{pk}$, the line tension $\tau_{lt}$ and the lattice friction $\tau_{Peierls}$.

$$\tau_{eff} = \tau^{pk} + \tau_{lt} - \text{sign}(\tau^{pk} + \tau_{lt}) \cdot \tau_{Peierls} \tag{2.2}$$

Note that some DD codes also integrate an image force term in the effective stress calculation which is otherwise generally computed using SPM or DCM. The projection of the Peach-Koehler force in the gliding plane is defined as:

$$\tau_{pk} = \frac{\boldsymbol{F}^{pk} \cdot \boldsymbol{g}}{b} \tag{2.3}$$

with $\boldsymbol{g}$ a glide unit vector and $\boldsymbol{F}^{pk}$ the Peach-Koehler force given by:

$$\boldsymbol{F}^{pk} = (\boldsymbol{\sigma} \cdot \boldsymbol{b}) \times \boldsymbol{\xi} \tag{2.4}$$

Where $\boldsymbol{\xi}$ is the dislocation line vector and the stress field $\boldsymbol{\sigma}$ deduced from the external stress $\boldsymbol{\sigma}_{app}$, internal stress $\boldsymbol{\sigma}_{int}$. $\boldsymbol{\sigma}_{app}$ is generally set homogeneously to each dislocation

segment or can be derived from a FEM simulation. On the other hand, the internal stress refers to the stress field produced by all dislocations and is the main purpose of DDD simulations.
In the case of curved dislocations, the internal stress is defined by equation 2.5 (*e.g.*, Ref.[HIR 82]). We will see in the following that DDD codes often rely on simplified expressions.

$$\begin{aligned} \sigma^{int}_{\alpha\beta} &= \frac{\mu}{8\pi} \oint \partial_i \partial_p \partial_p R [b_m \epsilon_{im\alpha} dx'_\beta + b_m \epsilon_{im\beta} dx'_\alpha] \\ &+ \frac{\mu}{4\pi(1-\nu)} \oint b_m \epsilon_{imk} (\partial_i \partial_\alpha \partial_\beta R - \delta_{\alpha\beta} \partial_i \partial_p \partial_p R) dx'_k \end{aligned} \tag{2.5}$$

The Peierls stress $\tau_{Peierls}$ (also known as the lattice friction stress) is the stress needed to move a dislocation at 0 K. It is commonly expressed as a fraction of the shear modulus $\mu$; for instances *e.g.,* around $10^{-5}$ $\mu$ in FCC metals.
Finally, the line tension $\tau_{lt}$ is the result of the self stress field that every dislocation produce per unit length. It is related to dislocation energy minimization reducing their length.

$$\tau_{lt} = \frac{\mu b}{4\pi(1-\nu)R}(1 - 2\nu + 3\nu\cos^2\theta)(\ln(\frac{L}{2b}) - \nu\cos(2\theta)) \tag{2.6}$$

were $\nu$ the Poisson ratio, $R$ is the curvature radius and $\theta$ the angle between the the dislocation line and the Burgers vector.

After the computation of $\tau_{eff}$ on dislocation nodes or segments, DDD codes usually compute dislocation velocity and integrate dislocation displacement along time. More complex dislocation mobility law can be taken account including *e.g.* thermally-activated mobility laws [PO 16].

### 2.1.3 Boundary conditions

Weinberger categorizes BCs used in DDD simulations into three main groups [WEI 16]: infinite, periodic and heterogeneous BCs (Figure 2.2). The simplest ones are the infinite BCs where the dislocation lines are considered to be embedded in an infinite medium. Generally, the stress produced by dislocations when using infinite BCs are solved considering homogeneous and infinite medium what makes simulations with infinite BC easy to implement. In this kind of model, the dislocation lines are allowed to move up to a certain distance far from any existing boundary what induces massive central processing unit (CPU) costs. So, simulations with infinite BC are used to idealized test cases.
Periodic boundary conditions (PBCs) mimic an infinite medium by replicating the simulation supercell in all directions. The replicas surrounding the main simulation cell are called

images. Using PBCs is another way to model infinite medium but with a bias associated to the replicated dislocation density. In this case however, any configuration or pattern with characteristic length larger than the supercell cannot be captured. The driving forces of dislocations are computed considering the total stress due to all dislocation inside all the replicas. In practice and avoiding high computational cost, only a limited number of replica is considered.

Heterogeneous BCs rely on interfaces and require stress correction, they will be discussed later.

Additional BCs can be found in the literature including free-BCs where dislocation are allowed to escape the sample (also called permeable-BCs), fixed-BCs where dislocations are stored at the boundary mimicking an impenetrable GB or even rotated-BCs introduced by Madec to avoid dislocation auto-annihilation [MAD 04]. The previous description of BCs can be combined *e.g.,* it is possible to model a thin film using periodic BCs in two directions and free-surfaces in the other (Figure 2.2 (c)). Numodis accounts for rotations as well as periodic, fixed and permeable BCs.

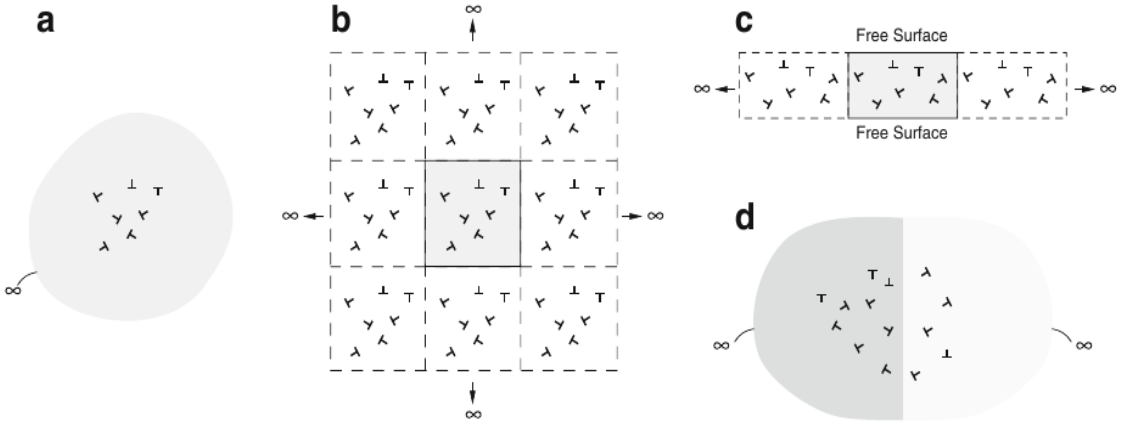

Figure 2.2: BCs in DDD. (a) infinite boundary conditions. (b) periodic boundary conditions. (c) heterogeneous boundary conditions and (d) a bimaterial interface in an infinite medium. Image from [WEI 16].

### 2.1.4 Initial configuration and loading modes

Most of DDD simulations rely on an initial dislocation microstructure. Depending on the target problem, the starting dislocation microstructure can influence simulation outcomes. Usually, several dislocation objects can be used to define the starting microstructure including FR sources but also dislocation loop or *infinite* dislocations. In this work, we have developed a nucleation routine that allows for homogeneous or heterogeneous dislocation nucleation events. This routine can be used to prevent the use of pre-existing

dislocation microstructure. We will come back on that later.
Several control modes are currently available in DDD codes. Simulation are generally controlled either applying a stress or a strain-rate. The stress control is quite straightforward as we have seen that stress calculation is one of the main item of DDD workflows. However, it might be sometimes required to run simulation at constant strain-rate as *e.g.,* to mimic experimental conditions of deformation. In this context, DDD codes rely on an interplay between the plastic strain as computed by the total area swept by dislocations and the total strain (elastic + plastic). Loading modes currently available in Numodis and El-Numodis will be introduced later.

### 2.1.5 Dislocation short-range interactions

Contact reactions between dislocations can lead to stable configurations that constitute barriers to further dislocation motion [KUB 13]. Those barriers significantly influence the evolution of the dislocation microstructure and thus affect the mechanical properties of materials. When two dislocations gliding in non-parallel planes interact, few potential reactions may take place. First, dislocations can cut through each other and continue their movement (*e.g.,* when dislocation have 90° Burgers vectors). In fact, they produce steps on the lines with Burgers vector size known as jogs [NIU 17] (Figure 2.3 (a)). The second option is the zipping of the two dislocations called *junction* (Figure 2.3 (c)). Dislocation junctions can be destroyed if stress is increased locally. Dislocation can also annihilate (Figure 2.3 (b)) if they have same Burgers vectors [KUB 92]. This reaction is called a *collinear* reaction [MAD 03]. Crossed-states also exist. The interaction between two dislocations is controlled by the Frank's law and the Kroupa equation [HIR 82]. The Frank's law suggests that two interacting dislocations with burger vectors $\boldsymbol{b_1}$ and $\boldsymbol{b_2}$ may form a junction if $\boldsymbol{b}_1^2 + \boldsymbol{b}_2^2 > (\boldsymbol{b}_1 + \boldsymbol{b}_2)^2$. On the other hand, the Kroupa equation relies on the ability of the two dislocations to attract or repel each other. A formed junction can also interact with a third dislocation (Figure 2.3 (e)). In this case, the arms of the third dislocation join the extreme of the zipped junction forming pinning points leading to the creation of a FR source [BUL 06]. Dislocation dipoles can also form when dislocations glide in close parallel planes [TET 62].

Generally, DDD codes detect dislocation contact reactions before they happen via an *obstacle detection* subroutine. Then, either the elastic theory or local rules are used to to generate the induced reaction. In Numodis, a *split* algorithm is run at the same time than velocity calculation to determine the evolution of all physical nodes connected to multiple segments and predict interactions. The main steps of the Numodis workflow are detailed in the following.

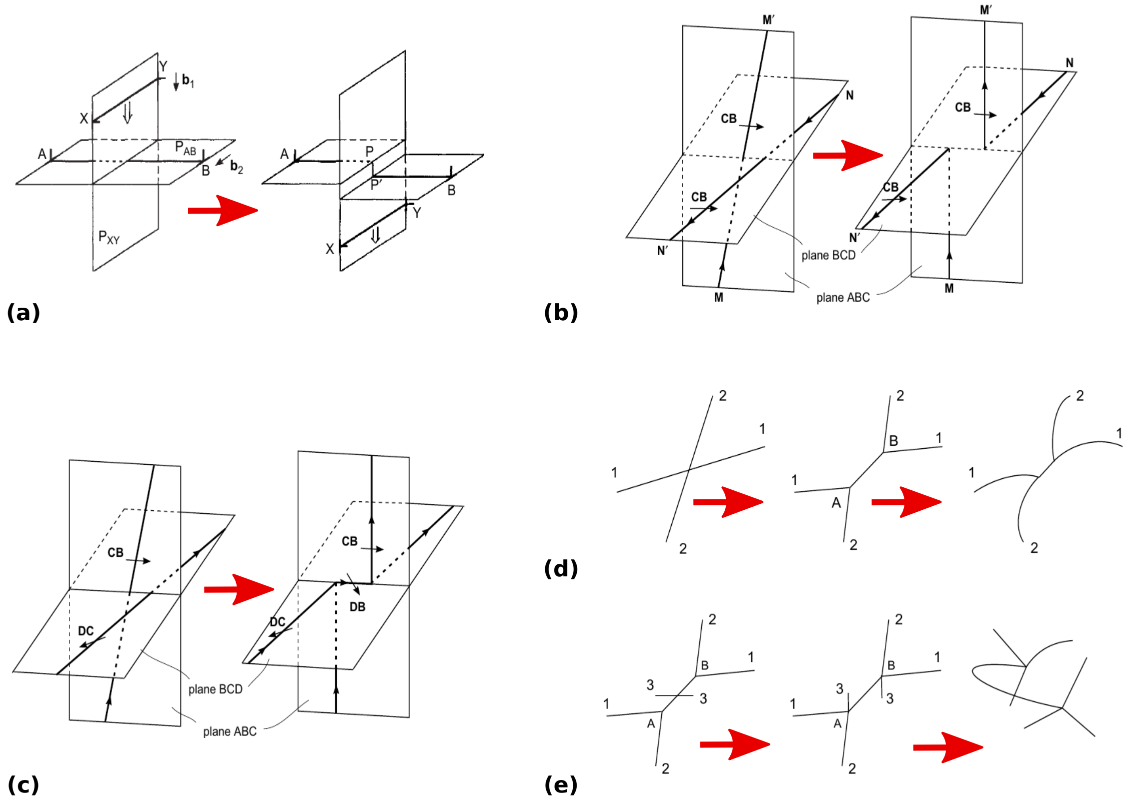
(a)
Y
b1
X
A
PAB
B
b2
PXY
A
P
P′
B
Y
X
(b)
M′
N
CB
CB
N′
M
plane BCD
plane ABC
M′
N
CB
CB
N′
M
(c)
CB
DC
plane BCD
plane ABC
CB
DC
DB
(d)
2
1
1
2
2
1
B
1
A
2
2
1
1
2
(e)
2
B
1
3
3
1
A
2
2
B
1
3
3
1
A
2

Figure 2.3: Examples of short range dislocation interaction. (a) Jog formation when two dislocations with Burgers vectors oriented at 90° interact together. (b) collinear reaction generated by two dislocations with same Burger vectors but opposite line directions. (c, d) junction formation between two interacting dislocations. (e) multi-junction formation (glissile junction case leading to a FR source). Figures from [KUB 13].

## 2.2 Introduction to Numodis

Numodis [DRO 14, SHI 15] is a DDD code developed by Dupuy (SRMA, CEA, France) and collaborators. It is written in object oriented C++ and its workflow is described in Figure 2.4.

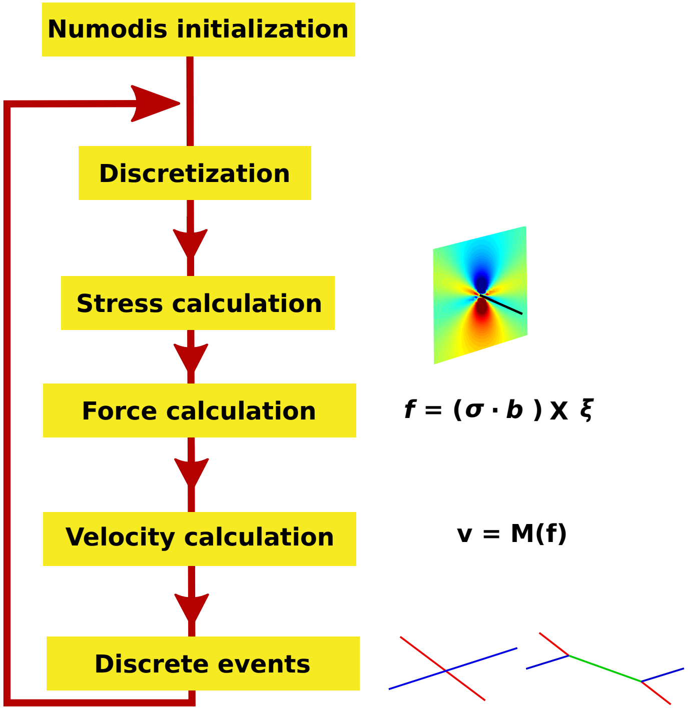
Numodis initialization
Discretization
Stress calculation
Force calculation
f = (σ · b ) X ξ
Velocity calculation
v = M(f)
Discrete events

Figure 2.4: Scheme of the main operations performed by Numodis at each simulation timestep, after the initialization of the code.

### 2.2.1 Nodal forces and energy

In Numodis, the movement of dislocations is related to the calculation of nodal forces $\boldsymbol{f}_i$. Nodal forces are the response of dislocation to internal or external stresses. In nodal representation, the degrees of freedom (DOF) of a node relies on its position $r_i$, the dislocation $b_i$ and $\boldsymbol{f}_i$ varies as the negative gradient of the node's energy,

$$\boldsymbol{f}_i = -\nabla(E_{tot}(r_i, b_i)) \tag{2.7}$$

The total energy of the node $E_{tot}$ is the sum of the elastic energy $E_{elastic}$ and the core energy $E_{core}$. $E_{elastic}$ for an infinite straight dislocation in case of isotropic elasticity is:

$$E_{elastic} = \frac{\mu b^2}{4\pi(1-\nu)}(1 - \nu \cos^2_{\theta}) \ln(\frac{R_0}{r_0}) \tag{2.8}$$

$R_0$ and $r_0$ are the outer and inner radii of the dislocation, respectively. As an approximation in Numodis, the core energy is considered as a fraction of $E_{elastic}$:

$$E_{core} = \alpha_{core}\frac{\mu b^2}{4\pi(1-\nu)}(1-\nu\cos^2_\theta)\ln(\frac{R_0}{r_0}) \tag{2.9}$$

Then, the nodal force can be rewritten as:

$$\boldsymbol{f}_i = \boldsymbol{f}_i^{elastic} + \boldsymbol{f}_i^{core} \tag{2.10}$$

$\boldsymbol{f}_i^{core}$ is computed using the derivative of the core energy. For $\boldsymbol{f}_i^{elastic}$, a virtual work argument is used rather than $E_{elastic}$ derivative. $\boldsymbol{f}_i^{elastic}$ is computed as the weight average of the Peach-Koehler force acting on the dislocation segment connected to the nodes and is represented as the line integral along all the segments connected to the node $i$.

$$\boldsymbol{f}_i^{elastic} = \int_c \boldsymbol{f}^{pk} N_i(x)dL(x) \tag{2.11}$$

Where $N_i(x)$ is a linear shape function defined for each node $i$ connected to a node $j$.

$$N_i(x) = \frac{\|x - r_j\|}{\|r_i - r_j\|} \tag{2.12}$$

In Numodis, $\boldsymbol{f}^{pk}$ relies on the internal stress calculation (contribution of dislocation) and the applied stress. During this thesis, the Weygand method [WEY 02] to handle dislocation image forces during $\boldsymbol{f}^{pk}$ calculation was developed and can now be used in standalone Numodis (it will be discussed further later). $\boldsymbol{f}_i^{core}$ corresponds to a part of the previous $E_{core}$ (typically a few percents) and is explicitly declared as a parameter in Numodis. Friction forces (overdamped dislocation glide) and static frictional forces are both considered when computing velocities. They are both embedded into a variational Galerkin approach as explained in [VAS 06].

### 2.2.2 Equation of motion and time integration

In the overdamped regime where the dislocation velocity is defined by forces, a first order differential equation of motion is solved leading to a mobility function $M$,

$$v_i = M(\boldsymbol{f}_j) \tag{2.13}$$

the mobility law $v_i$ can be as simple as the viscous glide model (equation 2.1) or more complicated (*e.g.,* thermally-activated mobility law). In any case, it is possible to define a viscous matrix $K$ for the dislocation nodes thanks to the line discretization and the principle of virtual work.

$$KV = F \tag{2.14}$$

Where $F$ is the nodal force and $V$ the nodal velocity to be determined. The viscous matrix $K$ can be decomposed in several sparse matrix thanks to the node connectivity (to speed up the calculation). In general, the nodal viscous matrix can be build using the previous described shape functions and the drag coefficient $B$ using the following equation

$$K_{ij} = \oint N_i(l)N_j(l)B(l)dl \tag{2.15}$$

Owing the nodal forces and the mobility model, the equation of motion of the nodes can be solved,

$$v_i = \frac{dr_i}{dt} = g_i(r_j) \tag{2.16}$$

where $g_i$ implicitly relies on both the nodal force and the mobility model at node $i$. Such first order ordinary differential equation can be integrated using a simple numerical integrator as the explicit Euler forward method:

$$r_i(t + \Delta t) = r_i(t) + v_i\Delta t \tag{2.17}$$

The precision of the computed velocity depends on the integration timestep $\Delta t$. Large $\Delta t$ will affect the stability as well as the precision of the final result. Some other methods can be implemented as the implicit trapezoidal, and the explicit Euler-trapezoid. The latter uses the predictor and corrector operators differences to perform an auto-correction of the timestep $\Delta t$.

### 2.2.3 Dislocation stress field calculation

Dislocations are characterized by stress and displacement fields that distort the crystal around them. The stress field generated by an edge or a screw dislocation can be calculated in Numodis using various derivations of the elastic theory including the classical formulation exposed in the Hirth and Lothe (HL) book or Li formalisms [LI 64, HIR 82].

Both formulations describe dislocation stress field everywhere except at the origin of the dislocation core ($r = 0$). This issue was recently solved by Cai and the non-singular dislocation theory that was also implemented recently into Numodis [CAI 06]. For the screw character, the non-singular theory stress field (line oriented along $z$) is given by,

$$\sigma_{xz}^{ns} = -\frac{\mu b y}{2\pi\rho_a^2}(1 + \frac{a^2}{\rho_a^2}) \tag{2.18}$$

$$\sigma_{yz}^{ns} = \frac{\mu b x}{2\pi\rho_a^2}(1 + \frac{a^2}{\rho_a^2}) \tag{2.19}$$

$$\sigma_{xx}^{ns} = \sigma_{yy}^{ns} = \sigma_{zz}^{ns} = \sigma_{xy}^{ns} = 0 \tag{2.20}$$

while the edge stress field (line oriented along $z$) is given by,

$$\sigma_{xx}^{ns} = -\frac{\mu b y}{2\pi(1-\nu)\rho_a^2}[1 + \frac{2(x^2 + a^2)}{\rho_a^2}] \tag{2.21}$$

$$\sigma_{yy}^{ns} = \frac{\mu b y}{2\pi(1-\nu)\rho_a^2}[1 - \frac{2(y^2 + a^2)}{\rho_a^2}] \tag{2.22}$$

$$\sigma_{zz}^{ns} = -\frac{\mu b \nu y}{2\pi(1-\nu)\rho_a^2}[1 + \frac{a^2}{\rho_a^2}] \tag{2.23}$$

$$\sigma_{xy}^{ns} = \frac{\mu b x}{2\pi(1-\nu)\rho_a^2}[1 - \frac{2y^2}{\rho_a^2}] \tag{2.24}$$

$$\sigma_{xz}^{ns} = \sigma_{yz}^{ns} = 0 \tag{2.25}$$

with $\rho_a = \sqrt{x^2 + y^2 + a^2}$ and $a$ an arbitrary constant associated to the dislocation core width. The parameter $a$ should be small but always larger than 0. In the case of $a < 0$, the Cai equations are identical to the classical singular solutions reported in HL book.

### 2.2.4 Dislocation displacement field calculation

In Numodis, the formulation of Barnett and collaborators [BAR 85, BAR 07] for a triangular dislocation loop is used (Figure 2.5) to compute the dislocation displacement filed $\boldsymbol{u}$.

$$\boldsymbol{u}(X) = -\frac{b}{4\pi}\varOmega_{ABC} - \frac{1-2\nu}{8\pi(1-\nu)}[\boldsymbol{f}_{ab} + \boldsymbol{f}_{bc} + \boldsymbol{f}_{ca}] + \frac{1}{8\pi(1-\nu)}[\boldsymbol{g}_{ab} + \boldsymbol{g}_{bc} + \boldsymbol{g}_{ca}] \tag{2.26}$$

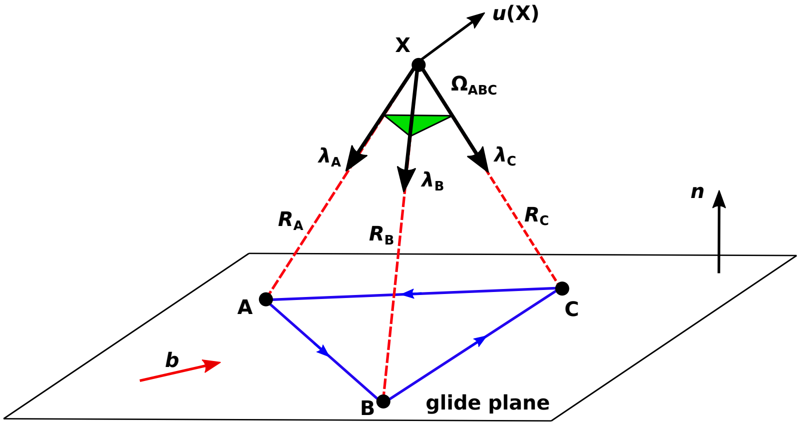

Figure 2.5: Triangular dislocation loop ABC used to calculate the displacement field $\boldsymbol{u}$ at point $X$ with Barnett formulation considering the contribution of the solid angle $\Omega_{ABC}$.

with $\Omega_{ABC}$ the solid angle from point $X$. $\boldsymbol{f}_{ab}, \boldsymbol{f}_{bc}, \boldsymbol{f}_{ca}$ and $\boldsymbol{g}_{ab}, \boldsymbol{g}_{bc}, \boldsymbol{g}_{ca}$ are given by:

$$\boldsymbol{f}_{ij} = (\boldsymbol{b} \times l_{ij}) \ln \left. \frac{|\boldsymbol{R}_j|}{|\boldsymbol{R}_i|} \frac{1 + \boldsymbol{\lambda}_j \cdot l_{ij}}{1 + \boldsymbol{\lambda}_i \cdot l_{ij}} \right) \tag{2.27}$$

$$\boldsymbol{g}_{ij} = [\boldsymbol{b} \cdot (\boldsymbol{\lambda}_i \times \boldsymbol{\lambda}_j)] \frac{\boldsymbol{\lambda}_i + \boldsymbol{\lambda}_j}{1 + \boldsymbol{\lambda}_i \cdot \boldsymbol{\lambda}_j} \tag{2.28}$$

with the indices $i, j$ referring to $A, B$ or $C$. The vectors for each point $A, B, C$ to $X$ are expressed by the quantities $\boldsymbol{R}_A = A - X$, $\boldsymbol{R}_B = B - X$, $\boldsymbol{R}_C = C - X$.
The solid angle associated to the area made by the triangle $ABC$ can be calculated with the formula:

$$\Omega = -4 \cdot \mathrm{sign}(\boldsymbol{\lambda}_A \cdot \boldsymbol{n}) \arctan \left( \sqrt{\tan(\frac{s}{2}) \tan(\frac{s-a}{2}) \tan(\frac{s-b}{2}) \tan(\frac{s-c}{2})} \right) \tag{2.29}$$

With:

$$s = \frac{a+b+c}{2} \tag{2.30}$$

$$\boldsymbol{\lambda}_A = \frac{\boldsymbol{R}_A}{\|\boldsymbol{R}_A\|} \tag{2.31}$$

$$a = \arccos(\boldsymbol{\lambda}_B \cdot \boldsymbol{\lambda}_C) \tag{2.32}$$

$$b = \arccos(\boldsymbol{\lambda}_A \cdot \boldsymbol{\lambda}_C) \tag{2.33}$$

$$c = \arccos(\boldsymbol{\lambda}_A \cdot \boldsymbol{\lambda}_B) \tag{2.34}$$

The Barnett solution for the dislocation displacement field provides more flexibility that the classical ones found in HL book. In particular, there is no restriction regarding to $\boldsymbol{b}$ to be strictly in the habit plane of the loop *i.e.,* the solution remains valid when $\boldsymbol{b}$ has a prismatic component. Bromage *et al.* show that any dislocation loop can be split into finite triangles [BRO 18]. Thus, it is possible to construct triangles with sides matching a line within the dislocation loop using any point outside of the loop. While it does not solve the case of an isolated dislocation segment, the Bromage argument makes Barnett solution usable to compute the displacement field of any closed dislocation.

### 2.2.5 Dislocation meshing

In Numodis, dislocation glide induces an increase/decrease of the distance between nodes. Nodes are added or deleted using two algorithms (called "merge" and "split") depending on the two neighbor nodes distance $L$ (Figure 2.6).

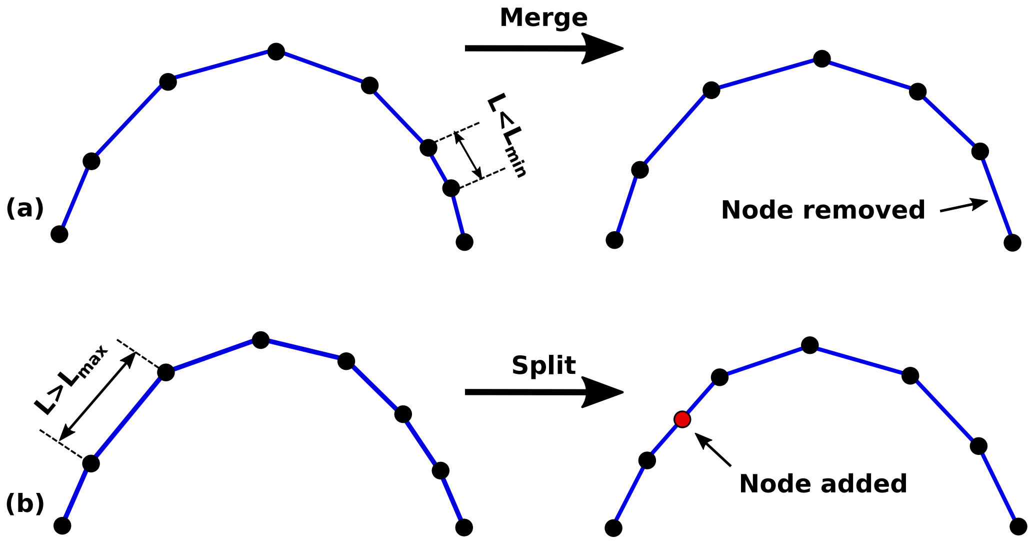

Figure 2.6: Split and merge algorithms used in Numodis to optimize the dislocation discretization. (a) If the distance between a pair of consecutive nodes $L$ gets lower than a minimum distance $L_{min}$ the merge algorithm will remove a node. (b) When the distance between any node get greater than $L_{max}$, a new node is inserted at the middle point by the split algorithm.

The parameters $L_{max}$ and $L_{min}$ define the conditions when a node is added or removed. If $L > L_{max}$ a node is inserted at the middle distance between the two interconnected nodes increasing the DOF. In the contrary, a node is removed if $L < L_{max}$ reducing the DOF.

$L_{max} > 2L_{min}$ is recommended to optimize simulation outcomes.
The “split” algorithm is run during the nodal velocity calculation and dislocation contact reactions. “Splittable” nodes are defined as not-pinned nodes with at least three segments connected. A check for “splittable” nodes and their possible evolution is performed at each timestep.

The split algorithm workflow can be described as follow:

1. Detect all the “splittable” nodes.
2. Determine all the possible outcomes of each “splittable” node.
3. Calculate force and velocity of all possible split option per “splittable” node.
4. Calculation of the power dissipation for each split option and consistency verification.
5. Choose the split option with the higher energy dissipation.

The previous algorithm also includes geometrical, crystallographic and energetic aspects. A similar remeshing and collision-detection approach is implemented in Paradis [ARS 07].

## 2.3 Introduction to Elmer and the finite-element method

The purpose of FEM is to solve a BVP using sets of partial differential equations whose analytical solution is too complex (or impossible) to be solve analytically [LAR 13]. FEM uses space and time discretization to obtain numerical approximate solutions of the BVP with a certain level of accuracy. The FEM workflow is mainly based on pre-processing, processing and post-processing routines. During pre-processing, the geometry of the problem and the discretization are defined. Usually, this step is done with the help of a graphic interface to define domain name, mesh type, *etc.* Then, the matrix formulation of the problem is done during the processing as well as the integration of the initial and boundary conditions together with the assembly of the global stiffness matrix. Post-processing is performed once the solution of the BVP is found. It includes the calculation of secondary quantities (*e.g.,* strain, stress) from the solution of the primary quantities (displacements). Also, interpolations from nodal to local (within an element) values are formally done at this stage.

### 2.3.1 Elmer software

Elmer is an open-source and parallel FEM software developed by Räback and collaborators at CSC-IT, Espoo (Finland) [MAL 13]. Elmer can be used to solve various kinds of differential equation sets that can be coupled in a generic manner making Elmer perfectly adaptable for multi-physics simulations. It is mostly implemented in modern

Fortran (about 75% of the code) and C/C++ providing a high-performance simulation framework. Elmer can be used for various kinds of applications including:

- Heat transfer
- Fluid mechanics
- Species transport
- Structural mechanics
- Acoustics
- Electromagnetism
- Microfluidics
- Levelset methods
- Quantum mechanics
- Mesh movement
- Particle tracker.

Elmer is made of several building blocks (ElmerGrid, ElmerSolver, etc.) each dedicated to a specific task (Figure 2.7). The code also allows the use of external solver for specific cases, BC or for post-processing convenience. It is continuously maintained and is often updated with new features provided either by the developer team or by the user community. Actually, Elmer simulations are performed following the classical aforementioned FEM workflow as shown in Figure 2.7 (a) *i.e.,* pre-processing (ElmerGrid, ElmerGUI), solver(ElmerSolver, Elmer-mpi) and post-processing (ElmerPost or external routines) and each component can be used independently. A user interface (ElmerGUI) that can be used during most of the simulation is also available.

During pre-processing, Elmer creates or imports the simulation domain and the mesh. It can be done in different ways with the help of some external softwares (Gmesh, NetGen, OpenCanscade, Salome, FreeCAD, Comsol multiphisics) or directly by creating a .grd file for simple 2D and 3D samples. To perform a simulation, Elmer requires four files as inputs: mesh.header, mesh.elements, mesh.boundary, mesh.nodes. Those files are written using the Elmer format. Among its various applications, ElmerGrid can convert several mesh formal files to the native Elmer format. Also it can be used to increase and evaluate mesh quality as well as create mesh partitions for parallel simulation together with METIS, a pre-processing tool of Elmer (Fig. 2.7 (b)).

The processing part involve the use of ElmerSolver. It is the main step of the FEM simulation in which several actions are performed including geometry reading, assembly, solution and saving. Here, Elmer reads a .sif file where several information are stored including:

1. Header: Location and name of input mesh folder, output folder path and name. An optional argument allows for checking keywords if external definitions are present

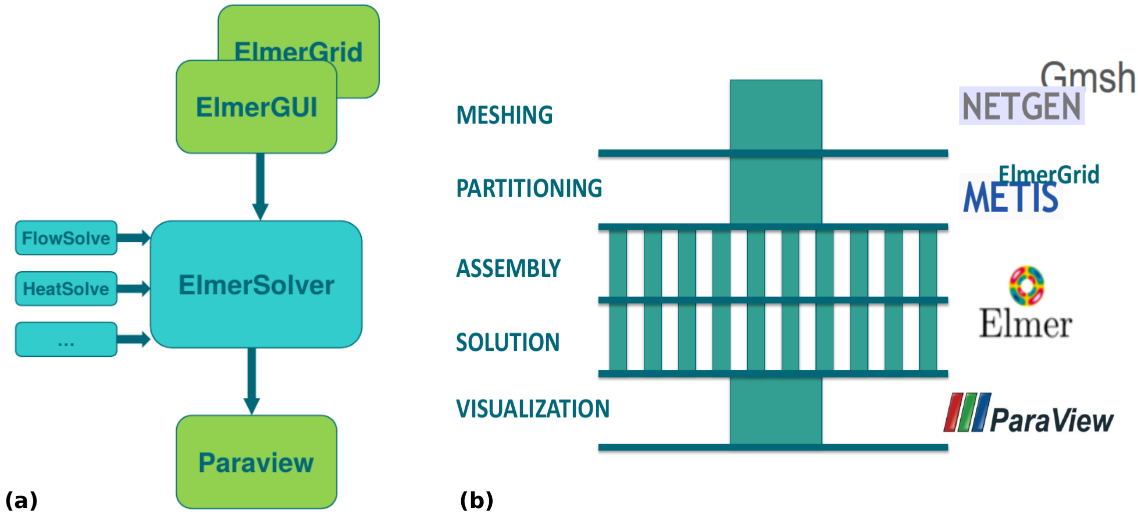

Figure 2.7: Elmer workflow. (a) Elmer workflow using its own interfaces for pre-processing and processing (ElmerSover). Paraview can be used for post-processing. (b) Elmer interacting with external pre-processing tools for a better meshing and domain partitioning when parallel calculations are realized.

withing the .sif file.

2. Simulation: Define the kind of coordinates (spherical, cartesian, etc.) and dimensions (2D, 3D), simulation type (steady state, transient, etc.), number of steps of the simulation, saving frequency and the name of the saving files.
3. Body: The physical model to be solved. Elmer can be used for multi-body (with different material properties and/or physics solver) simulations. Here is specified the relative number of bodies together with their associated equations and material properties. The body force (gravity, electric and magnetic fields, etc.) if present, initial conditions and BCs are also defined here. In the case of multi-body simulation, the body section is repeated as much as the total number of bodies present in the simulation.
4. Solver: The solver section set the kind of equation or physical problem to be solved as well as when they are solved (never, always, as well as before/after time-step, simulation or saving). Here is also declared the solution method as well as preconditions, stability criteria and breaking conditions. It is also possible to implement a number of external solver here to account for any new physics not included in Elmer or to performs some function as the assembly, interpolation or field conversion. El-Numodis particularly uses this property of Elmer that is able to call external solver or library without changing the source code.
5. Equation: Refers to the set of solvers for a body. Here some options can be set as well as explicitly ask for calculation of some variables. Also here is specified the number of active solvers to account for in multi-body simulations.
6. Body force: This section is declared if body forces are considered in the simulation.

Also direction, initial condition or source can be defined.

7. Material: Here is where materials parameters are declared. Different material sections should be declared if a multi-body simulation is run. the different parameters to be set are: density, Poisson ratio, Young's modulus, viscosity, heat conductivity, heat capacity, etc.
8. Boundary conditions: Here is defined the target mesh boundaries where a BC is defined. It includes Dirichlet, Neumann, Robin, etc. The BC definition can be done by variable declaration (using MATC), as a constant, or as an external user function (solver). It is possible to set normal or tangential quantities, as well as nodal, coordinate or element specific BCs.
9. Initial condition: Declares initial conditions for a body or mesh boundary. As well as in the BC section the initial conditions can be set by body, surface, node, using tables, arrays or functions.

Elmer has its own post-processor (ElmerPost) but users can also easily rely on high-performance post-processing software as *e.g.*, Paraview [AHR 05].

Elmer deals with 2D and 3D mesh types containing two kinds of elements (linear and quadratic). The elements to use depends among several factors including the geometrical shape of the simulation volume and the precision targeted.

### 2.3.2 Linear static elastic solver

In Elmer, the linear elastic solver calculates the displacement field by solving the Navier equations. The dynamical equation for elastic deformation of solid is written as:

$$\rho \frac{\partial^2 \boldsymbol{u}}{\partial t^2} - \nabla \cdot \boldsymbol{\sigma} = \boldsymbol{f} \tag{2.35}$$

where $\rho$ is the material density. The general thermal equation for the stress-strain tensor relationship follows the form:

$$\sigma^{ij} = C^{ijkl}\epsilon_{kl} - \beta^{ij}(T - T_0) \tag{2.36}$$

with $\epsilon$ the strain tensor and $C$ the stiffness matrix. For anisotropic materials, the elastic modulus (also called compliance matrix) is a fourth order tensor with 21 independent components (elastic constants). The heat expansion tensor $\beta$ allows to account for thermal calculation with $T_0$ the reference temperature of the stress-free state, and $T$ the temperature field. The linearized strain is:

$$\boldsymbol{\epsilon} = \frac{1}{2}(\nabla \boldsymbol{u} + (\nabla \boldsymbol{u})^T) \tag{2.37}$$

For isotropic materials, the elastic modulus is function of only two independent values: the Lame parameters (first: $\mu$, second: $\lambda$) or Young's modulus $E$ and Poisson ration $\nu$. The stress tensor in function of the Lame parameters is:

$$\boldsymbol{\sigma} = 2\mu\boldsymbol{\epsilon} + \lambda\nabla \cdot \boldsymbol{u} I - \beta(T - T_0)I \tag{2.38}$$

where $I$ is the identity matrix. The Lame parameters follow the relationships:

$$\lambda = \frac{E\nu}{(1+\nu)(1-2\nu)} \tag{2.39}$$

$$\mu = \frac{E}{2(1+\nu)} \tag{2.40}$$

the BC can be either Dirichlet type:

$$\boldsymbol{u}_i = \boldsymbol{u}_i^b \tag{2.41}$$

or Neumann (force) type:

$$\boldsymbol{\sigma} \cdot \boldsymbol{n} = \boldsymbol{g} \tag{2.42}$$

with $\boldsymbol{n}$ the normal vector. The default BC in Elmer implies that $\boldsymbol{g} = 0$. In this work, the differential equation solved by Elmer relies on linear statics elasticity. It corresponds to equation 2.43 without the time dependence

$$-\nabla \cdot \boldsymbol{\sigma} = \boldsymbol{f} \tag{2.43}$$

with the BC 2.41 and 2.42 known as the strong form of the BVP. The FEM derivation of the previous BVP implies to rewrite the formulation in therm of a variational or equation weak form [ALT 10]. It can be done by multiplying the equation 2.43 by a regular test function $u^*$.

$$\int_{\Omega}(\nabla \cdot \boldsymbol{\sigma} + \boldsymbol{f}) \cdot u^* d\Omega + \int_S (\boldsymbol{f} - \boldsymbol{\sigma}\boldsymbol{n}) \cdot u^* ds = 0 \tag{2.44}$$

Using divergence properties and Ostrogradski-Gauss theorem (divergence theorem), the previous integral representation can be reduced to the weak form of the BVP as shown in equation 2.45 converted to a linear matrix equation [LAR 13]:

$$-\int_{\Omega} Tr[\boldsymbol{\sigma}\boldsymbol{\epsilon}(u^*)]d\Omega + \int_{\Omega} \boldsymbol{f} \cdot u^* d\Omega + \int_{S} \boldsymbol{f} u^* ds \tag{2.45}$$

For each node of each element, the previous integral representation can be converted to a lineal matrix equation to be solved in the form $[k][u^*] = [f]$. Shape functions define the link between element nodes that are assembled in a general matrix equation:

$$[K][U] = [F] \tag{2.46}$$

where the BCs of each boundary node (if known) need to be inserted. Elmer uses the properties of sparse matrix to reduce the matrix size and optimize the calculation of the unknowns. The unknowns in the equation 2.46 are found by Elmer using either direct methods (Gauss elimination, Cholesky, Crout) or iterative method (Jacobi, Gauss-Seidel or conjugate gradient). The quantities $\epsilon$ and $\sigma$ are calculated from the displacement field during the post-processing step.

## 2.4 Conclusion

This chapter aims to introduce the basics of DDD and FEM methods as well as the both codes (Numodis for the DDD, Elmer for FEM) that are the roots of El-Numodis, the code developed during my PhD. The workflow of Numodis and its main equations were discussed with a special focus on the various kinds of BCs available. Most of these methods generally does not account for free surfaces. The FEM methodology and the Elmer software were also introduced in this chapter. In particular, one can notice that Elmer versatility allows for the easy integration of external solvers and drivers without modifying the main internal structure of the code what will be critical in the development of El-Numodis as presented in the following chapter.

## Chapter 2: to remember

- The discrete dislocation dynamics method allows to investigate dislocation dynamics using the continuum elastic theory.
- Numodis is a nodal three-dimensional discrete dislocation dynamics code developed by Laurent Dupuy and collaborators that is at the roots of the El-Numodis code.
- Most discrete dislocation dynamics simulation are performed using periodic boundary conditions and the contribution of the image force is not accurately accounted.
- The finite-element method allows to solve boundary value problems and is able to tackle surface problems not accounted in classical discrete dislocation dynamics simulations.
- Elmer is an open-source multiphysics finite element method code that will be used to solve the boundary value problems together with Numodis.

# Chapter 3

# El-Numodis

Most of the approaches used to study nanomechanical processes have their own limitations. Indeed, experimental techniques such as lab-on-chip or *in situ* transmission electron microscopy are expensive and difficult to apply while molecular dynamics simulations are constrained to very-high strain rates ($\sim 10^8$ s$^{-1}$) and limited sample size. In similar conditions of simulations, discrete dislocation dynamics provides a solution to both constrains but hardly accounts for surface effects. In this work, we developed a multi-scale simulation tool called El-Numodis based on coupling discrete dislocation dynamics and finite elements using the superposition method to solve complex boundary value problems (including free-surfaces) while running discrete dislocation dynamics simulations. This chapter is about the assembly of El-Numodis. First, a mathematical description of the boundary value problem solution using the superposition method is introduced. Then, technical details associated to the data interchange and format pairing between Numodis and Elmer are given. Finally, a description of the main features of El-Numodis (units conversion, interpolation and loads) is provided.

**Contents**

**3.1 The superposition method . . . . . . . . . . . . . . . . . . . . . . . 56**
**3.2 El-Numodis . . . . . . . . . . . . . . . . . . . . . . . . . . . . . . 58**
  3.2.1 Introduction to El-Numodis framework . . . . . . . . . . . . . . . . 58
  3.2.2 External drivers and main functions . . . . . . . . . . . . . . . . . 60
  3.2.3 Stress-to-force conversion . . . . . . . . . . . . . . . . . . . . . 62
  3.2.4 Stress interpolation . . . . . . . . . . . . . . . . . . . . . . . . . 64
  3.2.5 Loading . . . . . . . . . . . . . . . . . . . . . . . . . . . . . . . 65
  3.2.6 Mirror dislocation . . . . . . . . . . . . . . . . . . . . . . . . . . 67
**3.3 Conclusion . . . . . . . . . . . . . . . . . . . . . . . . . . . . . . 68**

## 3.1 The superposition method

The SPM was introduced by van der Giessen and Needleman in 1995 [Van 95] as a solution for 2D complex BVPs involving images forces. It consists in the correction of the dislocation self-stress and displacement fields $\tilde{\boldsymbol{\sigma}}(S)$ and $\tilde{\boldsymbol{u}}(S)$ originally computed by a DDD code (assuming an infinite medium) at a physical boundaries $S$ using a FEM elastic solver (Figure 3.1).
In more details, whatever the geometrical shape of the simulated structure, the SPM relies on the solution of the elastic BVP computed by FEM [CRO 14] as described by:

$$\begin{aligned} \nabla \cdot \hat{\boldsymbol{\sigma}} &= 0 \\ \hat{\boldsymbol{\sigma}} &= \boldsymbol{C} : \hat{\boldsymbol{\epsilon}} \\ \hat{\boldsymbol{\epsilon}} &= \frac{1}{2}\{\nabla\hat{\boldsymbol{u}} + [\nabla\hat{\boldsymbol{u}}]^T\} \end{aligned} \tag{3.1}$$

where $\hat{\boldsymbol{\sigma}}$ is the stress , $\hat{\boldsymbol{\epsilon}}$ and $\hat{\boldsymbol{u}}$ are the strain and displacement field generated by the FEM respectively and $\boldsymbol{C}$ is the linear elastic stiffness tensor. In this approach, this set of equations is constrained by Neumann and Dirichlet BCs:

$$\begin{aligned} \hat{\boldsymbol{\sigma}} \cdot \boldsymbol{n} &= \boldsymbol{T_{app}} - \tilde{\boldsymbol{T}} \\ \hat{\boldsymbol{u}} &= \boldsymbol{u_{app}} - \tilde{\boldsymbol{u}} \end{aligned} \tag{3.2}$$

with $\boldsymbol{T_{app}}$ and $\boldsymbol{u_{app}}$ the external applied traction and displacement BC and $\boldsymbol{n}$ the surface normal. $\tilde{\boldsymbol{T}}$ and $\tilde{\boldsymbol{u}}$ are the tractions and displacement at the boundaries produced by dislocations. Following the decomposition of Lubarda and Needleman [LUB 93, Van 95], the traction and displacements at the boundaries include the contribution of the total dislocation segments $n_{dd}$:

$$\begin{aligned}\widetilde{\boldsymbol{T}} &= \sum_{k=1}^{n_{dd}} \widetilde{\boldsymbol{\sigma}}^k \cdot \boldsymbol{n} \\ \widetilde{\boldsymbol{u}} &= \sum_{k=1}^{n_{dd}} \widetilde{\boldsymbol{u}}^k\end{aligned} \tag{3.3}$$

with $\widetilde{\boldsymbol{\sigma}}^k$ and $\widetilde{\boldsymbol{u}}^k$ are respectively the stress and displacement fields of dislocation segment $k$. In general, the FEM load is described imposing displacements or forces which implies that both; the external applied stress $\boldsymbol{T_{app}}$ and traction $\widetilde{\boldsymbol{T}}$ at each surface node $i$ should be converted to forces before the BC correction. In general, the expression for the nodal force due to the traction

$$\boldsymbol{F_i} = \int_{\Gamma^T} (\sum_{k=1}^{n_{dd}} \widetilde{\boldsymbol{\sigma}}^k \cdot \boldsymbol{n}) N_i^S d\Gamma^T \tag{3.4}$$

where $N_i^S$ is the shape function values of the node $i$ on the surface $S$. Similar formulation applies for $\boldsymbol{T_{app}}$.

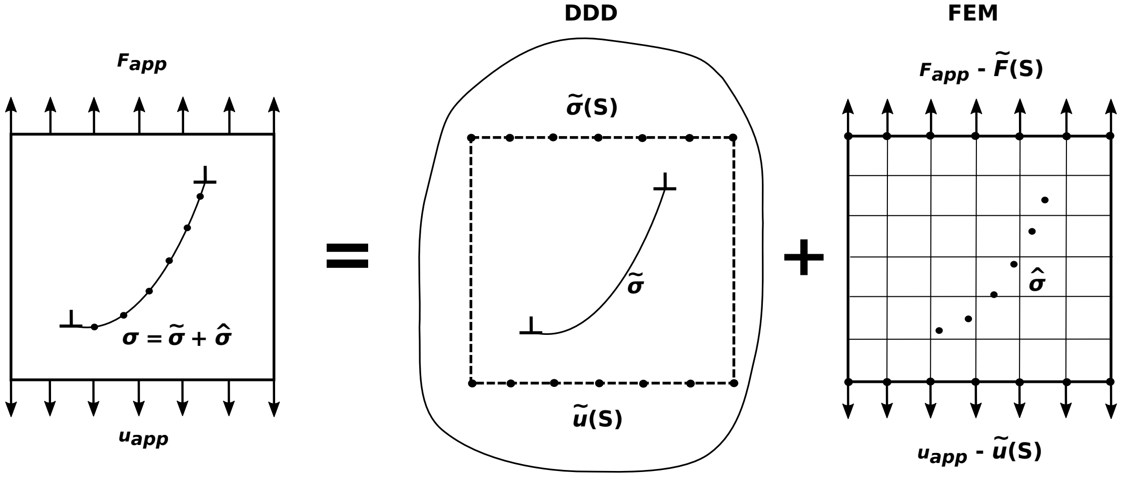
DDD
FEM
Fapp
$\widetilde{\sigma}$(S)
Fapp - $\widetilde{F}$(S)
$\sigma = \widetilde{\sigma} + \hat{\sigma}$
=
$\widetilde{\sigma}$
+
$\hat{\sigma}$
uapp
$\widetilde{u}$(S)
uapp - $\widetilde{u}$(S)

Figure 3.1: Scheme of the SPM principle. A finite-size volume containing dislocation submitted to BC $\boldsymbol{F_{app}}$ and $\boldsymbol{u_{app}}$ can be divided into a problem where the dislocations are considered submerged in an infinite medium in which their stress $\widetilde{\boldsymbol{\sigma}}$ and displacement $\widetilde{\boldsymbol{u}}$ fields at a virtual boundary $S$ are used to correct finite BVP. The finite stress $\hat{\boldsymbol{\sigma}}$ is then superimposed to the internal stress $\widetilde{\boldsymbol{\sigma}}$ at each dislocation segment.

The aforementioned theoretical description of the BVP can be implemented considering an elastic volume containing dislocations under either an external applied force $\boldsymbol{F_{app}}$ or a displacement $\boldsymbol{u_{app}}$ at least on two of it boundaries $S$ (Figure 3.1). This BVP can be decomposed into two ensembles. One where the dislocations are considered as immersed inside an infinite elastic medium and their stress field $\tilde{\boldsymbol{\sigma}}(S)$ and displacement field $\tilde{\boldsymbol{u}}(S)$ are calculated at points conforming the virtual surface $S$. A second where a linear FEM elastic solver calculates the stress $\hat{\boldsymbol{\sigma}}$ inside the elastic medium correcting original applied forces and displacements. The correction is made using the force and displacement fields generated by the dislocations *i.e.,* $\boldsymbol{F_{app}} - \tilde{\boldsymbol{F}}(S)$ and $\boldsymbol{u_{app}} - \tilde{\boldsymbol{u}}(S)$. Finally, the computed heterogeneous stress field $\hat{\boldsymbol{\sigma}}$ is superimposed to the internal stress $\tilde{\boldsymbol{\sigma}}$ at each dislocation segment,

$$\boldsymbol{\sigma} = \tilde{\boldsymbol{\sigma}} + \hat{\boldsymbol{\sigma}} \tag{3.5}$$

## 3.2 El-Numodis

### 3.2.1 Introduction to El-Numodis framework

One of the requirements when the development of El-Numodis started was to make it user-friendly, easy to understand and modify. For that purpose, El-Numodis is conceived using Elmer as the master program calling Numodis as an external library. As Numodis is an object-oriented code, each calculation performed inside a Numodis timestep is done using an independent function. For instance, there are independent functions to calculate forces, velocities, to export stresses at a certain position *etc.* Thus, it is possible to call all the functions of Numodis independently and externally without changing its internal structure. On the other hand, Elmer has the ability to use (or interact with) parts of external softwares what makes it particularly versatile. Finally, Elmer self-structure is easy to manage based on Fortran external functions integrated using its own compiler. This last point was one of the most important aspect influencing the design of El-Numodis basic structure.

Basically, an El-Numodis run can be schematized as an Elmer simulation that uses external functions to interchange data arrays with various Numodis functions. El-Numodis reads Elmer's mesh files, performs the calculations and saves they output files in a standard manner (*i.e.,* as Elmer usually does). External functions implemented in Elmer call the necessary Numodis functions before, during and after a simulation timestep. These functions are also in charge to read Numodis input files and save the DDD outputs as it is normally done by Numodis. Please note that El-Numodis has no maximum strain limitation. This means that the initial volume can be completely deformed what should require adaptive on-the-fly remeshing. It is worth to mention that, even if we will focus on incipient plasticity aspects in the following, large strain formalism has not been further investigated in the context of this PhD work. El-Numodis workflow is summarized in

Figure 3.2.

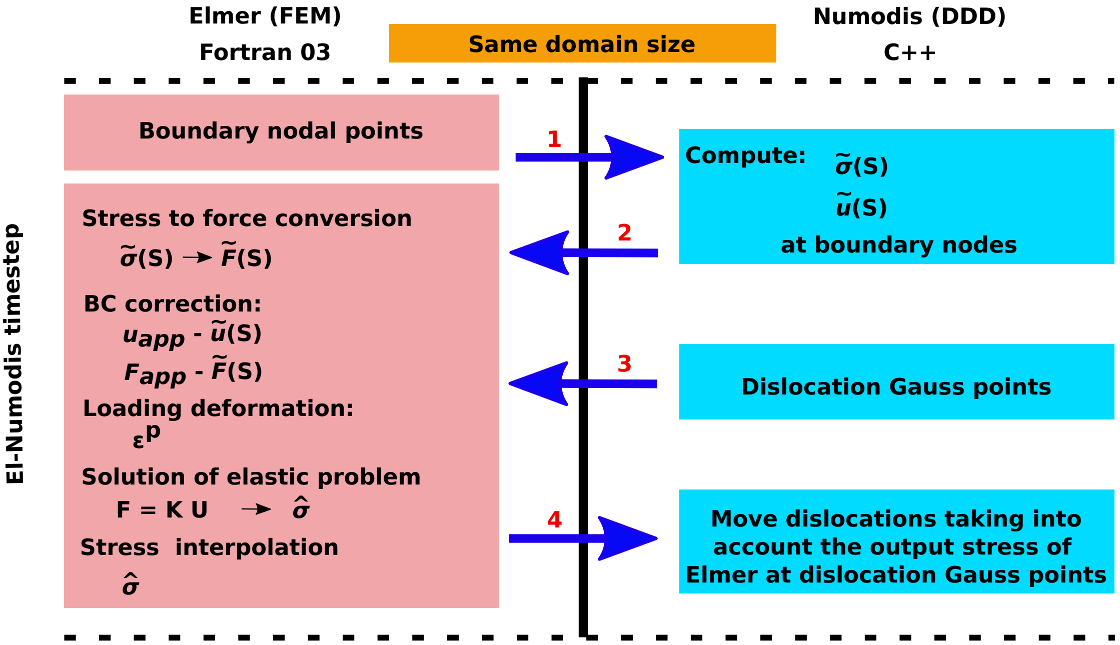
Elmer (FEM)
Fortran 03
Same domain size
Numodis (DDD)
C++
El-Numodis timestep
Boundary nodal points
1
Compute: $\tilde{\sigma}$(S) $\tilde{u}$(S) at boundary nodes
2
Stress to force conversion
$\tilde{\sigma}$(S) → $\tilde{F}$(S)
BC correction:
$u_{app}$ - $\tilde{u}$(S)
$F_{app}$ - $\tilde{F}$(S)
Loading deformation:
$\varepsilon^p$
Solution of elastic problem
F = K U → $\hat{\sigma}$
Stress interpolation
$\hat{\sigma}$
3
Dislocation Gauss points
4
Move dislocations taking into account the output stress of Elmer at dislocation Gauss points

Figure 3.2: Representation of the sequential communication between Elmer (Fortran) and Numodis (C++) within El-Numodis. The coupling consists in four main data interchanges between both codes at different moments within the same timestep. First: the nodes coordinates of the mesh surfaces are sent to Numodis. Second: Numodis returns (to Elmer) the stress field $\tilde{\boldsymbol{\sigma}}(S)$ and displacement fields $\tilde{\boldsymbol{u}}(S)$ at the node positions. Third: Numodis sends the dislocation Gauss points coordinates. Then, the stresses at the surface nodes are converted to nodal forces $\tilde{\boldsymbol{F}}(S)$ (see section 3.2.3), the assembly is performed and the solution of the linear elastic problem is calculated with the BC corrections $\boldsymbol{u_{app}} - \tilde{\boldsymbol{u}}(S)$ and $\boldsymbol{F_{app}} - \tilde{\boldsymbol{F}}(S)$. Fourth: the elastic stress at the dislocation Gauss points is interpolated from the nodal values of the elements involving each Gauss point using the element shape function (see section 3.2.4).

The assembly process in the SPM can be performed at various periodic timestep. Currently, El-Numodis performs the assembly process after each simulation step. While this increases the CPU costs, it allows for a more precise regularisation of the fields along time what was the first aim when developing the method. Note that this can be easily adapted by the user.

To facilitate the interchange of data between Numodis and Elmer, new drivers were implemented. Indeed, the declaration of variables and functions in C++ and Fortran 03 are made differently leading to misunderstanding between the data transmitted and received by each code. To solve this issue, drivers were implemented to change the variables and functions declarations and translate them from C++ to Fortran.

### 3.2.2 External drivers and main functions

El-Numodis relies on three Elmer external functions that call Numodis functions and performs the data interchange between the linear elastic solver of Elmer and the functions of Numodis. The structure of such DDD-FEM coupling implementation is illustrated in the Figure 3.3 and is explained in the following. El-Numodis DDD and FEM parts can be run on single processor or parallel, but the coupling itself is currently implemented serial. For this purpose, while the volume simulated in Elmer scales with the one of Numodis, both of them solve their relative tasks independently *i.e.,* the domain where the FEM computes the elastic stress is independent of where the DDD solves the dislocation dynamics. In order to avoid unnecessary data conversion and facilitate post-processing data analysis both domains are built with the same numerical size.

Concerning El-Numodis workflow, the first step consists in loading the FEM input and mesh files (Elmer initialization). There, the material properties, the loading, kind of variables to be saved, the output frequencies of the elastic variables (displacement, stress, strain) and the BCs are defined (see the steps of the Elmer .sif file in Chapter 2 for more details). The first driver called *NumodisExportBNodes* is in charge of identifying the boundaries of the simulation box and the corresponding BCs. Nodes coordinates associated to each BC as well as their respective identity (ID) are saved into data arrays. The solver initializes Numodis calling the functions that define the DDD simulation conditions (only done at $t = 0$). These functions check and read Numodis input files. The final task of *NumodisExportBNodes* is to retrieve the stress or displacement field at the boundary nodes as depending on respective associated BCs. Those “field” values are also stored in data arrays in the same order of the coordinates arrays preserving their arranged node IDs to simplify the next steps.
The second driver called is *NumodisImport.* It is in charge of building the matrix representation of the right hand side of the elastic solver $[F] = [K][U]$. It uses the set of node arrays associated to each BC and modifies its external value (load) according to either a Dirichlet or Neumann BC. Then, a correction is applied using the SPM. Here, a dedicated function (*SetLoad*) identifies the kind of simulation (creep, imposed stress or strain rate) and assigns the corresponding load value. The *SetLoad* function calls another internal function (*SaveLoadData*) to save the control parameters and deformation data that are used later to produce output data *e.g.,* the stress-strain curve, temporal evolution of the plastic strain, dislocation density, *etc.* Then, the assembly is performed using the functions *SetDirichletNumodis* or *SetStressNumodis.* The function *SetStressNumodis* is optimized to also account for traction-free BCs and is responsible for the stress-to-force field conversion explained in the following section 3.2.3. Finally, the elastic solver of Elmer provides the solutions of the corrected BVP solving the assembled $[F] = [K][U]$ equation and solves the displacement, stress and strain fields for all the nodes of the simulated domain.

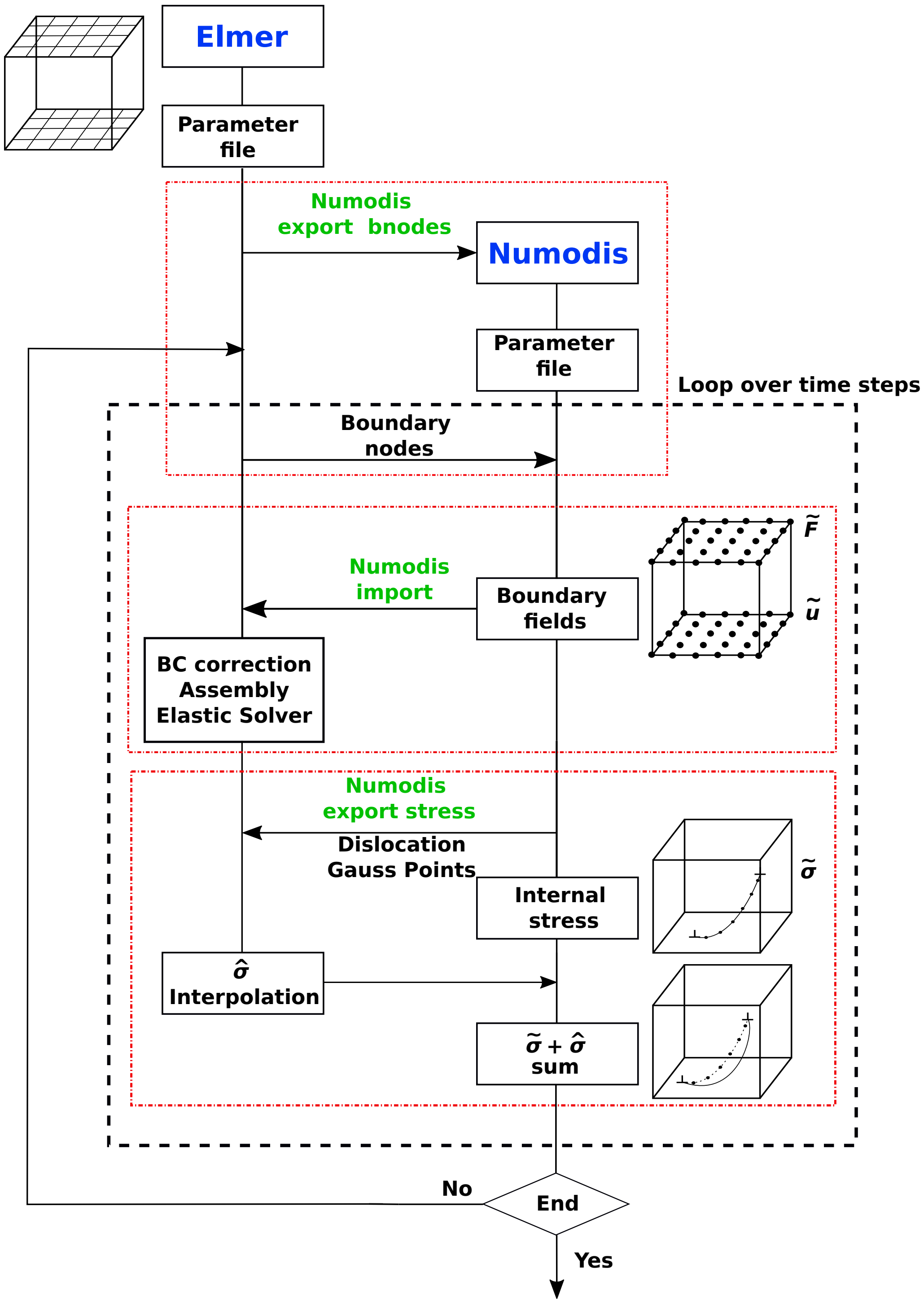
Elmer
Parameter file
Numodis export bnodes
Numodis
Parameter file
Loop over time steps
Boundary nodes
Numodis import
Boundary fields
$\tilde{F}$
$\tilde{u}$
BC correction Assembly Elastic Solver
Numodis export stress
Dislocation Gauss Points
Internal stress
$\tilde{\sigma}$
$\hat{\sigma}$ Interpolation
$\tilde{\sigma} + \hat{\sigma}$ sum
No
End
Yes

Figure 3.3: El-Numodis workflow. The FEM code Elmer masters the coupling using the Numodis DDD code as a library. The three main drivers associated to Elmer *i.e.*, *NumodisExportBNodes*, *NumodisImport* and *NumodisExportStress* are shown in green.

Afterwards, a last driver (*NumodisExportStress*) is run. It stores Gauss points of all the segments conforming the dislocation microstructure into an array and the stress value is interpolated using the implemented function *GetFemStress*. *GetFemStress* is in charge of identifying the element involved with each node, performs the global to local change of coordinates (of both the dislocation Gauss points and the element nodes) and performs an interpolation of the six elements of the stress tensor using the equations 3.7 and 3.8. After the interpolation, Numodis formal functions are called to compute forces (nodal, mirror, internal, core and friction). Then, the nodal velocity is computed and the nodes are moved before dislocation line remeshing. Besides, this function is also in charge of saving the DDD simulation data (dislocation node positions, energetic terms and plastic strain). Optionally in *NumodisExportStress*, a call to an external software (MedCoupling) can be done if the total stress of the dislocation needs to be saved. This solver is also in charged of a dislocation nucleation algorithm described in Chapter 5.

In El-Numodis, the elastic solver saving frequency may differ from the one of the DDD. It can be useful to increase the simulation speed if the elastic constants are not needed jointly in the analysis of the final results. However, same save periods are recommended. As already discussed, Elmer masters Numodis and as Elmer is written in Fortran 2008 while Numodis is written in C++11, these two cannot directly exchange their full internal data structure and functions from one to another. Now, as of today, only the interoperability between Fortran 2003 and ISO C has been standardized [ANS 04] imposing drastic limitations on exchanged data types. As a consequence, we developed several wrappers between Numodis and Elmer. In the first layer, the Numodis C++ class is encapsulated in a C wrapper hiding object oriented features behind a C interface. The second layer involves the `ISO_C_BINDING` mentioned before [ANS 04] to encapsulate the C command in a Fortran 2003 interface. The third layer consists in defining a Fortran 2008 Numodis module that embeds the previous Fortran 2003 interface. It should be noticed that the use of the Simplified Wrapper and Interface Generator (SWIG) [BEA 03] which has been recently been extended to Fortran [JOH 20] could be interesting in the future to simplify this rather complex architecture.

### 3.2.3 Stress-to-force conversion

The SPM relies on field conversions performed at the boundaries. The implementation of the corrected Neumann BC $\boldsymbol{F_{app}} - \tilde{\boldsymbol{F}}(S)$ is realized at points over a virtual surface using $\tilde{\boldsymbol{\sigma}}(S)$ converted into $\tilde{\boldsymbol{F}}(S)$. However, this requires to convert a stress applied on a surface to a force applied on nodes. Using the stress definition, we associate a weighted area to every point where the stress $\tilde{\boldsymbol{\sigma}}(S)$ is retrieved and where the corrected forces have to be computed. To make it simple, El-Numodis uses eight nodes hexahedron elements (bricks) at points on the surfaces where $\tilde{\boldsymbol{\sigma}}(S)$ needs to be calculated and where the corrected forces are applied.

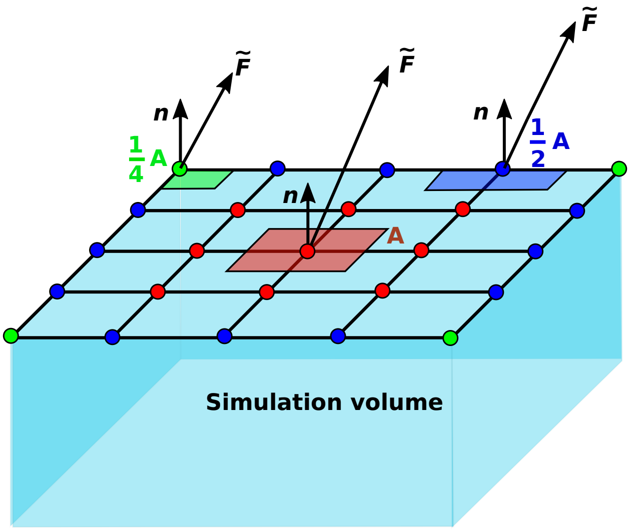

Figure 3.4: stress-to-force conversion. The volume is discretized using eight nodes hexahedron elements. Three different weighted area are present corresponding to nodes that are at the middle ($A$) of the grid, at the corners ($\frac{A}{4}$) or at the edges ($\frac{A}{2}$). Only the mesh at the surface is shown here for simplicity.

Three kind of nodes are defined depending of their location (Figure 3.4). The nodes located in the corners (green nodes on the figure) have a weighted area of $\frac{A}{4}$, since they have only one element to be associated to. In the same way the nodes located at the edges (blue) have a twice larger weighted area since they are connected to two elements. Finally, the nodes within the surface (red) have a weight area of $A$ (equivalent to four times a corner node) as attached to four elements. Thus, the forces $\tilde{\boldsymbol{F}}(S)$ produced by a dislocation at each node is calculated in first approximation by:

$$\tilde{\boldsymbol{F}}(S) = A\tilde{\boldsymbol{\sigma}}(S) \cdot \boldsymbol{n} \tag{3.6}$$

where $A$ is the weighted area at each node and $\boldsymbol{n}$ the normal vector of the element associated to the node. In the case of a non planar surface, each element is associated with a different normal vector and the average normal vector between the various elements involved is accounted. However, we recommend to use another kind of mesh in this case (non linear, tetrahedrons, pyramidal, *etc.*) for more accuracy on the stress-to-force conversion. Indeed, brick elements do not reproduce well the curvature associated to non planar (or rough) surfaces what may impact the calculation accuracy.

### 3.2.4 Stress interpolation

The calculation of $\hat{\boldsymbol{\sigma}}$ at the Gauss point of the dislocation segment also requires mathematical conversions since FEM only provides the displacement field at the nodes. Any other quantities are calculated in a post-processing step. For instances, the stress is calculated from strain that is calculated from the nodal displacement. Once the post-processing step of the stress calculation is done, another step is needed to compute it locally, at the dislocation Gauss points.

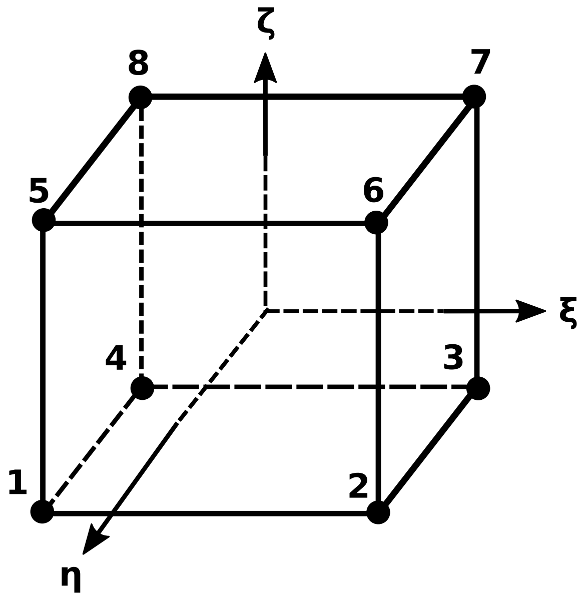

Figure 3.5: Eight nodes hexahedron element (brick) with the local coordinate system $(\xi, \eta, \zeta)$ and node enumeration used with the set of shape functions given by equation 3.7.

For that purpose, we developed a routine to detect the brick elements containing the dislocation Gauss points allowing the stress $\hat{\boldsymbol{\sigma}}$ interpolation from the nodal values of the brick using its set of shape functions. For an hexahedron element similar to the one described in Figure 3.5 the set of shape function is given by:

$$\begin{aligned}
N_1 &= \frac{1}{8}(1+\xi)(1-\eta)(1-\zeta)\\
N_2 &= \frac{1}{8}(1+\xi)(1+\eta)(1-\zeta)\\
N_3 &= \frac{1}{8}(1-\xi)(1+\eta)(1-\zeta)\\
N_4 &= \frac{1}{8}(1-\xi)(1-\eta)(1-\zeta)\\
N_5 &= \frac{1}{8}(1+\xi)(1-\eta)(1+\zeta)\\
N_6 &= \frac{1}{8}(1+\xi)(1+\eta)(1+\zeta)\\
N_7 &= \frac{1}{8}(1-\xi)(1+\eta)(1+\zeta)\\
N_8 &= \frac{1}{8}(1-\xi)(1-\eta)(1+\zeta)
\end{aligned} \tag{3.7}$$

where $(\xi, \eta, \zeta)$ are the local coordinates of the element. The dislocation Gauss point global coordinates $(X, Y, Z)$ also needs to be converted to the local reference system in order to use equations 3.7. Afterwards, the elastic stress at the dislocation Gauss point $\widehat{\boldsymbol{\sigma}}^{gp}$ (or any other variable) can be interpolated from the nodal quantities by:

$$\widehat{\sigma}_{ij}^{gp} = \sum_{n=1}^{8} N_n \widehat{\sigma}_{ij,n} \tag{3.8}$$

were $N_n$ refers to the shape function of the node $n$ and $\widehat{\sigma}_{ij,n}$ is the elastic stress components at the node $n$. Please note that the shape functions equations 3.7 need to be adapted if another type of element is used by El-Numodis but the interpolation procedure remains the same.

### 3.2.5 Loading

El-Numodis uses a combination of FEM BCs and DDD loading modes to run virtual deformation experiments. The different kinds of loads include imposed stress or strain rate simulations.

DDD simulations often rely on the projection of an homogeneous applied stress into glide planes and directions using Schmid factors to compute the shear stress. This approach is not valid anymore using El-Numodis due to the correction made by the SPM and the presence of interfaces or surfaces that make the load heterogeneous.

In creep simulations, the applied stress is kept constant during the whole simulation which allows to model microstructure relaxation. Due to its tensorial definition, the load can be of any kind (normal, shear, *etc.*) and is transformed afterwards to a force load as explained in section 3.2.3. The preset BCs in Elmer are traction-free BCs. In El-Numodis, the code identifies the boundaries labelled as traction-free and treats them applying an external zero stress value that is also corrected as imposed by the SPM. Also, constant stress rate simulations can be performed by defining the stress rate at a given boundary using internal library (*e.g.,* MATC) or importing data tables in El-Numodis.

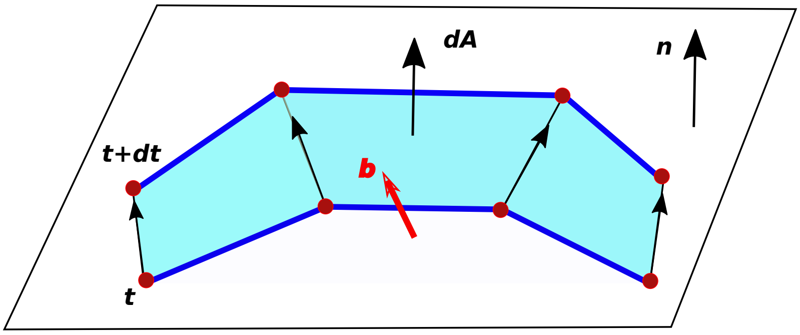

Figure 3.6: Plastic strain calculation. A dislocation originally located at the configuration represented at time $t$ moves to $t + dt$ position due to force and shear stress. The area $dA$ swept by the dislocation in its gliding plane during $dt$ is used to calculate the plastic strain increment using equation 3.9. Adapted from Bulatov and Cai [VAS 06].

El-Numodis also allows for constant strain rate simulations in a similar way than what is commonly done in experiments. Implementing constant stress or strain rate loads requires to recompute the applied stress every time period $dt$ to account for the plastic strain correction. When a dislocation segment moves, an effective plastic strain increment $d\epsilon^p$ is produced according to:

$$d\epsilon_{ij}^p = \frac{b_i n_j + b_j n_i}{2V} dA \tag{3.9}$$

where $V$ is the simulation volume. The total instant plastic strain is the sum over all dislocations gliding within the simulation cell. The plastic strain is cumulative and the total plastic strain $\varepsilon_p(t)$ is computed integrating the plastic strain along time. The total strain $\epsilon^{tot}$ is related to the imposed strain rate $\dot{\epsilon}$ by:

$$\epsilon^{tot}(t) = \int_0^t \dot{\epsilon} dt \tag{3.10}$$

$dt$ being the simulation timestep.

During constant strain rate simulation, El-Numodis (as Numodis) corrects any mismatch between the total strain and the plastic strain using the elastic strain $\epsilon^{el}$ and the Hook's law. As example, in the case of an imposed strain rate simulation with deformation applied along the $z$ direction, the elastic strain is:

$$\epsilon^{el}_{zz}(t) = \epsilon^{tot}_{zz}(t) - \epsilon^{p}_{zz}(t) \tag{3.11}$$

And the external applied stress is recomputed using the Hooke's law:

$$\sigma^{ext}_{zz}(t) = E\epsilon^{el}_{zz}(t) = E\left[\epsilon^{tot}_{zz} - \epsilon^{p}_{zz}(t)\right] \tag{3.12}$$

The aforementioned feedback loop is quite often used to manage loading processes in DDD simulations [VAS 06]. The strain rate correction is valid if the external load is provided trough an applied stress what is usually doable in FEM simulations assuming the stress-to-force conversion discussed above. However, load can also be defined using displacements at one or few boundaries in FEM. When it is the case, El-Numodis corrects the applied displacement $u_{app}$ using the plastic strain and the initial simulation box length $L_0$:

$$u_{app} = \left[\epsilon^{tot}_{zz} - \epsilon^{p}_{zz}(t)\right] L_0 \tag{3.13}$$

Constant strain rate simulations using displacements as loading lead to more precise simulation results (and less CPU costs) since they do not require the additional stress-to-force conversion step. Finally, El-Numodis can also run asymmetric loading including cases where fixed displacement is set at one boundary while load is applied to the opposite side (either applying stress or displacement), or even use different loads on opposite boundaries preserving the whole versatility of FEM Elmer BCs.

### 3.2.6 Mirror dislocation

A method called *mirror dislocation* that can be found in HL book, was revisited recently by Weygand *et al.* (for DDD simulations) allows to reduce the stress induced by nearby dislocations at a boundary [HIR 82, WEY 02]. During the PhD, this method was implemented in Numodis with the help of Dupuy to compare the efficiency of the SPM working with and without the mirror dislocation method. When a dislocation approaches a surface, the resulting local stress field is obtained adding the contribution of an out-of-the-box mirror dislocation to the original dislocation stress field. The bulk dislocation is detected once it reaches a certain cutoff distance from the surface ($r^{im}_c$) where El-Numodis replicates the dislocation portion contained between $r_c^{im}$ and the surface, on the other side of the surface, using planar symmetry as shown Figure 3.7.

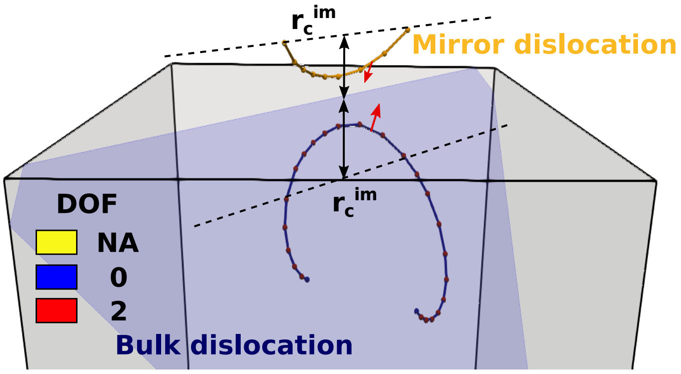

Figure 3.7: Mirror dislocation image construction as implemented in El-Numodis. Assuming a critical dislocation $r_c^{im}$, the bulk dislocation (blue curve) is replicated outside of the simulation box with opposite Burgers vector (yellow cube). The color scale represents the DOF of the nodes corresponding to the bulk dislocation.

The resulting mirror dislocation is characterized by a symmetric line orientation but opposite Burgers vector. While its stress field is accounted within the simulation cell in order to reduce the image forces, the mirror dislocation does not produce any plastic shear. Also, Numodis collision detection functions are used to identify a dislocation segment about to react with its mirrored counterpart, both emerging at the surface. In this case, the reaction leads to the annihilation of both dislocations due to the geometry of both defects leaving a ledge made of surface nodes (Figure 3.8). The surface nodes have the same mobility properties of bulk nodes, but are constrained to move only on the sample surface (with the possibility to pass from one surface to an adjacent one). Furthermore, ledges have the same properties than dislocation *i.e.*, they can superimpose when several dislocations reach the surface consecutively at the same location, they can also annihilate but do not produce any stress inside the sample. This later consideration might be improved in the future.

The image stress produced by the mirror dislocations can be used in DDD simulation to reduce the stress field at the surface and better account for dislocation *vs.* surface interaction in various cases *e.g.,* during dislocation nucleation. The impact on stress resolution of the mirror dislocation method, classical traction-free BC resolved by SPM and the combination of both will be discussed in the next chapters.

## 3.3 Conclusion

Chapter 3 resumes the main development aspects of El-Numodis *i.e.,* a code that couples the FEM code Elmer and the nodal code for DDD Numodis based on the SPM.

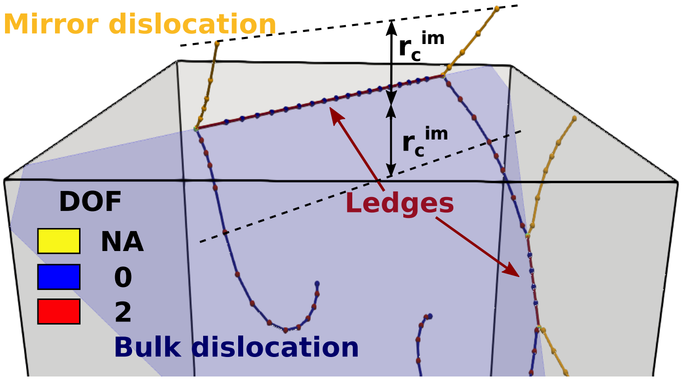

Figure 3.8: Ledges formed at the surface after the reaction of a bulk dislocation with its "mirror" counterpart. The color scale represents the DOF of the nodes corresponding to the "real" dislocation and the ledge.

The aim of El-numodis is to run dislocation dynamics simulations accounting in a better way for surfaces (or interfaces) interactions with dislocations. It relies on various drivers and wrappers that allow Elmer to master Numodis used here as a library. In addition of classical SPM features, El-Numodis also benefits of the mirror dislocations method of Weygand *et al.* and a dislocation nucleation algorithm (described in Chapter 5), both implemented during the PhD. The main features of the Elmer and Numodis codes are preserved within El-Numodis and the code is now available on demand. Several upgrades could be made in the future. First, I would recommend to parallelize the data interchange between the Elmer and Numodis, the later being now parallel (upgrade done in parallel of my PhD). Also, on-the-fly capabilities for re-meshing seem critical to improve large deformation capabilities. Also, El-Numodis uses the simplest 3D spatial discretization (8 nodes brick) but Elmer provides a bunch of elements that can be included in the libraries of El-Numodis. New interpolation methods based on shape functions associated to the new elements could be implemented.

## Chapter 3: to remember

- El-Numodis is a discrete dislocation dynamics/finite-element method code based on the superposition approach that uses the linear elastic solver of the finite-element software Elmer and the nodal discrete dislocation dynamics code Numodis.
- El-Numodis is implemented using Elmer as a leading platform calling Numodis functions as external libraries. The user interface of Elmer is used to control most of the simulation parameters.
- El-Numodis uses the finite-element method for the calculation of the image forces. It can be optionally combined to the mirror dislocation approach developed by Weygand and collaborators.
- El-Numodis is able to performs various kinds of deformation simulations including creep and imposed stress or strain rate simulations.

# Chapter 4

# Solving boundary problems

The image stress induced by the presence of surfaces plays an important role on the evolution of dislocation microstructures in mesoscale simulations and, when the length scale decreases, surface effects become stronger. In dislocation simulations, the correct evaluation of the image stress and surfaces effects are therefore of major importance. In this chapter, we evaluate the effect of surfaces and their implications in terms of image stress through a set of benchmarks and test simulations using El-Numodis.
First, self and image stress concepts are introduced relying on the descriptive examples found in the book of Hirth and Lothe [HIR 82] and both are investigated using El-Numodis. Then, El-Numodis is used to address stress-free boundary conditions in the cases of infinite and square-loop dislocations, both in half-infinite spaces. The precision of the method is tested regarding the mesh resolution and the activation (or not) of the mirror image dislocation method. Finally, this chapter ends up with an application on thin films tensile tests that illustrate the role of surfaces on the dislocation behavior and mechanical response.

## Contents

**4.1 Self-stress of an infinite dislocation . . . . . . . . . . . . . . . . . . . 72**
**4.2 Infinite edge dislocation near a free-surface . . . . . . . . . . . . . 74**
4.2.1 The image method . . . . . . . . . . . . . . . . . . . . . . . . . . . . 74
4.2.2 The Airy functions . . . . . . . . . . . . . . . . . . . . . . . . . . . . 77
4.2.3 Influence of the pseudo-mirror dislocation construction . . . . . . . . . 82
**4.3 Square-loop dislocation near a free-surface . . . . . . . . . . . . . 85**
4.3.1 The Gosling and Willis method . . . . . . . . . . . . . . . . . . . . . . 86
**4.4 Test case: thin films tensile test . . . . . . . . . . . . . . . . . . . . . 89**
4.4.1 Numodis *vs.* El-Numodis: surface effects comparison . . . . . . . . . . 95
**4.5 Conclusion . . . . . . . . . . . . . . . . . . . . . . . . . . . . . . . . 100**

## 4.1 Self-stress of an infinite dislocation

The aim of the SPM is to integrate the effects of realistic surfaces into DDD simulations by a rigorous treatment of the BVP [Van 95]. The correction is made for Neumann BC by using the self-stress $\tilde{\boldsymbol{\sigma}}$ of dislocations present in the simulation cell as computed at the boundaries. Such self-stress is calculated and provided by Numodis within the coupling scheme presented in Chapter 3. As a consequence the effective reproduction of the self-stress by El-Numodis has to be corroborated.

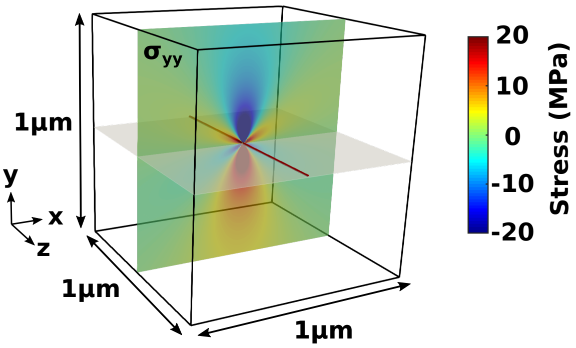

Figure 4.1: El-Numodis setup for self-stress tensor calculation of an infinite edge or screw dislocation. The simulation box is 1.0 μm long in the three directions. The infinite dislocation is located at the middle of the box. The $\tilde{\sigma}_{yy}$ component of the self-stress field is illustrated in a plane perpendicular to the dislocation line, here for an edge dislocation.

Theoretical expressions of the self-stress of infinite edge and screw dislocations can be found in the case of infinite medium in HL book [HIR 82]. The singular theory includes a set of expressions for the stress distribution that are valid except in the dislocation core.

In the same way, dislocations located close to a free-surface may generate intensive stress at the surfaces, including critical values associated to the core singularity. In order to avoid this problem, the non-singular theory of Cai [CAI 06] is used in El-Numodis (see section 2.2.3).

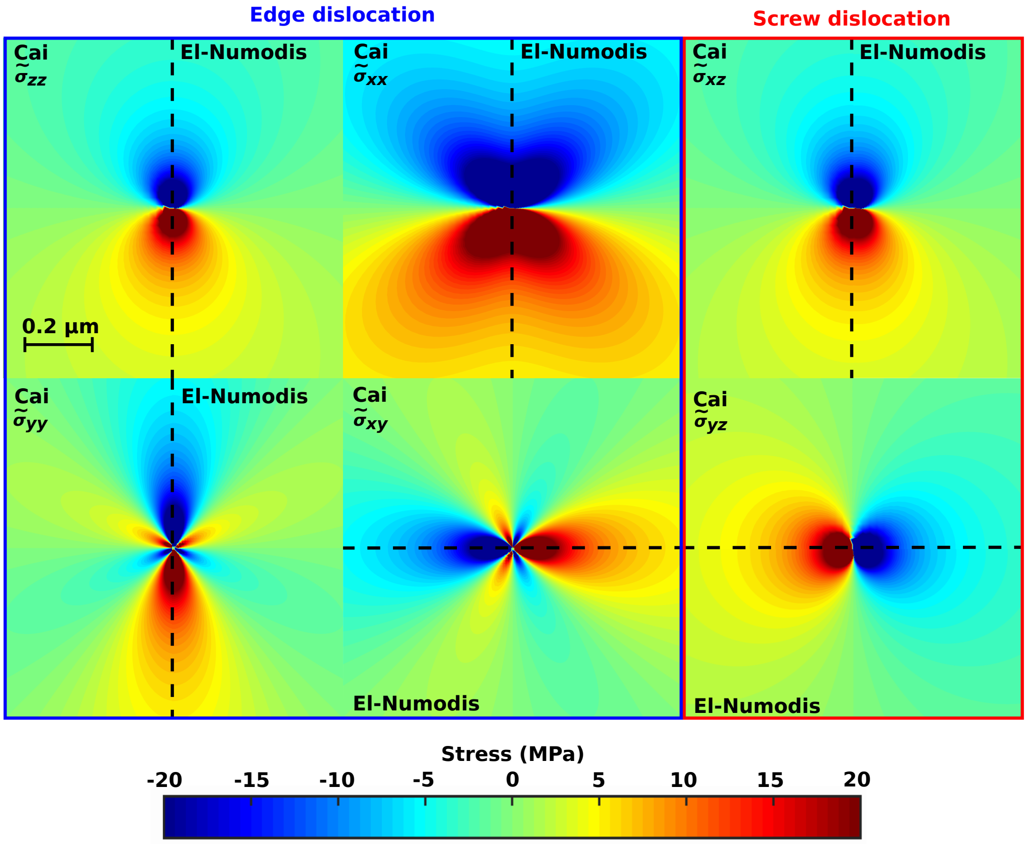

Figure 4.2: Self-stress for an infinite edge (four components inside the blue square) and screw (two components inside the red square) dislocations. For each components, the stress map is divided in two subspaces: left or top is the analytical Cai theory [CAI 06] calculated with MATLAB and right or bottom is its counterpart computed with El-Numodis. The dashed lines represents the boundary between the two approaches.

The distribution of the self-stress provided by Numodis or El-Numodis for a straight dislocation is confronted to the theoretical description provided by Cai (here computed using MATLAB). The simulation consists of a cube cell with dimensions 1×1×1 $\mu m^3$ (Figure 4.1). Copper lattice parameter ($a_0 = 3.61$ Å) and isotropic elasticity ($\lambda = 77.3$ GPa, $\mu = 42.0$ GPa, $\nu = 0.324$) are used for the example. The dislocation line is located right in the middle of the box and lies along the [001] direction. It is important to mention that this simulation represents a synthetic case where Cu materials properties are used only with the aim to obtain realistic values. The Burgers vectors points towards [100] and [010], respectively for the screw and edge dislocations. The self-stress is computed at a mid-plane normal to the dislocation line. Equations 2.18 to 2.25 provide theoretical references for infinite dislocations. In El-Numodis, the infinite dislocations can be modeled using infinite edge/screw object (already available in Numodis) or by creating a FR source long enough within the simulation box. Here we use the infinite dislocation object and use PBC along the dislocation line.

A one-to-one comparison of the self-stress based on the Cai theory computed with El-Numodis and MATLAB is shown in Figure 4.2. El-Numodis correctly reproduces the Cai theoretical expressions of the self-stress components as computed with MATLAB. This confirms the correct implementation of Cai theory within Numodis and El-Numodis. Also, we have verified that changing the BCs from periodic to fixed as well as small changes of cell dimensions along $x$ and $y$ do not significantly impact the results.

## 4.2 Infinite edge dislocation near a free-surface

In a finite body, the stress around a dislocation is affected by the presence of surfaces. This effect is more significant with the reduction of the distance to the surface. Stress-free BCs can be reached in mesoscale simulations generating an image dislocation outside the crystal to cancel the stress of the bulk dislocation at the surface. This image method is analogous to the concept of “image charges” in electrostatics [JAC 98].

### 4.2.1 The image method

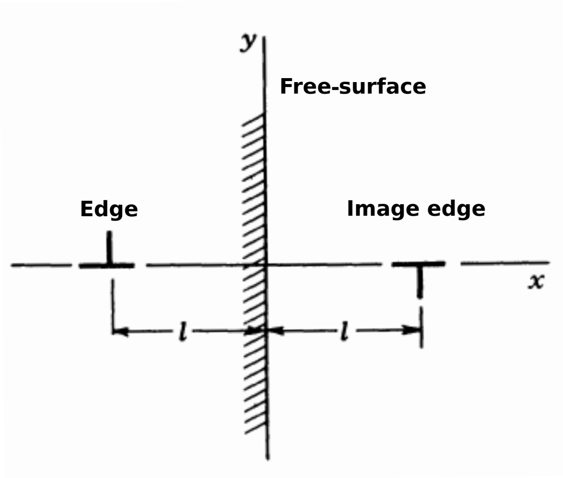

Figure 4.3: Image dislocation concept in the case of an infinite edge dislocation located at a distance $l$ from a free-surface. The left part ($y < 0$) represents the material side including the “real” edge dislocation while the right part ($y > 0$) contains the “image” edge dislocation with opposite Burger vector. Adapted from [HIR 82].

In HL book was proposed a solution to solve the stress-free BVP for a simple geometry and a straight-infinite dislocation using the image method. Considering that the self-stress for infinite dislocations has two non-zero components for screw dislocation and four non-zero component for the edge; it allows in some cases to simplify the three dimensional BVP into a two dimensional symmetric problem (as shown in Figure 4.3). Here the BVP consists in an infinite dislocation with a glide plane perpendicular to a perfectly flat surface and is solved by placing the image dislocation symmetrically on the other side of the surface (same glide plane, same distance, opposite Burgers vector).

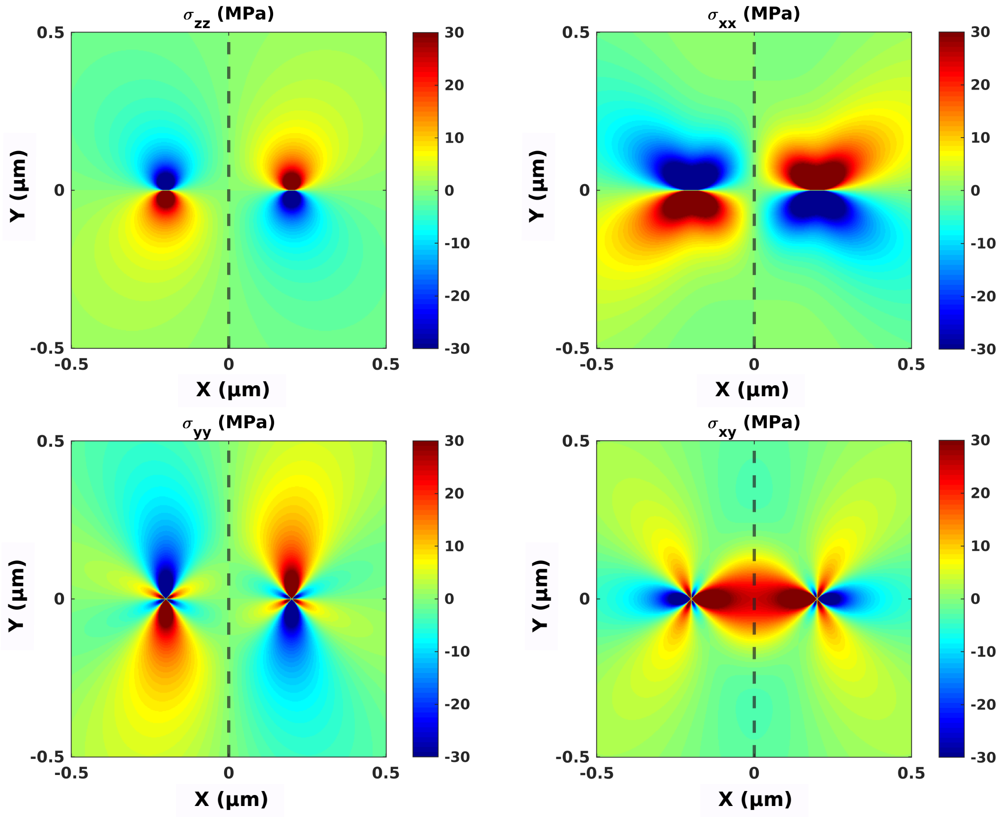

Figure 4.4: Stress maps for real (left) and image (right) edge dislocations computed using MATLAB. The dislocation is set at 0.2 µm from the virtual free-surface (dashed line). All components cancel at the free-surface except the $\sigma_{xy}$ due to symmetry.

The problem can be represented as two dislocations with opposite Burgers vectors set in the same slip plane and at a distance $2l$ from each other. Under such conditions, the stress generated by the image dislocation cancels the stress generated by the real one at the middle distance where the boundary is located. This problem is investigated here using MATLAB implementing the Cai theory in the cases of edges and screw dislocations. The distance between the dislocation and the virtual free-surface is set to 0.2 µm and the plot is produced using the elastic constants of copper and the setup is similar to the one depicted in Figure 4.3.

Results are shown Figures 4.4 and 4.5. As expected, the self-stress of the image edge dislocation superimposes to the one of the real dislocation and cancels it at the location of the hypothesized surface (dashed lines) for $\widetilde{\sigma}_{zz}, \widetilde{\sigma}_{xx}$ and $\widetilde{\sigma}_{yy}$ components but not for $\widetilde{\sigma}_{xy}$ (Figure 4.4). Similarly, $\widetilde{\sigma}_{xz}$ is canceled at the virtual surface for the screw character but not $\widetilde{\sigma}_{yz}$ as shown in Figure 4.5.

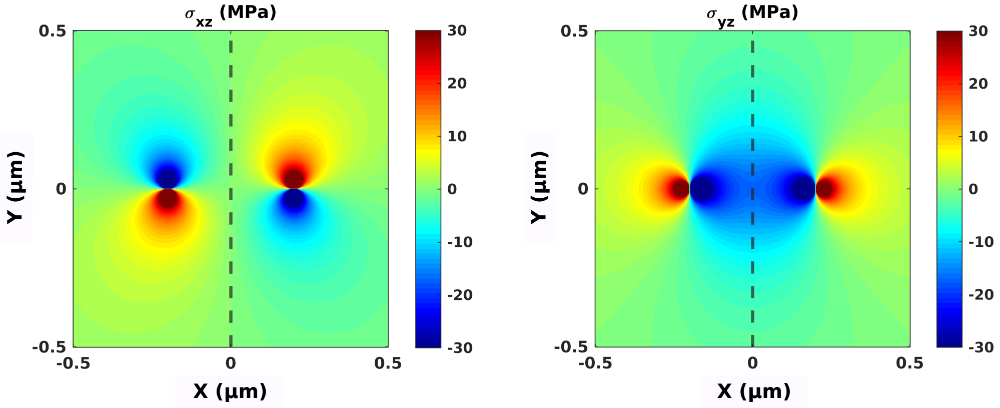

Figure 4.5: Stress maps for real (left) and image (right) screw dislocations. The dislocation to virtual free-surface (dashed line) distance is 0.2 µm. $\sigma_{xz}$ cancels at the virtual free-surface location but not $\sigma_{yz}$.

So, the image method is not sufficient to fully solve the BVP. The stress patterns generated by the dislocation lines are symmetric with respect to the glide plane. Moreover, inverting the sign of the Burger vector implies to rotate the stress pattern by 180°. It means that the components that cancel at the free-surface depend on the orientation of the free-surface regarding the glide plane. For instance, in Figure 4.4, the $\widetilde{\sigma}_{xy}$ component does not cancel because the hypothetical free-surface is parallel to the symmetry axis of the stress pattern. The same reasoning applies for the $\widetilde{\sigma}_{yz}$ component of the screw dislocation in Figure 4.5.

The previous analysis implies that using the image method to cancel the stress at a free-surface is not enough and some additional features need to be introduced to ensure the cancellation of the shear and normal stress components at the boundaries. In HL book, the concept of Airy functions was used to cancel the remaining stress components at the surface. This will be further detailed in the next section. One can notice that in the electrostatic theory, the force induced by a point charge is fully cancelled at the surface when using the image method. Indeed, the electric field of a punctual charge expands radially from the charge position and is not symmetric [JAC 98].

### 4.2.2 The Airy functions

In the previous section, we have seen that the dislocation image construction is not enough to ensure stress-free BCs. To solve this issue, Airy functions are used to analytically verify the stress-free BCs [HIR 82]. In the following, we use again the infinite edge dislocation protocol facing a free-surface (Figure 4.4) to detail the reliability of the Airy functions. Please note, that the following analysis is valid also for the screw dislocation character.

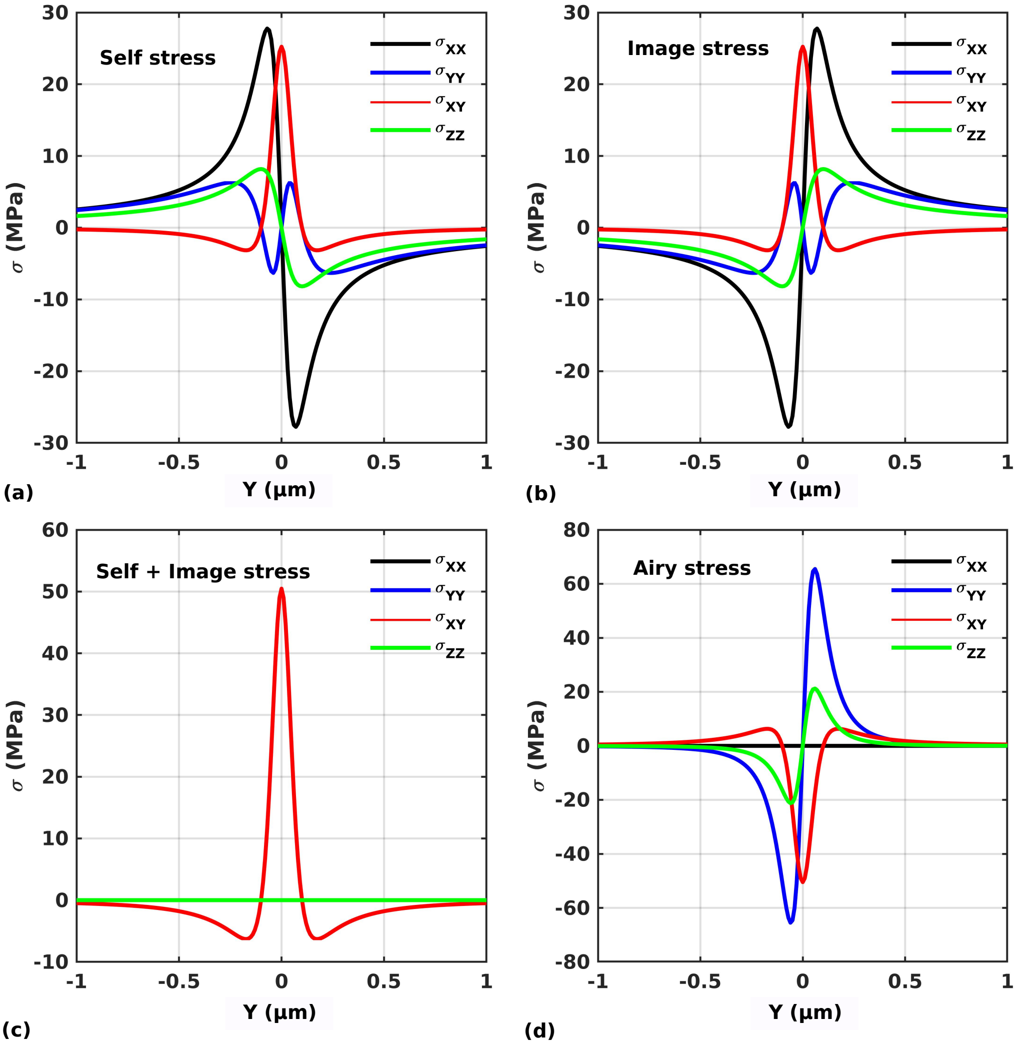

Figure 4.6: Stress components computed for an infinite edge dislocation located at 0.1 µm from a free-surface along the boundary (2 µm length). (a) self-stress ($\widetilde{\sigma}$) generate by the real dislocation, (b) image stress ($\sigma^{Im}$) generated by the image dislocation, (c) is the sum of the self and image stress. (d) the Airy stress function.

In Figure 4.6 (a), analytical $\widetilde{\sigma}_{xx}, \widetilde{\sigma}_{yy}, \widetilde{\sigma}_{xy}$, and $\widetilde{\sigma}_{zz}$ are plotted along a line of the virtual surface boundary using the Cai theory for a dislocation located at 0.1 µm of the surface.

The construction of the image stress (Figure 4.6 (b)) inverts symmetrically all the components along the $Y$ axis except $\widetilde{\sigma}_{xy}$ which is self-similar. Thus, stress is not canceled when summing self and image stresses at the virtual surface as shown in Fig. 4.6 (c). It is instead doubled and reaches 50 MPa in the region just in front of the dislocation line (in agreement to what is shown in Figure 4.4).

The Airy stress for an infinite edge dislocation [HIR 82] is given by equations 4.1 to 4.4.

$$\sigma_{xx}^{A} = -\frac{2\mu b l x y}{\pi(1-\nu)r^{6}}\left[3(l-x)^{2} - y^{2}\right] \tag{4.1}$$

$$\sigma_{yy}^{A} = \frac{\mu b l}{\pi(1-\nu)r^{6}}\left[4(l-x)^{3}y + 6(l-x)^{2}xy + 4(l-x)y^{3} - 2xy^{3}\right] \tag{4.2}$$

$$\sigma_{xy}^{A} = \frac{-\mu b l}{\pi(1-\nu)r^{6}}\left[(l-x)^{4} + 2x(l-x)^{3} - 6xy^{2}(l-x) - y^{4}\right] \tag{4.3}$$

$$\sigma_{zz}^{A} = \frac{4\mu b l \nu}{\pi(1-\nu)r^{6}}\left[(l-x)^{3}y + (l-x)y^{3}\right] \tag{4.4}$$

With $r = (l^{2} + y^{2})^{1/2}$ being the symmetric term respect to the center of coordinates ($X$,$Y$).

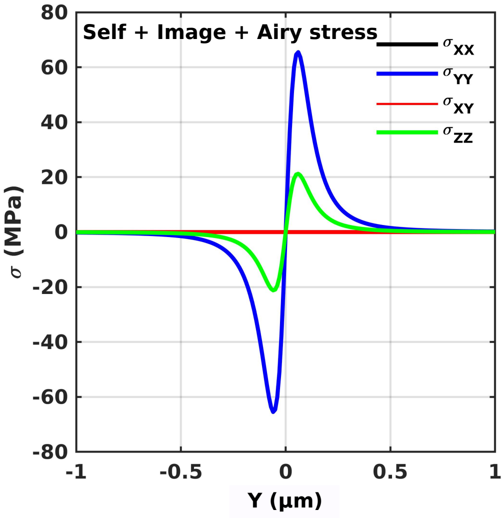

Figure 4.7: Superposition at the virtual free-surface of the self, image and Airy stress components for an infinite edge located at 0.1 µm from a free-surface

The Airy stress is plotted in Figure 4.6 (d) along the boundary as in the previous setup description. As it is plotted along a vertical line located at $x = 0$, $\sigma_{xx}^{A} = 0$ (equation 4.1). Remaining terms are not null and $\sigma_{xy}^{A}$ is in the same range than $\sigma_{xy}^{Im}$ (Figure 4.6 (c)) but with opposite sign (Figure 4.6 (d)). The total stress components $\sigma_{xx}^{T} = \widetilde{\sigma}_{xx} + \sigma_{xx}^{Im} + \sigma_{xx}^{A} +$

and $\sigma^T_{xy} = \widetilde{\sigma}_{xy} + \sigma^{Im}_{xy} + \sigma^A_{xy}$ that correspond to the normal and a shear components satisfy the stress-free BC (Figure 4.7) *i.e,* they are null at the virtual boundary.

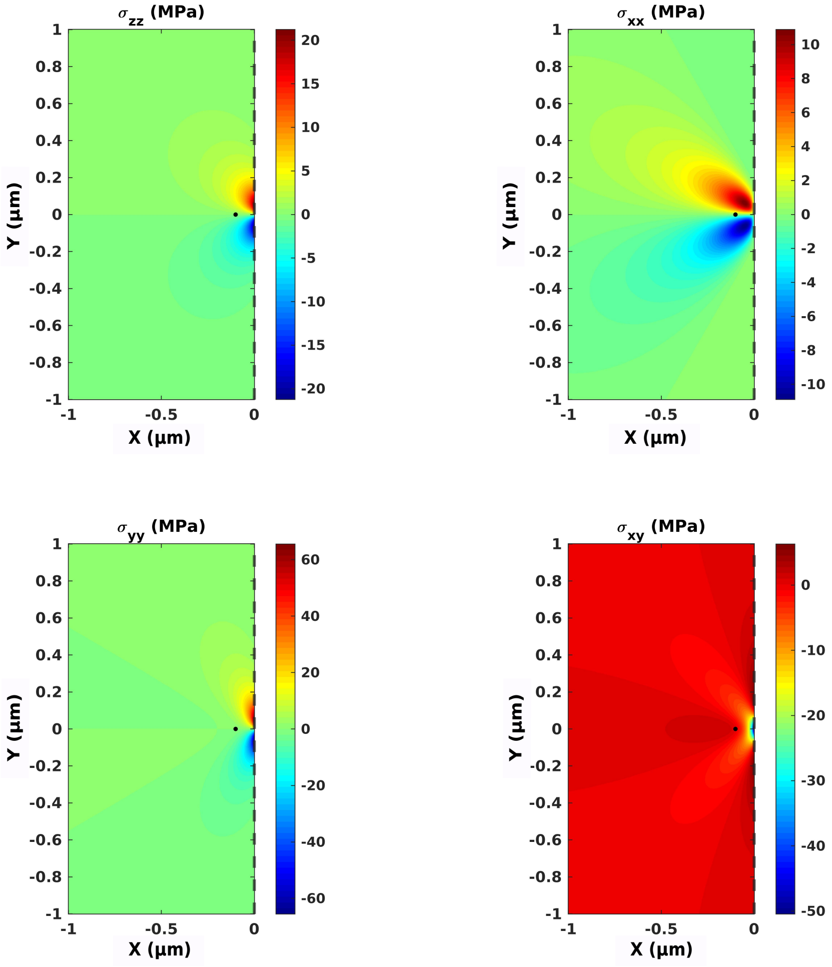

Figure 4.8: Airy stresses for an infinite edge dislocation (black dot) located at 0.1 µm from a free-surface (dashed line).

Figure 4.8 shows the four components of the Airy stress (equations 4.1 to 4.4) for the same edge dislocation setup. The stress map produces symmetric iso-stress curves with a pattern similar to the one of the self-stress. The component $\sigma^A_{xx}$ provides zero stress at the virtual free-surface (dashed line at $x = 0$) as shown previously in Figure 4.6 (d).

To test the implementation of the SPM method within El-Numodis, we designed a setup made of a slab with dimensions $1 \times 2 \times 1$ µm$^3$ as shown in Figure 4.9 (a). Still using copper as model material. An infinite edge dislocation (red line) is positioned at a distance 0.1 µm from a free-surface (green rectangle) with the slip system (blue plane) perpendicular to the free-surface. The opposite parallel surface is set as a fix boundary with zero displacement. The other surfaces are not considered in the SPM corrections assuming infinite size in the $Z$ and $Y$ directions. The simulation cell dimensions are $1 \times 2 \times 1$ µm meshed with eight nodes hexahedron refined around the dislocation line.

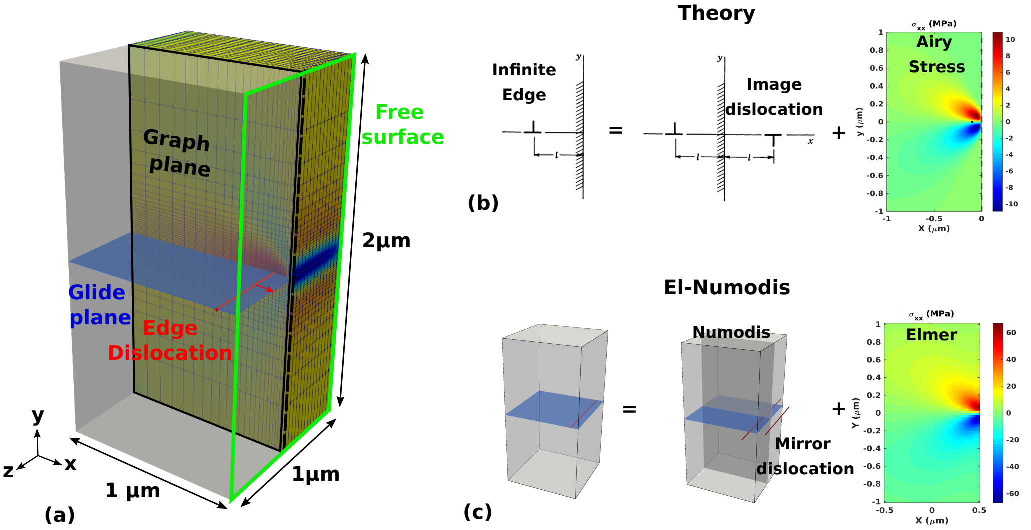

Figure 4.9: Infinite edge *vs.* free-surface computed using El-Numodis. (a) Setup, the infinite edge dislocation (red line) is located at 0.1 µm from the free-surface (green rectangle). The black-dashed line over the free-surface represents the location to inquire the stress component. The black square at the center of the box shows the place to construct the stress maps as represented in (c). (b) Scheme of total stress calculation produced by the superposition of the self, the image and the Airy stresses, (c) Similar scheme when applied to El-Numodis framework.

As previously mentioned, the total stress is defined as $\boldsymbol{\sigma^T} = \tilde{\boldsymbol{\sigma}} + \boldsymbol{\sigma^{Im}} + \boldsymbol{\sigma^A}$ (Figure 4.9 (b)). In the other hand, the superposition principle implies that the total stress is defined as $\boldsymbol{\sigma^T} = \tilde{\boldsymbol{\sigma}} + \hat{\boldsymbol{\sigma}}$ (Figure 4.9 (c)). Thus, $\hat{\boldsymbol{\sigma}} = \boldsymbol{\sigma^{Im}} + \boldsymbol{\sigma^A}$ provides an easy way to check the correct implementation of the BVP in El-Numodis comparing the FEM stress ($\hat{\boldsymbol{\sigma}}$) to the theoretical term $\boldsymbol{\sigma^{Im}} + \boldsymbol{\sigma^A}$, as it is done in Figure 4.10.

The stress maps constructed by the sum of the stresses $\boldsymbol{\sigma^A} + \boldsymbol{\sigma^{Im}}$ (Figure 4.10 (a)) and $\hat{\boldsymbol{\sigma}}$ as calculated by El-Numodis (Figure 4.10 (b)) at the graph plane are reproduced with certain similarities. $\hat{\boldsymbol{\sigma}}$ however tends to be less precise compared with its theoretical counterpart mainly due to two aspects. First, the solutions provided are valid for an infinite half-space *i.e.,* an infinite space with only one boundary to account for. In the FEM simulation, a finite volume is used and approximations are made to reproduce half spaces: in the previous simulation, the free boundary was subjected to Neumann BC with zero external applied stress and corrected by the SPM. Also, as it is done in FEM simulations involving loading or mechanical deformations, at least one boundary is set with a fixed displacement BC ($X = 1$ µm in Figure 4.9 (a)) that ensures the setup can

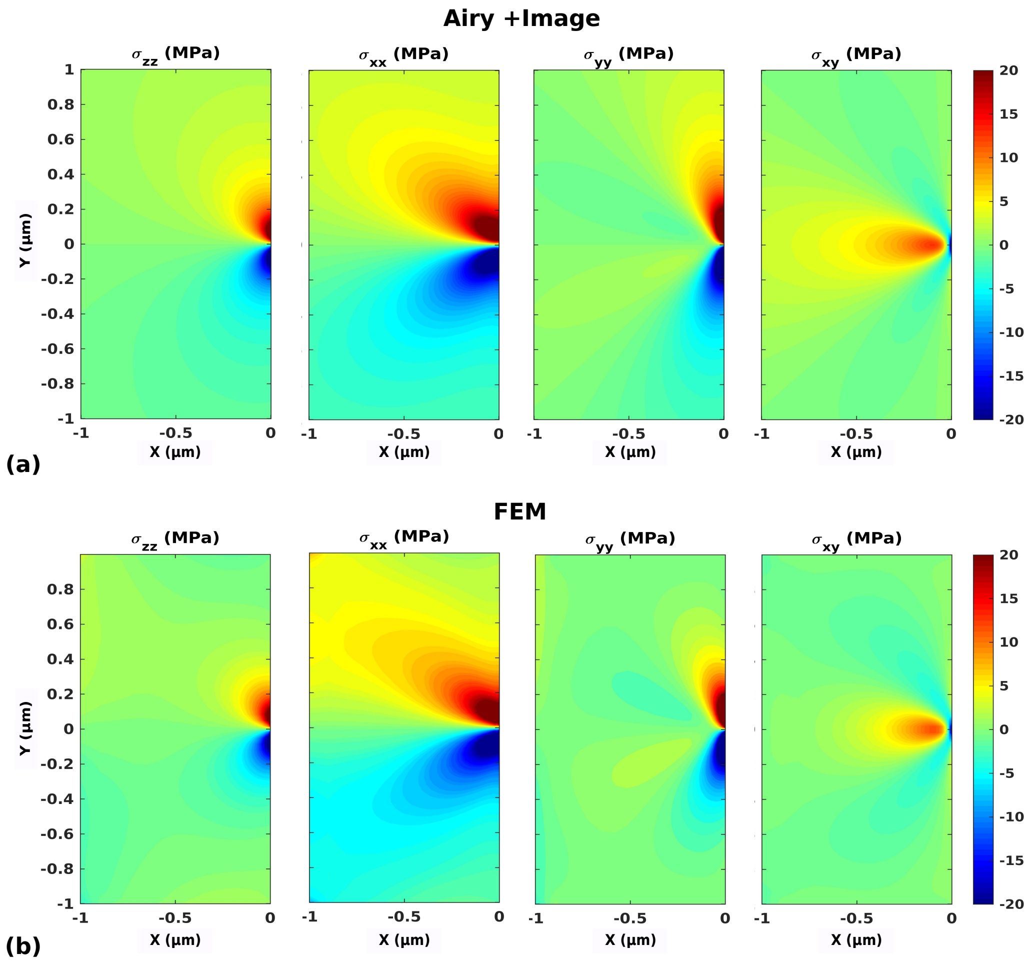

Figure 4.10: Comparison between the theoretical terms (a) $\boldsymbol{\sigma^A} + \boldsymbol{\sigma^{Im}}$ and (b) the FEM stress $\hat{\boldsymbol{\sigma}}$ produced by El-Numodis using the setup and the theoretical formulation of Figure 4.9.

withstand high-stress without displacing the simulation domain. The implementation of a rigid wall as the opposite face of the stress-free-surface together with the presence of boundaries (even if not corrected by the SPM) implies that stress in near-regions will not reproduce exactly the theoretical predictions. This is remarkable if a straight comparison is done between Figure 4.10 (a) and (b) stress maps. As a consequence, the color map for the FEM stress $\sigma_{xx}$ looks more stretched in the region near the fixed wall. In the same way, the area of higher values (red oval) is reduced for the component $\sigma_{xy}$. The other two components also reduces the size of the area of higher values of the stress maps symmetrically to the Y direction by the presence of boundaries associated to the FEM.

Secondly, FEM represents an approximate numerical tool to solve differential equations. As an approximate method, the solutions are obtained using spatial discretization grids. The quality of the mesh plays an important role in the precision of the numerical solution. In this study, the mesh grid is chosen to be refined around the dislocation line and in the region between the free-surface and the dislocation line (more than three elements in between the dislocation line and the free-surface). In the next section, we will partly discuss the influence of the mesh discretization on image stress calculation outcomes.

### 4.2.3 Influence of the pseudo-mirror dislocation construction

The pseudo-mirror method for the construction of image dislocations [WEY 02] (see section 3.2.6) was implemented with the help of Laurent Dupuy in Numodis and El-Numodis. The method is optional and the user can choose to use it or not. It was intended to manage dislocations leaving the sample and provides certain advantages to obtain the image stress compared to the sole FEM correction used up to now.

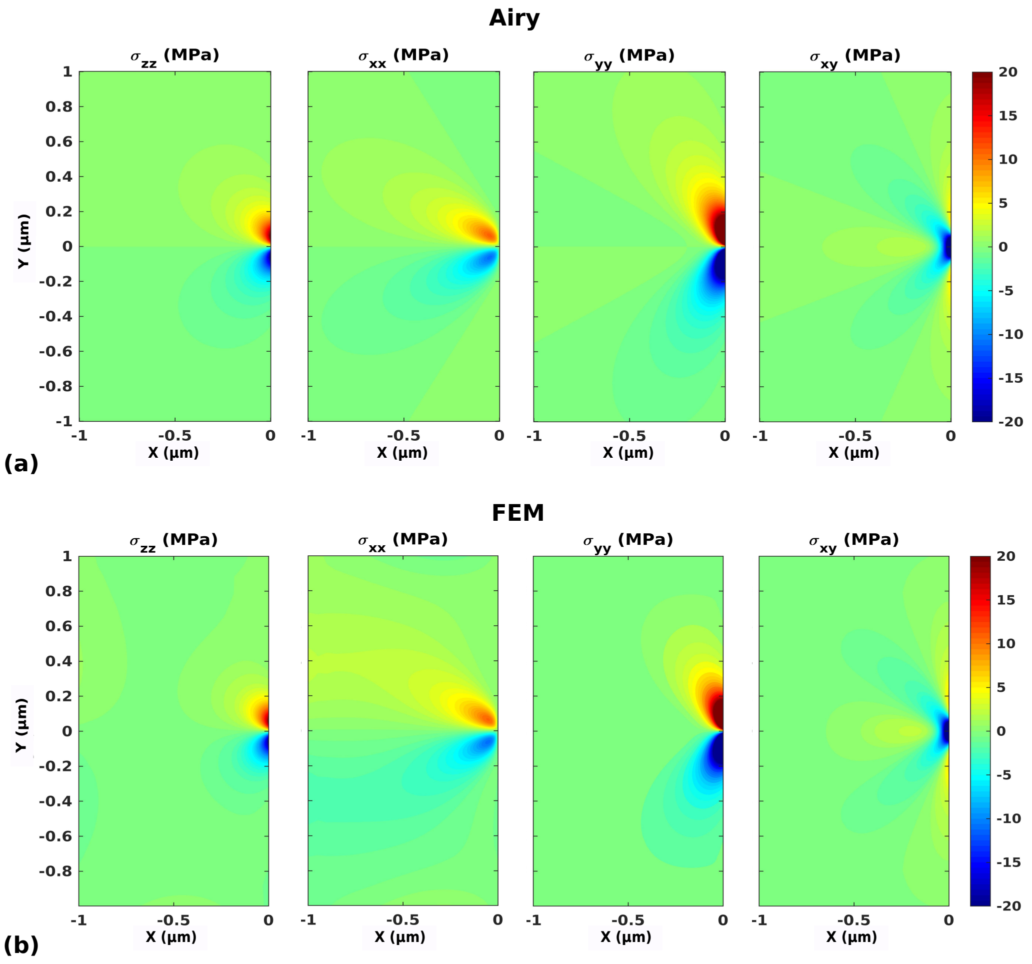

Figure 4.11: Comparison between the (a) theoretical $\boldsymbol{\sigma^A}$ and (b) the FEM stress computed by El-Numodis when the pseudo-mirror method is activated using the edge dislocation setup.

Here we use again the edge dislocation *vs.* free-surface setup with the pseudo-mirror method as implemented in El-Numodis. Under such conditions, El-Numodis generates a mirror dislocation outside the free-surface with a glide plane mirrored with respect to the real one. The mirror dislocation is a fictitious dislocation that is use only to compute the mirror stress $\boldsymbol{\sigma}^{\boldsymbol{Im}}$ to be added to the self-stress at the free boundary (it does not produce any shear).

In analogy to the stress comparison of the last section, the analytical total stress $\boldsymbol{\sigma}^{\boldsymbol{T}} = \widetilde{\boldsymbol{\sigma}} + \boldsymbol{\sigma}^{\boldsymbol{Im}} + \boldsymbol{\sigma}^{\boldsymbol{A}}$ (Figure 4.9 (b)) can be compared with the total stress $\boldsymbol{\sigma}^{\boldsymbol{T}} = \widetilde{\boldsymbol{\sigma}} + \boldsymbol{\sigma}^{\boldsymbol{Im}} + \hat{\boldsymbol{\sigma}}$ computed by El-Numodis (Figure 4.9 (c)). As shown in Figure 4.11, $\hat{\boldsymbol{\sigma}}$ compares successfully with $\boldsymbol{\sigma}^{\boldsymbol{A}}$ when pseudo-mirror method is activated in El-Numodis. These results are in better agreement than the previous case discussed in the last section. Thus, we conclude that using the pseudo-mirror dislocation approach represents a more accurate methodology than the sole FEM correction.

To confront the pseudo-mirror approach to the traditional image construction based on the SPM, we rely on the mesh discretization in El-Numodis. The FEM implementation is well known to be critically dependent on the type of mesh and the quality of the discretization. Here we focus on 8 nodes hexahedron meshes but test the mesh quality. The quality of the mesh can be improved by multiplying the number of elements or by refining where large stress gradients are expected.

The precision of the SPM within El-Numodis is tested accounting for four mesh qualities (Figure 4.12): 30, 60 and 120 regular elements in the three direction of the box (Figure 4.12 (a-c)) and an additional one using a refinement criterion around the dislocation line and near the free-surface (Figure 4.12 (d)). The mesh is refined using Gmsh algorithms “Using Bump” -4.9 and “Using Progression” 1.3.

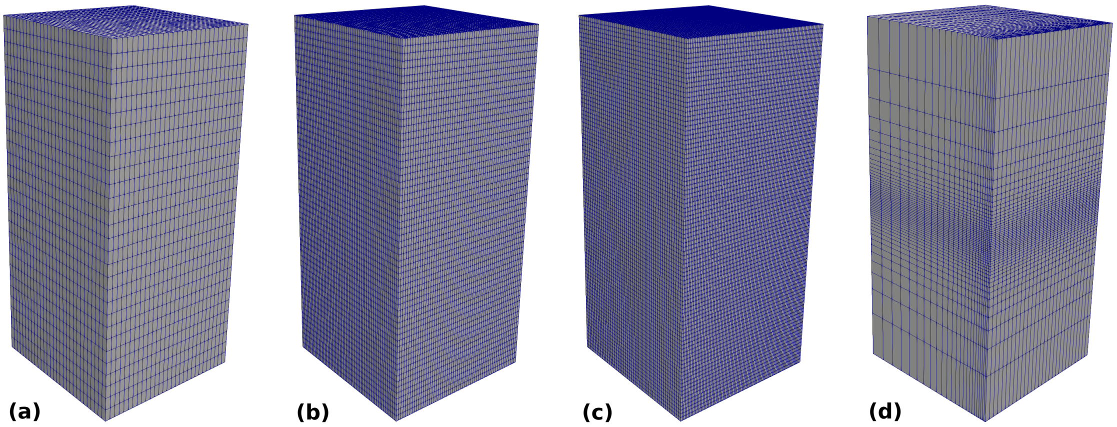

Figure 4.12: Various mesh discretizations for the edge dislocation *vs.* surface setup. (a, b, c) represents the setup with mesh distribution equally in the three directions with 30, 60 and 120 hexahedron elements per direction, respectively. (d) the setup is meshed with $25 \times 25 \times 60$ hexahedron refined around the dislocation line with the Gmsh options “Using Bump” -4.9 and “Using Progression” 1.3.

The influence of the mesh quality should have a direct impact in reaching the stress-free condition as well as the implementation of the pseudo-mirror method. It is then necessary to test the role of both aspects in the coupling. Figure 4.13 (a) is a recall of the stress reduction (infinite edge dislocation *vs.* free-surface) using El-Numodis and the theoretical model found in HL book for the normal ($\sigma_{xx}$) and shear ($\sigma_{xy}$) components. Theoretical results shows stress reduction at the free-surface from about 25-27 MPa to zero when $\boldsymbol{\tilde{\sigma}} + \boldsymbol{\sigma^{Im}} + \boldsymbol{\sigma^{A}}$ are added at the boundary ($x = 0$). El-Numodis counterpart using a mesh discretization of 120 elements as in Figure 4.12 (c) for the case when no pseudo-mirror construction is considered (denoted as *Sim*) shows very comparable results. Finally, the numerical results for $\boldsymbol{\tilde{\sigma}}$ and $\boldsymbol{\hat{\sigma}}$ have to be added. The *Sim* curved shows two important results. First, El-Numodis and theoretical self-stresses are not strictly identical due differences in the kind of BC implemented in El-Numodis. Again, the theorethical equations of the self-stress consider an infinite medium. In our case, the edge dislocation has a free-surface at 0.1 µm that makes the self-stress provided by El-Numodis different to the analytical curve especially in regions where other real surfaces are located, like the cell corners. Also another factor influencing this aspect is the fact that a such short distance from a free-surface the nature of the dislocation is important. The infinite edge dislocation is produced using a long-enough FR source that is replicated outside the box in order to reduce this effect near the center of the dislocation. However, the ending nodes of the dislocation line that lie at the external faces generate fictitious stresses that affect the stress distribution at the free boundary. This is why the two curves superimpose near $y = 0.0$ µm but differ in other regions. Second, the stress-free condition computed with El-Numodis shows non-zero stress. This outcome is related to the mathematical nature of the problem. El-Numodis is based on FEM that represents an approximated numerical tool with numerical errors. Besides, the precision of the FEM strongly depends on the mesh type and quality. One can notice that similar stress singularities at free-surface were already observed in simulations using the SPM [WEY 02] or the DCM approaches [JAM 16, HUA 17].

The influence of the mesh size is shown in Figure 4.13 (b) still in the case of the infinite edge dislocation facing the free-surface. All the configurations provided in Figure 4.12 with the pseudo-mirror method activated or not are described. Here the aim is to reproduce the Airy stress for the $\sigma_{xy}$ shear component (H&L red line) using El-Numodis. When the pseudo-mirror construction is activated (30 W, 60 W, 120 W and Ref W) then the $\boldsymbol{\hat{\sigma}}$ is directly compared to the Airy stress. When El-Numodis is used without pseudo-mirror dislocation (30, 60, 120, Ref), $\boldsymbol{\hat{\sigma}}$ is added to $\boldsymbol{\tilde{\sigma}}$ computed along the same line along the free-surface. In general, better results are obtained increasing the mesh quality. Refining the mesh along the dislocation line (Ref, Ref W) provides almost the same stress values independently if the pseudo-mirror method is activated or not. But when a coarse mesh is used, the pseudo-mirror dislocation method improves the results. It represents an important results if the computational efficiency is an important criterion. A simulation with a very well refined mesh or including a detection algorithm that recognizes a dislocation approaching a free-surface automatically refining the mesh in the near-region

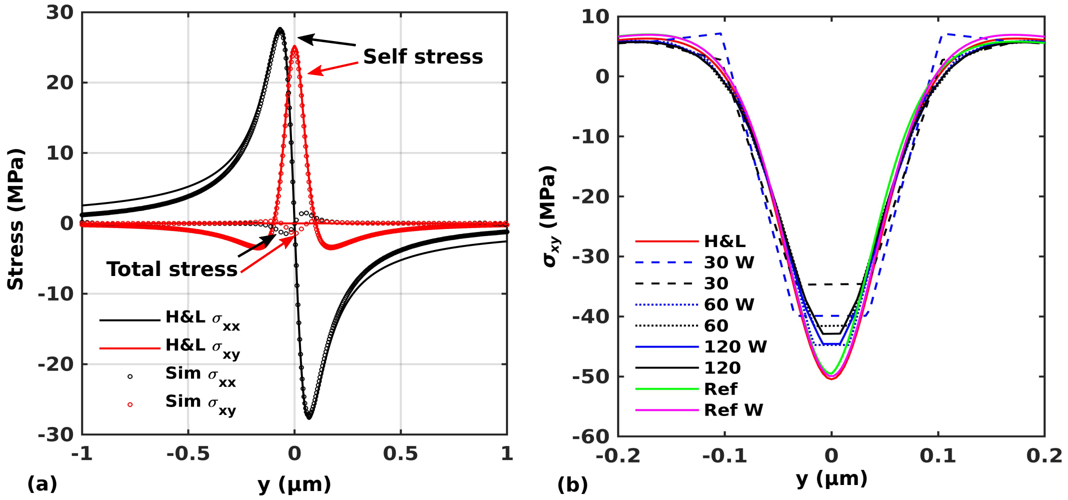

Figure 4.13: Stress reduction at free-boundary for an infinite edge dislocation facing a free-surface: influence of mesh and pseudo-mirror method. (a) El-Numodis is compared to the theoretical model found in HL book. Stress components are computed along line lying on the free-surface (see Figure 4.9 (a)), (b) El-Numodis $\sigma_{xy}$ (or $\sigma_{xy}$-$\sigma_{xy}^{Im}$ when accounting the mirroring dislocation method) correction as function of mesh refinement. Simulations are performed for mesh discretization of 30 (dashed curves), 60 (dotted curves) and 120 (full curves) 8-nodes hexahedron elements in the three directions of space, using the Weygand mirror dislocation method (W) or not. *Ref* curves rely on the aforementioned 30×60×30 with particular mesh refinement near the dislocation using Gmsh (Bump = -4.9 and Progression = 1.3). Results are compared to the $\sigma_{xy}^{A}$ of the model explained in Hirth & Lothe book (referred as H&L, red curve). Data are plotted along a vertical line passing by the middle of the $x$ -surface as shown in Figure 4.9 (a).

might improve the results. However, both simulations might have significant CPU costs and are out of the scope of the present study.

Based on this parametric study, we assume it is enough to use an intermediate mesh size (60 elements) with the pseudo-mirror dislocation method activated to have an acceptable stress accuracy.

## 4.3 Square-loop dislocation near a free-surface

In real experiments or even in massive DD simulations, it is hard to find situations where a perfectly straight dislocation is at the vicinity of a free-surface. For the FR case in DDD, the initial straight pinned dislocation bends into a circular shape and elongated dislocation loop. When such a curved dislocation is in the vicinity of a surface, the topological object that faces the planar surface is not a straight dislocation but rather a curved one. Furthermore, it is not infinite anymore. This effect is more evident with the reduction of the sample size, what makes surface effects even more relevant in this context. From the experimental side, dislocation microstructures are formed by a bunch of curved linear elements often compared to a spaghetti plate. In the following section, El-Numodis is tested against a more complex situation than the straight dislocation line *i.e.,* the dislocation square loop.

### 4.3.1 The Gosling and Willis method

The presence of a dislocation line inside any linear elastic material induces a stress field that can be calculated by a surface integral 4.5. This formulation is valid as soon as the appropriated Green tensor is used.

$$\sigma_{pq}(\boldsymbol{x'}) = -\int b_s c_{srkl} c_{pqmj} \frac{\partial}{\partial x'_j} G_{mk,j}(\boldsymbol{x}, \boldsymbol{x'}) dS_r \tag{4.5}$$

Where $\boldsymbol{c}$ is the elastic stiffness tensor and $\boldsymbol{G}$ is the Green tensor associated to a particular material. $\boldsymbol{x}$ and $\boldsymbol{x'}$ represent the field and source point of the Green tensor. $dS_r$ is the surface integration.

For an infinite medium, the previous integral can be transformed using the Stokes theorem into an integral over the dislocation line $C$ as:

$$\sigma_{pq}(\boldsymbol{x'}) = -\oint_C b_s S^{\infty}_{pqrs}(\boldsymbol{x} - \boldsymbol{x'}) dx'_r \tag{4.6}$$

where

$$S^{\infty}_{pqrs}(\boldsymbol{x} - \boldsymbol{x'}) = -c_{snkl} c_{pqmj} \epsilon_{njr} G^{\infty}_{m} k, l(\boldsymbol{x} - \boldsymbol{x'}) \tag{4.7}$$

represent the kernel of Mura formula 4.6 ([MUR 63]) , $\epsilon_{njr}$ is the completely antisymmetric unit tensor of order three.

If the medium is not infinite, the previous methodology is not applicable anymore. For the case of a dislocation loop in an infinite half space, Gosling and Willis (GW) propose a methodology to find the appropriated kernel $S^I$ by which the equation 4.5 still applies. The final integral has the form:

$$\sigma_{pq}(\boldsymbol{x'}) = -\oint_C b_s \left[ S^{\infty}_{pqrs}(\boldsymbol{x} - \boldsymbol{x'}) + S^{I}_{pqrs}(\boldsymbol{x}, \boldsymbol{x'}) \right] dx \tag{4.8}$$

leading to a direct calculation of the image stress field. More details can be found in [FIV 96, GOS 94].

The analytical approach of GW is confronted here to El-Numodis. Analytical results for the image stress are obtained for the case of a square loop inside a half space where only one free-surface is considered[1]. The line integral of the GW method provides the six components of the image stress tensor that are inquired along a line passing trough the center of the dislocation loop. The dislocation glide plane makes an angle of 54.7° with the bottom free-surface and the material is copper.

---

[1] This work was performed in collaboration with Marc Fivel (SIMAP, CNRS, INP Grenoble)

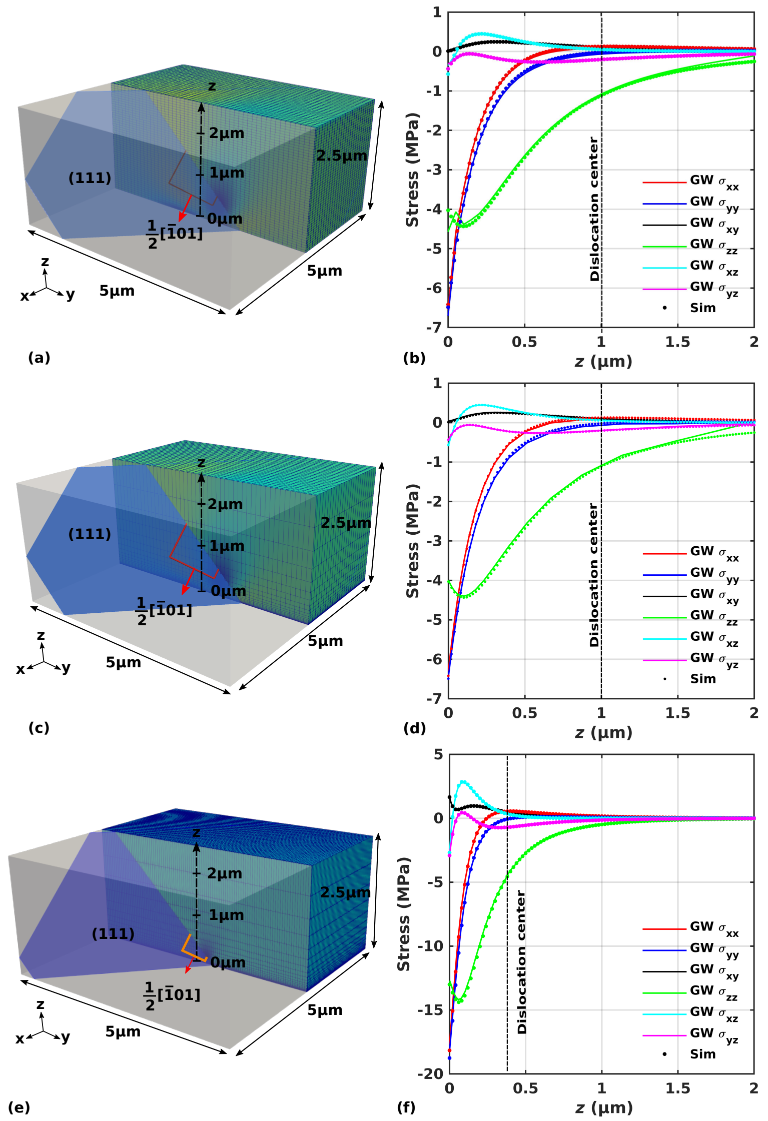

Figure 4.14: Interaction between a square $\frac{1}{2}[\bar{1}01](111)$ dislocation loop and a free-surface located at the bottom of the simulation cell. (a) 1 μm lateral side loop located at 1 μm using a regular mesh. (c) Same configuration suing a refined mesh at the bottom. (e) The distance from the free-surface to the dislocation is changed to 0.37 μm and the lateral side of the loop is adapted to 0.5 μm for a refined mesh at the bottom. (b,d,f) image stress calculated using the GW method (solid colored lines) compared to the image stress calculated with El-Numodis (colored dot) along the vertical and central dashed line depicted in (a,c,e).

In El-Numodis, a simulation box of $5 \times 5 \times 2.5$ μm$^3$ is created and oriented in the [001] direction. A square dislocation loop is inserted in the $\frac{1}{2}[\bar{1}01](111)$ slip system. The free-surface is located at the bottom of the box ($z = 0$). First, the lateral size of the loop and the distance from the loop center to the bottom free-surface is set to 1.0 μm. The opposite face at $z = 2.5$ μm is kept fix. A similar benchmark was also studied and reported by Fivel in [FIV 96] using the Tridis DDD software. A regular mesh discretization of 50 elements in each direction is used in Figure 4.14 (a). The comparison of the image stress obtained with El-Numodis to the GW analytical solution (Figure 4.14 (b)) shows a particularly fair agreement except near $z = 0$ µm (more identifiable on the $\sigma_{zz}$ component). Also, El-Numodis shows some errors near the 0 to 0.2 µm region for $\sigma_{zz}$ associated to the reduced number of elements used: only 2 elements are set below the 0.2 µm region. This local singularity is associated with wide stress gradients that are not accurately solved with the mesh used. Same simulations are repeated with an improved mesh near the bottom free-surface (Figure 4.14 (c)). This time only the Gmsh algorithm “Using Progression” 1.30 is used. Fig. 4.14 (d) shows that the indetermination is corrected once the mesh quality is improved by refinement. The good agreement between El-Numodis and GW stress in the case of a square dislocation loop facing a free-surface is another proof of the correct implementation of the SPM within El-Numodis.

With this test-case we have also verified the ability of El-Numodis to reduce the stress at the bottom surface characterized by stress-free BC *i.e.,* El-Numodis should be capable to reduce the few stress imposed by the square loop (at least the maximum -4 MPa for $\sigma_{zz}$) to the bottom surface to zero. In order the make the test more significant, we brought the square loop closer to the bottom surface to increase the induced surface stress. The orientation of the slip system implies that reducing the distance to the surface will also reduce the lateral side of the loop to not overpass the limit of the free-surface. A configuration made of a 0.5 µm lateral side loop located at 0.37 µm from the bottom surface was chosen keeping the same refinement mesh near the bottom surface (Figure 4.14 (e)). The image stress calculation shows that the normal components ($\sigma_{zz}$) goes now up to -13 MPa while the two shear, $\sigma_{xz}$ and $\sigma_{yz}$ reach -3 MPa (0.5 MPa before). In this case the effect of the lateral surfaces is clearly avoided (as compared to the infinite dislocation case).

To check the stress-free BC (Figure 4.15), the normal and shear components stress maps of the self and FEM stresses ($\hat{\boldsymbol{\sigma}}$) are inquired at the free-surface. $\hat{\boldsymbol{\sigma}}$ shows exactly the same stress maps regarding the self-stress but with opposite signs. The stress-free is then reached superimposing the dislocation self-stress and the FEM correction leading to an almost zero residual stress. This test-case confirms that for cases where a realistic object like a dislocation loop is used; El-Numodis is fully capable to solve BVP and verify stress-free BC reducing stress values in the order of few tens MPa to zero. Still, the presence of a residual stress can be associated to numerical issues or mesh refinement.

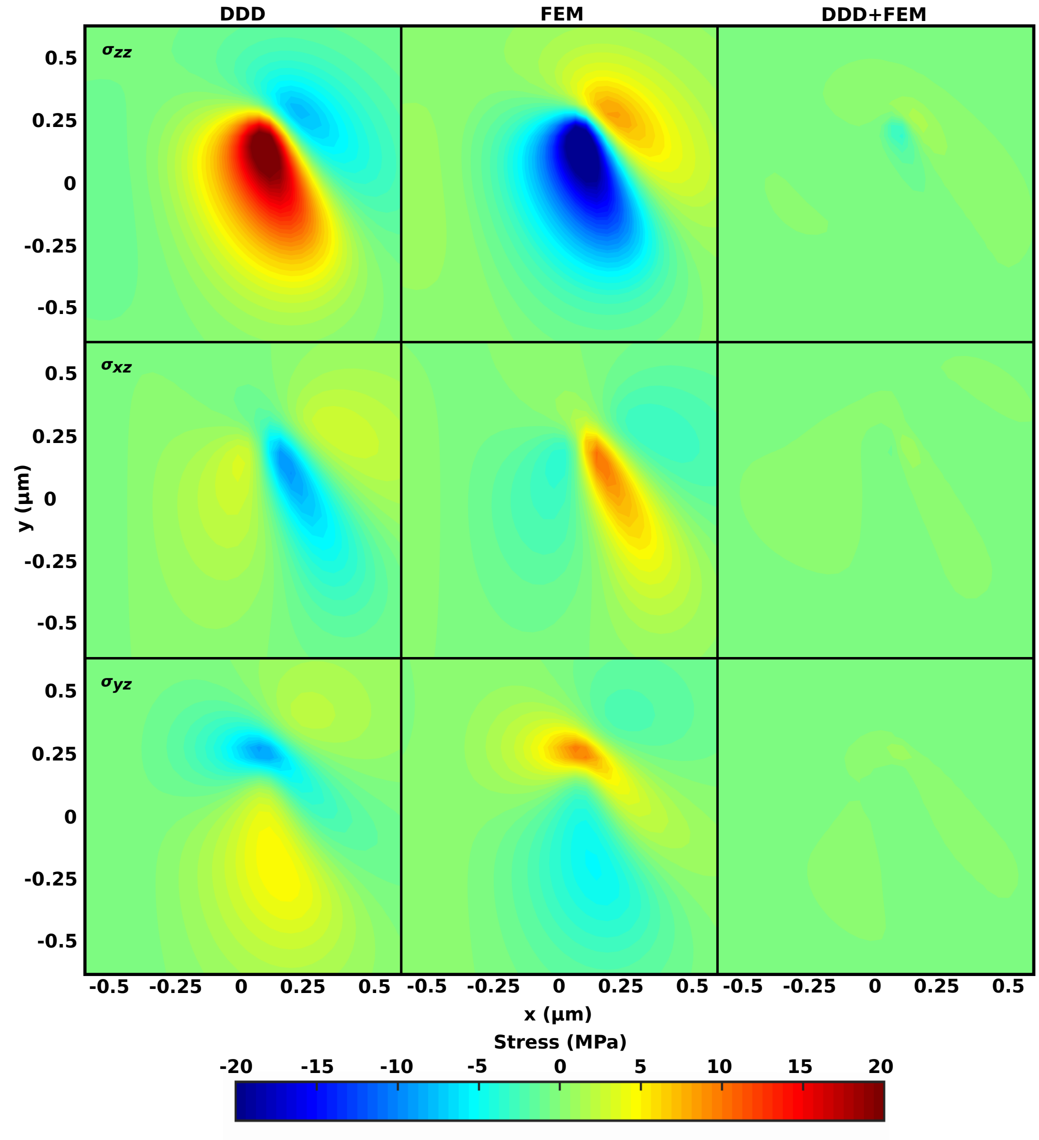

Figure 4.15: Surface-stress components computed with El-Numodis in the case of a square loop located at 0.37 μm from the free-surface. The three rows represent the normal ($\sigma_{zz}$) and the two shear ($\sigma_{xz}, \sigma_{yz}$) components over the surface. The first image column represent the self-stress of the loop computed at the surface, the second column is the FEM correction component, and the last is the superposition of the two previous fields. The images were made by zooming around an area of 1.21 μm$^2$ around the center of the free-surface.

## 4.4 Test case: thin films tensile test

In this section, we use El-Numodis to investigate the mechanics of thin films under tension. A ⟨100⟩-oriented copper thin film with 1.0 μm lateral size and 0.5 μm thickness (Figure 4.16) is created and meshed using regular size eight nodes hexahedrons discretized using 20 points in the [010] and [001] directions and 10 points along [100].

The initial microstructure consists in 25 FR sources of screw character of 0.2 μm length

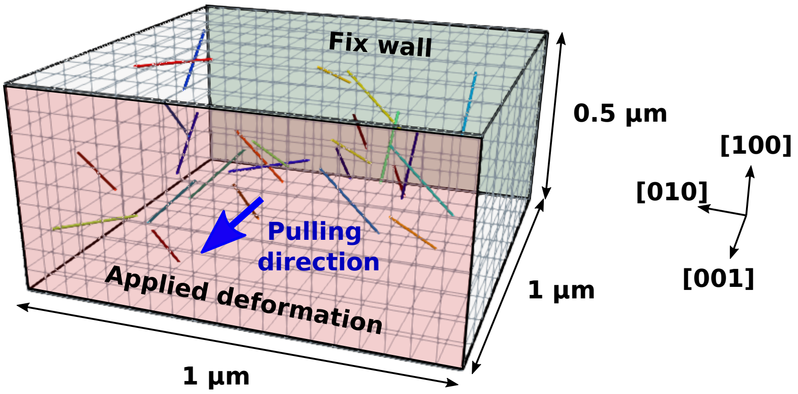

Figure 4.16: El-Numodis thin film simulation setup. The sample consists in a copper thin film of 0.5 µm thickness and 1.0 µm lateral sizes with cubic orientation in which FR sources are randomly distributed in various $\frac{1}{2}\langle 110\rangle\{111\}$ slip systems.

randomly located inside the sample. Dislocations slip systems correspond only to the main slip systems of FCC materials $\frac{1}{2}\langle 110\rangle\{111\}$. The starting dislocation network is generated using a homemade MATLAB routine that considers no recovering between dislocation FR sources as well as the full-inclusion of the dislocations within the simulation cell (no boundary overlap), at a minimum distance from the surfaces. The Figure 4.17 shows the dislocation distribution.

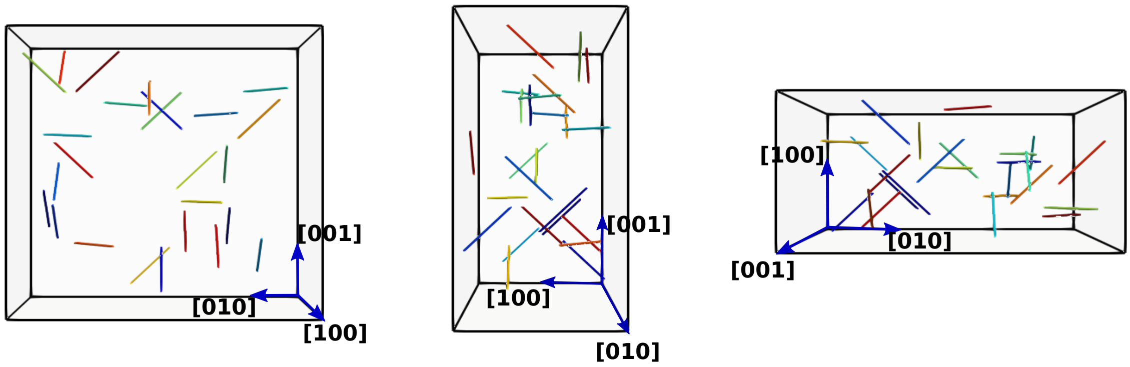

Figure 4.17: Views of the initial microstructure of the 0.5 µm thick thin film from three different angles. The initial screw FR sources are randomly distributed to avoid the dislocations to intercept the surfaces.

The sample is deformed pulling one of the (001) face (pink face in the Figure 4.16) at a constant strain rate of $10^{-6}$ ns$^{-1}$ while the opposite (001) face is kept fixed. The feedback loop algorithm is used to correct the applied stress at the surface (*i.e.*, where the deformation is applied) as described in Chapter 3. An initial stress of 145 MPa is imposed to avoid large CPU costs in the elastic regime. Such stress is enough to bend the FR sources without fully opening them. The rest of the lateral surfaces are submitted to traction-free BC and the pseudo-mirror dislocation method is activated using a 0.06 µm cutoff distance.

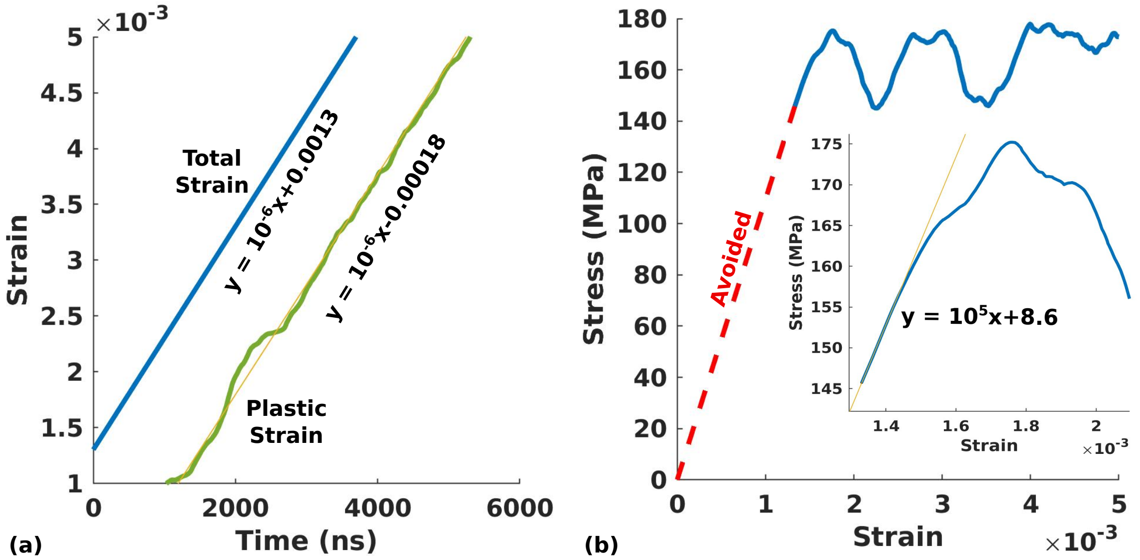

Figure 4.18: Strain-rate and stress response of the 0.5 µm thick thin film under traction. (a) Total (blue) and plastic (green) strains versus simulation time. (b) Computed stress-strain curve (blue) and the skipped elastic part (dashed red line).

Several tests were made to check the performances of El-Numodis when relying on time-dependent, “dynamic”, simulations. Figure 4.18 (a) represents the evolution of both; the total and plastic strain produced along time. A linear fit on the two curves allows to verify the imposed strain rate value of $10^{-6}$ ns$^{-1}$. This implies that the loading algorithm is correctly implemented in El-Numodis.

The simulated stress-strain curve is plotted in Figure 4.18 (b). The (effectively skipped) elastic regime (from 0 to 145 MPa) is shown and we have verified that the amount of plasticity produced by the dislocations during this interval is very small as confirmed by the fit of the end of the elastic regime (from 145 MPa up to 155 MPa) that perfectly reproduces the Young’s modulus of the material $E = 111.2$ GPa. Finally, stress-strain curves and plastic strain are illustrated in Figure 4.19 where it is confirmed that the plastic regime initiates at about 165 MPa, before the sample fully yields at about 177 MPa. At this stage, a larger amount of plasticity is produced by the mobile dislocations and El-Numodis’ applied stress correction is maximum.

In the following, we discuss the influence of the dislocation microstructure evolution on the mechanical response. The initial random microstructure is made of several FR sources distributed on the various FCC slip systems. The precise distribution and Schmid factors are described in Table 4.1. In this case, there is in total six slip systems with zero Schmid factors in which dislocations are not supposed to glide.

Figure 4.20 shows dislocation microstructure snapshots at various points along the

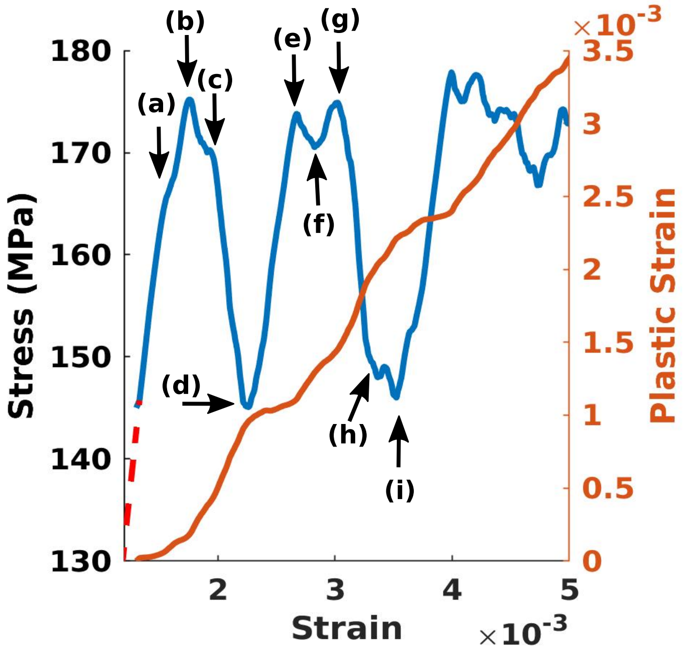

Figure 4.19: Stress-strain curve and plastic strain versus strain for the 0.5 μm thin film. The letters and arrows represent the main interactions during the simulation and the respective microstructural status is reflected in Figure 4.20.

Table 4.1: FCC slip systems used in the simulation, their Schmidt factor and the number of dislocation inserted.

| Index | Slip plane | Burgers vector | Schmidt factor | Number of dislocations |
|---|---|---|---|---|
| 1 | $(\bar{1}\bar{1}1)$ | $\frac{1}{2}[011]$ | 0.408 | 2 |
| 2 | $(\bar{1}\bar{1}1)$ | $\frac{1}{2}[1\bar{1}0]$ | 0 | 2 |
| 3 | $(\bar{1}\bar{1}1)$ | $\frac{1}{2}[101]$ | 0.408 | 2 |
| 4 | $(\bar{1}1\bar{1})$ | $\frac{1}{2}[011]$ | 0.408 | 1 |
| 5 | $(\bar{1}1\bar{1})$ | $\frac{1}{2}[10\bar{1}]$ | 0.408 | 2 |
| 6 | $(\bar{1}1\bar{1})$ | $\frac{1}{2}[110]$ | 0 | 1 |
| 7 | $(1\bar{1}\bar{1})$ | $\frac{1}{2}[0\bar{1}1]$ | 0.408 | 1 |
| 8 | $(1\bar{1}\bar{1})$ | $\frac{1}{2}[101]$ | 0.408 | 4 |
| 9 | $(1\bar{1}\bar{1})$ | $\frac{1}{2}[110]$ | 0 | 3 |
| 10 | $(111)$ | $\frac{1}{2}[0\bar{1}1]$ | 0.408 | 4 |
| 11 | $(111)$ | $\frac{1}{2}[10\bar{1}]$ | 0.408 | 3 |
| 12 | $(111)$ | $\frac{1}{2}[1\bar{1}0]$ | 0 | 0 |

stress-strain curve (Figure 4.19). Figure 4.20 (a) refers to the step (a) marked on the stress-strain curve. It is characterized by two dislocation-dislocation interactions. First, while opening, a $\frac{1}{2}[101](1\bar{1}\bar{1})$ dislocation is attracted towards a non-mobile one in $\frac{1}{2}[1\bar{1}0](\bar{1}\bar{1}1)$ and create a junction. After the reaction, both dislocations do not move anymore for the rest of the simulation. Second, the widely open $\frac{1}{2}[101](\bar{1}\bar{1}1)$ dislocation contact with the $\frac{1}{2}[101](1\bar{1}\bar{1})$ one and further annihilate as having same Burgers vectors (Figure 4.20 (b)). Figure 4.20 (b) shows the moment when the first change of slope of the plastic strain curve is observed characterizing the yield point. The plastic strain at this stage is produced mostly due to the gliding of a $\frac{1}{2}[101](\bar{1}\bar{1}1)$ (in red) and a $\frac{1}{2}[10\bar{1}](\bar{1}1\bar{1})$ (in blue) dislocations.

While stress starts decreasing, some interactions between dislocations occurs and influencing the stress-strain curve. For instances, Figure 4.20 (c) shows three of those interactions. c1 represent the re-crossing of two dislocations that interacted before (explained in (a-b)). As a result of this crossing a FR source is created, where the pinning points are made of two small arms of two dislocations of same character. Due to its particularly small length, the resulting FR will require more stress to glide. Thus, this dislocation portion will not participate to plasticity and will only oscillate, until it will be re-crossed again later on. In c2, the arm of one $\frac{1}{2}[101](\bar{1}\bar{1}1)$ dislocation crosses a bending FR source ($\frac{1}{2}[011](\bar{1}1\bar{1})$). Also, c3 illustrates the future junction and split of the opened $\frac{1}{2}[10\bar{1}](111)$ dislocation with a bending one of slip system $\frac{1}{2}[10\bar{1}](\bar{1}1\bar{1})$. One of the arms product following this split will interact again with the open part of the original dislocation and will recover the original FR source. The other part will continue to glide until it forms a ledge at the bottom surface of the sample (showed in Figure 4.20 (d)). Figure 4.20 (d) corresponds to the first minimum observed on the stress-train curve. At this stage, several dislocations are completely opened (or almost) and the instantaneous plastic strain is reduced. As a consequence, the applied stress increases. Several interactions need to be discussed at this stage. d1 represents the step explained in the last sentence of the previous paragraph. The occurrence of a junction and the split of two dislocations in slip systems $\frac{1}{2}[0\bar{1}1](111)$ (blue leaving traces at top and bottom) and $\frac{1}{2}[10\bar{1}](\bar{1}1\bar{1})$ is marked by d2. As the dislocation continues to glide, one part of the splitting outcome will generate a loop that will cancel the trace at the bottom of the sample signaled as d3.

Figure 4.20 (e) illustrates a similar situation than in the case of Figure 4.20 (b), but occurring here at a lower stress. Indeed, the process can still happen as the dislocations are more widely open here. The two red arrows identify the two dislocations that glide easily *i.e.*, one producing a huge amount of plastic strain triggering the correction of the applied stress. Also the region marked as e1 represents the cancelling of the trace created at the bottom surface (see Figure 4.20 (d) for reference) due to stress heterogeneities created by the red FR source opening nearby.

The snapshot of Figure 4.20 (f) shows the evolution of some dislocations with almost a linear shape (blue dislocations marked with red arrows). The slow glide of those dislocations produce a non significant amount of plasticity; leading to a re-increase of the applied stress. f1 shows the effect of the images forces acting to bend a dislocation near the cube faces.

In Figure 4.20 (g) is captured the moment where the applied stress decreases again. Similarly to previous situations, the two dislocations opening near the top left corner (marked with red arrows) are responsible for most of the plastic strain produced. However, the arms of the two dislocations ($\frac{1}{2}[10\bar{1}](111)$ in blue and $\frac{1}{2}[011](\bar{1}\bar{1}1)$ in red) dislocations, propagating through the traces of the bottom face, join and zip into a new junction (marked as g1). At the same time, this new dislocation acts as a pinning point; making a retard in the way the two FR sources glide. The way this two FR sources interact also trigger the glide of the dislocation marked as g2 ($\frac{1}{2}[0\bar{1}1](1\bar{1}\bar{1})$) that was not gliding before, and the respective trace can be seen in Figure 4.20 (h).

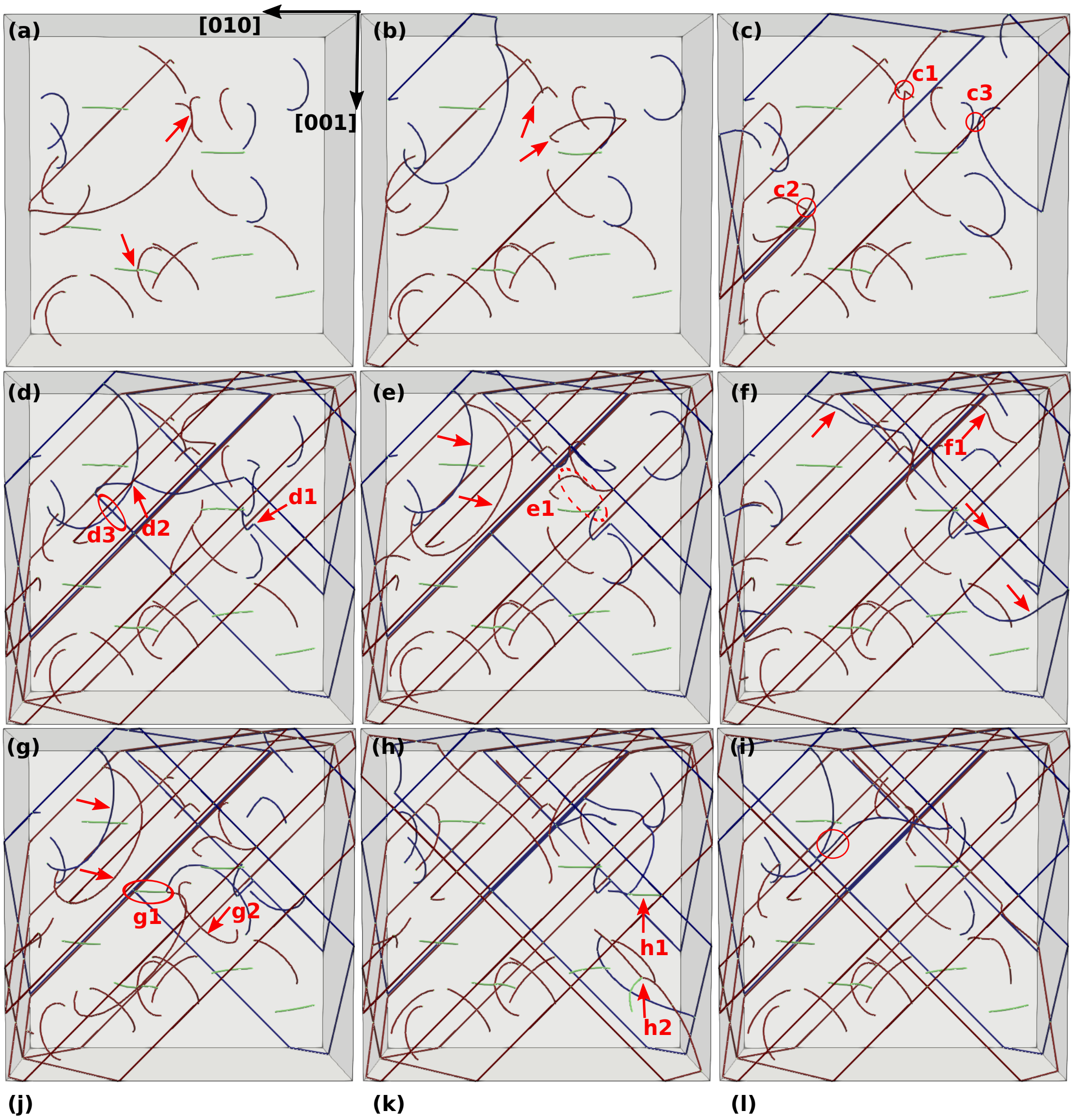

Figure 4.20: Snapshots of the simulation of a 0.5 µm thin film using a cutoff distance of 600 Å. The snapshots matches the marks on the stress-strain curve of Figure 4.19. The arrows and marks are used as guide to the description in the text. Dislocations are colored as follow: slip systems with index 5 and 11 are in blue, indices 2, 6 and 9 are in green and indices 1, 3, 4, 7, 8 and 10 are in red.

Another interaction is shown in Figure 4.20 (h). It is a consequence of the reunion of the arms of the red dislocation (previously marked in g1) gliding at the top face and interacting with the original $\frac{1}{2}[10\bar{1}](111)$ FR source (h1). This interaction brings the new zipped dislocation to the top surface, acting like a pin for the blue dislocation. In the other hand, h2 shows the interaction of the g2 dislocation with the non-mobile one in the bottom-right corner of the simulation cell. The variations observed after point (h) in the stress-strain curve are related to the cancelling of h1 and to the recovering of h2 dislocations. The minimum marked as (i) in the stress-strain curve is similar to the event described in Figure 4.20 (d). Almost all dislocations are in the initial stage, and only two glide, creating a small amount of plasticity that tends to increase the applied stress.

### 4.4.1 Numodis *vs.* El-Numodis: surface effects comparison

To better understand the effect of the surfaces on the plastic response of the thin film; the simulation performed with El-Numodis in the previous section is reproduced here using Numodis only. The aim is to check the differences regarding the method used when considering surfaces. At the moment, the surfaces can be considered using El-Numodis with or without the pseudo-mirror construction (just imposing the cutoff to zero) using the PermeableCuboid BCs where dislocations can escape the sample from the surfaces. Numodis also allows to account for surfaces relying on the pseudo-mirror construction and PermeableCuboid BCs. Using PermeableCuboid BCs in El-Numodis and setting a cutoff distance to zero; implies that the simulation will be performed using the traditional SPM (without the mirror dislocation method). In the other hand, using Numodis and PermeableCuboid BCs with cutoff distance equal to zero deactivates any surface effects in terms of stress *i.e.,* the surfaces only act as a penetrable interface, while increasing the cutoff distance activate the mirror dislocation method (and induced additional stress fields) in the DDD. The various cases are tested with the pseudo-mirror image method and a cutoff distances equal to 600 Å (C600) or without it (C0), as illustrated in Figure 4.21. The plastic responses of Numodis simulations are compared to those of El-Numodis with the same cutoff values in Figure 4.21 (a) (denoted as ElNumC0 and ElNumC600).

The stress-strain curve of NumC0 shows a larger yield stress when compared with the other three cases meaning that the surface-effect generated by the pseudo-mirror reconstruction in Numodis (NumC600) already induces the weakening of the sample. The same softening effect is observed in El-Numodis with and without the pseudo-mirror method (respectively ElNumC600 and ElNumC0). For El-Numodis simulations, the differences in the yield value is about 1 MPa and the rest of the plastic parts evolves almost identically. It confirms that turning the mirror dislocation method off is almost entirely compensated by the FEM correction in this case. The difference between those four simulations in terms

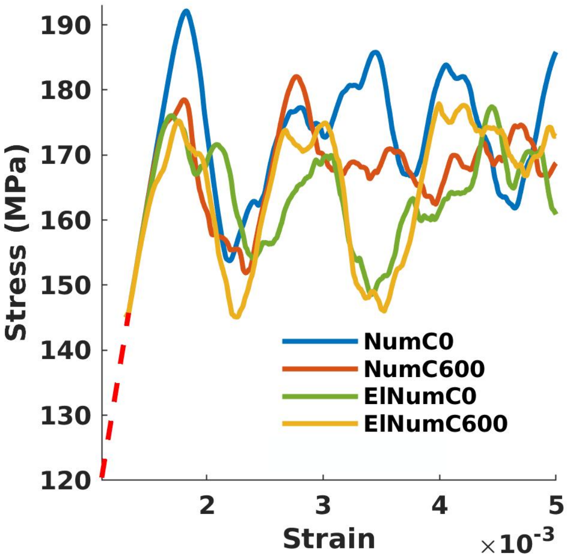

Figure 4.21: Stress-strain curves for a 0.5 µm thick thin film under tension using Numodis and El-Numodis with and without the pseudo-mirror image construction (NumC0/ElNumC0 from one side, NumC600/ElNumC600 from the other).

of dislocation evolution can be explained using dislocation miscrostructure snapshots at the yield point (Figure 4.22). For NumC0, the dislocations don't feel the surfaces and the stress inside the sample is considered to be homogeneous. Under such conditions, most of gliding dislocations are in high Schmid factor slip systems (Table 4.1 ). Quickly after yielding, two dislocations (labelled 1 and 2) make a junction that is not present in the other cases. Part of the dislocation 1 is observed to reach the plane (100) at $x = 0$. The dislocation labelled 3 widely opens due to the high stress and dislocation labelled 5 reaches the surfaces (001) at $z = 1$ and (100) at $x = 0$.

For NumC600 (Figure 4.22 (b)), surfaces tend to open faster dislocation 1 (responsible of the junction and zipping process mentioned for NumC0) that never reacts with the dislocation 2. For this simulation, the dislocation reaches both (100) and the (010) surfaces. Also, dislocation 5 (that is indeed the nearest to the surface) opens widely with respect to the previous Numodis simulation. This means that the plastic strain produced is already high and the feedback loop starts decreasing significantly the external stress at a smaller value compared to NumC0.

For ElNumC0, the dislocation 1 opens faster due to the action of the surfaces while dislocation 3 and 5 are less opened. It shows that the force exerted by the surface attracts some particular dislocations from the current microstructure while the rest may not feel such high attractive force. This effect is clearly seen in ElNumC600 sample were dislocation 4 opens with the help of surfaces (both the FEM action and the pseudo-mirror construction) while dislocation 5 is not felling any effect from the surface.

These test-cases show the influence of surfaces in small-scale objects. The stress-strain

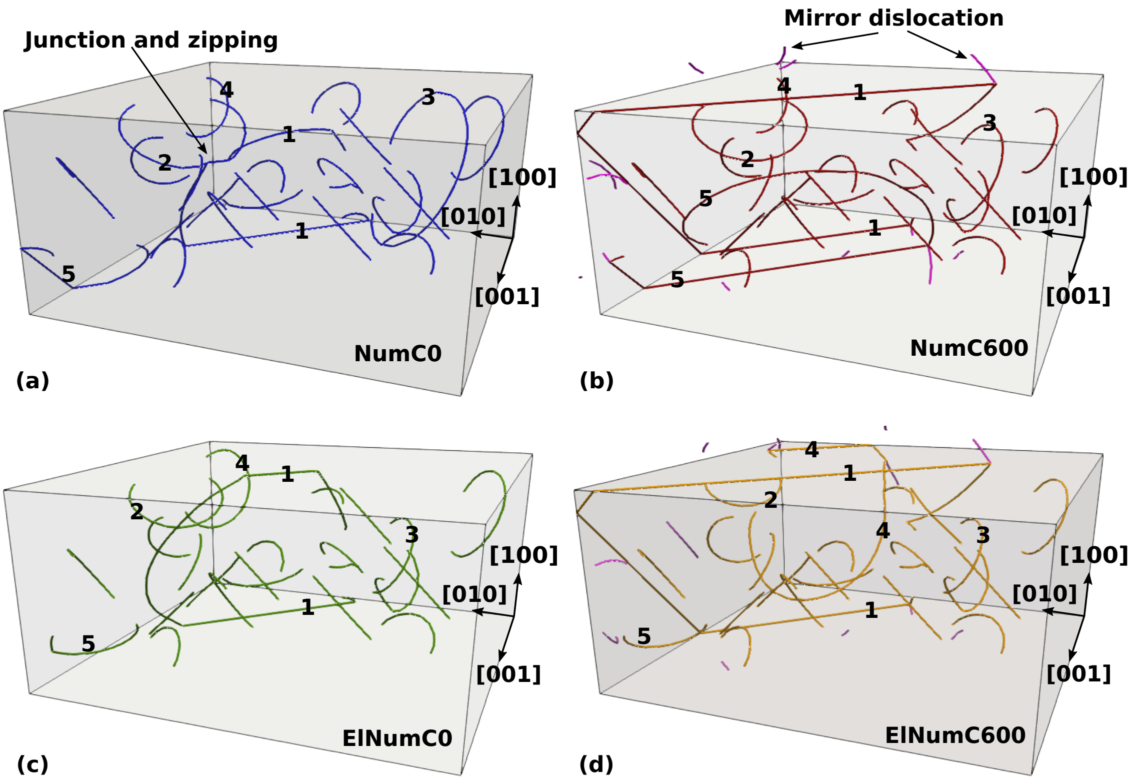

Figure 4.22: Evolution of the dislocation microstructure at the yield point for NumC0 (a), NumC600 (b), ElNumC0 (c) and ElNumC600 (d). The pink dislocations represent mirrored dislocation constructed with a cutoff of 600 Å. The most important dislocations are identified with number labels.

curves shows that the microstructure react to different stress situations during all the simulations. NumC0 and ElNumC600 have both different yield stress values but the flow stress seems to stabilizes almost at the same stress range about 170 MPa meaning that here, at larger strains, the flow stress is controlled by the bulk rather than the surfaces (in the contrary to the yield point). Besides, the mechanical response provided by NumC600 looks pretty similar to those generated by El-Numodis.

For this specific setup; using El-Numodis with or without the construction of a pseudo-mirror dislocation is almost equivalent: the influence of the pseudo-mirror method being compensated by the sole FEM contribution, and the few differences observed in the microstructural evolution might be related to the mesh density. In the same way, NumC600 provides almost the same results compared to those obtained with El-Numodis confirming that the pseudo-mirror dislocation method and FEM can compensate each other when relying on the effects of surfaces. Also, in this specific case, we have to admit the moderate influence of surfaces. To further investigate it at the nanoscale, we proceed with a thinner film of 0.25 µm thickness (Figure 4.23) with similar properties except a fresh random dislocation distribution made of similar FR sources (Figure 4.24).

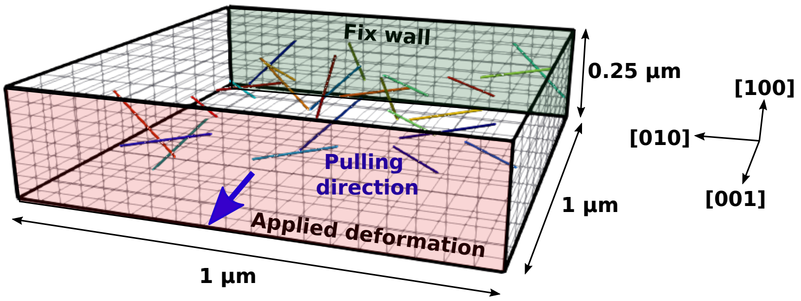

Figure 4.23: El-Numodis thin film of 0.25 µm thickness and 1.0 µm lateral size with cubic orientation in which FR sources are randomly distributed in various $\frac{1}{2}\langle 110\rangle\{111\}$ slip systems. Traction BCs are applied on the (001) lateral surface.

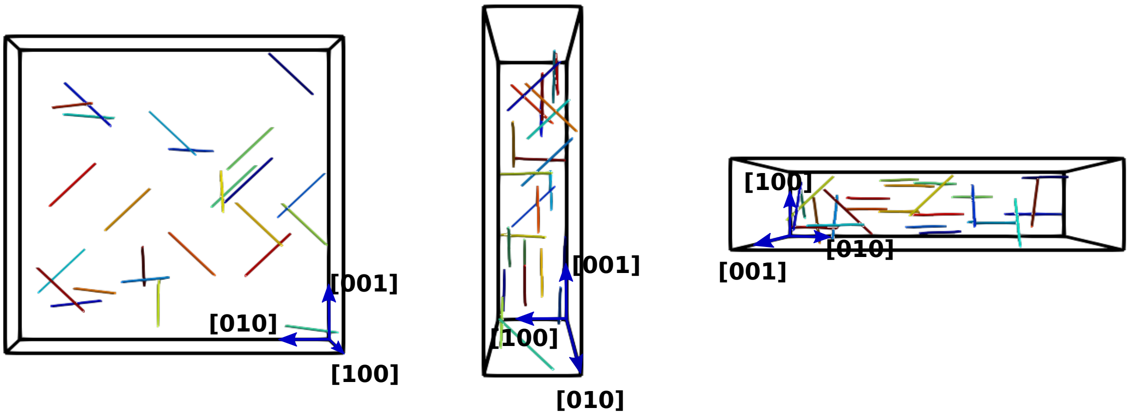

Figure 4.24: View of the initial dislocation microstructure in the 0.25 µm thick thin film from three different angles. The initial screw character FR sources are randomly generated to avoid interception between the dislocations and the surfaces.

The stress-strain curves for the 0.25 µm thick thin film is shown in Figure 4.25 for NumC0 and ElNumC600 samples (with same denomination as in the previous case). The pure DDD simulation exhibits a higher yield stress when compared to El-Numodis (196 and 175 MPa, respectively) and, overall, a harder mechanical response all along the simulation. When compared with the 0.5 µm thickness sample, two aspects can be noticed. First, the yield point differences between NumC0 and ElNumC600 increases from 17 MPa in the thicker film to 19 MPa in the thinner one. Also, stress-strain curves do not cross or superimpose each other anymore and the flow stress are now significantly different. Here, surfaces in El-Numodis behave as sinks that help the opening of the FR sources towards the surfaces in a similar way that in the aforementioned TEM lamella case [KOH 20].

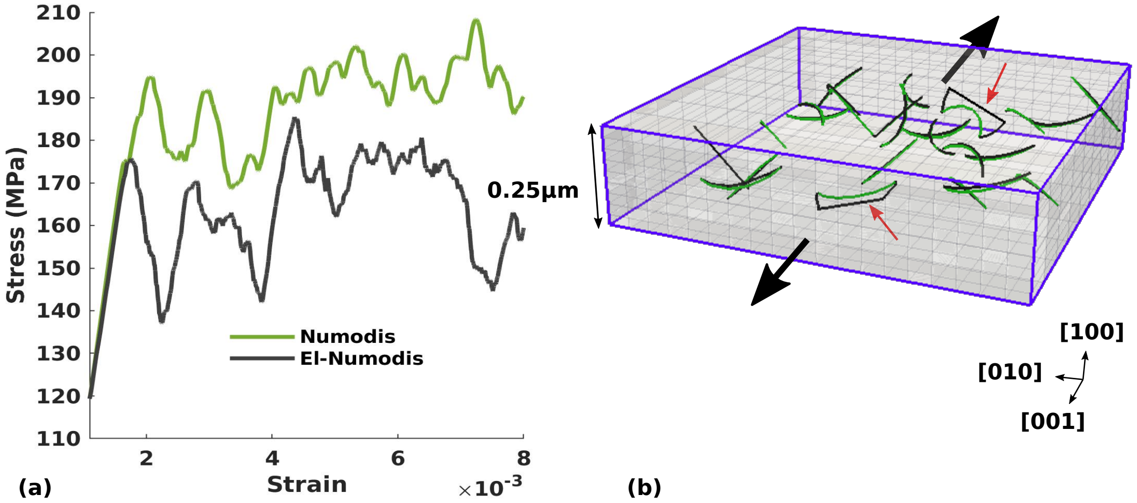

Figure 4.25: Deformation of the 0.25 µm thick thin film under tension using Numodis and El-Numodis using the pseudo-mirror image construction in El-Numodis simulation only with a cutoff of 600 Å. (a) stress-strain curves, (b) dislocation microstructure at the yield point.

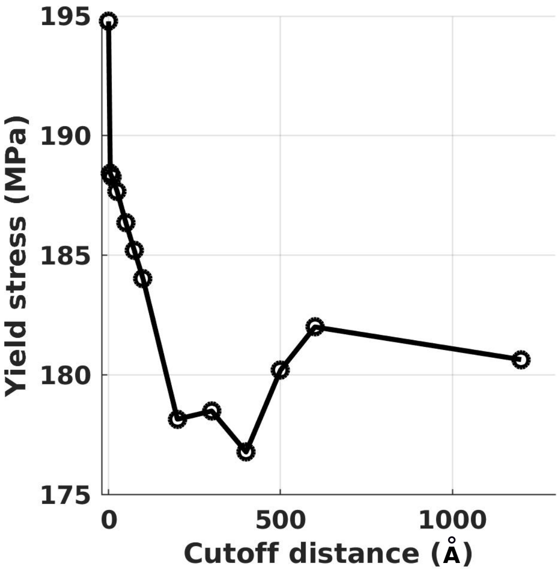

Figure 4.26: Yield stress as a function of the cutoff distance for the 0.25 µm thin film.

Finally, using the same simulation setup using the 0.25 µm thickness thin film, we have investigated the effect of the cutoff radius of the pseudo-mirror dislocation method for Numodis. Overall, the yield point tend to decrease when increasing the cutoff distance. A sensible reduction is observed for cutoff in the range from 0 to 450 Å. For higher values the yield stress tend to reincrease a little (Figure 4.26). This behavior is associated to the distance of influence of the stress produced by the virtual dislocation constructed at the external surface. Indeed, a small cutoff distance implies that the pseudo-mirror dislocations will be of small size and will appear at small distance from surfaces. In the other hand, when large cutoff values are used, the effect of the pseudo-mirror dislocations can reach distances deep in the sample and their effects may be detected early in the simulation. A preliminary study was also performed with El-Numodis, and a different situation was observed. A cutoff distance between 5 to 100 Å keeps the yield point approximately at the same value of of 157 MPa, the sole FEM compensating the pseudo-mirror method in computing the image stress. Increasing the cutoff over this range promotes oscillations of the yield point. It is important to mention that this study was done using the same regular coarse mesh of the previous test. As a consequences, the oscillation observed may be an indication that the cutoff distance (for El-Numodis) may be dependent of the quality and type of mesh used by the FEM. Additional simulations including several mesh distributions should be performed to provide a more detailed description of the pseudo-mirror dislocation cutoff on the yield stress.

## 4.5 Conclusion

In this chapter, El-Numodis was tested to reproduce the self-stress of infinite edge and screw dislocations reproducing satisfactorily the analytical solutions proposed by Cai [CAI 06]. The theory of mirror dislocation was explored using the formulation found in [HIR 82] for the cases of infinite dislocations showing that, at least, one component of the stress tensor was not cancelled at surface where stress-free conditions were applied. The remaining components have shown to vanish depending on the orientation of the slip system with respect to the free-surface. The introduction of Airy functions allows to reach stress-free conditions by canceling the shear and normal stress components over a surface. After implementation of the Weygand method for mirror dislocation [WEY 02], El-Numodis was used to investigate infinite dislocation *vs.* surface interactions. The results have shown that, when relying on a refined mesh, El-Numodis provided the same results than the theory, reproducing the image stress whether or not the pseudo-mirror dislocation construction is used. However, different results were obtained in the case of coarser meshes. To improve the results, we can think about a dynamically refinement of the mesh in regions where the dislocation interacts with the free-surface. Such refinement conditions need a detection algorithm and a refinement protocol that are out of the scope of the present study. When a coarse mesh is used, the SPM with pseudo-mirror dislocations provides better results than the traditional case. This is an important point to account since the computational costs of the FEM is strictly depending of the number of element in the simulation box. Having the pseudo-mirror method allows to use coarser meshes without degrading the quality of the image stress at acceptable computational costs. The differences found between the theory and El-Numodis were associated to the construction of the infinite dislocation that implies apparition of residual stresses in the lateral faces of the half-infinite space, this directly affecting the reduction of the stress at the free-surface.

In the more realistic case of a finite dislocation loop, El-Numodis was compared to the analytical line integral method of GW. In this case, the errors associated to the interaction of the dislocation with the stress-free-surfaces (like in the infinite edge test case) of the half-infinite space were avoided. A regular mesh was first used leading to an image stress that shows some differences regarding the analytical results due to element discretization. Such effect was corrected by refining the mesh near the free-surface. Using the same configuration the loop was put at a nearest distance of the free-surface in order to induce stress values in the order of 10 to 20 MPa in the free-surface where El-Numodis has again proved its ability to solve the BVP. Finally, we have investigated thin films under tension. Thin films with two different thickness were tested using El-Numodis to simulate the effect of surfaces as compared to pure DDD simulations. Surfaces were introduced in three ways: by pseudo-mirror reconstruction of the image dislocation, by coupling with Elmer using the SPM and by a combination of the two methods. Results show that surfaces induce a weakening of the sample yield stress. Within the thinner film, the differences with and without surface effects have shown to increase. Increasing the cutoff distance of the pseudo-mirror image dislocation construction reduces the yield stress (at least in standalone Numodis) but further studies should be made in order to identify the optimal cutoff value. For El-Numodis, the impact of the cutoff distance is dependent of the mesh quality. Further studies with different mesh refinement are necessary in order to have a complete description of the impact of the pseudo-mirror construction on the mechanical response.

## Chapter 4: to remember

- The superposition method as implemented in El-Numodis provides a correct description of the traction-free boundary conditions.
- Using the pseudo-mirror dislocation constructions allows for an accurate image stress evaluation when coarse mesh are used.
- The image forces computed by El-Numodis for the infinite dislocation and the square loop test-cases embedded in a half-infinite space correctly reproduce the analytical solutions (found in Hirth and Lothe book, Gosling-Willis models, respectively).
- The control tests performed during thin films deformation simulations ensures the correct implementation of the loading algorithm.
- For thin films under traction accounting for surfaces using the superposition method and the pseudo-mirror image dislocation method, both tend to weaken the sample.
- Increasing the cutoff of the pseudo-mirror image dislocation method decreases the yield stress in discrete dislocation dynamics simulations.

# Chapter 5

# Compression of MgO nanoparticles

Surface dislocation nucleation plays a key role in the deformation of originally defect-free nanoparticles and the prevalence of surface effects can not be neglected when modeling deformation at the nanoscale. With El-Numodis, the effect of surfaces is accounted using the superposition method. However a methodology is needed to run simulations without initial dislocation microstructure. For this purpose, we developed a new approach allowing heterogeneous (or homogeneous) dislocation nucleation based on site activation energies using kinetic Monte-Carlo and the transition state theory.

The chapter starts with a description of the relevant equations for the transition state theory when applied to dislocation nucleation. Then, two dislocation nucleation algorithms implemented in El-Numodis are presented. First, a *simplified* algorithm that helped us to familiarize with the approach and the transition state theory is proposed. The second *extended* approach is more quantitative and opens the route to the comparison with molecular dynamics nanocompression simulation recently performed on MgO nanocubes. Using activation energies and dislocation radii data (computed using a multi-step nudged elastic band approach by Amodeo *et al.*[AMO 21a]) as El-Numodis inputs and the superposition method, we have been able to reproduce and interpret at the mesoscale dislocation nucleation events observed in previous molecular dynamics simulations [ISS 15]. In particular, here we give a close look to the influence of temperature, strain rate and sample size on the evolution of the dislocation microstructure.

This study provides a first attempt of El-Numodis capabilities when applied to model nanomechanical tests in real conditions of deformation.

**Contents**

**5.1 Introduction to dislocation nucleation and harmonic transition state theory . . . . . . . . . . . . . . . . . . . . . . . . . . . . . . . . . . . . . 104**

**5.2 Dislocation nucleation in El-Numodis . . . . . . . . . . . . . . . . . 106**

5.2.1 Simplified approach (constant stress) . . . . . . . . . . . . . . . . . . . . . 106

5.2.2 Extended approach: application to MgO nanoparticles . . . . . . . . . 114

**5.3 Mesoscale modeling of dislocation nucleation in MgO nanoparticles under compression . . . . . . . . . . . . . . . . . . . . . . . . . . 122**

5.3.1 Deformation at extreme strain rate . . . . . . . . . . . . . . . . . . . . . . 122

5.3.2 Towards experimental conditions of deformation . . . . . . . . . . . . 127

**5.4 Conclusion . . . . . . . . . . . . . . . . . . . . . . . . . . . . . . . . . 137**

## 5.1 Introduction to dislocation nucleation and harmonic transition state theory

At the nanoscale, dislocation nucleation plays an important role in incipient plastic deformation of crystals. Both continuous and atomistic models were used to investigate dislocation nucleation [ZHU 08, JEN 11a, RYU 11, MOR 11, GOD 04, AMO 17, ROY 19, LEE 20]. Limitations arises in the uses of continuous models based on the size of the critical dislocation nucleus, that can be comparable to few lattice parameters. Moreover, continuous models are mostly based on linear elasticity, while nucleation process occurs at high local and global strains, where the stress-strain relation is non linear anymore. MD does not include such limitations and is used to reveal important details about nucleation. Unfortunately the time scale of MD is typically in the order of few nanoseconds (with time steps in the femtosecond) what makes it limited to extremely high strain-rate about 10 orders of magnitude larger than classical experimental strain rates. Modeling dislocation nucleation as a function of stress and temperature under experimental conditions of deformation is thus still a major challenge. An alternative approach, is to combine reaction rate theories with atomistic models. Atomistic simulations such as the NEB approach [HAN 98, HEN 00] can be used to compute the activation barrier, which is further used within the reaction rate theory to predict the dislocation nucleation rate. The mathematical treatment described in the following can be found in [ZHU 08, JEN 11b, RYU 11]. Both the TST or the Becker-Doring theory provide an expression for the nucleation rate at constant stress $\sigma$ and temperature $T$,

$$\nu = N\nu_0 \exp\left[-\frac{\Delta G(\sigma, T)}{k_B T}\right] \tag{5.1}$$

with $N$ the number nucleation sites, $\nu_0$ is an attempt frequency considered in the range of the Debye frequency, $\Delta G$ is the activation free energy for a nucleation, $k_BT$ is the thermal energy therm (with $k_B$ the Boltzmann constant).

To find an expression as function of the constant applied strain rate loading such as $\dot{\sigma} = E\dot{\epsilon}$, the derivative of equation 5.1 is calculated:

$$\frac{d\nu}{d\sigma} = \frac{\nu \Omega_0}{k_BT} \tag{5.2}$$

where $\Omega_0 = -\frac{\partial \Delta G_0(\sigma)}{\partial \sigma}$ is known as the activation volume. Following the development explained in [GUZ 16] is possible to write $\frac{d\nu}{d\sigma} = -\frac{\nu^2}{\dot{\sigma}}$. Combining the last formula with equation 5.2 and the definition of the strain rate; an adequate expression for constant applied strain rate results as:

$$\frac{\Delta G(\sigma, T)}{k_BT} = \ln \frac{k_BTN\nu_0}{E\dot{\epsilon}\Omega(\sigma, T)} \tag{5.3}$$

In a first approximation the effect of the temperature on the activation free energy, one can write:

$$\Delta G = \Delta G_0(\sigma)(1 - \frac{T}{T_m}) \tag{5.4}$$

with $T_m$ the surface disordering temperature and $\Delta G_0(\sigma)$ the activation energy on the zero temperature potential energy surface. Thus, the activation volume becomes,

$$\Omega(\sigma, T) = (1 - \frac{T}{T_m})\Omega_0(\sigma) \tag{5.5}$$

Considering known the activation volume $\widehat{\Omega}$ at a given stress $\hat{\sigma}$; an expression for the activation energy near $\hat{\sigma}$ can be define linearly in the form $\Delta G_0(\sigma) = \Delta G_0^* - \sigma\widehat{\Omega}$ [1], with the nucleation barrier in the absence of applied stress defined as: $\Delta G_0^* = \Delta G_0(\sigma) + \hat{\sigma}\widehat{\Omega}$ [ZHU 08]. Thus, the nucleation stress $\sigma$ as a function of the strain rate is:

$$\sigma = \sigma_{\text{athermal}} - \frac{k_BT}{\Omega} \ln \frac{k_BTN\nu_0}{E\dot{\epsilon}\Omega} \tag{5.6}$$

with the athermal nucleation stress defined as $\sigma_{\text{athermal}} = \frac{\Delta G_0^*(\sigma)}{\widehat{\Omega}}$ representing the stress required to nucleate a dislocation at zero temperature. This kind of approach requires to determine the activation parameters $(\Delta G_0^*, \widehat{\Omega})$ related to a given nucleation site [ZHU 08, RYU 11]. Equations 5.1 to 5.6 are here provided using global notations while most of the variables introduced can be locally defined at a nucleation site $i$. This includes *e.g.,* $\nu_i$

---

[1] This expression is equivalent to $\Delta G_0(\sigma) = \Delta G_0(\hat{\sigma}) - \widehat{\Omega}(\sigma - \hat{\sigma})$

and $\nu_{0,i}$, $\Delta G_i$ and $\Delta G_{0,i}$, $\sigma_i$ or even $T_i$. Both notations will be used in the following.

Afterwards, the previous theoretical description is combined to a statistical approach in order to develop two nucleation models usable in DDD/FEM simulations. The first one is a simplified approach that accounts for constant stress where three nucleation sites are selected based on a temperature-dependent kinetic Monte-Carlo (KMC) scheme. Computational conditions are assigned to each nucleation site in order to avoid instantaneous repetitive nucleation events at the same site *i.e.*, a site where a dislocation just nucleated is not accounted anymore for a certain time. The method is applied to a copper cuboid sample used here as a test-case. The second model is more complex and accounts for a database for dislocation nucleation activation energy computed using a multi-step NEB approach by Amodeo *et al.* for MgO nanocubes where the local stress controls the availability of the nucleation sites [AMO 21a].

## 5.2 Dislocation nucleation in El-Numodis

### 5.2.1 Simplified approach (constant stress)

The dislocation nucleation period $\delta t_{KMC}$ is defined as a function of the nucleation rate per site $\nu_i$:

$$\delta t_{KMC} = \frac{1}{\sum_i \nu_i} \tag{5.7}$$

where $i$ relies on each nucleation site. Thus, the probability for a dislocation to nucleate at site $i$ during time $\delta t_{KMC}$ is computed as:

$$S_i = \nu_i.\delta t_{KMC} \tag{5.8}$$

In the following, we investigate the role of $T$ within the aforementioned nucleation theory at constant stress *i.e.,* assuming constant $\Delta G_{0,i}$. For that purpose, we design a virtual cuboid sample of size $500 \times 500 \times 500$ nm$^3$ made of FCC copper ($\lambda = 77.3$ GPa, $\mu = 42.0$ GPa, $\nu = 0.324$). Activation energies for surface dislocation nucleation $\Delta G_{0,i}$ are roughly similar to those commonly reported for FCC metals are used (see Table 5.1). Three nucleation sites are defined and the local nucleation rate $\nu_i$ is computed using a per-site version of equation 5.1 and a constant activation energy per site $\Delta G_{0,i}$. In Table 5.1, the larger value corresponds to a nucleation site located in the middle of a lateral face ($s$) of the cubic sample. Two sites with the same activation energy are introduced at the two distinct corners of the cube ($c1$ and $c2$) considering $\nu_0 = 3.14 \times 10^{13}$ s$^{-1}$ and a constant $T_m = 700$ K. Equation 5.8 provides the nucleation probability for each nucleation site $i$, and satisfies the condition: $\sum S_i = 1$. It means that each site has a “window of opportunity" in a cumulative probability array that is selected using KMC.

Table 5.1: Parameters used for dislocation nucleation investigations at constant stress. Two sites are available for dislocation nucleation from corners ($c1$ and $c2$) and one from a surface center ($s$). The dislocation critical radius $r_c$ is imposed to 200 Å whatever the nucleation site. The nucleation coordinates $x_{pos}$, $y_{pos}$ and $z_{pos}$ are normalized by the sample size.

| Site | $\Delta G_{0,i}$ (eV) | $r_c$(Å) | $x_{pos}$ | $y_{pos}$ | $z_{pos}$ |
|---|---|---|---|---|---|
| $c1$ | 0.2 | 200.0 | 0.0 | 0.0 | 1.0 |
| $c2$ | 0.2 | 200.0 | 0.0 | 1.0 | 1.0 |
| $s$ | 0.5 | 200.0 | 1.0 | 0.5 | 0.5 |

During the nucleation process, uniformly distributed random numbers (URNs) are generated to pick one of the nucleation site at $T = 250$ and 650 K.

#### 5.2.1.1 Post-nucleation site shutdown

In real experiments, a dislocation nucleation event changes the local stress landscape and, as a consequence, the local nucleation probability is modified *on-the-fly.* Dislocation nucleation induces stress relaxation and if other similar nucleation site are available, it becomes probable that a subsequent nucleation event will take place from another favorable site (large local stress, low $\Delta G_i$). In the simplified nucleation approach, we assume that this process is equivalent to the temporary shutdown of the original nucleation site. In the following, we apply this reasoning to the previous case. Results are shown in Figure 5.1. On the one hand, when a dislocation nucleates from a site *e.g.,* the site $s$, we cancel it from the available site list and makes it unavailable for a subsequent SDN event. So, the probability distribution is changed to 50 % for the $c1$ or $c2$ remaining sites, both being characterized by the same activation energy (Figure 5.1 (b)). In the other hand; if $c1$ is chosen first, the probability distribution increases for both $c2$ and $s$ of the same relative amount. The trivial case where only one site remains available is obtained when a second KMC call is performed from any of the previous two situations. In this approach, the site shutdown period is a crucial parameter that can be set to 1 or few timesteps.

#### 5.2.1.2 Algorithm and implementation

$\nu_i$ and $\Delta G_i$ expressions as derived from Equations 5.1 and 5.4 were implemented in El-Numodis and the workflow of the SDN simplified approach is described in Figure 5.2. The nucleation algorithm is executed at the beginning of the *NumodisExportStress* routine (see El-Numodis main algorithm in section 3.2.2). It is called at each timestep of the simulation. where, depending on the temperature and $\delta t_{DDD}$, two possible scenarios can happen leading to a single or multiple KMC calls during a DDD simulation step $\delta t_{DDD}$.

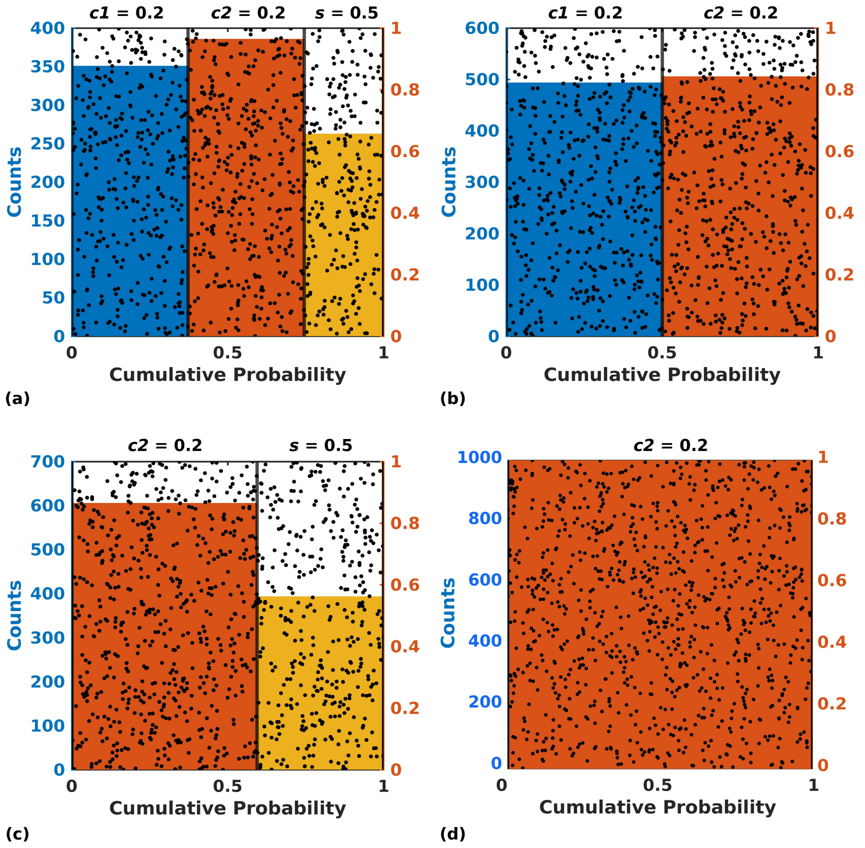

Figure 5.1: Consecutive SDN events (simplified approach). Black dots are 1000 URN generated in [0,1]. The color bars represents the amount of dots inside each region. (a) Initial conditions, (b) after turning off site $s$, or (c) after turning off site $c1$. The same results are obtained if $c2$ is turned off instead $c1$, (d) after turning off site consecutively $c1$ and $s$. Right orange axis is used only to facilitate the black dots plots.

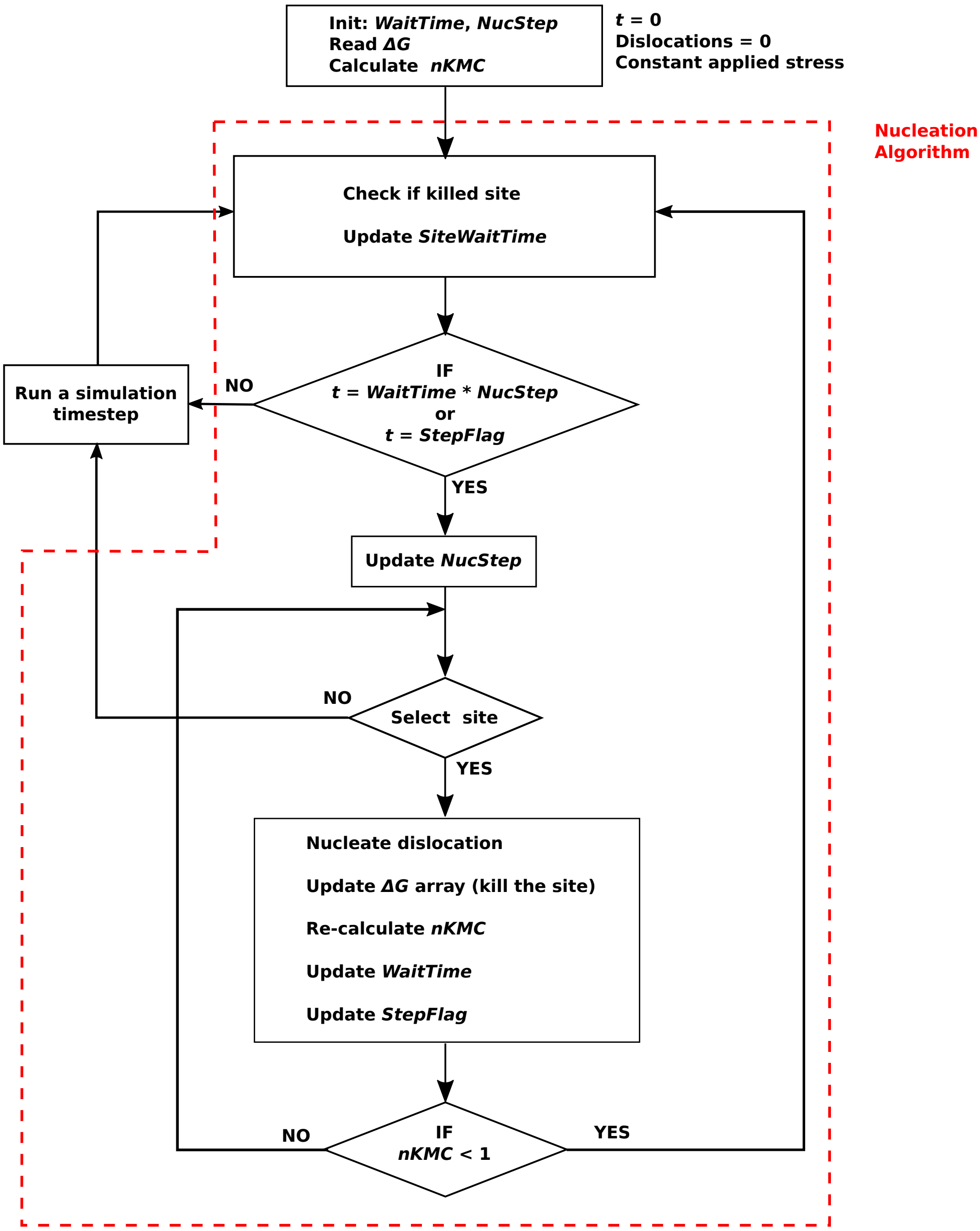
Init: WaitTime, NucStep
Read ΔG
Calculate nKMC
t = 0
Dislocations = 0
Constant applied stress
Nucleation Algorithm
Check if killed site
Update SiteWaitTime
IF
t = WaitTime * NucStep
or
t = StepFlag
NO
Run a simulation timestep
YES
Update NucStep
NO
Select site
YES
Nucleate dislocation
Update ΔG array (kill the site)
Re-calculate nKMC
Update WaitTime
Update StepFlag
NO
IF
nKMC < 1
YES

Figure 5.2: Simplified (constant stress) dislocation nucleation algorithm workflow.

The nucleation algorithm is able to read an external database, store the variables into one dimensional arrays and update control parameters. During the execution of El-Numodis, the nucleation algorithm is called for the first time (at $t = 0$) to read the external database containing nucleation parameters as *e.g.,* those in Table 5.1. The number of KMC calls per DDD step $nKMC$ is provided by :

$$nKMC = \frac{\delta t_{DDD}}{\delta t_{KMC}} \tag{5.9}$$

where $\delta t_{KMC}$ is given by equation 5.7. Here is a list of important variables and parameters for the simplified nucleation algorithm:

- *WaitTime* is a per-site parameter that the refers to the shutdown period of a site (*e.g.,* 60 steps)
- *SiteWaitTime* is an array that contents the remaining number of steps left all the sites remain shutdown (*e.g.,* 60 - $n$ where $n$ is an elapsed number of steps)
- *NucStep* is a control variable that is increased by 1 every time you have a nucleation event.
- *StepFlag* is the KMC call frequency *i.e.,* $\frac{1}{nKMC}$

All these variables are first initiated at $t = 0$. After $t = 0$, the nucleation algorithm checks if a site is available for dislocation nucleation or not. Then, the nucleation algorithm is called in the two following cases. First is when the number of simulation steps reaches initial *WaitTime* or $NucStep \times WaitTime$, *NucStep* behaving like a counter increased by one (update *NucStep* every time a nucleation event is performed). Second is when the regular nucleation frequency of the system $StepFlag = \frac{1}{nKMC}$ is reached. Once the simulation reaches any of the two values *WaitTime* × *NucStep* or *StepFlag*, a KMC call is performed and the value of *nKMC* is recomputed. After a nucleation event, a site is shutdown by momentarily increasing its activation energy $\Delta G_{0,i}$ by a factor 20 (inside the $\Delta G_0$ array) once the corresponding site has been selected for nucleation. Then, the *SiteWaitTime* array is updated after each step. This process precludes from immediate nucleation events at same site and allows the dislocation to glide during *WaitTime* El-Numodis timesteps. This process is repeated within the same El-Numodis timestep during the whole time *nKMC* remains larger than 1. Once $nKMC < 1$, El-Numodis steps out of the dislocation nucleation loop and continues with its usual workflow. This process is repeated every El-Numodis timestep.

In summary, the simplified dislocation nucleation approach relies on the variables *WaitTime* and *StepFlag* that embody the competition between the regular nucleation frequency imposed by the system and the possible reactivation of shutdown nucleation sites that updates the number of KCM calls per DDD timestep *nKMC* each time a dislocation nucleation event happens.

#### 5.2.1.3 Applications

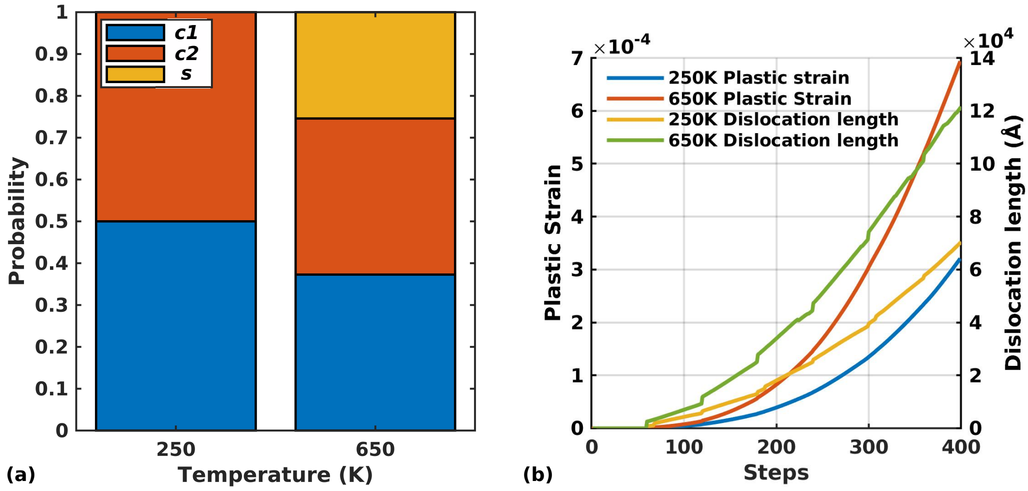

Figure 5.3: Dislocation nucleation simulation (simplified approach) in a Cu cuboid deformed at 1 GPa applied stress and at $T =$ 250 and 650 K, (a) cumulative probability computed at corners ($c1$ and $c2$) and mid-surface ($s$) sites, (b) Plastic strain (blue and red) and dislocation length (yellow and green) computed a *WaitTime* $=$ 60 steps.

Here again we use our simulation framework made of a copper cuboid sample with the three nucleation sites described in Table 5.1 using normalized coordinates. In this example, dislocation nucleation is restricted to surfaces (heterogeneous case) where quarter and half dislocation loops can nucleate from corners/vertical edges and surfaces/horizontal edges respectively, propagating into the sole $\frac{1}{2}[\bar{1}01](111)$ slip system[2]. The sample is meshed with regular eight nodes hexahedrons and the BVP stress correction is performed by Elmer only (no pseudo-mirror dislocation construction used). Compression simulations are performed at temperatures of 250 and 650 K under a constant applied stress of 1 GPa and $T_m =$ 700 K. *WaitTime* is set to 60 steps and $\delta t_{DDD} = 0.05$ ns. Figure 5.3 (a) shows the initial dislocation nucleation probability per site (*i.e.,* without site off) for both temperatures as computed using equation 5.1. As shown in Figure 5.4, SDN can only happen from the two corners sites at $T = 250$ K. The probability calculated for $c1$ and $c2$ are both about $S_{c1,c2} \sim 0.5$ while $S_s = 6.47 \times 10^{-5}$ *i.e.,* there is no chance to observe dislocation emitted from site $s$ in this case, as confirmed by simulation snapshots shown in Figure 5.4.

Figure 5.4 shows again the competition between the *WaitTime* and *StepFlag* variables. The first nucleation event occurs at *WaitTime* $=$ 60 and at site $c1$ (blue point), selected randomly by the KMC among the 3 available sites. At this stage, the recalculation of *nKMC* provides a value smaller than zero, what precludes additional nucleation attempts during the current timestep. Moreover, the calculation of *StepFlag* shows that the next nucleation event should take place after eight steps, as it is shown in Figure 5.4 (b). This nucleation event takes place compulsory at site $c2$ (red point), as the probability of nucleation at site $s$ is still small for low-T and the site $c1$ is shutdown for a number of steps equal to *WaitTime* since the first nucleation event. Then, nucleation periodically happens and the $c$ sites alternate continuously with nucleation events every each 60 steps (Figure 5.4 (a, c, d, f, g, i)); with a second attempt after 8 steps (Figure 5.4 (b, e, h)). Figure 5.3 (b) shows the evolution of the plastic strain and the dislocation density evolution as function of the simulation step from which dislocation nucleation events can be identified by the hints on the dislocation density curves.

---

[2] Note that homogeneous dislocation nucleation was also developed in the context of this study based on the nucleation of dislocation loops, using the same strategy than the one applied for the heterogeneous case.

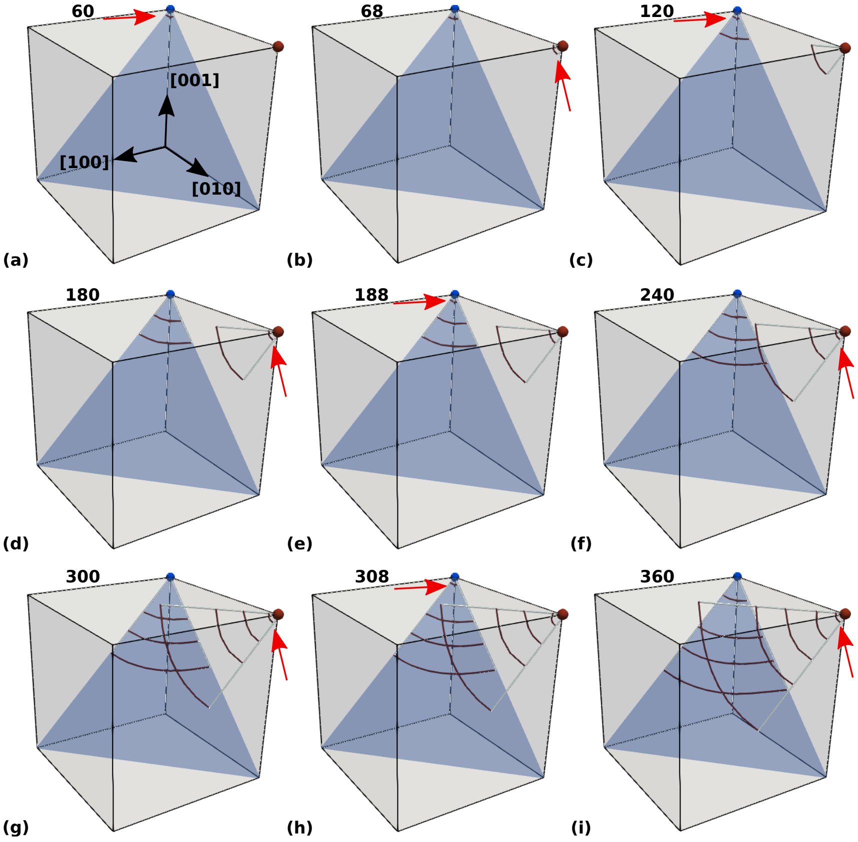

Figure 5.4: Dislocation nucleation at the surface of copper cuboid under compression using El-Numodis at low temperature (250 K). Dislocation quarter loops are nucleated from the two predefined nucleation sites at corners ($c1$ and $c2$, respectively blue and brown dots). Red arrows illustrate particular features commented in the text. The number at the top of each sub-figure relies on the simulation step.

As expected from the TST, nucleation at site $s$ is observed at higher temperature *i.e.,* at $T = 650$ K, where $S_{c1,c2} = 0.37$ and $S_s = 0.26$. Simulation results are illustrated in

Figure 5.5. At $T = 650$ K, the first nucleation event occurs after 60 steps as conditioned by *WaitTime*. At this temperature, the nucleation probability at site $s$ increases and nucleation becomes favorable (Figure 5.5). After the first and second nucleation attempts, *nKMC* remains >1. It only starts to decrease once the three sites have been requisitioned at least once for dislocation nucleation. Dislocation nucleation from the three sites occurs every 60 steps during the whole simulation as shown in Figure 5.5. Raising the temperature here does not just increase the nucleation probability at site $s$ but also the nucleation rate. Also, this simple toy simulation with a simplified nucleation algorithm already shows some particular features as the displacement of the dislocation embryo near site $s$ (Figure 5.5 (d)) leading to the collapse of the dislocation (Figure 5.5 (d,e)). Also, the dislocation nucleated at site $s$ at step 300 asymmetries rather than opening in a circular fashion and drifts along the surface along the $[0\bar{1}1]$ direction. At step 360, a new nucleation event from site $s$ leads to the merging (annihilation/recombination) of the previous two dislocations.

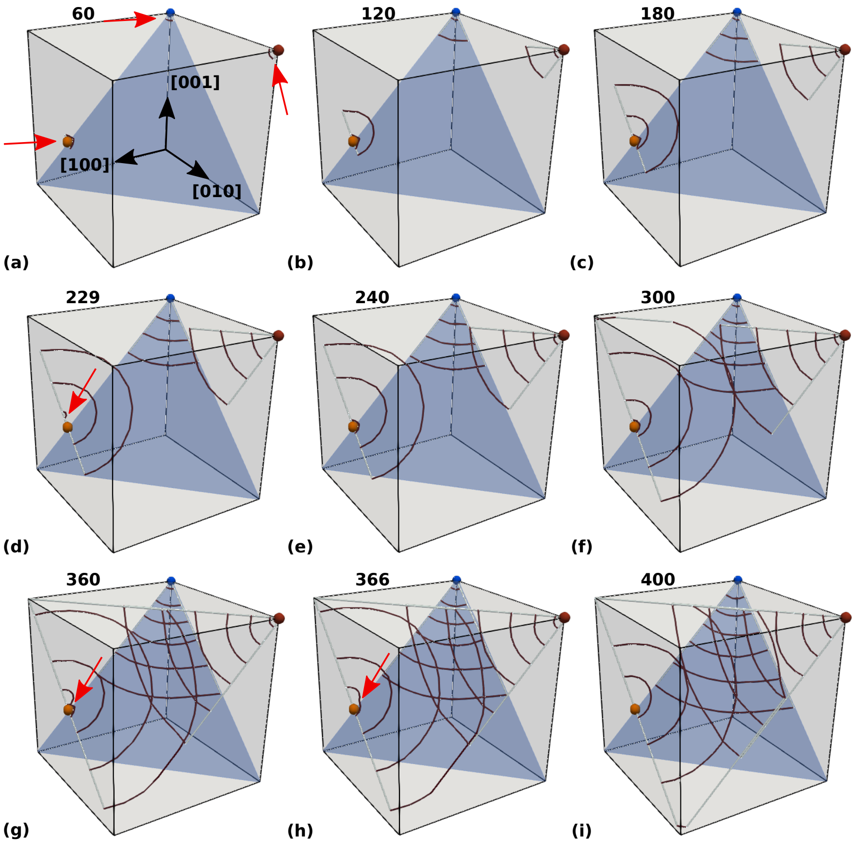

Figure 5.5: Dislocation nucleation at the surface of copper cuboid under compression using El-Numodis at high temperature (650 K). Quarter dislocation loops are nucleated from predefined nucleation sites at corners ($c1$ and $c2$, respectively blue and brown dots), half-loops are nucleated at site $s$ (orange dot).

### 5.2.2 Extended approach: application to MgO nanoparticles

In the rest of the PhD manuscript, we use El-Numodis to model dislocation nucleation during MgO nanoparticle deformation under compression. For that purpose, we built an extended version of the nucleation algorithm especially designed for constant strain rate simulations. One of the specificity of the extended dislocation nucleation algorithm is that it can integrate $\Delta G_{0,i}$ SDN databases, computed for MgO NPs at the atomic scale by Amodeo *et al.* [AMO 21a]. In this section, we first introduce the work of Amodeo *et al.* where the problem is investigated at the atomic scale before describing the extended dislocation nucleation algorithm.

#### 5.2.2.1 Introduction to atomic-scale dislocation nucleation in MgO nanoparticles

As already emphasized in the work of Issa *et al.*, the extremely high strength of ceramic nanocrystals under compression arises from the necessity to nucleate highly energetic dislocations, presumably from the sample surfaces [ISS 15]. Nevertheless, the work of Issa *et al.* focusing on MgO NPs under compression is marked by the difference of several orders of magnitude between experimental and MD strain rates (see Chapter 1 for more details). To bypass MD limitations, Amodeo *et al.* used an original multi-steps NEB approach to compute the activation energy of SDN in MgO NCs as a function of the dislocation center position [AMO 21a]. Amodeo and co-workers derived dislocation activation energies per site $\Delta G_{0,i}$ and radii $r_{c,i}$ maps and used them together with the TST to predict nucleation rates.

*The multi-step nudged elastic band approach*

Amodeo *et al.* first computed the NEB minimum energy path for the nucleation of a dislocation at the lateral surface of a $Lx = Lz = 7.5$ nm and $Ly = 15$ nm wire, before refining the path calculation after slicing the wire in several NCs to get the desired dislocation centre location (Figure 5.6). Simulations are performed for an applied strain of 11.1 % *i.e.,* the critical strain for SDN reported by Issa *et al.* [ISS 15] in MD simulations at $10^8$ s$^{-1}$ strain rate. By this two-steps slicing approach, the dislocation nucleation process is monitored and happens from selected sites characterized by vertical and horizontal coordinates (referred as $y_i/L$ and $h_p/L$) following a grid point-to-point process. Examples of relaxed NEB minimum energy paths for dislocation nucleated at $h_p/L = 0.75$ and distances $y_i/L = 0.0$ to 0.5 at 0 K are shown in Figure 5.6 (b) with activation energies $\Delta G_{0,i}$ varying from 0.8 to 1.1 eV. Note that Amodeo's $\Delta E$ and $k$ corresponds in this manuscript to $\Delta G_0$ and $\nu$ respectively.

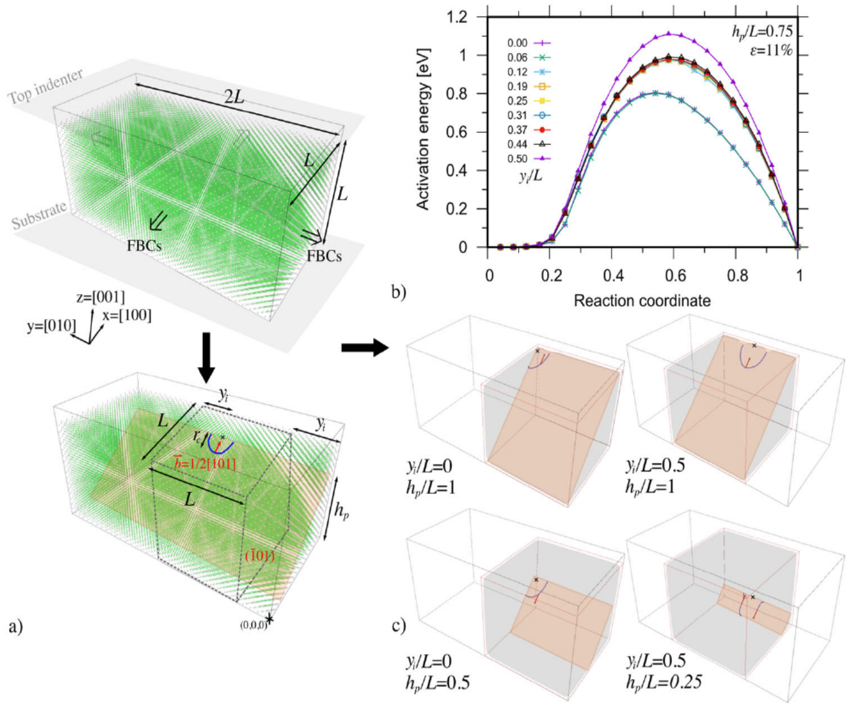

Figure 5.6: Multi-steps NEB approach used to compute energy barriers for SDN in MgO nanocubes. (a) Top: MgO wire starting configuration as compressed by a flat indenter along $z$ with free BCs (FBCs) along $x$ and $y$ directions. Bottom: illustration of typical cube carved out from the original wire showing a dislocation loop with nucleation radius $r_c$ nucleated from the middle of a lateral (100) surface, (b) example of surface dislocation energy barriers for normalized lateral position $y_i/L$ ranging from 0 to 0.5 and normalized vertical position $h_p/L = 0.75$. (c) Examples of configurations for dislocation nucleation at corners, mid-top edge, mid-side edge and the lower mid-surface. From [AMO 21a].

*Atomic-scale description of dislocation nucleation energy and rate in MgO nanoparticles*

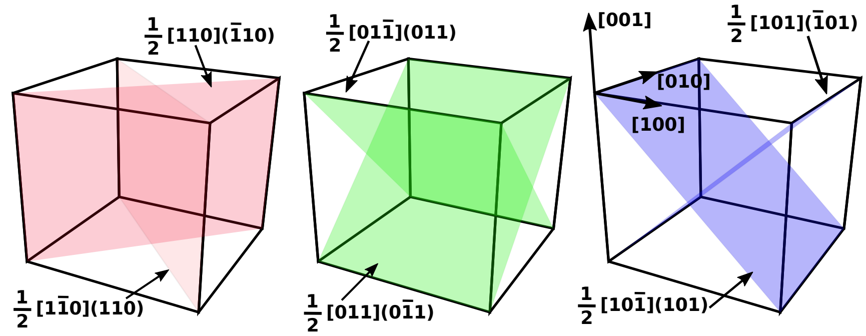
$\frac{1}{2}[110](\bar{1}10)$
$\frac{1}{2}[01\bar{1}](011)$
[001]
$\frac{1}{2}[101](\bar{1}01)$
[010]
[100]
$\frac{1}{2}[1\bar{1}0](110)$
$\frac{1}{2}[011](0\bar{1}1)$
$\frac{1}{2}[10\bar{1}](101)$

Figure 5.7: $\frac{1}{2}\langle 110\rangle\{110\}$ slip systems in MgO.

Considering the symmetries of both the sample and the mechanical test (Schmid factors), Amodeo *et al.* computed the activation energy for SDN on a surface grid for a single $\frac{1}{2}\langle 110\rangle\{110\}$ slip system (while 4 are available) and then use symmetries to 1) fulfill the rest of the current surface, 2) derive the activation energy for other surfaces and 3) intuit the activation energy of other symmetric slip systems (actually two orthogonal $\frac{1}{2}\langle 110\rangle\{110\}$ slip systems per surface are favored). $\frac{1}{2}\langle 110\rangle\{110\}$ slip systems in MgO are described in Figure 5.7. Note that under $\langle 100\rangle$-uniaxial compression, two of the $\frac{1}{2}\langle 110\rangle\{110\}$ slip systems have a Schmid factor equal to 0. This process allowed to build the full map of the activation energy along the boundaries of the NC as shown in Figure 5.8. The multi-steps NEB approach shows that the nucleation of 1/4 dislocation loops at corners and side edges are particularly favorable as well as 1/2 loops nucleated deep in the middle surfaces (Figure 5.8 (b)).

Higher values of $\Delta G_{0,i}$ are observed for the rest of the surfaces that is also characterized by forbidden sites, where no stable SDN events were shown by the multi-step NEB approach. Note that under the uniaxial compression conditions, no dislocation were considered to emerge from the top and bottom surfaces of the NP due to BCs. For the slip system S1 (Figure 5.8 (a)), the bottom region of the NC is particularly unfavorable and dislocations rather nucleate in the orthogonal slip system S2. Finally the authors used the TST to compute dislocation nucleation rate at 300 and 1000 K as shown Figures 5.8 (c,d) and interpret previous MD observations made in MgO nanocubes [ISS 15].

#### 5.2.2.2 Extension of the dislocation nucleation algorithm

*Site and local stress dependence*

To account for the site dependence of dislocation nucleation in El-Numodis, we have upgraded the simplified dislocation nucleation approach to account for local stress vari-

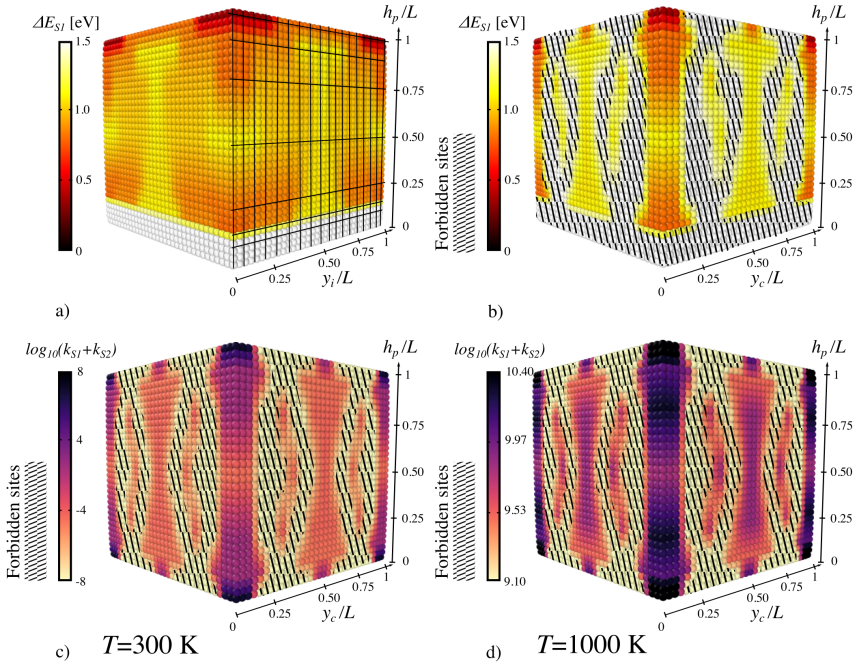

Figure 5.8: Maps of the activation energy and rate for SDN in an MgO NC at 0 K and 11 % strain. (a) grid description and activation energy in slip system S1, (b) activation energy for S1 per nucleation sites (in color) and the forbidden sites (hatching), (c) Dislocation nucleation rate at 300 K for S1 and S2 (d) same at 1000 K. From [AMO 21a].

ations and manage energy databases (no artificial site kill anymore when compared to the simplified approach). In this extended approach, the local stress is retrieved at each nucleation site (before and after nucleation) and is used to compute $\nu_i$ based on local $\Delta G_0$ and then $\delta t_{KMC}$ when solving the BVP. This approach also means that once a dislocation is nucleated, the stress at and around the nucleation site is reduced (see example in Figure 5.9) impacting directly the updated value of $\delta t_{KMC}$. Moreover, the probability to nucleate a new dislocation in the affected region becomes lower, up to the next increase of the local stress.

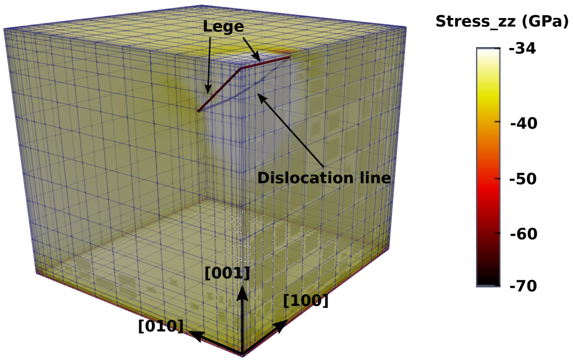

Figure 5.9: Local stress reduction induced by the nucleation of a $\frac{1}{2}[110](\bar{1}10)$ dislocation in a 4.2 nm edge size MgO NP. Dislocation nucleation happens here at $\sigma_{zz}$ =38 GPa stress while the local stress around the nucleation center is reduced down to 34 GPa.

In the extended nucleation algorithm, the condition to have a nucleation event is achieved by comparing two timescales *i.e.,* the simulation time $t_{DDD}$ and the nucleation time $t_{KMC}$ (Figure 5.10). The new algorithm workflow is presented in Figure 5.10. Before detecting if a nucleation event should happen or not the previous quantities are updated using equations $t_{KMC} = t_{KMC} + \delta t_{KMC}$ and $t_{DDD} = t_{DDD} + \delta t_{DDD}$. The extended algorithm proceeds to check if the nucleation condition is fulfilled testing $t_{DDD} > t_{KMC}$. If false, the algorithm steps out and the simulation continued with a regular DDD step else the KMC algorithm is called. Several slip systems can be accounted using this method once their relative $\Delta G_{0,i}$ is defined (assuming an additional KMC step). Each time a dislocation is nucleated, $t_{KMC}$ is updated and the algorithm rechecks if $t_{DDD} > t_{KMC}$ and continue to proceed as shown in the workflow.

Thus, the extended algorithm can also handle situations where only one or several dislocations are nucleated during a single timestep due to the compulsory recalculation of $t_{KMC}$ after every nucleation attempt.

*Nucleation sites and databases*

The extended version of the nucleation algorithm allows to account for $\Delta G_{0,i}$ and $r_{c,i}$

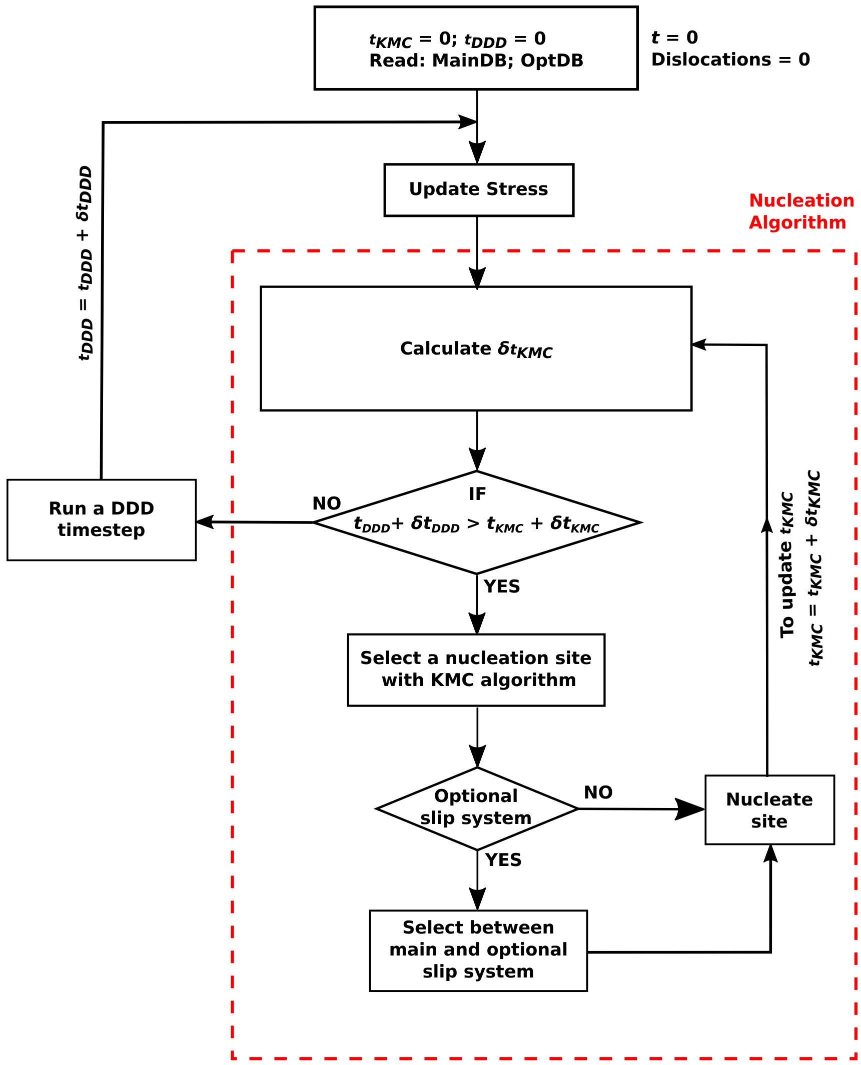
t_KMC = 0; t_DDD = 0
Read: MainDB; OptDB
t = 0
Dislocations = 0
Update Stress
Nucleation Algorithm
t_DDD = t_DDD + δt_DDD
Calculate δt_KMC
Run a DDD timestep
NO
IF
t_DDD + δt_DDD > t_KMC + δt_KMC
YES
To update t_KMC
t_KMC = t_KMC + δt_KMC
Select a nucleation site with KMC algorithm
Optional slip system
NO
Nucleate site
YES
Select between main and optional slip system

Figure 5.10: Extended dislocation nucleation algorithm implemented in El-Numodis. The extended model is used for constant strain rate simulations and accounts for more realistic local stress variations.

using fitting equations or grid data. Based on the multi-step NEB data of Amodeo *et al.* [AMO 21a] computed at $\varepsilon = 11.1$ % and additional data computed at at 7, 8, 9.1 and 10.1% strains[3] computed by Amodeo and collaborators, we built a database with normalize nucleation centre coordinates, $\Delta G_{0,i}$ and $r_{c,i}$ as function of stress to be used by El-Numodis. Using the data at various strains and derived nucleation stress, $\Delta G_{0,i}$ and $r_{c,i}$ were adjusted as function of stress for each nucleation site using a Kocks model (equation 5.10) and a linear law, respectively. Note that here we assume the equivalence between the critical compression stress and the local critical stress at site $i$ due to the cubic shape of the sample that suggests homogeneous stress distribution under compression (see *e.g.,* [KIL 18, AMO 21b]).

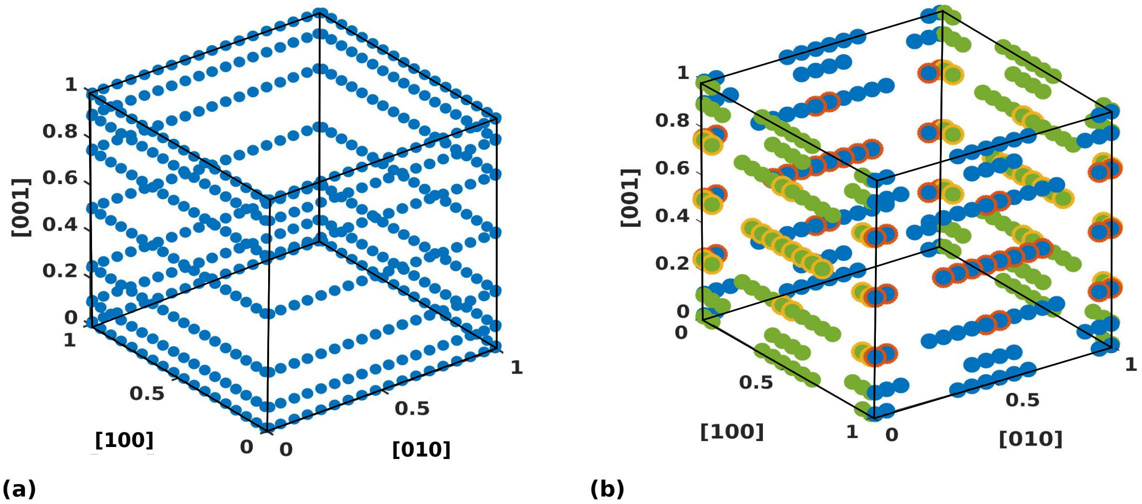

Figure 5.11: Design of the dislocation nucleation database for dislocation nucleation in MgO NPs. (a) All the sites considered in the database, (b) Nucleation sites on the lateral surfaces after the filtering process. Blue and green solid circles refer to the slip systems illustrated in Figure 5.7. Surrounded circles refers to the sites were two conjugate slip systems are available.

The original data of Amodeo include effective and forbidden nucleation sites (similar to the one of Figure 5.8 (a)) and is composed of discrete points arranged in 7 glide planes that intercepts the external surfaces with $z$ at $h_p/L$ equals 0.01, 0.1, 0.25, 0.5, 0.75, 0.9 and 0.99 (Figure 5.11 (a)). For certain points along $h_p/L = 0.25$, $h_p/L = 0.5$ and $h_p/L = 0.75$, a second slip system with its relative $\Delta G_{0,i}$ and $r_{c,i}$ is provided (points surrounded with red and orange circles in Figure 5.11 (b)), as in the work of Amodeo *et al.* [AMO 21a]. One should notice the reduced number of points available in Figure 5.11 (b) due to 1) the presence of forbidden sites [AMO 21a] and 2) a nucleation point $i$ is removed from the database and not considered in the nucleation algorithm if it has less than 2 values of strains (over the 5 investigated by Amodeo). This is because nucleation sites are dependent of the strain values. Moreover, to lead to a stable $\Delta G_{0,i}$, more than 2 points are required for the fitting procedure (see Figure 5.13). Activation parameters are stored in the two tables $MainDB$ that contains site information for the primary slip system and $OptDB$ that relies on the second one.

---

[3] Corresponding nucleation stresses are of about 18.9, 23.6, 28.1 and 33.2 GPa increasing the strain.

Here we reprocessed the data to integrate them as an El-Numodis database. As in the original work of Amodeo *et al.*, data are first treated on a grid subset and then further extended to the entire sample using symmetries (Figure 5.12). $\Delta G_{0,i}$ and $r_{c,i}$ were interpolated on the strain range investigated by Amodeo *et al.* and then extrapolated. One can note that low strain data might be characterized by significant discrepancies due to the lack of data below $\varepsilon$=7 %. However, these should have a limited impact as we will see that the nucleation probability radically decreases at lower stress.

$$\Delta G_i(\sigma) = \Delta G_{0,i}[1 - (\frac{\sigma(\varepsilon)}{\sigma_{ath,i}})^{p_i}]^{q_i} \tag{5.10}$$

where $\sigma_{ath,i}$ is an athermal stress and $p_i$ and $q_i$ are dimensionless activation parameters.

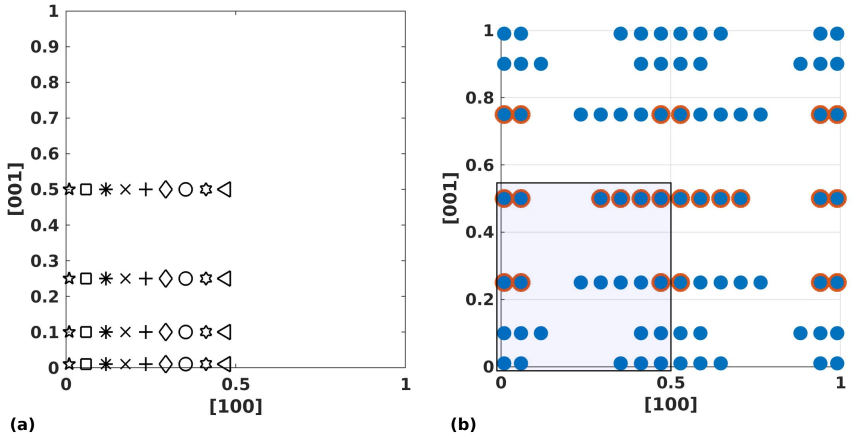

Figure 5.12: Surface symmetries and construction of the dislocation nucleation site database, (a) Different marking to all possible points per nucleation plane inside the rectangle subgrid. (b) nucleation sites (blued dots) used for the database generated at 7.0, 8.0, 9.1, 10.1 and 11.1 % strain. The red circles refer to sites where two orthogonal slip systems are available. The black rectangle illustrates the subgrid where atomistic data $\Delta G_0$ and $r_c$ were originally computed by Amodeo *et al.* [AMO 21a]. The rest of the data are mirrored out of the rectangle in the [001] and [100] directions.

The Figure 5.13 shows fitting examples for $\Delta G_{0,i}$ and $r_{c,i}$ computed at the ($h_p/L = 0.01$, $y_i/L = 0.01$) nucleation site. For $\Delta G_{0,i}$, the fitting procedure shows that the parameter $q$ is in all cases between 1.0 and 1.1. For the sake of simplicity during this study we assume $q = 1$ as it was done in [ZHU 08]. In this case, fitting results give $\Delta G_{0,i} = 39.99$ eV, $\sigma_{ath} = 23.82$ GPa and $p_i = 2.78$ with $R^2 = 0.99$ and $R^2_{adj} = 0.96$. On the other hand, $r_{c,i} = m_i\sigma + n_i$ is fitted here with $m$=-1.21 Å/GPa and $n = 33.44$ Å with $R^2 = 0.87$. Two databases are finally created *i.e.*, one with the data for all sites and their primary

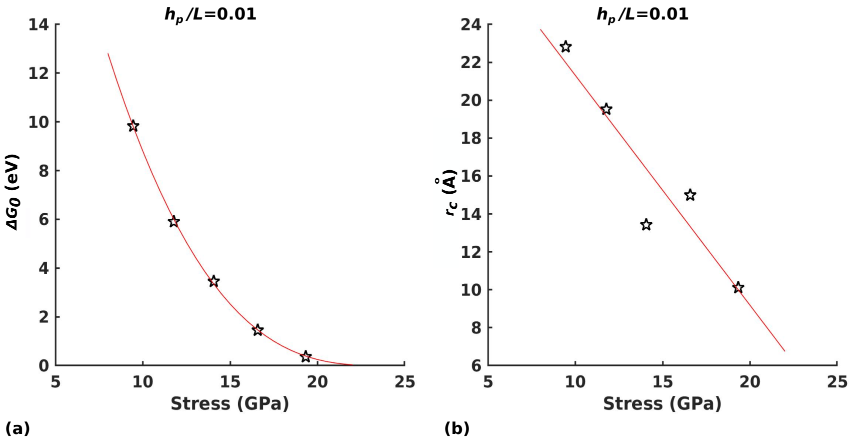

Figure 5.13: Examples of activation parameter fits in function of the shear stress (*i.e.*, half the compressive stress) with (a) $\varDelta G_{i,0}$ using a Kocks law and (b) $r_{c,i}$ using a linear equation.

slip system and a second one with the information related to the additional slip system (yellow and red circles in Figure 5.11 (b)).

## 5.3 Mesoscale modeling of dislocation nucleation in MgO nanoparticles under compression

### 5.3.1 Deformation at extreme strain rate

In this section, El-Numodis is used to model nanocompression tests of MgO NPs at constant strain rate using the atomistically-informed database for SDN presented in the previous section. Results are compared to MD simulations for NCs with size ranging from 4.2 to 12.6 nm [ISS 15]. The samples are meshed using 20 × 20 × 20 eight nodes hexahedrons refined at the edges (see Figure 5.9 as reference) with "using Bump=0.05" Gmsh algorithm. As in the previous case, the stress correction when solving the BVP is performed using SPM without the mirror image dislocation method. A viscous mobility law was used with a damping coefficient $B = 5 \times 10^{-4}$ Pa·s. Poisson ration and Young's modulus were set to 0.18 and 275.43 GPa, respectively. As in the former MD, El-Numodis simulations are performed at a strain rate of $10^8$ $\mathrm{s}^{-1}$ at room temperature using $\delta t_{DDD} =$ 1 ps (this latter being about 1000× larger than the MD timestep). $T_m = 1550$ K is used as in Amodeo *et al.* [AMO 21a]. In the aforementioned conditions of deformation, both the MD on one side and the TST associated to NEB energy barriers (Equations 5.1 to 5.6) on the other side predict a nucleation stress of about 38-40 GPa [AMO 21a]. Therefore, here we run El-Numodis with an initial applied stress of 30 GPa what allows to reduce the CPU costs in the initial linear elastic regime, where, theoretically, no dislocation should nucleate in MgO NCs at the MD timescale.

#### 5.3.1.1 Mechanical response

The stress-strain curves and temporal evolution of the plastic strain are illustrated in Figure 5.14, as function of the sample size. Stress-strain curves are characterized by an initial elastic load up to a first stress peak that corresponds to the first dislocation nucleation event *i.e.,* at about 38 GPa and 11 % strain. Assuming the difference of BCs between SPM (applied strain BCs) and MD simulations (displacement-controlled indenter forced field), yield stress and critical strain computed by the two methods are in particularly good agreement (Figure 5.15). As for MD, SPM results show a particularly limited size-effect on the yield stress possibly induced by the cubic shape of the sample that is believed to avoid any size-effect due to homogeneous stress distribution within the whole sample under uniaxial compression [AMO 17, KIL 18, AMO 21b]. After the first dislocation nucleation events, the stress decreases as constrained by the feedback loop after a significant amount of strain was produced in a limited period. Once the dislocations escape the sample, the stress increases again (elastic reload) up to the next nucleation events. One can note that at such high strain rate, subsequent stress peaks for nucleation are strictly comparable to the original one using SPM, emphasizing the weak probabilistic propensity of the dislocation nucleation mechanism at high strain rate. Also, these results slightly differ from MD where post-yield surface modifications induced by dislocation shearing modify the activation energy landscape at the surface (effect not yet accounted in El-Numodis). Besides, the main differences between SPM and MD outcomes arise from the amplitude of the stress drops, especially after the first nucleation event, that show minimum stress values ranging from 27 to 17 GPa in El-Numodis, while lower values of about few GPa are obtained in the MD. In our opinion this difference is due to the difference of dislocation velocities between the two simulations as well as to the different kinds of BCs. The former can be corroborated by changing the value of the drag coefficient of the mobility law.

#### 5.3.1.2 Corner dislocation nucleation

At room temperature and extreme strain rate, El-Numodis simulations show dislocation nucleation from corners (without preferential corner) whatever the sample size, as shown in Figure 5.16. This behavior can be interpreted using the same arguments than for the 3-sites copper NC described in section 5.2.1.3 *i.e.,* the difference between $\Delta G_{0,i}$ at the various nucleation sites is too large to allow nucleation elsewhere at such low temperature. So, the KMC method just ensures that one of the 8 corners is selected only based on its activation energy and local stress (that changes once the first dislocations nucleates). It is important to recall that each corner provides the possibility to nucleate dislocations into two different slip systems.

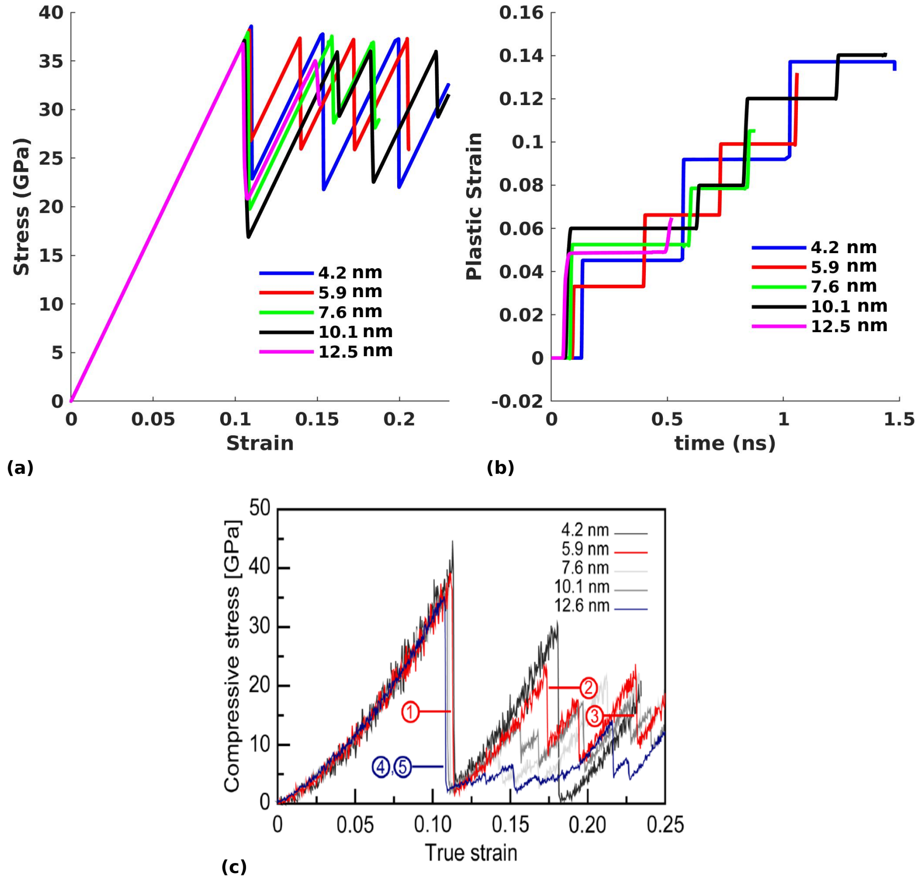

Figure 5.14: Mechanical response of MgO NPs under compression at $10^8$ $s^{-1}$ strain rate for various sample sizes at room temperature using SPM and El-Numodis as compared to MD simulations. (a) SPM stress-strain curve, (b) SPM plastic strain versus time. (c) MD stress-strain curves computed using LAMMPS (from [ISS 15]).

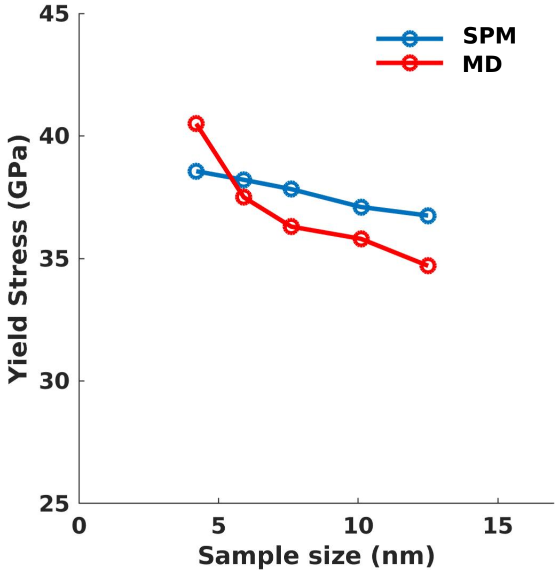

Figure 5.15: MgO NCs yield strength versus sample size: SPM (El-Numodis) vs. MD (LAMMPS).

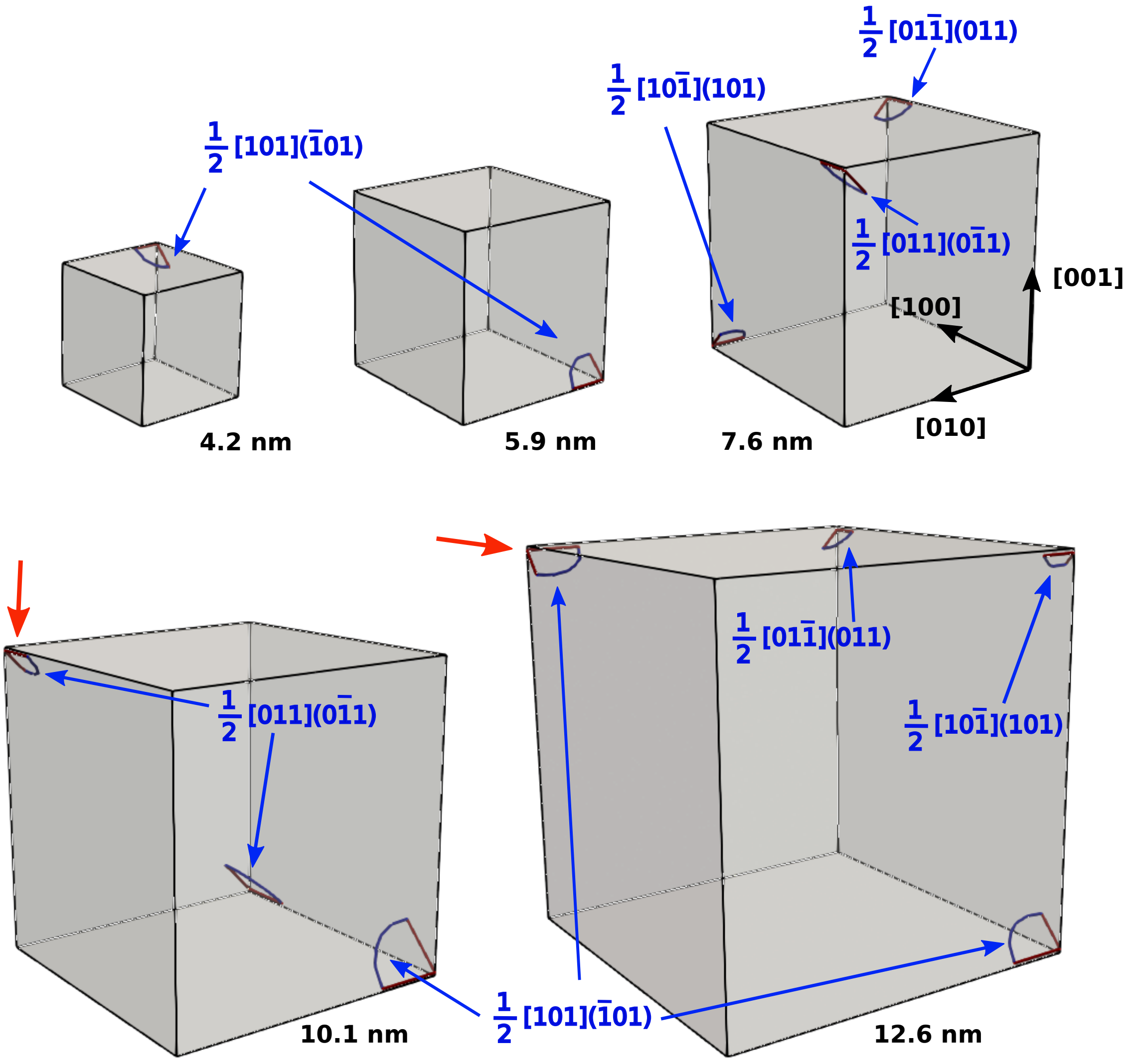
$\frac{1}{2}[01\bar{1}](011)$
$\frac{1}{2}[10\bar{1}](101)$
$\frac{1}{2}[101](\bar{1}01)$
$\frac{1}{2}[011](0\bar{1}1)$
[001]
[100]
[010]
4.2 nm
5.9 nm
7.6 nm
$\frac{1}{2}[011](0\bar{1}1)$
$\frac{1}{2}[01\bar{1}](011)$
$\frac{1}{2}[10\bar{1}](101)$
$\frac{1}{2}[101](\bar{1}01)$
10.1 nm
12.6 nm

Figure 5.16: Corner dislocation nucleation at the yield stress in various sizes MgO NCs deformed at a constant strain rate of $10^8$ s$^{-1}$ and room temperature using El-Numodis.

Simulation results of Figure 5.16 show that the number of dislocations that nucleate after the yield point raises when increasing the sample size. For instances, only one dislocation is nucleated for samples of 4.2 and 5.9 nm edge size at the yield point, while three dislocations nucleate for the 7.6 and 10.1 nm. Also, four (or more) dislocations nucleate for the sample of 12.6 nm. In this last case the four dislocations are generated starting by two nucleation events at the same timestep, when the applied stress reaches the yield stress. The last two dislocations (red arrow, Figure 5.16) also nucleate during the same DDD timestep, but three DDD steps after the first nucleation event. In addition to their velocity, the amount of dislocations that nucleate impact the magnitude of the stress drop of Figure 5.14 (a). When a dislocation nucleates and expand crossing the sample, the total plastic strain generated is proportional to the area swept by the defect.

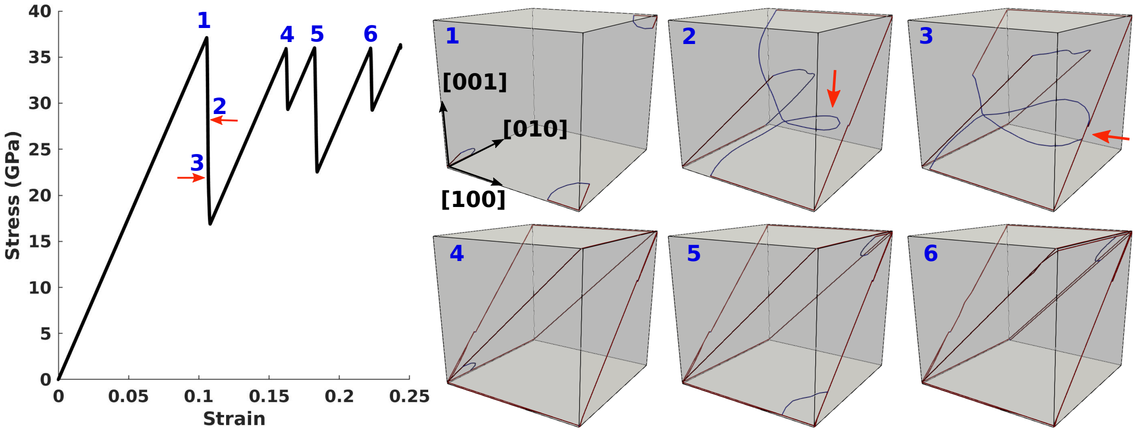

Figure 5.17: Dislocation microstructure and stress-strain curve for the 10.1 nm MgO NC deformed using El-Numodis at imposed strain rate ($10^8$ s$^{-1}$) and room temperature.

Figure 5.17 shows the evolution of the dislocation microstructure at different stage of the stress-strain curve for the 10.1 nm NC. At 37.1 GPa (label 1) two $\frac{1}{2}[011](0\bar{1}1)$ and one $\frac{1}{2}[101](\bar{1}01)$ dislocations nucleate from the corners of the sample. The plastic strain produced reduces the external load but the stress remains large enough to ensure dislocation glide. The two dislocations glide in parallel planes separated by a very small distance. The dislocations attract each other and the interaction produces a loop (step 2) inside the NC. The dislocation loop portion is attracted by one of the lateral surfaces by action of the images forces (step 3) where it is divided into two dislocations arms. The dislocation microstructure continues to evolve until each dislocation arm escapes the sample. At this stage, the applied stress starts to increase (due to the lack of dislocation in the sample) up to the nucleation stress where another nucleation event is noticed (step 4). This time, only one $\frac{1}{2}[101](\bar{1}01)$ dislocation nucleates at the bottom of the sample, exactly at the same site where one of the previous dislocation was nucleated. This is traduced in a smaller stress drop on the stress-strain curve due to the relatively small amount of plastic strain induced (see Figure 5.14 (b)). Indeed, as shown Figure 5.14 (b) strain is produced by increments of various amplitudes, that, in average, obey the imposed strain rate. The dislocation escapes the sample and the stress increases again until a new $\frac{1}{2}[011](0\bar{1}1)$ dislocation nucleates. At the same time, another $\frac{1}{2}[101](\bar{1}01)$ dislocation nucleates (step 5) in one of the top corners. This process composed of stress increase-nucleation-dislocation glide-dislocation starvation-stress reload repeats until step 6 where only one dislocation nucleates. It is important to notice the similitude between the corner nucleation observed in SPM and MD and the observations made in *in situ* TEM experiments shown in Figure 5.18.

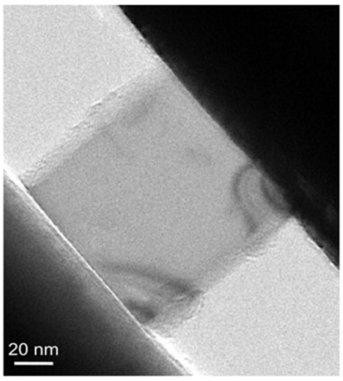

Figure 5.18: *in situ* TEM image of corner dislocation nucleation in MgO NP. Image from [AMO 21a].

## 5.3.2 Towards experimental conditions of deformation

### 5.3.2.1 Influence of strain rate

In this section, we focus on the influence of strain rate and temperature on the nucleation process. For this purpose, we use small MgO NPs to reduce the CPU costs but we assume that the conclusions drawn here should not depend on sample size assuming the deformation operates within the dislocation nucleation/exhaustion regime. The influence of size will be discussed in a next section.

To study the influence of the strain rate on the yield strength, a 4.2 nm edge size MgO NC similar to the one described in the previous chapter, is deformed using different strain rates ranging from typical MD $10^9$ s$^{-1}$ down to $10^{-2}$ s$^{-1}$, closer to laboratory conditions of deformation. For these simulations, the adaptive $\delta t_{DDD}$ timestep varies from 1 ps to 10 ms decreasing the strain rate[4]. Results are presented in Figure 5.19.

---

[4] Please note that Numodis timestep is further reduced when a dislocation is about to react locally with an obstacle or when a node wants to move on a wide distance

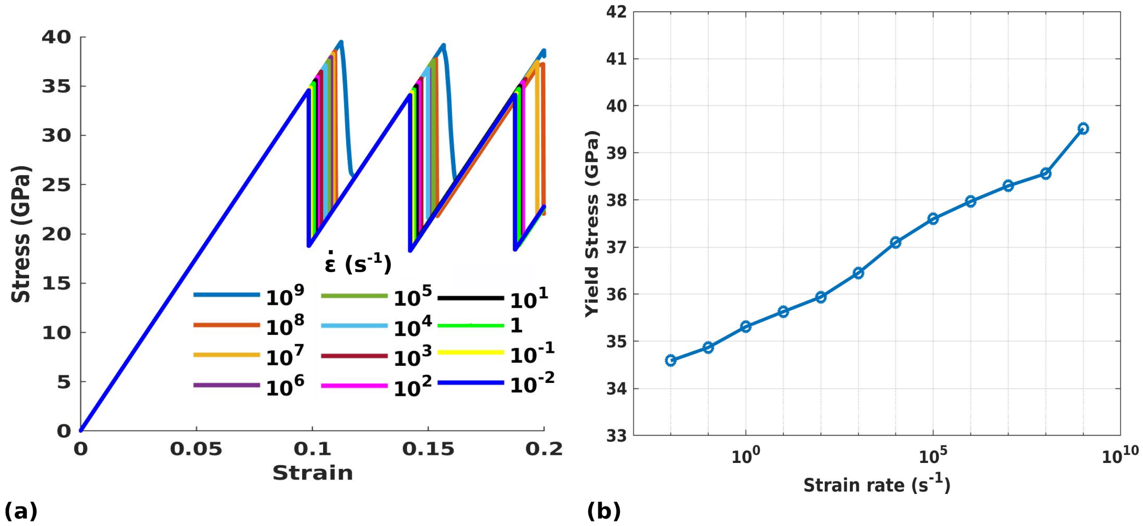

Figure 5.19: Mechanical response of a 4.2 nm MgO NC deformed at different strain rates using El-Numodis at room temperature. (a) strain-stress curves. (b) yield strength variations with strain rate.

Typical of sub-10 nm nanocrystals in MD, only one dislocation nucleates at the yield point and accommodates sole the whole plastic strain at high strain rate using El-Numodis and the SPM method. Surprisingly, a similar behavior is observed down to the lower strain rates where dislocation nucleation also happens randomly from one of the eight corners of the sample, independently from the strain rate. The plot of Figure 5.19 (b) shows the decrease of the yield stress with the strain rate *i.e.,* a variation of the yield stress ranging from 39.52 down to 34.59 GPa is noticed on the investigated strain rate range, equivalent to a yield stress decrease of about 13 %.

The plastic strain increment $\delta\varepsilon_p$ produced by a single dislocation gliding in a $\{110\}$ slip plane passing through a nanocube of edge length $L$ side-to-side is equal to,

$$\delta\varepsilon_p = h_p(L)\frac{b.\sqrt{2}}{L^2} \tag{5.11}$$

where $h_p(L)$ (ranging from 0 to $L$) relies on the height from which the slip plane intersects the sample lateral surface.

Thus, the maximum of $\delta\varepsilon_p$ produced by a dislocation in the aforementioned case is about $\delta\varepsilon_p = b.\sqrt{2}/L = \sim 10$ %. At the yield stress, the dislocation velocity is the 10 000 m/s range assuming a viscous law and a damping coefficient $B = 5 \times 10^{-4}$ Pa·s. At such extreme velocity, the dislocation will cross the 4.2 nm edge length sample within few hundreds or thousands MD timestep (N.A.: about 6 ps while MD timesteps are commonly about 0.001 ps). This suggests that the instant strain rate at the yield point is about $10^5 - 10^6$ $s^{-1}$, only compatible with MD feedback control and way larger than experimental expectations, explaining by the way why we always see only one dislocation in aforementioned simulations. Of course increasing the NP size would decrease $\delta\varepsilon_p$ but only linearly, what would still make the plastic strain achieved by a small amount of dislocations consequent in larger nanoparticles. On the other hand, the corner constant location is associated to the low temperature (300 K) as previously discussed. This outcome helps to understand mechanical instabilities associated to strain bursts (or load drops) in nanomechanical experiments.

The particularly large energy barrier for dislocation nucleation in MgO and other ceramics (over 1 eV, about ten times larger than in fcc metals) is partly responsible for the large nucleation stress. While the sensitivity of nucleation stress to the strain rate enters a log term in the classical TST (see equation 5.6), it is known to significantly change the nucleation stress in metal nanocrystals with variations sometimes about 50 % (1-5 GPa) when decreasing the strain rate from the MD range to the experimental one (see *e.g.,* in Cu [ZHU 08]). Here we show that the influence of strain rate on the nucleation stress in ceramics MgO where highly energetic dislocations have to be nucleated is way lower and there is finally not much differences in terms of nucleation stress when passing from MD conditions of deformation to laboratory one. Implicitly, these results strongly encourage the use of MD to study incipient plasticity and dislocation nucleation processes in ceramic nanocrystals, even more than NEB or atomistically-informed mesoscale method especially when no further information on the dislocation dynamics are required. In the next section, we continue our investigations on the nucleation regime describing temperature effects.

#### 5.3.2.2 Influence of temperature

Here we used the same aforementioned setup to investigate the effect of temperature on the mechanical response MgO NCs. Simulations are performed at 5, 300 and 1000 K for two different strain rates *i.e.,* $10^8$ and $10^{-2}$ s$^{-1}$, MD and experimental nanocompression ranges respectively.

Here we assume a viscous dislocation mobility law whatever the temperature range. While this choice can be slightly controversial if we bear in mind that MgO $\frac{1}{2}\langle 110\rangle\{110\}$ slip systems exhibit lattice friction up to 600 K (see Chapter 1), we assume that the mobility should not be thermally-activated anymore while stress widely overshoots the GPa stress range. So, without more information on dislocation mobility in this extreme-stress regime, a viscous mobility law with a constant (and arbitrary) $B = 5{\times}10^{-4}$ Pa·s damping coefficient is used whatever the temperature, as in the simulations presented in section 5.3.2.1. The elastic constants were not changed with temperature variations.

Stress-strain curves are presented in Figure 5.20 and examples of dislocation microstructures at the yield stress are shown in Figure 5.21. For $\dot{\varepsilon} = 10^8$ s$^{-1}$ and $T = 5$ K, only one $\frac{1}{2}[101](\bar{1}01)$ dislocation is nucleated at the center of a lateral surface near the top of the

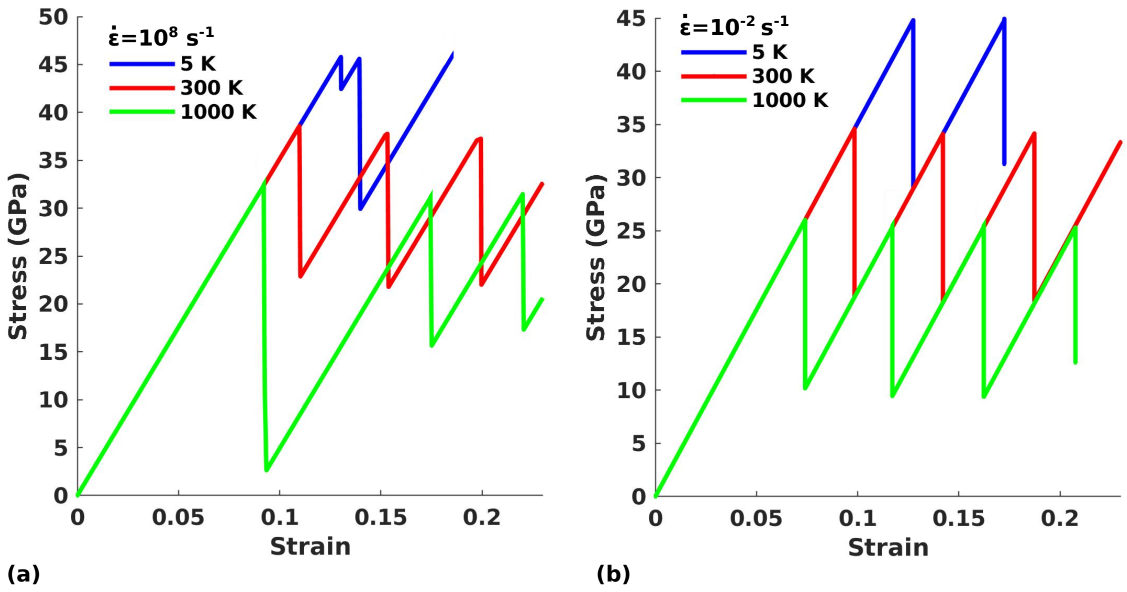

Figure 5.20: Mechanical response of 4.2 nm sized MgO NCs under compression as function of temperature and strain rate computed using El-Numodis, (a) $10^8$ s$^{-1}$ (MD range), (b) $10^{-2}$ s$^{-1}$ (experimental range).

sample at a yield stress of 45.8 GPa. One can notice that in this case, we easily observe dislocation nucleation in the orthogonal slip system *i.e.,* the dislocation does not glide in (101) but $(\bar{1}01)$. The total amount of plastic strain accommodated by this dislocation once it propagates and leaves the sample is of particularly small amplitude (as shown by the small stress drop of Figure 5.20 (a)) due to do both the location of the nucleation site and the chosen slip system. As consequence, the elastic reload is particularly short and a second dislocation nucleates once the stress reaches the 45.8 GPa. This time, nucleation occurs from one of the corners and produce a larger amount of plastic strain as well as an extended stress drop.

At 300 K, a single dislocation also nucleates from one of the corners but at lower yield stress (38.8 GPa). The dislocation analysis and the stress-strain curve reveal the subsequent nucleation of another single dislocation after the elastic reload and the first dislocation escapes the sample. At $T = 1000$ K, four dislocations nucleate simultaneously at 32.6 GPa; two from corners and two from edges. This nucleation/glide event is correlated to the larger stress drop observed during the simulation (Figure 5.20 (a)). The following nucleation events only show single dislocation nucleation from the corners.

The same kind of simulations performed at $\dot{\varepsilon} = 10^{-2}$ s$^{-1}$ show a comparable behavior under temperature with only single dislocation that nucleates from the surfaces and yield stress that reduces from 44.8 to 26.0 GPa while the temperature increases (Figures 5.20 (b) and 5.21 (d-f)). Thus, as shown in the previous subsection, decreasing the strain rate

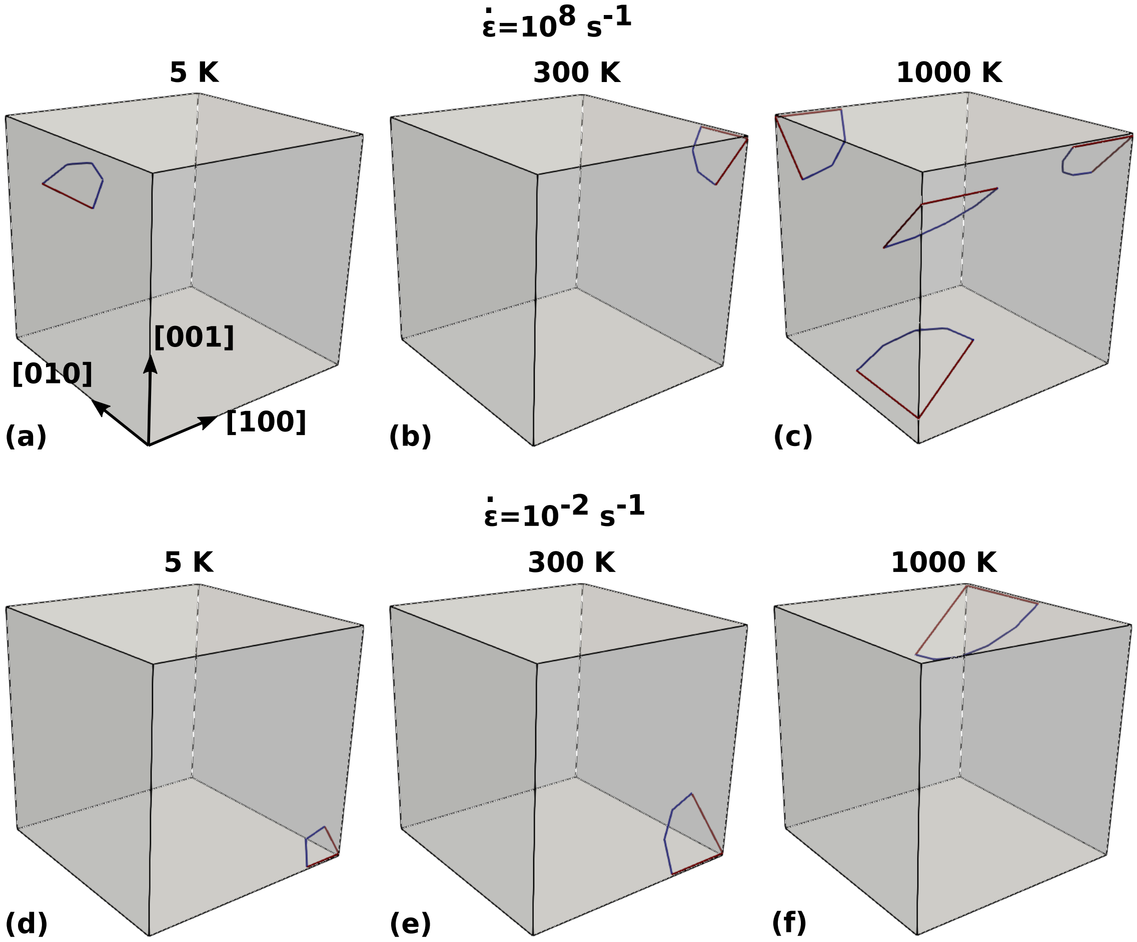

Figure 5.21: El-Numodis simulations of dislocation nucleation in a 4.2 nm edge size MgO NCs under compression computed at 5, 300 and 1000 K at (a-c) $10^8$ s$^{-1}$ and (d-f) $10^{-2}$ s$^{-1}$ strain rates.

slightly decreases the yield stress with a larger impact at high temperature.

The stress reduction observed during the simulations at various temperatures suggests that increasing the temperature produces a weakening of the material. Indeed, the nucleation stress is significantly temperature sensitive as can be seen in Figure 5.22. For larger strain rate ($\dot{\varepsilon} = 10^{-8}$ s$^{-1}$) the nucleation stress drops of 30 % between 5 and 1000 K. While for slower strain rates, the stress differences increases up to a 42 % in the same temperature range. These results can be compared with those obtained for FCC metal NWs [ZHU 08] even if in the case of MgO ceramics, the influence of strain rate remains limited at room temperature. From equation 5.6, we can relate explicitly the dependence of the nucleation stress with the strain rate and temperature. $T$ stands in and outside the log term (in the contrary to $\dot{\varepsilon}$ that only stays in) what implies that the nucleation stress is more sensitive to $T$ when compared to the strain rate, and this effect is stronger when the activation volume $\Omega = bA$ (with $A$ the critical area covered by the freshly nucleated dislocation) is small, like in SDN events at large stress. So, small activation volume also

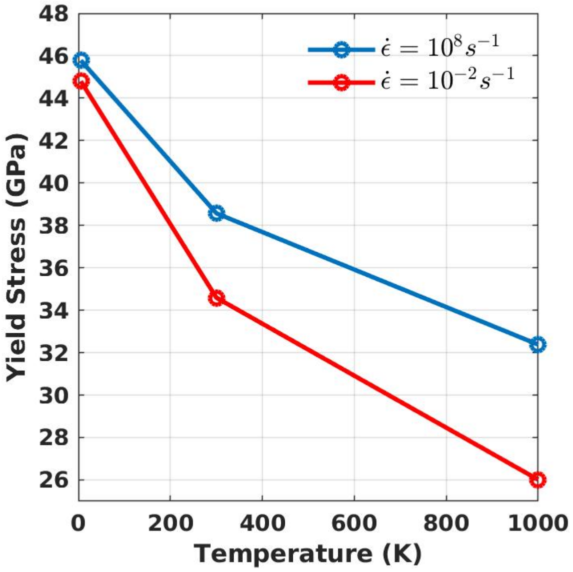

Figure 5.22: MgO NCs yield stress dependence on temperature and strain rate as computed by El-Numodis.

accounts for the stress reduction observed in Figure 5.19 in simulations computed at various strain rates.

The temperature also affects the location where dislocation nucleation takes place. Indeed, we have shown in section 5.2.1.3 that temperature affects the nucleation probability at all sites. Here in the cases of sub-10 nm MgO NCs, the number of lateral surface nucleation sites is larger than the one of corner and edges sites while their activation energy is often about 10× larger. So, even at higher temperature, we still observe lots of SDN events incoming from corners and edges (at this sample size).

All along the two previous subsections, we have discussed the role of strain rate, temperature and their association on the yield strength of ceramic MgO NPs under compression. These simulations were performed in a particularly small volume that we believe does not impact the results while discussing the dislocation nucleation/exhaustion regime. In the last subsection of this chapter, we start investigating the role of size on this same regime of deformation in order to approach NPs size investigated in the experiments.

#### 5.3.2.3 Size-effects and limitations

To study the role of sample size on the mechanical properties of MgO ceramic NPs, several cubic shaped samples with size ranging from 25 to 250 nm were designed. Here we use the same 20 × 20 × 20 number of elements refined at the edges and corners but with a scalable characteristic size. The number of nucleation site remains constant whatever the sample size. Usual tests with larger numbers of elements were performed without quantitatively changing the results. Here we use the same material properties and BCs than those used in the previous simulations presented in the manuscript. Three strain rates are tested *i.e.,* 1, $10^4$ and $10^8$ $s^{-1}$ with $\delta t_{DDD}$ ranging from 10 µ$s$ to 1 ps raising the strain rate.

| $\dot{\varepsilon}$ ($s^{-1}$) | **Sample size (nm)** | | | | | | |
|---|---|---|---|---|---|---|---|
| | 25 | 50 | 75 | 100 | 150 | 200 | 250 |
| $10^8$ | 38.88 | 39.61 | 39.91 | - | - | - | - |
| $10^4$ | 37.33 | 37.46 | 37.47 | 37.50 | 37.28 | - | - |
| 1 | 35.60 | 35.61 | 35.72 | 35.70 | 35.72 | 35.90 | - |

Table 5.2: Yield stress values (GPa) for simulations performed at three different strain rates for sample size ranging from 25 to 250 nm. "-" refer to instabilities related to the saturation of the nucleation process.

Yield stress as function of sizes and strain rates are presented in Table 5.2 where stress does not vary explicitly with size. These results confirm the absence of size-effect on the yield stress in MgO NCs. While this result contradicts the experiments of Issa *et al.* [ISS 15, ISS 21], it corroborates the thesis formulated in [AMO 21b, KIL 18] and the recent experiments of [CHE 22], this later having confirmed a yield stress of about 33 GPa for 60 nm edge size MgO NCs using *in situ* TEM nanocompression, comparable to theoretical predictions. For the 25 nm edge size NC, the yield stress is about 38.9, 37.3 and 35.6 GPa decreasing the strain rate. The number of dislocations nucleated at the yield stress are shown in Table 5.3 and we can observe that the larger the NP, the larger the number of dislocations that nucleate. Here in the 25 nm edge size sample, the number of dislocations that first nucleate is respectively 12, 5 and 1, decreasing the strain rate. For the 50 nm sample, the yield stress does not vary so much when the compared to the smaller sample *i.e.,* 39.61, 37.46 and 35.61 GPa decreasing the strain rate (differences lower than 2 %). However, the number of dislocations that nucleate at the yield stress increases from 12 to 18 at $10^8$ $s^{-1}$ strain rate. These numbers can be discussed regarding the number of dislocations nucleated for samples size ranging from 4.2 (1 dislocation) to 12.6 (4 dislocations) nm deformed under the same conditions of deformation (see Figure 5.16). This effect is even more dominant in 75 mm edge size sample with a number of dislocation increasing from 1 to 44 increasing the strain rate. Also, the number of dislocation nucleated is very sensitive to strain rate (in the contrary to the yield stress) when the sizes increases and the SDN period at the yield strength is extended in larger sample / lower strain rate. This result might have serious implications related to size-effect in the experiments where it could be at the origin of the formation of dislocation microstructure when mechanical instabilities develop at the yield point (strain burst).

To better understand the influence of size and strain rate on the SDN process, nucleation in the 50 nm edge size sample is described in Figure 5.23. For the slower strain rates,

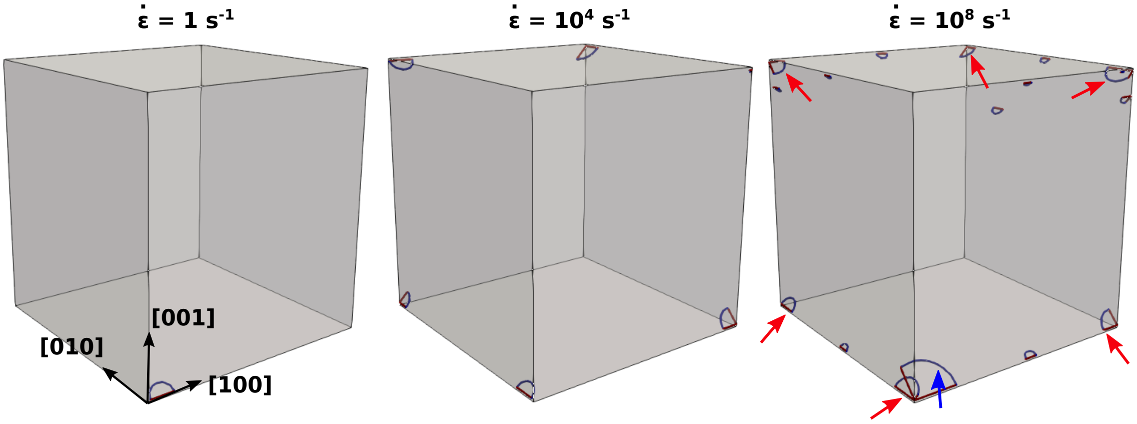
$\dot{\varepsilon}$ = 1 s$^{-1}$
$\dot{\varepsilon}$ = 10$^{4}$ s$^{-1}$
$\dot{\varepsilon}$ = 10$^{8}$ s$^{-1}$
[001]
[010]
[100]

Figure 5.23: Dislocation nucleation at the yield stress for a 50 nm edge dize MgO NPs at various strain rates. The number of defects nucleated increase with the strain rate. the blue arrow show a dislocation nucleated few steps before the red ones. The unmarked dislocations nucleate later on.

*i.e.*, 1 and $10^4$ s$^{-1}$; 1 and 5 dislocations respectively nucleate at the yield point. The 5 dislocations nucleate at the same DDD timestep producing an immediate change in the slope of the stress-strain curve (yield point) that in this case, is equal to the nucleation stress. But it is different at $\dot{\varepsilon} = 10^8$ s$^{-1}$ when the elastic load of the sample reaches the nucleation stress, one dislocation is nucleated. The single dislocation propagates during few simulation steps (4 steps) when 6 additional dislocations nucleate. After two DDD steps, remaining dislocations are emitted and no further nucleation event is observed. This peculiar behavior reflects the competition between $t_{KMC}$ and $t_{DDD}$. The variable $t_{KMC}$ is directly related to the activation energies and the applied stress (Figure 5.13). In sub-10 nm samples, the amount of plastic strain produced by a single dislocation that nucleates is particularly large and induce a wild correction of the applied stress to not overshoot the imposed strain rate. This not true anymore in larger samples where the amount of plastic strain produced by a single dislocation is reduced drastically, and the correction to the applied stress is almost zero. As a consequence, the applied stress continues to increase after the first nucleation event following the imposed rate what impacts $t_{KMC}$ leading to more SDN events. This situation repeats up to the moment when a large enough amount of plastic strain is generated to correct the applied stress and $t_{KMC}$ reaches the off condi-

| $\dot{\varepsilon}$ (s$^{-1}$) | **Sample size (nm)** | | | | | | |
|---|---|---|---|---|---|---|---|
| | 25 | 50 | 75 | 100 | 150 | 200 | 250 |
| $10^8$ | 12 | 18 | 44 | - | - | - | - |
| $10^4$ | 5 | 5 | 6 | 15 | 28 | - | - |
| 1 | 1 | 1 | 1 | 1 | 1 | 1 | - |

Table 5.3: Number of dislocations that nucleate at the yield stress as function of sample size and strain rate. "-" refer to instabilities related to the saturation of the nucleation process.

tion of nucleation.

Also, the $\delta t_{DDD}$ used as a simulation parameter impacts the equilibrium between $t_{KMC}$ and $t_{DDD}$. Here, due time constrains we sometimes had to use a slightly large timestep, especially for low strain rate simulations assuming we will constrain the study to dislocation nucleation and not to further dislocation dynamics. However, $\delta t_{DDD}$ also influences the amplitude of the stress response. It means that using a small $\delta t_{DDD}$ might lead to situations where few dislocations are nucleated during one timestep while increasing it might raise the the number of dislocation nucleated within a timestep, this having consequences on the stress relaxation process (as already discussed). To test this hypothesis, five simulations were done (50 nm edge size sample) at high strain rate varying $\delta t_{DDD}$ from 0.1 to $10^{-5}$ ns. Results show statistical changes in the nucleation procedure (*e.g.,* regarding the number of dislocation appearing) but the final amount of dislocation nucleated and the yield stress remain the same whatever the timestep used.

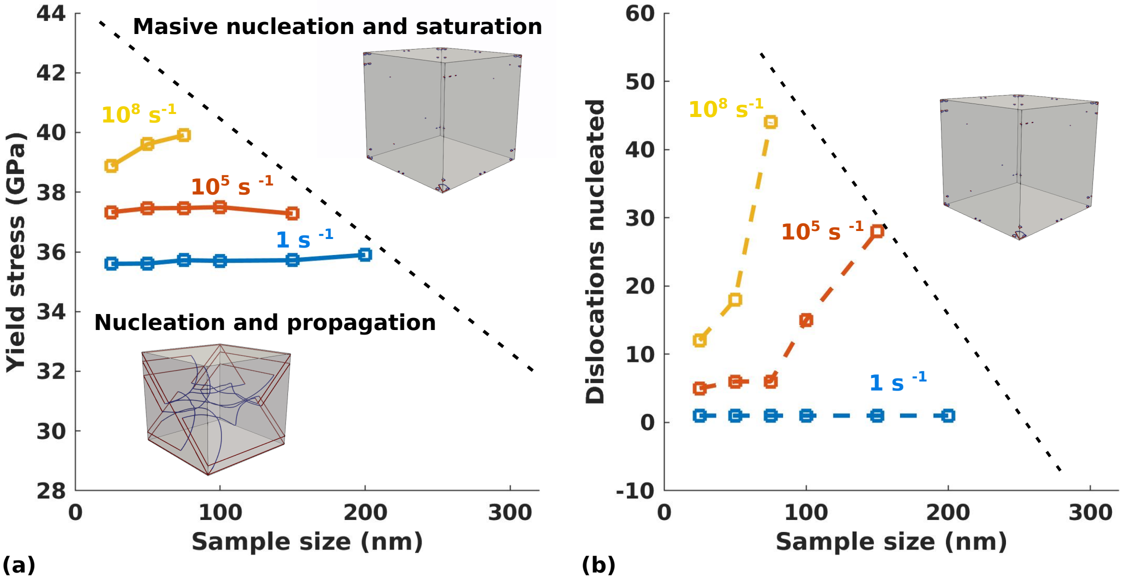

Figure 5.24: Size-effects in MgO NCs under compression computed using El-Numodis. Effect size and strain rate on (a) the yield stress (b) on the number of dislocations that nucleate.

Finally, increasing the size we have reached the limitations of the nucleation regime (Figure 5.24). Indeed, El-Numodis feedback control conflicts for larger sizes and is not able to satisfy the conditions of imposed strain rate *i.e.,* all available nucleation sites are used. As already discussed, the deformation is controlled by a low amount of dislocations for lower sizes that is even diminished at low strain rate. However, increasing the dimensions of the sample, more and more dislocations nucleate at the yield point up to a limit where all the nucleation sites emit dislocations.

At this stage, when the effective plastic strain produced is lower than the imposed plastic strain, the applied stress continuously increases. The increase in the applied stress reduces the radius of nucleated dislocations and the overall plastic strain produced is not high enough for the SPM to reduce the applied stress (at the yield point). Also, parts of the dislocations collapse due to image forces (and their small radius) and El-Numodis has to nucleate new dislocations again. This regime is characterized by the black dashed line in Figure 5.24. In the lab conditions of strain rate, this saturation process could be related to the mechanical instabilities often observed at yield point in nanomechanical experiments. Of course, here the method used is characterized by reduced number of nucleation sites as compared to the experiments, but the drastically increasing amount of dislocations required to plastify nanosamples with size over 100 – 200 nm could explain size-effects observed in experiments, as *e.g.,* the nucleation-to-multiplication transition observed in MgO NCs at 200 nm critical size (see Figure 5.25) shown by Issa and collaborators [ISS 21].

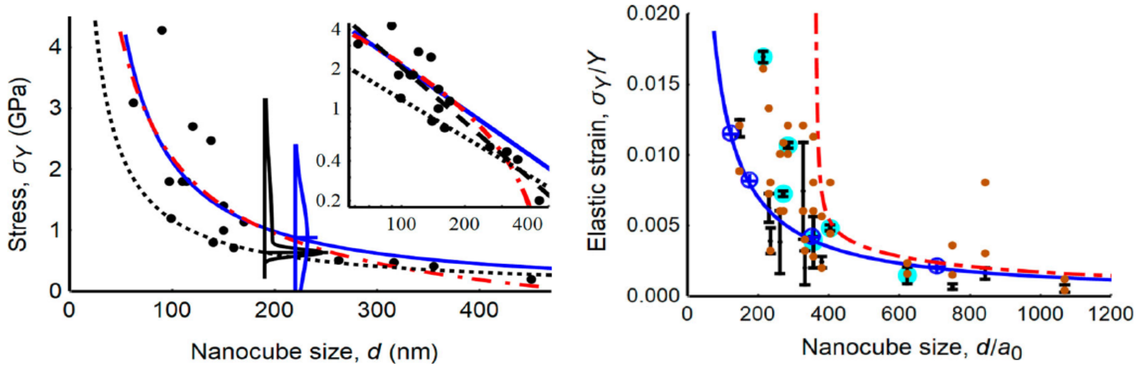

**(a)** **(b)**

Figure 5.25: Nucleation-to-multiplication transition in MgO Ncs under compression, (a) Size-effect on the yield stress , (b) dependence of the elastic strain on the normalize nanocube size. Figure form [ISS 21]

The simulations show that the saturation process is strain rate sensitive. For deformations using $\dot{\varepsilon} = 10^8$ s$^{-1}$, the transition occurs between 75 to 100 nm for $\dot{\varepsilon} = 10^4$ s$^{-1}$ and $\dot{\varepsilon} = 1$ s$^{-1}$, the transition occurs between 150 – 200 and 200 – 250 nm, respectively. At higher strain rate, the number of dislocations increases drastically when increasing size. This effect is moderated at lower strain rate down to a single dislocation nucleated for the deformation at $\dot{\varepsilon} = 1$ s$^{-1}$ in the 25 – 200 nm size range. At lower strain rate, the increase of the applied stress is very slow, when a dislocation is nucleated the value of $t_{KMC}$ is affected and no more dislocation needs to be nucleated. This allows the nucleated dislocation to propagate long enough, creating a considerable amount of plastic strain with almost no increase of the applied stress. Thus, lower rate simulations generate less nucleation events. Then, when the transition size is reached the number of dislocation to be nucleated increases drastically. This effect is particularly notable in lab conditions of strain rate, where we go from a single dislocation to saturation between 200 and 250 nm size.

## 5.4 Conclusion

In this chapter, we introduced the dislocation nucleation algorithm integrated in El-Numodis. Two approaches are presented: a simplified approach that is applied to a copper test-case and an extended approach here applied to a more quantitative study: the deformation of MgO NCs under compression. In the first approach, SDN in the copper cuboid relies on three nucleation sites (with various activation energies) that are used to start investigating dislocation nucleation using TST and KMC under constant applied stress. Two relatively lower activation energy values are assigned to two different corner nucleation sites and one higher value is used for a mid-surface nucleation site. By direct implementation the TST equations into a MATLAB script, it was possible to study the evolution of the probability density of individual nucleation sites based on their activation energies before and after nucleation events. For instance, sites with lower activation energies have shown a larger probability densities and *vice versa*. Besides, the shutdown of nucleation sites (once nucleated) tends to increase the nucleation probability within the remaining ones.
After preliminary tests, a simplified dislocation nucleation algorithm was implemented in El-Numodis. It consists on a simple scheme where the applied stress is considered to be homogeneously distributed trough all the sample. In this simplified approach, the nucleation is calculated using TST accounting for a "waiting time" after a nucleation event (site shutdown) to avoid repetitive nucleation from the same location. The simulation was applied at two different temperatures using $\sum S_i = 1$ to ensure successful nucleation.
An extended version of the nucleation algorithm dedicated to constant strain rate simulations is then described. This more complex approach was applied to dislocation nucleation in MgO NPs for which an activation energy database was derived from a multi-step NEB method at the atomic [AMO 21a]. This time, a competition between the simulation real time and the nucleation time obtained from TST equations influence the nucleation stress and rate. The particularity of this per-site approach (in comparison to the simplified model) is to be able to account for local stress variations, in the vicinity of the surface. It allows for a better selection of the nucleation site and automatically include/exclude a site from where a dislocation has previously nucleated. After a dislocation nucleation event, the simulation shows a temporary stress reduction near the nucleation site (including several neighboring sites) automatically cancelling the whole domain until the local stress reincreases. The model was applied to MgO NCs under compression, using similar parameters than those used by Issa *et al.* [ISS 15] for MD simulations. Finally, the extended model is used to investigate the effect of temperature, strain rate and sample size. Assuming the simplifications made in our approach, results obtained using El-Numodis are pretty close to those inferred from atomistic simulations.

**Chapter 5: to remember**

- Two dislocation nucleation algorithms were integrated to El-Numodis based on the transition state theory and kinetic Monte-Carlo approaches. It relies on activation energy selection criteria.
- A simplified model is here applied to copper nanocubes while an extended version of the algorithm is applied to MgO ceramic nanocubes.
- At low temperature, corners dislocation nucleation prevail.
- At high temperature, corners and center dislocation nucleation event are observed.
- Higher temperatures promote more nucleation events in a shorter time.
- The use of activation energy nudged elastic band databases within a transition state theory framework allows to reproduce the results inferred from molecular dynamics nanocompression tests in the case of MgO nanocubes using El-Numodis.
- Atomistically-informed El-Numodis is a reliable way to study the effect of sample size, strain rate and temperature on the mechanical properties of nanoparticles.
- Simulations varying strain rate and sample size at room temperature allow to parse conditions where the deformation of MgO nanocubes is nucleation-controlled.
- Increasing the strain rate increases the yield stress while increasing the temperature reduces it.
- Nucleation is more sensitive to temperature, especially at lower strain rate.

# Conclusion and perspectives

The present PhD manuscript relies on the development of a multi-scale simulation tool called El-Numodis based on the superposition method to investigate the mechanical properties of nano- and micro-crystals. El-Numodis, allows for simulations on a wide time and size scales using discrete dislocation dynamics coupled to finite-element method, possibly informed by lower-scale simulations. The code can handle various situations where surfaces can influence the mechanical response, starting from a predefined dislocation microstructure or nucleating new defects from the surfaces or from the bulk. El-Numodis was conceived in a simple way taking advantages of the object-oriented programming roots of Numodis. As a result, El-Numodis will be easily upgradeable in the future by any person with discrete knowledge in programming. In the following, the main outcomes of my PhD thesis are recalled and discussed.

Initially, the main purpose of El-Numodis was to build a multi-scale simulation framework accounting for surfaces forces in mechanical simulations. To evaluate the correct implementation of the software, the exact theoretical solution of basic problems involving image stress calculations were compared to El-Numodis outcomes. Before any comparison, the first step consisted in verifying that the discrete dislocation dynamics functions correctly reproduced dislocation stress fields. Stress distributions for infinite edge and screw dislocations as computed by El-Numodis were successfully compared to the analytical outcomes of the non singular theory of Cai [CAI 06]. Following the theoretical steps found in the book of Hirth and Lothe [HIR 82], we have verified the role of the Airy function on stress-free boundary conditions investigating precision and mesh quality. We have shown that a refined mesh in stress-concentrated regions was able to generate better results than using a regular fine mesh everywhere. El-Numodis was also tested successfully against the square loop dislocation case and the Gosling and Willis theory [GOS 94, FIV 96]. All this cases have shown the crucial role played by mesh refinement. Also, the pseudo-mirror image dislocation construction introduced by Weygand *et al.* [WEY 02] was implemented in El-Numodis (and Numodis standalone) and tested in this work. We confirmed that solving BVPs using the pseudo-mirror dislocation method and the superposition method together allows to use coarser finite-element mesh. Normally, the use of coarser meshes in finite-elements simulations allows to save computational processing time at the cost of precision sacrifices. However, the combination of both finite-elements and pseudo-mirror dislocations method allows to maintain a considerable precision with an acceptable mesh quality in El-Numodis. Using face-centered cubic thin film as a playground, we have studied the effect of surfaces and the stress corrections carried by the superposition method, the pseudo-mirror construction and the combination of both methods together. On thicker films, we have shown than the finite element method with or without the mirror-image construction, reduces stress value at the yield point when compared to pure discrete dislocation dynamics simulation, however, without significant differences on the flow stress emphasizing the weak influence of surfaces in larger size samples. Nevertheless, surface effects were increased when considering a thinner sample and a direct comparison between Numodis and El-Numodis outcomes ended up in an increase of the yield stress differences and in a net change regarding the flow stress. Finally, we have seen that the cutoff used in the pseudo-mirror dislocation method might have an impact on simulations results and further investigations would be required to better understand the role of the cutoff and properly set it.

The last part of the thesis was dedicated to the implementation of a dislocation nucleation algorithm and its application MgO ceramic nanoparticles. Indeed, two versions referred as *simplified* and *extended* respectively were implemented in El-Numodis. Both are based on the transition state theory and kinetic Monte-Carlo including dislocation nucleation energy barrier at various nucleation sites as inputs. The simplified version allows for constant stress simulations while the extended one was later used in imposed strain rate simulations. The simplified algorithm allowed to test the correct implementation of new objects such as half and quarter dislocation loops heterogeneous dislocation nucleation processes in El-Numodis. At the same time, it has provided significant piece of information on understanding the effect of temperature, how to tune the nucleation probability at each site as well as on the relation between the number of nucleation attempts and the simulation timestep. The extended version of the nucleation algorithm allows to describe surface dislocation nucleation in a framework where the local stress can vary. It was applied here to surface dislocation nucleation in MgO nanoparticles under compression, a topic for which site-dependent surface dislocation nucleation energy barriers are available from the literature [AMO 21a]. The atomistically-informed nucleation algorithm was developed accounting for activation energy maps and nucleation radii. Imposed strain rate simulations for various size of MgO nanocubes were performed and we have first performed a comparison between El-Numodis and molecular dynamics published data. The simulations showed the prevalence of corner nucleation over surface nucleation, as reported in the seminal work of Issa *et al.* [ISS 15]. The nucleation stress computed using El-Numodis at $\varepsilon = 11$ % were found to be in particularly good agreement with molecular dynamics outcomes of Issa *et al.* Some differences were found regarding to post-nucleation stress drops as well as the triggered stress of the subsequent nucleation events. The second relies on the limits of the nucleation model used. Indeed, El-Numodis does not integrate the formation of surface step when a dislocation nucleate (or escape) from the sample surface. Thus, simulations involving dislocation nucleation and starvation cycles are expected to happen at the same triggered stress. Also, the different stress drop amplitude between superposition method and molecular dynamics is believed to be attributed to the difference in terms of dislocation mobility law. Also El-Numodis is for now constant-shape (small-deformation principle) what could influence the mechanics at larger strains. All are development paths for the coming years.

The final goal of the PhD was originally to be able to test nanoparticles in the laboratory conditions of deformation *i.e.,* at lower strain rate than in molecular dynamics and for at least 100-nm sized nanoparticles. In particular, we wanted to verify the possible transition from a pure nucleation/exhaustion regime to a bulk-like multiplication deformation regime *i.e.,* answering the question "At what time and size scales does a dislocation microstructure stabilizes within a nanoparticle?". This was only partially fulfilled and we have been able to investigate the effects of strain rate, temperature and nanoparticles size only on the yield stress of MgO nanoparticles (and not to investigate larger-strain properties) and not on dislocation dynamics properties at larger strains. Indeed, we identified a yield stress reduction of only 12 % when the imposed strain rate was reduced from $10^9$ (molecular dynamics conditions) to $10^{-2}$ $s^{-1}$ (experimental conditions of deformation), in agreement with the transition state theory. This is particularly limited, especially when compared to metals that can reach yield stress decrease more than 50 % lowering the strain rate [ZHU 08]. This result confirm the particular high-strength of ceramic under compression and the fact that molecular dynamics is particularly suited to investigate the mechanical properties of ceramic nanocrystals. On the other hand, the yield strength was found to be more sensitive to temperature (in comparison to strain rate) what could have significant implications when sintering ceramics at intermediate and high temperatures. Finally, three different values of strain rates were used on simulations with sample size ranging from 25 to 250 nm. Overall, increasing the sample size increases the number of dislocation that nucleate when the sample yields and this effect compete with strain rate *i.e.,* the larger the strain rate the larger the number of defects that nucleate. Pushing the limits of El-Numodis, we have identified conditions (in terms of size and strain rate) where surface dislocation nucleation saturates the number of available sites at the surface of the sample leading to peculiar behaviors. In this regime, one can imagine that dislocations will later be able to form dislocation microstructure, as observed in the work of Issa *et al.* for comparable critical sizes [ISS 21]. However, further investigations are required to finally conclude about this major question.

## Perspectives

My PhD thesis lets some directions to be explored regarding hybrid dislocation dynamics/finite-element simulations. Some of them are related to specific topics such as the use of the transition state theory when relying on the surface dislocation nucleation process or the study of small-scale deformation. In the following, perspectives are exposed starting from basics associated to computational performances.

First, while Elmer and Numodis are both parallel, El-Numodis was conceived as a non parallel method. Indeed, when starting the development of El-Numodis, Numodis was still single processor software and I had at that time no skills on parallel coding. Thus, I recommend to parallelize the data interchange between the both codes (even if it is not the most expensive part of the coupling). Also, El-Numodis is currently using hexahedron elements to mesh the samples. For simulation cells with non regular shapes, I recommend to quickly introduce more versatile mesh elements such as 20 or 28 nodes hexahedron, or 10 nodes tetrahedron that are commonly used in finite-element simulations. This would require to adapt stress to force and interpolation algorithms as described in sections 3.2.3 and 3.2.4. Also, a possibility to remesh simulation volumes on-the-fly would be a real plus. Still in terms of computational costs, El-Numodis could be optimized by performing the assembly process only once at the beginning of the simulation or periodically during the simulation process. This would largely contribute to the decrease of the computational costs.

Concerning simulation of small-scale objects using superposition method, modeling deformation using displacement controlled boundary conditions has not been studied while theory elements are provided in Chapter 3. Further tests on displacement fields are needed to ensure right calculations of the dislocation displacement fields, before validating imposed strain rates simulations using displacement controlled boundary conditions. Also, the pseudo-mirror dislocation method needs to be further investigated to better understand the effect of the cutoff distance on the influence of surfaces on dislocations. Indeed, investigations ran here on thin films revealed that an incorrect cutoff distance selection can affect simulation outcomes such as the yield stress.

The influence of temperature on the surface dislocation nucleation process needs to be evaluated in larger samples. During this work, only the smaller samples were used to investigate temperature effects and it does not allow for the full investigation of the process. Moreover, the surface dislocation nucleation database might be interpolated and the number of nucleation sites increased when enlarging the sample size in order to more rigorously account for potential size-effect. Finally, the investigation of the size dependence should be continued in order to emphasize the transition between a pure nucleation/exhaustion regime in nano-objects and the bulk-like multiplication regime in larger samples.

# References

[AHR 05] Ahrens J. P., Geveci B., Law C. C.
ParaView: An End-User Tool for Large-Data Visualization. *The Visualization Handbook*, 2005.

[AKB 12] Akbulut M.
Nanoparticle-Based Lubrication Systems. *Journal of Powder Metallurgy and Mining*, vol. 01, n° 01, 2012, p. 1–3.

[ALA 15] Alam P.
Mechanical Properties of Bio-Nanostructured Materials. *Handbook of Mechanical Nanostructuring*, vol. 1, 2015, p. 211–233.

[ALT 10] Altenbach H., Eremeyev V. A., Lebedev L. P.
On the existence of solution in the linear elasticity with surface stresses. *ZAMM Zeitschrift fur Angewandte Mathematik und Mechanik*, vol. 90, n° 3, 2010, p. 231–240.

[AMO 17] Amodeo J., Lizoul K.
Mechanical properties and dislocation nucleation in nanocrystals with blunt edges. *Materials and Design*, vol. 135, 2017, p. 223–231.

[AMO 21a] Amodeo J., Maras E., Rodney D.
Site dependence of surface dislocation nucleation in ceramic nanoparticles. *npj Computational Materials*, vol. 7, n° 60, 2021, p. 1–7.

[AMO 21b] Amodeo J., Pizzagalli L.
Modeling the mechanical properties of nanoparticles: a review. *Comptes Rendus Physique*, vol. 22, n° S3, 2021, p. 35–66.

[ANS 04] ANSI I.
. ISO/IEC 1539-1: 2004 (E): Information technology—Programming languages—Fortran Part 1: Base Language. pages xiv+ 569, 2004.

[ARS 07] Arsenlis A., Cai W., Tang M., Rhee M., Oppelstrup T., Hommes G., Pierce T. G., Bulatov V. V.
Enabling strain hardening simulations with dislocation dynamics. *Modelling and Simulation in Materials Science and Engineering*, vol. 15, n° 6, 2007, p. 553–595.

[BAR 85] Barnett D. M.
The displacement field of a triangular dislocation loop. *Philosophical Magazine A:*

*Physics of Condensed Matter, Structure, Defects and Mechanical Properties*, vol. 51, n° 3, 1985, p. 383–387.

[BAR 07] Barnett D. M., Balluffi R. W.
The displacement field of a triangular dislocation loop-a correction with commentary. *Philosophical Magazine Letters*, vol. 87, n° 12, 2007, p. 943–944.

[BEA 03] Beazley D. M.
Automated scientific software scripting with SWIG. *Future Generation Computer Systems*, vol. 19, n° 5 SPEC, 2003, p. 599–609.

[Bel 17] Bel Haj Salah S., Gerard C., Pizzagalli L.
Influence of surface atomic structure on the mechanical response of aluminum nanospheres under compression. *Computational Materials Science*, vol. 129, 2017, p. 273–278.

[BEN 07] Benkassem S., Capolungo L., Cherkaoui M.
Mechanical properties and multi-scale modeling of nanocrystalline materials. *Acta Materialia*, vol. 55, n° 10, 2007, p. 3563–3572.

[BER 15] Bertin N., Upadhyay M. V., Pradalier C., Capolungo L.
A FFT-based formulation for efficient mechanical fields computation in isotropic and anisotropic periodic discrete dislocation dynamics. *Modelling and Simulation in Materials Science and Engineering*, vol. 23, n° 6, 2015, p. 1–31.

[BER 19] Bertin N.
Connecting discrete and continuum dislocation mechanics: A non-singular spectral framework. *International Journal of Plasticity*, vol. 122, 2019, p. 268–284.

[BIA 13] Bian J. J., Wang G. F.
Atomistic deformation mechanisms in copper nanoparticles. *Journal of Computational and Theoretical Nanoscience*, vol. 10, n° 9, 2013, p. 2299–2303.

[BIA 18] Bian J. J., Yang L., Niu X. R., Wang G. F.
Orientation-dependent deformation mechanisms of bcc niobium nanoparticles. *Philosophical Magazine*, vol. 98, n° 20, 2018, p. 1848–1864.

[BOU 10] Bouaziz O., Estrin Y., Bréchet Y., Embury J. D.
Critical grain size for dislocation storage and consequences for strain hardening of nanocrystalline materials. *Scripta Materialia*, vol. 63, n° 5, 2010, p. 477–479.

[BRO 18] Bromage B., Tarleton E.
Calculating dislocation displacements on the surface of a volume. *Modelling and Simulation in Materials Science and Engineering*, vol. 26, n° 8, 2018.

[BUL 06] Bulatov V. V., Hsiung L. L., Tang M., Arsenlis A., Bartelt M. C., Cai W., Florando J. N., Hiratani M., Rhee M., Hommes G., Pierce T. G., De La Rubia T. D.
Dislocation multi-junctions and strain hardening. *Nature*, vol. 440, n° 7088, 2006, p. 1174–1178.

[CAI 06] Cai W., Arsenlis A., Weinberger C. R., Bulatov V. V.
A non-singular continuum theory of dislocations. *Journal of the Mechanics and Physics of Solids*, vol. 54, n° 3, 2006, p. 561–587.

[CAL 12] Calvié E., Joly-Pottuz L., Esnouf C., Clément P., Garnier V., Chevalier J., Jorand Y., Malchère A., Epicier T., Masenelli-Varlot K.
Real time TEM observation of alumina ceramic nano-particles during compression. *Journal of the European Ceramic Society*, vol. 32, n° 10, 2012, p. 2067–2071, Elsevier Ltd.

[CAL 14] Calvié E., Réthoré J., Joly-Pottuz L., Meille S., Chevalier J., Garnier V., Jorand Y., Esnouf C., Epicier T., Quirk J. B., Masenelli-Varlot K.
Mechanical behavior law of ceramic nanoparticles from transmission electron microscopy in situ nano-compression tests. *Materials Letters*, vol. 119, 2014, p. 107–110.

[CHA 10] Chang H. J., Fivel M., Rodney D., Verdier M.
Simulations multi-échelles de l'indentation de métaux CFC: De l'atome au milieu continu. *Comptes Rendus Physique*, vol. 11, n° 3-4, 2010, p. 285–292.

[CHE 17] Cheng G., Yin S., Chang T. H., Richter G., Gao H., Zhu Y.
Anomalous Tensile Detwinning in Twinned Nanowires. *Physical Review Letters*, vol. 119, n° 25, 2017, p. 1–6.

[CHE 19] Chen Y., Renner P., Liang H.
Dispersion of nanoparticles in lubricating oil: A critical review. *Lubricants*, vol. 7, n° 1, 2019.

[CHE 20a] Chen S., Aitken Z. H., Wu Z., Yu Z., Banerjee R., Zhang Y. W.
Hall-Petch and inverse Hall-Petch relations in high-entropy CoNiFeAlxCu1-x alloys. *Materials Science and Engineering A*, vol. 773, 2020, Page 138873.

[CHE 20b] Cheng G., Yin S., Li C., Chang T. H., Richter G., Gao H., Zhu Y.
In-situ TEM study of dislocation interaction with twin boundary and retraction in twinned metallic nanowires. *Acta Materialia*, vol. 196, 2020, p. 304–312.

[CHE 22] Chen S., Liu F., Liu B., Chen X., Ke X., Zhang M., Tang X., Guan P., Zhang Z., Shan Z., Yu Q.
Reaching near-theoretical strength by achieving quasi-homogenous surface dislocation nucleation in MgO particles. *Materials Today*, vol. 55, 2022, p. 37-45.

[CRO 14] Crone J. C., Chung P. W., Leiter K. W., Knap J., Aubry S., Hommes G., Arsenlis A.
A multiply parallel implementation of finite element-based discrete dislocation dynamics for arbitrary geometries. *Modelling and Simulation in Materials Science and Engineering*, vol. 22, n° 3, 2014, Page 035014.

[CUI 15] Cui Y., Liu Z., Zhuang Z.
Quantitative investigations on dislocation based discrete-continuous model of crystal

plasticity at submicron scale. *International Journal of Plasticity*, vol. 69, 2015, p. 54–72.

[CUI 16] CUI Y.
*The Investigation of Plastic Behavior by Discrete Dislocation Dynamics for Single Crystal Pillar at Submicron Scale.* Springer, 2016.

[CUI 20] CUI Y., DING M., SUI T., ZHENG W., QIAO G., YAN S., LIU X.
Role of nanoparticle materials as water-based lubricant additives for ceramics. *Tribology International*, vol. 142, 2020, Page 105978, Elsevier Ltd.

[DAI 16] DAI W., KHEIREDDIN B., GAO H., LIANG H.
Roles of nanoparticles in oil lubrication. *Tribology International*, vol. 102, 2016, p. 88–98, Elsevier.

[DEV 11] DEVINCRE B., MADEC R., MONNET G., QUEYREAU S., GATTI R., KUBIN L.
Modeling crystal plasticity with dislocation dynamics simulations: the 'microMegas' code. vol. 1 de *Mechanics of nano-objects*, p. 81–100 2011.

[DON 06] DONNELLY S. E., HINKS J. A., EDMONDSON P. D., PILKINGTON R. D., YAKUSHEV M., BIRTCHER R. C.
In situ transmission electron microscopy studies of radiation damage in copper indium diselenide. *Nuclear Instruments and Methods in Physics Research, Section B: Beam Interactions with Materials and Atoms*, vol. 242, n° 1-2, 2006, p. 686–689.

[DRO 14] DROUET J., DUPUY L., ONIMUS F., MOMPIOU F., PERUSIN S., AMBARD A.
Dislocation dynamics simulations of interactions between gliding dislocations and radiation induced prismatic loops in zirconium. *Journal of Nuclear Materials*, vol. 449, n° 1-3, 2014, p. 252–262.

[DU 15] DU Z., ZENG X. M., LIU Q., LAI A., AMINI S., MISEREZ A., SCHUH C. A., GAN C. L.
Size effects and shape memory properties in ZrO2 ceramic micro- and nano-pillars. *Scripta Materialia*, vol. 101, 2015, p. 40–43.

[ELA 08] EL-AWADY J. A., BULENT BINER S., GHONIEM N. M.
A self-consistent boundary element, parametric dislocation dynamics formulation of plastic flow in finite volumes. *Journal of the Mechanics and Physics of Solids*, vol. 56, n° 5, 2008, p. 2019–2035.

[ELS 07] ELSSFAH E. M., TANG C. C., ZHANG J., SONG H. S., DING X. X., QI S. R.
Low-temperature performance of Al4B2O9 nanowires. *Materials Research Bulletin*, vol. 42, n° 3, 2007, p. 482–486.

[Esh 66] ESHELBY J. D.
A simple derivation of the elastic field of an edge dislocation. *British Journal of Applied Physics*, vol. 17, n° 9, 1966, p. 1131–1135.

[FAN 05] FAN G. J., CHOO H., LIAW P. K., LAVERNIA E. J.
A model for the inverse Hall-Petch relation of nanocrystalline materials. *Materials*

*Science and Engineering A*, vol. 409, n° 1-2, 2005, p. 243–248.

[FAR 05] Farkas D., Hyde B.
Improving the ductility of nanocrystalline bcc metals. *Nano Letters*, vol. 5, n° 12, 2005, p. 2403–2407.

[FED 03] Fedorov A. A., Gutkin M., Ovid'ko I. A.
Transformations of grain boundary dislocation pile-ups in nano- and polycrystalline materials. *Acta Materialia*, vol. 51, n° 4, 2003, p. 887–898.

[FIN 20] Fincher C. D., Ojeda D., Zhang Y., Pharr G. M., Pharr M.
Mechanical properties of metallic lithium: from nano to bulk scales. *Acta Materialia*, vol. 186, 2020, p. 215–222.

[FIV 96] Fivel M. C., Gosling T. J., Canova G. R.
Implementing image stresses in a 3D dislocation simulation. *Modelling and Simulation in Materials Science and Engineering*, vol. 4, n° 6, 1996, p. 581–596.

[FIV 97] Fivel M.
Etudes numériques à différentes échelles de la déformation plastique des monocristaux de structure cfc. Thèse de doctorat, INP Grenoble, 1997.

[FIV 98] Fivel M. C., Robertson C. F., Canova G. R., Boulanger L.
Three-dimensional modeling of indent-induced plastic zone at a mesoscale. *Acta Materialia*, vol. 46, n° 17, 1998, p. 6183–6194.

[GAO 10] Gao Y., Liu Z. L., You X. C., Zhuang Z.
A hybrid multiscale computational framework of crystal plasticity at submicron scales. *Computational Materials Science*, vol. 49, n° 3, 2010, p. 672–681, Elsevier B.V.

[GER 17] Gerberich W., Tadmor E. B., Kysar J., Zimmerman J. A., Minor A. M., Szlufarska I., Amodeo J., Devincre B., Hintsala E., Ballarini R.
Review Article: Case studies in future trends of computational and experimental nanomechanics. *Journal of Vacuum Science Technology A: Vacuum, Surfaces, and Films*, vol. 35, n° 6, 2017, Page 060801.

[GOD 04] Godet J., Pizzagalli L., Brochard S., Beauchamp P.
Theoretical study of dislocation nucleation from simple surface defects in semiconductors. *Physical Review B - Condensed Matter and Materials Physics*, vol. 70, n° 5, 2004, p. 1–8.

[GOE 20] Goel S., Knaggs M., Goel G., Zhou X. W., Upadhyaya H. M., Thakur V. K., Kumar V., Bizarri G., Tiwari A., Murphy A., Stukowski A., Matthews A.
Horizons of modern molecular dynamics simulation in digitalized solid freeform fabrication with advanced materials. *Materials Today Chemistry*, vol. 18, 2020.

[GOS 94] Gosling T. J., Willis J. R.
A line-integral representation for the stresses due to an arbitrary dislocation in an

isotropic half-space. *Journal of the Mechanics and Physics of Solids*, vol. 42, n° 8, 1994, p. 1199–1221.

[GRE 11] Greer J. R., De Hosson J. T. M.
Plasticity in small-sized metallic systems: Intrinsic versus extrinsic size effect. *Progress in Materials Science*, vol. 56, n° 6, 2011, p. 654–724, Elsevier Ltd.

[GRO 70] Groves P. P., Bacon D. J.
The dislocation loop near a free surface. *Philosophical Magazine*, vol. 22, n° 175, 1970, p. 83–91.

[GRO 03] Groh S., Devincre B., Kubin L. P., Roos A., Feyel F., Chaboche J. L.
Dislocations and elastic anisotropy in heteroepitaxial metallic thin films. *Philosophical Magazine Letters*, vol. 83, n° 5, 2003, p. 303–313.

[GRO 04] Groh S., Devincre B., Feyel F., Kubin L., Roos A.
Discrete-continuum modeling of metal matrix composites plasticity. *Mesoscopic Dynamics in Fracture Process and Strength of Materials*, , 2004, p. 1–10.

[GRY 89] Gryaznov V. G., Kaprelov A. M., Romanov A. E.
Size effect of dislocation stability in small particles and microcrystallites. *Scripta metallurgica*, vol. 23, n° 8, 1989, p. 1443–1448.

[GUO 18] Guo D., Song S., Luo R., Goddard W. A., Chen M., Reddy K. M., An Q.
Grain Boundary Sliding and Amorphization are Responsible for the Reverse Hall-Petch Relation in Superhard Nanocrystalline Boron Carbide. *Physical Review Letters*, vol. 121, n° 14, 2018, p. 1–6.

[GUZ 16] Guziewski M., Yu H., Weinberger C. R.
*Modeling Dislocation Nucleation in Nanocrystals*, p. 373–411. Springer International Publishing, Cham, 2016.

[HAL 51] Hall E. O.
The deformation and ageing of mild steel: III Discussion of results. *Proceedings of the Physical Society. Section B*, vol. 64, n° 9, 1951, p. 747–753.

[HAN 98] Hannes J., Greg M., Karsten W. J.
*Nudged elastic band method for finding minimum energy paths of transitions*, p. 385-404. 1998.

[HAN 04] Hansen N.
Hall–Petch relation and boundary strengthening. *Scripta materialia*, vol. 51, n° 8, 2004, p. 801–806, Elsevier.

[HAR 99] Hartmaier A., Fivel M. C., Canova G. R., Gumbsch P.
Image stresses in a free-standing thin film. *Modelling and Simulation in Materials Science and Engineering*, vol. 7, n° 5, 1999, p. 781–793.

[HEA 53] Head A. K.

Edge dislocations in inhomogeneous media. *Proceedings of the Physical Society. Section B*, vol. 66, n° 9, 1953, p. 793–801.

[HEN 00] Henkelman G., Uberuaga B. P., Jónsson H.

A climbing image nudged elastic band method for finding saddle points and minimum energy paths. *The Journal of Chemical Physics*, vol. 113, n° 22, 2000, p. 9901-9904.

[HIN 09] Hinks J. A.

A review of transmission electron microscopes with in situ ion irradiation. *Nuclear Instruments and Methods in Physics Research, Section B: Beam Interactions with Materials and Atoms*, vol. 267, n° 23-24, 2009, p. 3652–3662.

[HIR 82] Hirth J. P., Lothe J.

*Theory of dislocations.* John Willey and Sons John Willey and Sons, 01 1982.

[HUA 17] Huang M., Liang S., Li Z.

An extended 3D discrete-continuous model and its application on single- and bi-crystal micropillars. *Modelling and Simulation in Materials Science and Engineering*, vol. 25, n° 3, 2017, p. 1 – 35.

[HUL 11] Hull D., Bacon D. J.

*Introduction to dislocations.* Elsevier, 5 édition, 2011.

[HUN 11] Hunter A., Saied F., Le C., Koslowski M.

Large-scale 3D phase field dislocation dynamics simulations on high-performance architectures. *International Journal of High Performance Computing Applications*, vol. 25, n° 2, 2011, p. 223–235.

[ISH 97] Ishino S.

A review of in situ observation of defect production with energetic heavy ions. *Journal of Nuclear Materials*, vol. 251, n° I 997, 1997, p. 225–236.

[ISS 15] Issa I., Amodeo J., Réthoré J., Joly-Pottuz L., Esnouf C., Morthomas J., Perez M., Chevalier J., Masenelli-Varlot K.

In situ investigation of MgO nanocube deformation at room temperature. *Acta Materialia*, vol. 86, 2015, p. 295-304.

[ISS 21] Issa I., Joly-Pottuz L., Amodeo J., Dunstan D. J., Esnouf C., Réthoré J., Garnier V., Chevalier J., Masenelli-Varlot K.

From dislocation nucleation to dislocation multiplication in ceramic nanoparticle. *Materials Research Letters*, vol. 9, n° 6, 2021, p. 278–283.

[JAC 98] Jackson J. D.

*Classical Electrodynamics.* John Willey and Sons John Willey and Sons, 08 1998.

[JAM 16] Jamond O., Gatti R., Roos A., Devincre B.

Consistent formulation for the Discrete-Continuous Model: Improving complex dislocation dynamics simulations. *International Journal of Plasticity*, vol. 80, 2016, p. 19–37.

[JAN 11] Jang D., Greer J. R.
Size-induced weakening and grain boundary-assisted deformation in 60 nm grained Ni nanopillars. *Scripta Materialia*, vol. 64, n° 1, 2011, p. 77–80, Acta Materialia Inc.

[JEN 10] Jennings A. T., Burek M. J., Greer J. R.
Microstructure versus Size: Mechanical properties of electroplated single crystalline Cu nanopillars. *Physical Review Letters*, vol. 104, n° 13, 2010, p. 1–4.

[JEN 11a] Jennings A. T., Greer J. R.
Heterogeneous dislocation nucleation from surfaces and interfaces as governing plasticity mechanism in nanoscale metals. *Journal of Materials Research*, vol. 26, n° 22, 2011, p. 2803–2814.

[JEN 11b] Jennings A. T., Li J., Greer J. R.
Emergence of strain-rate sensitivity in Cu nanopillars: Transition from dislocation multiplication to dislocation nucleation. *Acta Materialia*, vol. 59, n° 14, 2011, p. 5627–5637.

[JOH 20] Johnson S. R., Prokopenko A., Evans K. J., Carver J., Morris K.
Automated Fortran-C++ Bindings for Large-Scale Scientific Applications. *Computing in Science and Engineering*, vol. 22, n° 5, 2020, p. 84–94.

[KAN 07] Kang K., Cai W.
Brittle and ductile fracture of semiconductor nanowires - molecular dynamics simulations. *Philosophical Magazine*, vol. 87, n° 14-15, 2007, p. 2169–2189.

[KEL 98] Keller R.-M., Baker S. P., Arzt E.
Quantitative analysis of strengthening mechanisms in thin Cu films: Effects of film thickness, grain size, and passivation. *Journal of Materials Research*, vol. 13, n° 5, 1998, p. 1307–1317.

[KIE 11] Kiener D., Minor A. M.
Source truncation and exhaustion: Insights from quantitative in situ TEM tensile testing. *Nano Letters*, vol. 11, n° 9, 2011, p. 3816–3820.

[KIL 18] Kilymis D., Gérard C., Amodeo J., Waghmare U. V., Pizzagalli L.
Uniaxial compression of silicon nanoparticles: An atomistic study on the shape and size effects. *Acta Materialia*, vol. 158, 2018, p. 155–166, Acta Materialia Inc.

[KIL 19] Kilymis D., Gérard C., Pizzagalli L.
Ductile deformation of core-shell Si-SiC nanoparticles controlled by shell thickness. *Acta Materialia*, vol. 164, 2019, p. 560–567.

[KIM 08] Kim J. Y., Greer J. R.
Size-dependent mechanical properties of molybdenum nanopillars. *Applied Physics Letters*, vol. 93, n° 10, 2008, p. 1–4.

[KOC 03] Koch C. C.
Optimization of strength and ductility in nanocrystalline and ultrafine grained metals. *Scripta Materialia*, vol. 49, n° 7, 2003, p. 657–662.

[KOH 20] Kohnert A. A., Tummala H., Lebensohn R. A., Tomé C. N., Capolungo L.

On the use of transmission electron microscopy to quantify dislocation densities in bulk metals. *Scripta Materialia*, vol. 178, 2020, p. 161–165.

[KOL 07] Kolesnikova A. L., Ovid'ko I. A., Romanov A. E.

Dislocation-disclination transformations and the reverse Hall-Petch effect in nanocrystalline materials. *Technical Physics Letters*, vol. 33, n° 8, 2007, p. 641–644.

[KOM 01] Komanduri R., Raff L. M.

A review on the molecular dynamics simulation of machining at the atomic scale. *Proceedings of the Institution of Mechanical Engineers, Part B: Journal of Engineering Manufacture*, vol. 215, n° 12, 2001, p. 1639–1672.

[KOR 11] Korte S., Clegg W. J.

Discussion of the dependence of the effect of size on the yield stress in hard materials studied by microcompression of MgO. *Philosophical Magazine*, vol. 91, n° 7-9, 2011, p. 1150–1162.

[KRA 10] Kraft O., Gruber P. A., Mönig R., Weygand D.

Plasticity in confined dimensions. *Annual Review of Materials Research*, vol. 40, n° 1, 2010, p. 293–317.

[KUB 92] Kubin L. P., Canova G., Condat M., Devincre B., Pontikis V., Bréchet Y.

Dislocation Microstructures and Plastic Flow: A 3D Simulation. *Solid State Phenomena*, vol. 23-24, 1992, p. 455–472.

[KUB 13] Kubin L. P.

*Dislocations, Mesoscale Simulations and Plastic Flow.* Oxford University Press, 2013.

[LAI 13] Lai A., Du Z., Gan C. L., Schuh C. A.

Shape memory and superelastic ceramics at small scales. *Science*, vol. 341, n° 6153, 2013, p. 1505–1508.

[LAM 20] Lam T. N., Lee S. Y., Tsou N. T., Chou H. S., Lai B. H., Chang Y. J., Feng R., Kawasaki T., Harjo S., Liaw P. K., Yeh A. C., Li M. J., Cai R. F., Lo S. C., Huang E. W.

Enhancement of fatigue resistance by overload-induced deformation twinning in a CoCrFeMnNi high-entropy alloy. *Acta Materialia*, vol. 201, 2020, p. 412–424, Elsevier Ltd.

[LAR 13] Larson M. G., Bengzon F.

*The Finite Element Method: Theory, Implementation, and Applications (Texts in Computational Science and Engineering).* 2013.

[LAV 75] Lavrentev F. F., Pokhil Y. A.

Relation of dislocation density in different slip systems to work hardening parameters for magnesium crystals. *Materials Science and Engineering*, vol. 18, n° 2, 1975, p. 261–270.

[LEB 01] Lebensohn R. A.
N-site modeling of a 3D viscoplastic polycrystal using Fast Fourier Transform. *Acta Materialia*, vol. 49, n° 14, 2001, p. 2723–2737.

[LEB 12] Lebensohn R. A., Kanjarla A. K., Eisenlohr P.
An elasto-viscoplastic formulation based on fast Fourier transforms for the prediction of micromechanical fields in polycrystalline materials. *International Journal of Plasticity*, vol. 32-33, 2012, p. 59–69.

[LEE 07] Lee C. L., Li S.
A half-space Peierls-Nabarro model and the mobility of screw dislocations in a thin film. *Acta Materialia*, vol. 55, n° 6, 2007, p. 2149–2157.

[LEE 08] Lee C. L., Li S.
The size effect of thin films on the Peierls stress of edge dislocations. *Mathematics and Mechanics of Solids*, vol. 13, n° 3-4, 2008, p. 316–335.

[LEE 14] Lee S., Im J., Yoo Y., Bitzek E., Kiener D., Richter G., Kim B., Oh S. H.
Reversible cyclic deformation mechanism of gold nanowires by twinning-detwinning transition evidenced from in situ TEM. *Nature Communications*, vol. 5, 2014, p. 1–10.

[LEE 20] Lee S., Vaid A., Im J., Kim B., Prakash A., Guénolé J., Kiener D., Bitzek E., Oh S. H.
In-situ observation of the initiation of plasticity by nucleation of prismatic dislocation loops. *Nature Communications*, vol. 11, n° 1, 2020, p. 1–11, Springer US.

[LEM 99a] Lemarchand C., Chaboche J. L., Devincre B., Kubin L. P.
Multiscale modelling of plastic deformation. *J. Phys. IV France*, vol. 9, n° PR9, 1999, p. 271–277.

[LEM 99b] Lemarchand C., Devincre B., Kubin L. P., Chaboche J. L.
Coupled meso-macro simulations of plasticity: validation tests. *Materials Research Society Symposium - Proceedings*, vol. 538, 1999, p. 63–68.

[LEM 01] Lemarchand C., Devincre B., Kubin L. P.
Homogenization method for a discrete-continuum simulation of dislocation dynamics. *Journal of the Mechanics and Physics of Solids*, vol. 49, n° 9, 2001, p. 1969–1982.

[LI 64] Li J. C.
Stress field of a dislocation segment. *Philosophical Magazine*, vol. 10, n° 108, 1964, p. 1097–1098.

[LI 13] Li X., Wang C., Xiao J., Qin Y.
Applications of nanotechnology in hip implants. *Advanced Materials Research*, vol. 662, 2013, p. 218–222.

[LIA 05] Liang H., Upmanyu M., Huang H.
Size-dependent elasticity of nanowires: Nonlinear effects. *Physical Review B - Condensed Matter and Materials Physics*, vol. 71, n° 24, 2005, p. 1–4.

[LIU 09] Liu Z. L., Liu X. M., Zhuang Z., You X. C.
A multi-scale computational model of crystal plasticity at submicron-to-nanometer scales. *International Journal of Plasticity*, vol. 25, n° 8, 2009, p. 1436–1455.

[LOT 82] Lothe J., Indenbom V. L., Chamrov V. A.
Elastic Field and Self-Force of Dislocations Emerging at the Free Surfaces of an Anisotropic Halfspace. *Physica Status Solidi (B)*, vol. 111, n° 2, 1982, p. 671–677.

[LU 07] Lu A. H., Salabas E. L., Schüth F.
Magnetic nanoparticles: Synthesis, protection, functionalization, and application. *Angewandte Chemie - International Edition*, vol. 46, n° 8, 2007, p. 1222–1244.

[LUB 93] Lubarda V. A., Blume J. A., Needleman A.
An analysis of equilibrium dislocation distributions. *Acta Metallurgica Et Materialia*, vol. 41, n° 2, 1993, p. 625–642.

[MAD 03] Madec R., Devincre B., Kubin L., Hoc T., Rodney D.
The role of collinear interaction in dislocation-induced hardening. *Science*, vol. 301, 2003, p. 1879–1882.

[MAD 04] Madec R., Kubin L. P.
Dislocation Interactions and Symmetries in BCC Crystals. Kitagawa H., Shibutani Y., Eds., *IUTAM Symposium on Mesoscopic Dynamics of Fracture Process and Materials Strength*, vol. 115, Dordrecht, 2004 Springer Netherlands, p. 69–78.

[MAD 13] Madec R., Veyssière P., Saada G.
Frank-Read source mechanism, mobile dislocation density exhaustion and flow stress anomaly in L12 alloys: A dislocation dynamics study. *Philosophical Magazine*, vol. 93, n° 1-3, 2013, p. 222–234.

[MAL 13] Malinen M., Råback P.
*Elmer finite element solver for multiphysics and multiscale problems*, vol. 19, p. 101-113. 09 2013.

[MAR 04] Marian J., Cai W., Bulatov V. V.
Dynamic transitions from smooth to rough to twinning in dislocation motion. *Nature Materials*, vol. 3, n° 3, 2004, p. 158–163.

[MCD 08] McDowell M. T., Leach A. M., Gall K.
On the elastic modulus of metallic nanowires. *Nano Letters*, vol. 8, n° 11, 2008, p. 3613–3618.

[MEY 06] Meyers M. A., Mishra A., Benson D. J.
Mechanical properties of nanocrystalline materials. *Progress in Materials Science*, vol. 51, n° 4, 2006, p. 427–556.

[MIA 17] Miao Y., Harp J., Mo K., Bhattacharya S., Baldo P., Yacout A. M.
In-situ TEM ion irradiation investigations on U3Si2 at LWR temperatures. *Journal of Nuclear Materials*, vol. 484, 2017, p. 168–173, Elsevier Ltd.

[MIC 08] Michler G.H. Godehardt R. A. R.
*Problems Associated with the Electron Microscopy*, p. 175–183. Springer Berlin Heidelberg, Berlin, Heidelberg, 2008.

[MOH 07] Mohanraj V. J., Chen Y.
Nanoparticles - A review. *Tropical Journal of Pharmaceutical Research*, vol. 5, n° 1, 2007, p. 561–573.

[MOR 73] Mori T., Tanaka K.
Average stress in matrix and average elastic energy of materials with misfitting inclusions. *Acta Metallurgica*, vol. 21, n° 5, 1973, p. 571–574.

[MOR 11] Mordehai D., Lee S. W., Backes B., Srolovitz D. J., Nix W. D., Rabkin E.
Size effect in compression of single-crystal gold microparticles. *Acta Materialia*, vol. 59, n° 13, 2011, p. 5202–5215.

[MOU 94] Moulinec H., Suquet P.
A fast numerical method for computing the linear and nonlinear mechanical properties of composites. *Comptes rendus de l'Académie des sciences. Série II, Mécanique, physique, chimie, astronomie*, vol. 318, n° 11, 1994, p. 1417–1423.

[MOU 98] Moulinec H., Suquet P.
A numerical method for computing the overall response of nonlinear composites with complex microstructure. *Computer Methods in Applied Mechanics and Engineering*, vol. 157, n° 1-2, 1998, p. 69–94.

[MUR 63] Mura T.
Continuous distribution of moving dislocations. *Philosophical Magazine*, vol. 8, n° 89, 1963, p. 843–857.

[MUR 87] Mura T.
*Mechanics of elastic and inelastic solids.* Martinus Nijhoff Publishers, 2 édition, 1987.

[NAG 15] Nagase T., Rack P. D., Noh J. H., Egami T.
In-situ TEM observation of structural changes in nano-crystalline CoCrCuFeNi multicomponent high-entropy alloy (HEA) under fast electron irradiation by high voltage electron microscopy (HVEM). *Intermetallics*, vol. 59, 2015, p. 32–42.

[NIU 17] Niu X., Luo T., Lu J., Xiang Y.
Dislocation climb models from atomistic scheme to dislocation dynamics. *Journal of the Mechanics and Physics of Solids*, vol. 99, 2017, p. 242–258.

[ODE 01] Odegard G. M., Gates T. S., Nicholson L. M., Wise K. E.
Equivalent-continuum modeling of nano-structured materials. *NASA Technical Memorandum*, vol. 62, n° 210863, 2001, p. 1–21.

[OH 09] Oh S. H., Legros M., Kiener D., Dehm G.
In situ observation of dislocation nucleation and escape in a submicrometre aluminium single crystal. *Nature Materials*, vol. 8, n° 2, 2009, p. 95–100.

[PAD 01] Padmanabhan K. A.
Mechanical properties of nanostructured materials. *Materials Science and Engineering A*, vol. 304-306, n° 1-2, 2001, p. 200–205.

[PAN 93] Pande C. S., Masumura R. A., Armstrong R. W.
Pile-up based hall-petch relation for nanoscale materials. *Nanostructured Materials*, vol. 2, n° 3, 1993, p. 323–331.

[PAR 09] Park H. S., Cai W., Espinosa H. D., Huang H.
Mechanics of crystalline nanowires. *MRS Bulletin*, vol. 34, n° 3, 2009, p. 178–183.

[PAR 14] Paranjpe M., Müller-Goymann C. C.
Nanoparticle-mediated pulmonary drug delivery: A review. *International Journal of Molecular Sciences*, vol. 15, n° 4, 2014, p. 5852–5873.

[PET 53] Petch N. J.
The cleavage strength of polycrystals. *Journal of the Iron and Steel Institute*, vol. 174, 1953, p. 25–28.

[PO 14] Po G., Mohamed M. S., Crosby T., Erel C., El-Azab A., Ghoniem N.
Recent Progress in Discrete Dislocation Dynamics and Its Applications to Micro Plasticity. *Jom*, vol. 66, n° 10, 2014, p. 2108–2120.

[PO 16] Po G., Cui Y., Rivera D., Cereceda D., Swinburne T. D., Marian J., Ghoniem N.
A phenomenological dislocation mobility law for bcc metals. *Acta Materialia*, vol. 119, 2016, p. 123–135, Elsevier Ltd.

[QIN 15] Qin Q., Yin S., Cheng G., Li X., Chang T. H., Richter G., Zhu Y., Gao H.
Recoverable plasticity in penta-twinned metallic nanowires governed by dislocation nucleation and retraction. *Nature Communications*, vol. 6, 2015, p. 1–8.

[ROY 09] Roy S., Pericàs M. A.
Functionalized nanoparticles as catalysts for enantioselective processes. *Organic and Biomolecular Chemistry*, vol. 7, n° 13, 2009, p. 2669–2677.

[ROY 19] Roy S., Gatti R., Devincre B., Mordehai D.
A multiscale study of the size-effect in nanoindentation of Au nanoparticles. *Computational Materials Science*, vol. 162, n° July 2018, 2019, p. 47–59, Elsevier.

[RUB 17] Rubio-Cervilla J., González E., Pomposo J. A.
Advances in single-chain nanoparticles for catalysis applications. *Nanomaterials*, vol. 7, n° 10, 2017, Page 341.

[RYO 18] Ryou H., Drazin J. W., Wahl K. J., Qadri S. B., Gorzkowski E. P., Feigelson B. N., Wollmershauser J. A.
Below the Hall-Petch Limit in Nanocrystalline Ceramics. *ACS Nano*, vol. 12, n° 4, 2018, p. 3083–3094.

[RYU 11] Ryu S., Kang K., Cai W.

Predicting the dislocation nucleation rate as a function of temperature and stress. *Journal of Materials Research*, vol. 26, n° 18, 2011, p. 2335–2354.

[SCH 98] Schiøtz J., Di Tolla F. D., Jacobsen K. W.

Softening of nanocrystalline metals at very small grain sizes. *Nature*, vol. 391, n° 6667, 1998, p. 561–563.

[SHE 19] Shen Q., Song Q., Li H., Xiao C., Wang T., Lin H., Li W.

Fatigue strengthening of carbon/carbon composites modified with carbon nanotubes and silicon carbide nanowires. *International Journal of Fatigue*, vol. 124, 2019, p. 411–421.

[SHI 15] Shi X. J., Dupuy L., Devincre B., Terentyev D., Vincent L.

Interaction of <1 0 0> dislocation loops with dislocations studied by dislocation dynamics in $\alpha$-iron. *Journal of Nuclear Materials*, vol. 460, 2015, p. 37–43.

[SON 08] Song J., Tranchida D., Vancso G. J.

Contact mechanics of UV/ozone-treated PDMS by AFM and JKR testing: Mechanical performance from nano- to micrometer length scales. *Macromolecules*, vol. 41, n° 18, 2008, p. 6757–6762.

[SUR 04] Suryanarayana C.

Nanostructured Materials Recent Developments , Present Issues , and Future Prospects. *Nanostructured Materials*, , n° March, 2004, p. 85–92.

[TAN 06] Tang M., Cai W., Xu G., Bulatov V. V.

A hybrid method for computing forces on curved dislocations intersecting free surfaces in three-dimensional dislocation dynamics. *Modelling and Simulation in Materials Science and Engineering*, vol. 14, n° 7, 2006, p. 1139–1151.

[TET 62] Tetelman A. S.

Dislocation dipole formation in deformed crystals. *Acta Metallurgica*, vol. 10, n° 9, 1962, p. 813–820.

[UCH 04] Uchic M. D., Dimiduk D. M., Florando J. N., Nix W. D.

Sample dimensions influence strength and crystal plasticity. *Science*, vol. 305, n° 5686, 2004, p. 986–989.

[UCH 09] Uchic M. D., Shade P. A., Dimiduk D. M.

Plasticity of micrometer-scale single crystals in compression. *Annual Review of Materials Research*, vol. 39, n° 1, 2009, p. 361–386.

[Van 95] Van der Giessen E., Needleman A.

Discrete dislocation plasticity: A simple planar model. *Modelling and Simulation in Materials Science and Engineering*, vol. 3, n° 5, 1995, p. 689–735.

[VAS 06] Vasily V. Bulatov W. C.

*Computer Simulations of Dislocations.* Oxford University Press, 2006.

[VAT 10] Vattré A., Devincre B., Roos A.

Orientation dependence of plastic deformation in nickel-based single crystal superalloys: Discrete-continuous model simulations. *Acta Materialia*, vol. 58, n° 6, 2010, p. 1938–1951.

[VAT 14] Vattré A., Devincre B., Feyel F., Gatti R., Groh S., Jamond O., Roos A.

Modelling crystal plasticity by 3D dislocation dynamics and the finite element method: The Discrete-Continuous Model revisited. *Journal of the Mechanics and Physics of Solids*, vol. 63, n° 1, 2014, p. 491–505.

[VOL 07] Volterra V.

Sur l'équilibre des corps élastiques multiplement connexes. *Annales scientifiques de l'École Normale Supérieure*, vol. 3e série, 24, 1907, p. 401–517.

[Wan 95] Wang, N. Wang, Z. Aust, K. T. Erb U.

Effect of grain size on mechanical properties of nanocrystalline materials. *Acta Metallurgica Et Materialia*, vol. 43, n° 2, 1995, Page 519.

[WAN 01] Wang Y. U., Jin Y. M., Cuitiño A. M., Khachaturyan A. G.

Nanoscale phase field microelasticity theory of dislocations: Model and 3D simulations. *Acta Materialia*, vol. 49, n° 10, 2001, p. 1847–1857.

[WEI 12] Weinberger C. R., Cai W.

Plasticity of metal nanowires. *Journal of Materials Chemistry*, vol. 22, n° 8, 2012, p. 3277–3292.

[WEI 16] Weinberger C. R., Garritt J Tucker

*Springer Series in Materials Science 245 Multiscale Materials Modeling for Nanomechanics*. 2016.

[WEY 02] Weygand D., Friedman L. H., Van Der Giessen E., Needleman A.

Aspects of boundary-value problem solutions with three-dimensional dislocation dynamics. *Modelling and Simulation in Materials Science and Engineering*, vol. 10, n° 4, 2002, p. 437–468.

[WIL 96] Williams D. B., Carter C. B.

*The Transmission Electron Microscope*, p. 3–17. Springer US, Boston, MA, 1996.

[WU 12] Wu W., Schäublin R., Chen J.

General dislocation image stress of anisotropic cubic thin film. *Journal of Applied Physics*, vol. 112, n° 9, 2012.

[XIA 03] Xiang Y., Cheng L. T., Srolovitz D. J., Weinan E.

A level set method for dislocation dynamics. *Acta Materialia*, vol. 51, n° 18, 2003, p. 5499–5518.

[YAN 04] Yan L., Khraishi T. A., Shen Y. L., Horstemeyer M. F.

A distributed-dislocation method for treating free-surface image stresses in three-dimensional dislocation dynamics simulations. *Modelling and Simulation in Materials Science and Engineering*, vol. 12, n° 4, 2004.

[YAN 17] Yang L., Bian J. J., Wang G. F.
Impact of atomic-scale surface morphology on the size-dependent yield stress of gold nanoparticles. *Journal of Physics D: Applied Physics*, vol. 50, n° 24, 2017, IOP Publishing.

[YAS 01] Yasin H., Zbib H. M., Khaleel M. A.
Size and boundary effects in discrete dislocation dynamics: Coupling with continuum finite element. *Materials Science and Engineering A*, vol. 309-310, 2001, p. 294–299.

[YOF 61] Yoffe E. H.
A dislocation at a free surface. *Philosophical Magazine*, vol. 6, n° 69, 1961, p. 1147–1155.

[YU 15] Yu Q., Legros M., Minor A. M.
In situ TEM nanomechanics. *MRS Bulletin*, vol. 40, n° 1, 2015, p. 62–68.

[YU 18] Yu H., Xin Y., Wang M., Liu Q.
Hall-Petch relationship in Mg alloys: A review. *Journal of Materials Science and Technology*, vol. 34, n° 2, 2018, p. 248–256.

[ZAE 11] Zaefferer S.
A critical review of orientation microscopy in SEM and TEM. *Crystal Research and Technology*, vol. 46, n° 6, 2011, p. 607–628.

[ZBI 02a] Zbib H. M., De la Rubia T. D., Bulatov V.
A multiscale model of plasticity based on discrete dislocation dynamics. *Journal of Engineering Materials and Technology, Transactions of the ASME*, vol. 124, n° 1, 2002, p. 78–87.

[ZBI 02b] Zbib H. M., Diaz de la Rubia T.
A multiscale model of plasticity. *International Journal of Plasticity*, vol. 18, n° 9, 2002, p. 1133–1163.

[ZEN 17] Zeng X. M., Du Z., Tamura N., Liu Q., Schuh C. A., Gan C. L.
In-situ studies on martensitic transformation and high-temperature shape memory in small volume zirconia. *Acta Materialia*, vol. 134, 2017, p. 257–266.

[ZHA 10] wang Zhang H., Liu Y., heng Sun S.
Synthesis and assembly of magnetic nanoparticles for information and energy storage applications. *Frontiers of Physics in China*, vol. 5, n° 4, 2010, p. 347–356.

[ZHO 10] Zhou C., Biner S. B., LeSar R.
Discrete dislocation dynamics simulations of plasticity at small scales. *Acta Materialia*, vol. 58, n° 5, 2010, p. 1565–1577.

[ZHU 04] Zhu Y. T., Liao X.
Nanostructured metals: Retaining ductility. *Nature Materials*, vol. 3, n° 6, 2004, p. 351–352.

[ZHU 08] ZHU T., LI J., SAMANTA A., LEACH A., GALL K.
Temperature and strain-rate dependence of surface dislocation nucleation. *Physical Review Letters*, vol. 100, n° 2, 2008, Page 025502.

# FOLIO ADMINISTRATIF

## THESE DE L'INSA LYON, MEMBRE DE L'UNIVERSITE DE LYON

NOM : GONZALEZ JOA DATE de SOUTENANCE : 12/12/2022
(avec précision du nom de jeune fille, le cas échéant)

Prénoms : JAVIER ANTONIO

TITRE : Mesoscale dislocation simulation accounting for surfaces using the superposition method: application to nanomechanics

NATURE : Doctorat

Numéro d'ordre : 2022ISAL0129

Ecole doctorale : ED 34: Matériaux de Lyon

Spécialité : Science des Matériaux

RESUME :

Les nano-objets (fils, particules, films minces) sont connus pour leurs propriétés mécaniques exceptionnelles au regard de leurs homologues massifs. Diverses techniques expérimentales (TEM, SEM, diffraction des rayons X) sont utilisées pour étudier les nano-objets, complétées par des approches numériques telle que la Dynamique Moléculaire (DM). Bien que fournissant des détails à l'échelle atomique, la DM reste limitée en termes de taille et de vitesse de déformation, ouvrant la porte à d'autres méthodes comme la Dynamique des Dislocations Discrète (DDD). La DDD permet de décrire l'évolution d'une population de dislocations à l'échelle du grain mais est généralement utilisée dans des ensembles quasi-infinis en utilisant des cellules de simulation particulièrement grandes ou des conditions limites périodiques. Par conséquent, la DDD seule ne peut fournir une description physique des surfaces d'un échantillon, surfaces à l'origine de nombreux processus à l'échelle nanométrique.

Cette étude vise à modéliser mieux et plus fidèlement la mécanique des nano-objets en tenant compte des interactions complexes entre les dislocations et les surfaces. Pour ce faire, un nouvel outil appelé El-Numodis a été développé. El-Numodis repose sur le couplage du code de DDD Numodis au code d'éléments finis Elmer en utilisant la méthode de superposition. Nous présentons ici les étapes de développement d'El-Numodis (pilotes de couplage, forces d'image des dislocations, algorithme de nucléation, etc.) ainsi que plusieurs applications incluant des problèmes d'élasticité classiques dans lesquels des surfaces sont impliquées. A titre d'exemple, la modélisation de films minces métalliques montre l'influence majeure des surfaces sur la mécanique des nano-objets. Enfin, El-Numodis est utilisé pour modéliser la mécanique de nanoparticules céramiques où la nucléation de dislocation informée de manière atomistique, combinée à la théorie de l'état de transition, permet d'étudier le rôle de la température et de la vitesse de déformation sur la déformation de nanocubes de MgO.

MOTS-CLÉS : dynamique des dislocations, méthode de superposition, nano-objets, forces images

Laboratoire (s) de recherche : MATEIS, UMR CNRS 5510

Directeurs de thèse: Jonathan Amodeo, CNRS, Aix-Marseille Univ.
Michel Perez, INSA Lyon

Président de jury :

Composition du jury :
Rapporteur : Dan Mordehai, Technion, Israel
Rapporteur : Fabien Onimus, CEA Saclay
Examinatrice : Karine Masenelli-Varlot, INSA Lyon
Examinatrice : Celine Gerard, ENSMA
Examinateur : David Rodney, Univ. Lyon
Examinateur : Laurent Pizzagalli, Iniv. Poitiers